HYDRODYNAMIC INTERACTIONS AND MOTION OF BACTERIA AT LOW REYNOLDS NUMBER

by

Mehdi Jabbarzadeh

A dissertation submitted to the faculty of
The University of Utah
in partial fulfillment of the requirements for the degree of

Doctor of Philosophy

Department of Mechanical Engineering

The University of Utah

May 2018

The University of Utah Graduate School

STATEMENT OF DISSERTATION APPROVAL

The dissertation of **Mehdi Jabbarzadeh**

has been approved by the following supervisory committee members:

Henry Fu	, Chair	**2/23/2018** Date Approved
Keunhan Park	, Member	**2/23/2018** Date Approved
Marc Calaf	, Member	**2/23/2018** Date Approved
Meredith Metzger	, Member	**2/23/2018** Date Approved
Christel Hohenegger	, Member	**2/26/2018** Date Approved

and by **Tim Ameel** , Chair/Dean of

the Department/College/School of **Mechanical Engineering**

and by David B. Kieda, Dean of The Graduate School.

ABSTRACT

Microorganism motility supports many features in the microbial world and is closely linked to their abilities to find food, mate, and colonize, which are essential to their survival. While swimming, the organisms interact with their fluid environment in a manner quite different from our common human experience in fluids, making it interesting to understand the physics of such low Reynolds number hydrodynamics. In this dissertation, I discuss four different aspects of locomotion in viscous fluids.

We first study the suitable choice of computational method for swimming and pumping with a helical flagellar filament at a low Reynolds number. Comparing the most commonly used approaches to solve Stokes equations numerically, we provide a guideline for the optimal choice of the tuning parameters for a wide helical geometries range balancing the accuracy and computational time expenses.

We then study the effect of helical cell bodies on the swimming speed and trajectory by comparing to rod-shaped geometries. We validate our numerical model with experiments from high-frame-rate digital tracking and image processing for both helical and straight mutant (*Helicobacter pylori*) swimming mucin and broth solution. We find that the helicity of the cell body makes at most a 15% contribution to the additional thrust and change in swimming speed.

We also study the single-flagellated bacterial flicks and instabilities due to hook and flagellum flexibilities. We find that dynamic instability initiates bacterial flick and

then flexibility of the flagellar filament plays an important role in reorientation of the swimmer.

Finally, we consider hydrodynamic interactions of a swimmer with a complex biological environment and other passive particles in viscous fluid. We examine long-range hydrodynamic interactions of a simple swimmer near spherical and filamentous obstacles and find that swimming velocity fluctuation is closely related to the correlations in density and orientations of obstacles. For the hydrodynamic interactions and approach of organisms with passive particles, we find exact solutions for the approach of spherical shapes in the cases that the swimmer is driven by a localized constant force and with distributed propulsion (*squirmer model*). We study the feasibility of approach and find that an organism can approach any similar size or bigger target compared to the organism's size, but approaching smaller targets depends on the current strength generated by the swimmer.

TABLE OF CONTENTS

ACKNOWLEDGEMENTS

I would like to start by thanking my supervisor professor Henry Fu. I am deeply grateful for having the opportunity to collaborate with him during my PhD at the University of Utah. He has not only been my compass for technical thinking, but also a great help for developing my nonacademic skills.

I am thankful to my doctoral committee members for taking their time to provide constructive comments about my research work over the past years. I sincerely thank all the research project collaborators and sponsors, paper co-authors and contributors, and faculty and staff members who shared their knowledge and experience to help me complete my graduate studies.

I would like to credit my lab-mates and research faculties since without them, it would have been a much harder job to live in a whole new country and do a PhD. I would like to especially thank Amir Mirbagheri, Farshad Meshkati, James D. Martindale, and Kiarash Samsami for the uncountable little and big things they have done for me.

CHAPTER 1

INTRODUCTION

Microorganism motility affects many aspects of life, including infections, reproduction, and life ecosystems. Locomotion can greatly aid organisms' survival and is closely linked to the ability of finding food, mating, and colonizing new environments. Bacterial motion happens in a viscous flow at low Reynolds number where viscous effects are dominant and is different from our common experience at high Reynolds number. This lack of intuition about the physics governing swimming at low Reynolds number makes it interesting to study locomotion in detail to understand biology as well as to design microscale artificial swimmers.

Many researchers have studied swimming dynamics, measuring the swimming speeds and trajectories, and have then compared them to mathematical models (e.g., case review by [1]). Most commonly, the models used are the simplest possible and for swimmers in unbounded Newtonian fluid. For instance, the most common strategies used by organisms for their locomotion are a rotating flagellum or beating cilia. Mathematical models treat these using a rigid rotating helical flagellar filament or progressive waves of a ciliated surface, especially for spherical or ellipsoidal cell bodies [2]–[6].

However, besides swimming in unbounded fluids, many organisms live in complex

biological environments, confined media, or they interact with other cells and particles nearby. The approaches to model these interactions are different from the models used for a single cell in an unbounded domain and hydrodynamic interactions play an important role. It is desirable to have mathematical models that can capture these effects, such as by modeling complex environments with viscoelastic models of the fluids, or directly studying the hydrodynamic interactions of the swimmer with other objects or confined media [1], [5], [7]–[11].

In this dissertation, I discuss studies adding three different aspects of locomotion to the simplest models of swimming most commonly used so far, namely: the effect of helical cell bodies on the swimming speed and trajectory of organisms, the effect of flexibility of the hook and flagellum on the swimming dynamics, and the effect of hydrodynamic interactions of swimmers with complex environments and passive objects in the fluid.

From experimental observations, it is usually easier to measure the swimming speed, trajectory, and body rotation rate of the cell body. Taking advantage of the linearity of the Stokes equation governing the Newtonian viscous flow and employing appropriate mathematical and numerical models, one may match experimental observations to find the properties of the swimming cell, such as flagellum rotation rates, motor torques, or flow fields around the swimmer. Different numerical methods with different level of accuracy and computational expenses have been developed to solve the Stokes equation. For instance, resistive force theory (RFT) and slender body theory (SBT) are less computationally expensive and are useful for slender objects (especially slender flagella) while boundary element methods (BEM) and the method of regularized Stokeslets can be implemented for any object or swimmer moving in viscous fluid. In Chapter 2, we discuss

the different numerical approaches and their applications in modeling swimming and pumping of a wide range of helical filaments.

Using an appropriate approach to model swimming dynamics, we can study many parameters that can affect swimming dynamics and mobility of bacteria including different geometries or environmental properties of the viscous fluid. Organisms can be found in a wide variety of cell body shapes and a wide range of geometries of the flagellum helices. For a flagella-propelled bacteria, the rotating helical flagellum provides propulsion for the swimmer, and because the swimmer is force- and torque- free, the cell body counter-rotates. For a spherical or ellipsoidal cell body, these rotations do not produce any additional thrust due to symmetry. However, geometries of the cell body can alter swimming speed because the drag on the cell body depends on its shape and in some cases, for example helical cells, may have additional contributions to the propulsive thrust. In Chapter 3, we study the effect of the cell body on the swimming speed and trajectory of a flagellated swimmer.

Most mathematical and numerical methods are designed to study rigid body motion of the organisms. In these efforts, the single or bundle of the flagellum is considered as a rigid helical filament rotating behind a rigid cell body [12], [13], [14], [15], [16], [4], [17], [18], [19]. However, the most recent experiments show that the flexibility of the hook or flagellum may play an important roll in mobility of bacteria [12]–[19]. For multi-flagellated bacteria, the flexibility of the hook is essential in bundling and reorientation of bacteria in run and tumble motion. On the other hand, for the single-flagellated bacteria, the buckling of the hook and flexibility of the flagellum are the key parameters for the run-reverse-flick mobility. Thus, it is necessary to analyze the effects of the flexibility to

understand mobility and swimming of bacteria. Hence we will discuss these effects and their effects on the swimming dynamics of the single-flagellated bacterium in Chapter 4.

Some microorganisms swim through complex biological environments. For instance, *H. pylori* swims through gastric mucus, and mammalian sperm swim through the cervical mucus, both of which are more complicated than simple Newtonian fluids. These kinds of biological environments are viscoelastic gels made of cross-linked polymeric networks immersed in a liquid with behavior closer to solids rather than a fluid. Hydrodynamic interactions with a complex biological environment affect swimming speed of the organisms depending on the lengthscale of the swimmer and microstructure of the fluid. When the lengthscale of a synthetic media is much smaller than the organism, one may use continuum models with a constitutive law describing non-Newtonian behavior for the fluid [20]–[27]. On the other hand, when the lengthscale of the organism and microstructural heterogeneity are comparable, the fluid cannot be considered as a homogeneous media and hydrodynamic interactions with the microstructures become more important, changing the swimming speed of the swimmer. In Chapter 5, we use a simple three-sphere swimmer directly interacting with spherical and filamentous objects immersed in the fluid to measure the swimming speed fluctuations due to such interactions in comparison to the unbounded swimming velocity.

Other kinds of interactions occur when the organisms want to intentionally directly approach other passive or active particles, for instance during feeding and mating processes. For these cases, the organisms and targets are too close to each other and hydrodynamic interactions become more important, which hinder the approach and manipulation processes of the microorganisms and target particles. When two surfaces are

very close to each other, numerical solutions become difficult to use and it is appropriate to obtain exact solutions to accurately study hydrodynamic interactions. In Chapter 6, we considered a spherical swimmer and targets and find exact solutions for hydrodynamic interactions and study the approach of different swimmer:target size ratios.

1.1 Organization of the dissertation

In Chapter 2, we examine the proper choice of numerical method for obtaining accurate results for two physical scenarios: a swimmer with a head or a pump in Stokes flow. We compare the accuracy of resistive force theory, slender body theory, and a centerline distribution of regularized Stokeslets for a range of helical filament to establish guidelines for the choice of numerical method. This paper was published as D. Martindale, M. Jabbarzadeh, and H. C. Fu, "Choice of computational method for swimming and pumping with nonslender helical filaments at low Reynolds number," Phys. Fluids, vol. 28, no. 2, p. 21901, 2016.

In Chapter 3, we examine the swimming ability of the helical-body-shaped *H. pylori* bacteria and compare swimming velocities to the rod-shaped bacteria. We use the method of regularized Stokeslets to model helical- and rod-shaped bacteria and directly compare swimming velocities and trajectories to the experimental observations. We find that the helical shape makes at most a 15-percentage contribution to propulsive thrust compared to the rod shape. This paper was published as M. A. Constantino, M. Jabbarzadeh, H. C. Fu, and R. Bansil, "Helical and rod-shaped bacteria swim in helical trajectories with little additional propulsion from helical shape," Sci. Adv., vol. 2, no. 11, pp. e1601661–e1601661, 2016.

In Chapter 4, we study effects of the hook's flexibility on the bacteria's swimming speed and trajectory for wide range hook stiffnesses and flagellum configurations. We develop an efficient simplified spring model for the hook by linearizing the Kirchhoff rod. We investigate flagellar and swimming dynamics for a range of hook flexibilities and flagellar orientations relative to the cell body and compare the results to models without hook flexibility. We find that as the hook stiffness decreases, steady-state orbits of the flagellum first become unstable before the hook buckles, which may suggest a new mechanism of flick initiation in run-reverse-flick motility. This paper was published as M. Jabbarzadeh and H. C. Fu, "Dynamic instability in the hook-flagellum system that triggers bacterial flicks," Phys. Rev. E, vol. 97, no. 1, p. 12402, 2018.

In Chapter 5, we study hydrodynamic interactions of a swimmer and obstacles in the viscous flow. We consider a simple three-bead swimmer to calculate swimming velocity fluctuations near spherical and filamentous obstacles. We show that hydrodynamic interactions of the swimmer with the heterogeneities lead to fluctuations in swimming velocities that depend on correlations in density and orientation of filamentous networks in the media. This paper was published as M. Jabbarzadeh, Y. Hyon, and H. C. Fu, "Swimming fluctuations of micro-organisms due to heterogeneous microstructure," Phys. Rev. E, vol. 90, no. 4, p. 43021, 2014.

In Chapter 6, we study the approach and interactions of the microorganism with target particles in viscous flow. We assume a spherical swimmer with localized and distributed propulsion approach to a spherical target particle along their centerline. We investigate the feasibility of approach for different swimmer:target size ratio. We show that the feasibility of the approach depends on the type of swimmer and swimmer:target ratio.

This chapter is in preparation for submission to a journal.

1.2 Swimming at low Reynolds number

To study swimming behavior of an organism, it is necessary to find the velocity ($\boldsymbol{u}$) and pressure (p) distribution around the swimmer. For an incompressible Newtonian fluid with density ρ and dynamic viscosity μ, the flow satisfies the Navier-Stokes equations and mass conservation,

$$\rho\left(\frac{\partial}{\partial t}+\boldsymbol{u}\cdot\boldsymbol{\nabla}\right)\boldsymbol{u}=-\boldsymbol{\nabla}p+\mu\boldsymbol{\nabla}^2\boldsymbol{u},\quad \boldsymbol{\nabla}\cdot\boldsymbol{u}=0. \tag{1.1}$$

with appropriate boundary conditions for the organism, which could be either as deformable or rigid bodies.

The Reynolds number is a dimensionless quantity that represents the ratio of the typical inertial force $\sim \rho(\boldsymbol{u}\cdot\boldsymbol{\nabla u})$, to the viscous force $\sim \mu\boldsymbol{\nabla}^2\boldsymbol{u}$ in the Navier-Stokes equation 1.1. Thus, for an organism with characteristic length L swimming with typical velocity U, the Reynolds number is $Re = \rho\, L\, U/\mu$. Microorganisms swim at low Reynolds number, which viscous forces dominate in the flow. For example, considering motion in water with density about $1000[kg/m^3]$ and viscosity of $0.001[Pa\ s]$, the bacterium *E. coli* with $U \approx 10\ \mu\ m/s$ and $L \approx 1-10\mu\ m$, the Reynolds number is $Re \approx\ 10^{-5}-10^{-4}$ [3] Marine bacteria *Vibrio alginolyticus* with $U \approx\ 50\ \mu\ m/s$ and $L \approx\ 5\ \mu\ m$ have a Reynolds number $Re \approx\ 10^{-4}$ [28]. For larger ciliated swimmers such as *Paramecium* with $U \approx 1mm/s$ and $L \approx\ 1mm$, the Reynolds number is $Re \approx\ 0.1$ [29]. All these examples show that Reynolds number for microswimmers is very small ($Re \ll 1$) and it is appropriate to work at zero Reynolds number limit ($Re = 0$) to study fluid mechanics of the microorganisms, for which the Navier-Stokes (equations 1.1) simplify to the Stokes

equations

$$-\boldsymbol{\nabla} p + \mu \boldsymbol{\nabla}^2 \boldsymbol{u} = 0, \quad \boldsymbol{\nabla} \cdot \boldsymbol{u} = 0. \tag{1.2}$$

The Stokes equation is linear and has a time reversal property that leads to an important consequence for locomotion called the Scallop theorem. The Scallop theorem states that for an organism swimming in Stokes flow, the net swimming velocity (or net displacement) is zero if an organism executes a cycle of configuration that is indistinguishable from its time-reversed cycle. The reasoning here is that a swimmer moves forward with velocity U in half of the cycle and moves backward with velocity $-U$ on the other half because the two motions are indistinguishable (changing $t \to -t$, $U \to -U$ also satisfies the Stokes equation [30] and would result in back-and-forth motion along a line, with no net locomotion). Microorganisms break time reversal symmetry by many methods. Flagellated swimmers propagate waves from the cell body to the tail by rotation of a helical flagellum. Ciliated micro-swimmers execute a forward and return pattern of stroke that is not time symmetric.

Finally working in the zero limit of Reynolds number, the effect of the inertia is zero and Newton's law becomes a simple statement balancing instantaneous external and fluid forces and torques,

$$\boldsymbol{F}(t)_{ext} + \boldsymbol{F}(t) = \boldsymbol{0}, \quad \boldsymbol{N}(t)_{ext} + \boldsymbol{N}(t) = \boldsymbol{0}. \tag{1.3}$$

Most organisms have comparable density to the fluid and are considered as neutrally buoyant swimmers. Therefore, in the absence of any other external force ($\boldsymbol{F}(t)_{ext} = \boldsymbol{0}$) and torques ($\boldsymbol{N}(t)_{ext} = \boldsymbol{0}$), the swimming cell is force- and torque-free. This condition requires that subparts of a swimmer should exert force and torque on each other to balance force- and torque-free conditions on the whole swimmer. For instance, for a

flagellated swimmer, the drag force and torque on the cell body balance force and torque from the rotating flagellum and cause counter-rotation of the cell body with respect to the flagellar filament. Also, net force balance (equation 1.3) holds for each subpart, where external force includes forces exerted by the rest of swimmer on that subpart.

1.3 References

[1] E. Lauga and T. R. Powers, "The hydrodynamics of swimming microorganisms," *Reports Prog. Phys.*, vol. 72, no. 9, p. 96601, 2009.

[2] A. C. Balazs, A. Bhattacharya, A. Tripathi, and H. Shum, "Designing bioinspired artificial cilia to regulate particle--surface interactions," *J. Phys. Chem. Lett.*, vol. 5, no. 10, pp. 1691–1700, 2014.

[3] H. C. Berg, *E. coli in Motion*. Springer Science & Business Media , 2008.

[4] T. Fujita and T. Kawai, "Optimum shape of a flagellated microorganism," *JSME Int. J. Ser. C Mech. Syst. Mach. Elem. Manuf.*, vol. 44, no. 4, pp. 952–957, 2001.

[5] J. J. Molina, Y. Nakayama, and R. Yamamoto, "Hydrodynamic interactions of self-propelled swimmers," *Soft Matter*, vol. 9, no. 19, pp. 4923–4936, 2013.

[6] J. R. Blake, "A spherical envelope approach to ciliary propulsion," *J. Fluid Mech.*, vol. 46, no. 1, pp. 199–208, 1971.

[7] H. Shum, E. A. Gaffney, and D. J. Smith, "Modelling bacterial behaviour close to a no-slip plane boundary: the influence of bacterial geometry," in *Proceedings of the Royal Society of London A: Mathematical, Physical and Engineering Sciences* , 2010, vol. 466, no. 2118, pp. 1725–1748.

[8] A. J. Reynolds, "The swimming of minute organisms," *J. Fluid Mech.*, vol. 23, no. 2, pp. 241–260, 1965.

[9] J. R. Blake and A. T. Chwang, "Fundamental singularities of viscous flow," *J. Eng. Math.*, vol. 8, no. 1, pp. 23–29, 1974.

[10] D. F. Katz, J. R. Blake, and S. L. Paveri-Fontana, "On the movement of slender bodies near plane boundaries at low Reynolds number," *J. Fluid Mech.*, vol. 72, no. 3, pp. 529–540, 1975.

[11] M. A. R. Koehl and J. R. Strickler, "Copepod feeding currents: food capture at low

Reynolds number.,” *Limnol. Oceanogr.*, vol. 26, no. 6, pp. 1062–1073, 1981.

[12] K. D. Young, “The selective value of bacterial shape,” *Microbiol. Mol. Biol. Rev.*, vol. 70, no. 3, pp. 660–703, 2006.

[13] F. A. Samatey, H. Matsunami, K. Imada, S. Nagashima, and others, “Structure of the bacterial flagellar hook and implication for the molecular universal joint mechanism,” *Nature*, vol. 431, no. 7012, p. 1062, 2004.

[14] K. Son, D. R. Brumley, and R. Stocker, “Live from under the lens: exploring microbial motility with dynamic imaging and microfluidics,” *Nat. Rev. Microbiol.*, vol. 13, no. 12, p. 761, 2015.

[15] N. Watari and R. G. Larson, “The hydrodynamics of a run-and-tumble bacterium propelled by polymorphic helical flagella,” *Biophys. J.*, vol. 98, no. 1, pp. 12–17, 2010.

[16] P. J. A. Janssen and M. D. Graham, “Coexistence of tight and loose bundled states in a model of bacterial flagellar dynamics,” *Phys. Rev. E*, vol. 84, no. 1, p. 11910, 2011.

[17] H. Shum and E. A. Gaffney, “The effects of flagellar hook compliance on motility of monotrichous bacteria: a modeling study,” *Phys. Fluids*, vol. 24, no. 6, p. 61901, 2012.

[18] P. Kanehl and T. Ishikawa, “Fluid mechanics of swimming bacteria with multiple flagella,” *Phys. Rev. E*, vol. 89, no. 4, p. 42704, 2014.

[19] Y. Shimogonya, Y. Sawano, H. Wakebe, Y. Inoue, A. Ishijima, and T. Ishikawa, “Torque-induced precession of bacterial flagella,” *Sci. Rep.*, vol. 5, p. 18488, 2015.

[20] Y. Magariyama and S. Kudo, “A mathematical explanation of an increase in bacterial swimming speed with viscosity in linear-polymer solutions,” *Biophys. J.*, vol. 83, no. 2, pp. 733–739, 2002.

[21] J. R. Vélez-Cordero and E. Lauga, “Waving transport and propulsion in a generalized Newtonian fluid,” *J. Nonnewton. Fluid Mech.*, vol. 199, pp. 37–50, 2013.

[22] E. Lauga, “Propulsion in a viscoelastic fluid,” *Phys. Fluids*, vol. 19, no. 8, p. 83104, 2007.

[23] H. C. Fu, T. R. Powers, and C. W. Wolgemuth, “Theory of swimming filaments in viscoelastic media,” *Phys. Rev. Lett.*, vol. 99, no. 25, p. 258101, 2007.

[24] H. C. Fu, C. W. Wolgemuth, and T. R. Powers, “Beating patterns of filaments in

viscoelastic fluids," *Phys. Rev. E*, vol. 78, no. 4, p. 41913, 2008.

[25] H. C. Fu, C. W. Wolgemuth, and T. R. Powers, "Swimming speeds of filaments in nonlinearly viscoelastic fluids," *Phys. Fluids*, vol. 21, no. 3, p. 33102, 2009.

[26] J. Teran, L. Fauci, and M. Shelley, "Viscoelastic fluid response can increase the speed and efficiency of a free swimmer," *Phys. Rev. Lett.*, vol. 104, no. 3, p. 38101, 2010.

[27] G. J. Elfring, O. S. Pak, and E. Lauga, "Two-dimensional flagellar synchronization in viscoelastic fluids," *J. Fluid Mech.*, vol. 646, pp. 505–515, 2010.

[28] L. Xie, T. Altindal, S. Chattopadhyay, and X.-L. Wu, "Bacterial flagellum as a propeller and as a rudder for efficient chemotaxis," *Proc. Natl. Acad. Sci.*, vol. 108, no. 6, pp. 2246–2251, 2011.

[29] T. Ishikawa, M. P. Simmonds, and T. J. Pedley, "Hydrodynamic interaction of two swimming model micro-organisms," *J. Fluid Mech.*, vol. 568, pp. 119–160, 2006.

[30] S. Childress, "Mechanics of swimming and flying, volume 2 of Cambridge Studies in Mathematical Biology ." Cambridge University Press, Cambridge , 1981.

CHAPTER 2

CHOICE OF COMPUTATIONAL METHOD FOR SWIMMING AND PUMPING WITH NONSLENDER HELICAL FILAMENTS AT LOW REYNOLDS NUMBER

PHYSICS OF FLUIDS **28**, 021901 (2016)

Choice of computational method for swimming and pumping with nonslender helical filaments at low Reynolds number

J. D. Martindale, M. Jabbarzadeh, and H. C. Fu
Department of Mechanical Engineering, University of Nevada, Reno, Nevada 89557, USA

(Received 16 June 2015; accepted 5 January 2016; published online 2 February 2016)

The flows induced by biological and artificial helical filaments are important to many possible applications including microscale swimming and pumping. Microscale helices can span a wide range of geometries, from thin bacterial flagella to thick helical bacterial cell bodies. While the proper choice of numerical method is critical for obtaining accurate results, there is little guidance about which method is optimal for a specified filament geometry. Here, using two physical scenarios — a swimmer with a head and a pump — we establish guidelines for the choice of numerical method based on helical radius, pitch, and filament thickness. For a range of helical geometries that encompass most natural and artificial helices, we create benchmark results using a surface distribution of regularized Stokeslets and then evaluate the accuracy of resistive force theory, slender body theory, and a centerline distribution of regularized Stokeslets. For the centerline distribution of regularized Stokeslets or slender body theory, we tabulate appropriate blob size and Stokeslet spacing or segment length, respectively, for each geometry studied. Finally, taking the computational cost of each method into account, we present the optimal choice of numerical method for each filament geometry as a guideline for future investigations involving filament-induced flows. © *2016 AIP Publishing LLC.* [http://dx.doi.org/10.1063/1.4940904]

I. INTRODUCTION

Low Reynolds number flows induced by filaments are commonly encountered in microscale scenarios. They occur in the swimming of microorganisms such as bacteria and spermatozoa,[1] as well as artificial flagella.[2–6] Furthermore, cilia- and flagella-induced microscale pumping is used in applications such as particle transport in biological systems[7,8] and the regulation and transport of fluids by fabricated systems utilizing bacterial flagella.[9] Filament-induced flows have been modeled using Resistive Force Theory (RFT), slender body theory (SBT), and boundary element methods (BEMs). For the slender filaments encountered in flagellar (bacterial and eukaryotic) swimming, there is some guidance in the literature as to which of these methods to use. Resistive force theory has been found to be inaccurate relative to slender body theory results,[10] while slender body theory and boundary element methods have compared favorably.[11,12] Recently, it has been shown that for slender helical filaments, RFT also gives misleading results in comparison to experiments.[13] However, not all helical filaments of interest are as slender as flagella, and there is less guidance available for the choice of method for thicker filaments. Thicker helical filaments can be realized in the helical cell bodies of many motile bacteria and are also important for magnetically actuated microscale swimming used for microrobotics, which could be used in medical applications such as *in vivo* surgery.[2,3,6,14,15]

While accurate and efficient computational models are needed for these filament-induced flows, it has not been established that which methods are appropriate for a given geometry given the wide range of filament thicknesses and helical pitches encountered, making it difficult for practitioners to make an informed choice without extensive numerical studies. Here, we compare the popular RFT, SBT, and two other methods based on the use of regularized Stokeslets. Each has different advantages and disadvantages in terms of ease of use, accuracy, and computational cost. Our objective

is to evaluate the accuracy and computational requirements of these methods across the range of geometries encountered in microscale applications in order to provide a guideline which may be used to make an informed choice of which numerical method to use for a given filament geometry.

What helical geometries are observed in the study of biological and artificial pumping and swimming applications? Consider a rigid helical filament whose geometry depends on three dimensionless parameters (see Fig. 1(a)): the ratio of the filament radius to helical radius $\tilde{a} = a/R$, the ratio of helical pitch to helical radius $\tilde{p} = p/R$, and the number of turns. In this study, we vary the parameters $\tilde{a}$ and $\tilde{p}$ to encompass the range of geometries encountered across most applications. Because Rodenborn *et al.*[13] find that the accuracy of SBT and the method of regularized Stokeslets are not dependent on total arclength, in this study we keep the arclength fixed at 3 pitch lengths.

Bacterial flagella are the thinnest filaments in our study with a radius of $a = 0.012$ μm.[16] For bacteria such as *Salmonella* and *E. coli*, the flagella may undergo polymorphic transformations between helical forms categorized by the number (n) of "R"-type protofilaments in the flagellum.[16–18] These polymorphic forms have a wide variation in both $\tilde{a}$ and $\tilde{p}$. For example, the normal ($n = 2$) form has values of $\tilde{a} = 0.023$ and $\tilde{p} = 1.611$, while the curly I ($n = 5$) form, seen in flagellar unbundling, has values of $\tilde{a} = 0.029$ and $\tilde{p} = 8.724$.[18] In Fig. 1(b), we have noted $\tilde{a}$ and $\tilde{p}$ for the $n = 1, 2$, and 9 polymorphic forms. These different bacterial flagellar forms are important not only for swimming and chemotaxis but also in micropumping applications. While we do not take into account the fluid structure interactions in this study, our results are relevant to any approach which would add deformations to the hydrodynamic interactions, such as for understanding the hydrodynamics associated with transformations between polymorphic configurations of these bacterial flagella.

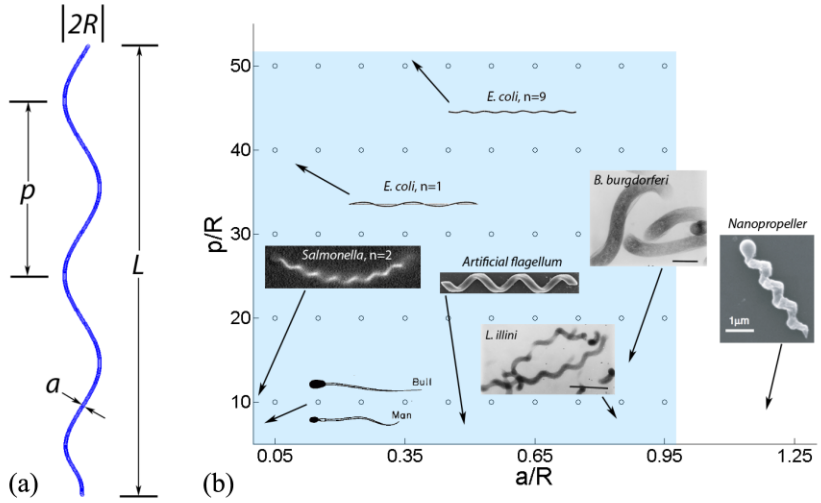

FIG. 1. (a) Geometry for helical filament in terms of filament radius a, helical pitch p, helical radius R, and helical length L. (b) Range of $\tilde{a} = a/R$ and $\tilde{p} = p/R$ values spanned by natural and artificial examples.[3,4,16,19,28] The shaded region indicates the geometry range investigated in this study; circles represent the specific investigated geometries. [*Nanopropeller* reprinted with permission from Ghosh *et al.*, "Dynamical configurations and bistability of helical nanostructures under external torque," Phys. Rev. E **86**, 031401 (2012). Copyright 2012 American Physical Society. *Artificial flagellum* reprinted with permission from C. Peters, O. Ergeneman, B. J. Nelson, and C. Hierold, in *2013 IEEE 26th International Conference on Micro Electro Mechanical Systems (MEMS)* (IEEE, 2013), pp. 564-567. Copyright 2013 IEEE. *Salmonella, n* = 2 reprinted with permission from N. Darnton and H. C. Berg, "Force-extension measurements on bacterial flagella: Triggering polymorphic transformations," Biophys. J. **92**, 2230-2236 (2007). Copyright 2007 Elsevier. *Bull, Man spermatozoa* reprinted with permission from C. Brennen and H. Winet, "Fluid mechanics of propulsion by cilia and flagella," Annu. Rev. Fluid Mech. **9**, 339–398 (1977). Copyright 1977 Annual Reviews Inc. *L. illini and B. burgdorferi* reprinted with permission from S. Goldstein, K. Buttle, and N. Charon, "Structural analysis of the Leptospiraceae and Borrelia burgdorferi by high-voltage electron microscopy," J. Bacteriol **178**, 6539–6545 (1996). Copyright 1996 American Society for Microbiology.]

At the slender end of the spectrum, we also find the flagella of various mammalian spermatozoa, whose waveforms were presented by Brennen and Winet.[19] Human spermatozoa have a filament radius of $a \approx 0.25$ μm, around 20 times larger than that of bacterial flagella. However, due to their larger helical radius, their values of $\tilde{a}$ and $\tilde{p}$ are on the same order as those of bacterial flagella, with $\tilde{a}$ ranging from 0.01 for bull spermatozoa to 0.05 for human spermatozoa, and $\tilde{p} \approx 10$.[19]

For the slender regime of bacterial and eukaryotic flagella, Brennen and Winet note that the slender body theory originally proposed by Lighthill[20] or the resistive force theory of Gray and Hancock[21] should be applicable. Although there are many well-known variants of slender body theory,[22–26] in this study, as a representative SBT, we use the implementation proposed by Higdon,[27] which is equivalent to Lighthill's and which provides a relatively easy to implement numerical framework.

Rodenborn *et al*. focus on the slender regime up to $\tilde{a} = 0.0625$, but thicker helical filaments are common. For example, spirochetes have helical or wavy cell bodies, such as *L. illini*, with $\tilde{a} = 0.835$ and $\tilde{p} = 7.977$, and *B. burgdorferi*, with $\tilde{a} = 0.868$ and $\tilde{p} = 14.895$.[28] Along with these spirochetes, thick filaments include artificial swimmers such as the magnetically actuated nanopropellers fabricated and studied by Ghosh *et al*.[2,3,29] with $\tilde{a} = 1.188$ and $\tilde{p} = 5.688$, and the artificial flagella studied by Peters and others[4,5] with $\tilde{a} = 0.483$ and $\tilde{p} = 5.517$. In this regime, we would expect the previously mentioned theories to fail as the filament is no longer slender.[27] Instead, to obtain accurate results, typically one must employ a BEM.[30] As a simple implementation of a BEM, we utilize the method of regularized Stokeslets, which covers the surface of an object with continuous analogues of the classical Stokes flow singularities[14,31–34] and has gained popularity due to its ease of use. Recent work on swimming sperm[35] and the beating patterns of cilia[8] have also distributed regularized Stokeslets along filament centerlines rather than at the surface, which yields significant savings in computational effort, so we also examine such centerline distributions of regularized Stokeslets. Optimal parameters have been found for centerline distributions for slender ellipsoids,[36] which may be used to model straight rods, but not for helical filaments.

To summarize the range of biological and artificial helical filaments encountered in microscale applications, in Fig. 1(b), we plot a number of the examples mentioned above in $\tilde{a}$ and $\tilde{p}$ space. In the following investigation, we will examine geometries with $\tilde{a}$ between 0.05 and 0.95 in increments of 0.1, and $\tilde{p}$ between 10 and 50 in increments of 10, which encompass most of the physical and artificial microswimmers seen in Fig. 1(b).

Our investigation evaluates the accuracy of resistive force theory, the centerline distribution of regularized Stokeslets, and the slender body theory for two physical scenarios by comparing to benchmark results obtained from surface distributions of regularized Stokeslets, which are verified by convergence studies. The first scenario we consider is that of a swimmer with an ellipsoidal head and helical flagellum (seen in Fig. 2). The swimmer is force-free ($\mathbf{F} = \mathbf{0}$) and is driven by setting a constant relative angular velocity $\boldsymbol{\omega}$ between the body and flagellum. The outputs we use to evaluate accuracy in this scenario are the translational velocity $\mathbf{V}$ and the total torque $\mathbf{N_f}$ on the flagellum. The second scenario we consider is a pump created by a rotating helical filament attached to a no-slip plane (seen in Fig. 2). Since the filament is fixed to a plane, the translational velocity is $\mathbf{V} = \mathbf{0}$, and to drive the pump, we apply a constant torque $\mathbf{N}$ to the filament. The outputs used

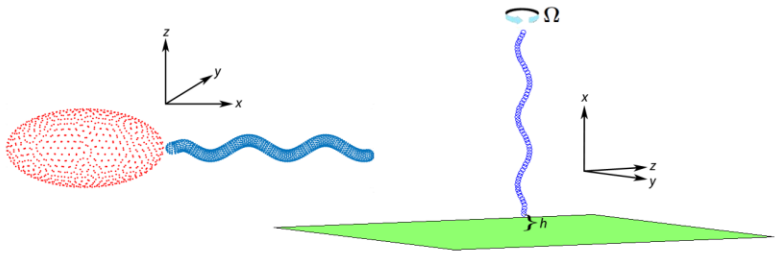

FIG. 2. The two physical scenarios modeled in this study: swimmer (left), pump (right).

to evaluate accuracy are the total force on the filament $\mathbf{F}$ and the angular velocity $\mathbf{\Omega}$. These two scenarios differ enough that they may be used as representatives for a broad range of applications.

Finally, we combine evaluation of the accuracy of resistive force theory, slender body theory, and the centerline distribution of regularized Stokeslets with an analysis of the relative computational cost for each method. The end result is a framework that can guide the choice of an optimal numerical method for a given filament geometry, which we hope will be broadly useful to researchers encountering flows caused by helical filaments in microscale applications.

II. NUMERICAL METHODS

In practice, SBT and methods involving regularized Stokeslets involve a similar procedure: the flow is created by an unknown force distribution, either on a surface for the method of regularized Stokeslets or on the filament centerline for slender body theory and centerline regularized Stokeslets. No-slip boundary conditions are imposed by setting the flow velocities at a set of collocation points equal to the velocity specified from the kinematics of the object. The result is the formation of a linear system of equations which may be solved to find the force distribution and hence velocity field everywhere. In equations, if $\mathbf{r}^0$ is the origin of the body frame, $\mathbf{V}$ is the translational velocity, and $\mathbf{\Omega}$ is the angular velocity about $\mathbf{r}^0$, then the velocity at point α is given by

$$\mathbf{u}(\mathbf{r}^\alpha) \equiv \mathbf{u}^\alpha = \mathbf{V} + \mathbf{\Omega} \times \Delta\mathbf{r}^\alpha, \tag{1}$$

where $\Delta\mathbf{r}^\alpha = \mathbf{r}^\alpha - \mathbf{r}^0$. Since this is a linear equation, we may write it in terms of the 3×6 matrix $\mathbf{k}^\alpha$,

$$\mathbf{u}^\alpha = \mathbf{k}^\alpha \begin{pmatrix} \mathbf{V} \\ \mathbf{\Omega} \end{pmatrix} = \begin{pmatrix} 1 & 0 & 0 & 0 & \Delta r_z^\alpha & -\Delta r_y^\alpha \\ 0 & 1 & 0 & -\Delta r_z^\alpha & 0 & \Delta r_x^\alpha \\ 0 & 0 & 1 & \Delta r_y^\alpha & -\Delta r_x^\alpha & 0 \end{pmatrix} \begin{pmatrix} \mathbf{V} \\ \mathbf{\Omega} \end{pmatrix}. \tag{2}$$

This allows us to represent the velocity at the collocation points of the system as

$$\mathbf{U} \equiv \begin{pmatrix} \mathbf{u}^1 \\ \vdots \\ \mathbf{u}^N \end{pmatrix} = \begin{pmatrix} \mathbf{k}^1 \\ \vdots \\ \mathbf{k}^N \end{pmatrix} \begin{pmatrix} \mathbf{V} \\ \mathbf{\Omega} \end{pmatrix} \equiv \mathbf{K} \begin{pmatrix} \mathbf{V} \\ \mathbf{\Omega} \end{pmatrix}, \tag{3}$$

where $\mathbf{K} \in \mathbb{R}^{3N \times 6}$. Note that we use a capital letter $\mathbf{U}$ to represent the $3\mathrm{N} \times 1$ vector containing the N velocities of all collocation points and similarly a capital $\mathbf{K}$ which is composed of all N $\mathbf{k}^\alpha$. To satisfy no-slip boundary conditions, the velocity specified by the kinematics is set equal to the fluid velocity at the collocation points. Thus, the fluid velocity vector $\mathbf{U}$ can also be written as

$$\mathbf{U} = \begin{pmatrix} \mathbf{g}^{1,1} & \mathbf{g}^{1,2} & \dots & \mathbf{g}^{1,N} \\ \mathbf{g}^{2,1} & \mathbf{g}^{2,2} & \dots & \mathbf{g}^{2,N} \\ \vdots & \vdots & \ddots & \vdots \\ \mathbf{g}^{N,1} & \mathbf{g}^{N,2} & \dots & \mathbf{g}^{N,N} \end{pmatrix} \begin{pmatrix} \mathbf{p}^1 \\ \vdots \\ \mathbf{p}^N \end{pmatrix} \equiv \mathbf{GP}, \tag{4}$$

where $\mathbf{G} \in \mathbb{R}^{3N \times 3N}$ and $\mathbf{P} \in \mathbb{R}^{3N \times 1}$ contains the 3×1 force $\mathbf{p}^\alpha$ at each collocation point. We call the submatrices $\mathbf{g}^{\alpha,\beta} \in \mathbb{R}^{3\times 3}$ the *kernel*. The kernel represents the velocity at point α due to a force at point β. Each numerical method in our study can be specified by choosing a different kernel.

A. BEM for flagellar filament above a no-slip plane

For the case of a rotating helical filament attached to a no-slip plane, we choose $\mathbf{r}^0 = \mathbf{0}$ at the attachment point at the plane surface (see Fig. 2) and represent the total force and torque on the body as

$$\mathbf{F} = \sum_{\alpha=1}^{N} \mathbf{p}^\alpha, \tag{5}$$

$$\mathbf{N} = \sum_{\alpha=1}^{N} \Delta\mathbf{r}^{\alpha} \times \mathbf{p}^{\alpha}, \tag{6}$$

which can be written as

$$\begin{pmatrix} \mathbf{F} \\ \mathbf{N} \end{pmatrix} = \mathbf{K}^T \mathbf{P}. \tag{7}$$

Enforcing the no-slip boundary condition on the surface of the filament lets us to form a relationship between the velocities $\mathbf{V}$ and $\boldsymbol{\Omega}$, and the total force $\mathbf{F}$ and torque $\mathbf{N}$ on the filament. Solving Eq. (4) for $\mathbf{P} = \mathbf{G}^{-1}\mathbf{U}$ and using Eqs. (3) and (7),

$$\begin{pmatrix} \mathbf{F} \\ \mathbf{N} \end{pmatrix} = \mathbf{K}^T \mathbf{G}^{-1} \mathbf{K} \begin{pmatrix} \mathbf{V} \\ \boldsymbol{\Omega} \end{pmatrix} = \mathbf{R} \begin{pmatrix} \mathbf{V} \\ \boldsymbol{\Omega} \end{pmatrix} = \begin{pmatrix} \mathbf{R_T} & \mathbf{R_C} \\ \mathbf{R_C}^T & \mathbf{R_R} \end{pmatrix} \begin{pmatrix} \mathbf{V} \\ \boldsymbol{\Omega} \end{pmatrix}, \tag{8}$$

where $\mathbf{R} = \mathbf{K}^T\mathbf{G}^{-1}\mathbf{K}$ is the resistance matrix with 3×3 translational, rotational, and coupling components denoted by $\mathbf{R_T}$, $\mathbf{R_R}$, and $\mathbf{R_C}$, respectively. We apply a constant torque $\mathbf{N}$ tangential to the axis of the filament and set the translational velocity $\mathbf{V} = \mathbf{0}$ since the filament remains anchored above the $x = 0$ plane. These constraints yield the system

$$\begin{pmatrix} \mathbf{F} \\ \mathbf{N} \end{pmatrix} = \begin{pmatrix} \mathbf{R_C} \\ \mathbf{R_R} \end{pmatrix} \boldsymbol{\Omega}, \tag{9}$$

with solution

$$\boldsymbol{\Omega} = \mathbf{R_R}^{-1}\mathbf{N}, \tag{10}$$

$$\mathbf{F} = \mathbf{R_C}\mathbf{R_R}^{-1}\mathbf{N}. \tag{11}$$

B. BEM for swimmer with ellipsoidal head

For the swimmer with an ellipsoidal head, we choose the origin of the body-fixed frame $\mathbf{r^0}$ as the flagellum attachment point on one end of the head (see Fig. 2). A surface distribution of regularized Stokeslets is always used to model the head, and these collocation points are denoted as $\mathbf{r_h^{\alpha_1}}$ for $1 \le \alpha_1 \le N_1$. The collocation points on the flagellum are denoted as $\mathbf{r_f^{\alpha_2}}$ for $1 \le \alpha_2 \le N_2$. In this scenario, $\mathbf{V}$ and $\boldsymbol{\Omega}$ represent the translation and rotation about the origin. Here, the kinematics specify

$$\mathbf{u_h}(\mathbf{r_h^{\alpha_1}}) = \mathbf{u_h^{\alpha_1}} = \mathbf{V} + \boldsymbol{\Omega} \times \Delta\mathbf{r_h^{\alpha_1}}, \tag{12}$$

$$\mathbf{u_f}(\mathbf{r_f^{\alpha_2}}) = \mathbf{u_f^{\alpha_2}} = \mathbf{V} + \boldsymbol{\Omega} \times \Delta\mathbf{r_f^{\alpha_2}} + \mathbf{k}_{\times}^{\alpha_2}\boldsymbol{\omega}, \tag{13}$$

where $\boldsymbol{\omega} = (\omega, 0, 0)^T$ is the specified relative rotation rate between the head and flagellum and

$$\mathbf{k}_{\times}^{\alpha_2} = \begin{pmatrix} 0 & \Delta r_z^{\alpha_2} & -\Delta r_y^{\alpha_2} \\ -\Delta r_z^{\alpha_2} & 0 & \Delta r_x^{\alpha_2} \\ \Delta r_y^{\alpha_2} & -\Delta r_x^{\alpha_2} & 0 \end{pmatrix}.$$

As in Section II, this is a linear system of equations and can be written as

$$\begin{pmatrix} \mathbf{U_h} \\ \mathbf{U_f} \end{pmatrix} \equiv \begin{pmatrix} \mathbf{u_h^1} \\ \vdots \\ \mathbf{u_h^{N_1}} \\ \mathbf{u_f^1} \\ \vdots \\ \mathbf{u_f^{N_2}} \end{pmatrix} = \begin{pmatrix} \mathbf{k}^{\alpha_1=1} \\ \vdots \\ \mathbf{k}^{\alpha_1=N_1} \\ \mathbf{k}^{\alpha_2=1} \\ \vdots \\ \mathbf{k}^{\alpha_2=N_2} \end{pmatrix} \begin{pmatrix} \mathbf{V} \\ \boldsymbol{\Omega} \end{pmatrix} + \dot{\mathbf{L}} \equiv \mathbf{K} \begin{pmatrix} \mathbf{V} \\ \boldsymbol{\Omega} \end{pmatrix} + \dot{\mathbf{L}}, \tag{14}$$

where $\mathbf{K} \in \mathbb{R}^{3(N_1+N_2)\times 6}$, $\mathbf{U_h} \in \mathbb{R}^{3N_1\times 1}$ is the velocity at each collocation point on the head, $\mathbf{U_f} \in \mathbb{R}^{3N_2\times 1}$ is the velocity at each collocation point on the flagellum, and $\dot{\mathbf{L}} \in \mathbb{R}^{3(N_1+N_2)\times 1}$ is

$$\dot{\mathbf{L}} = \begin{pmatrix} \mathbf{0} \\ \vdots \\ \mathbf{0} \\ \mathbf{k}_\times^{\alpha_2=1} \\ \vdots \\ \mathbf{k}_\times^{\alpha_2=N_2} \end{pmatrix} \boldsymbol{\omega}.$$

On the other hand, the hydrodynamics specify

$$\begin{pmatrix} \mathbf{U_h} \\ \mathbf{U_f} \end{pmatrix} = \begin{pmatrix} \mathbf{G_{hh}} & \mathbf{G_{hf}} \\ \mathbf{G_{fh}} & \mathbf{G_{ff}} \end{pmatrix} \begin{pmatrix} \mathbf{P_h} \\ \mathbf{P_f} \end{pmatrix} = \mathbf{GP}, \tag{15}$$

where $\mathbf{G_{hh}} \in \mathbb{R}^{3N_1 \times 3N_1}$ and $\mathbf{G_{fh}} \in \mathbb{R}^{3N_2 \times 3N_1}$ give the velocity on the head and flagellum, respectively, due to the point forces $\mathbf{p_h^{\alpha_1}}$ located on the head, and $\mathbf{G_{hf}} \in \mathbb{R}^{3N_1 \times 3N_2}$ and $\mathbf{G_{ff}} \in \mathbb{R}^{3N_2 \times 3N_2}$ give the velocity on the head and flagellum, respectively, due to the point forces $\mathbf{p_f^{\alpha_2}}$ located on the flagellum. Enforcing no-slip boundary conditions requires that the kinematic and hydrodynamic velocities to be equal, which yields the equation

$$\mathbf{G} \begin{pmatrix} \mathbf{P_h} \\ \mathbf{P_f} \end{pmatrix} = \mathbf{K} \begin{pmatrix} \mathbf{V} \\ \boldsymbol{\Omega} \end{pmatrix} + \dot{\mathbf{L}}. \tag{16}$$

In this scenario, we also require that the net force and net torque be zero, so Eq. (7) implies

$$\mathbf{0} = \mathbf{K}^T \begin{pmatrix} \mathbf{P_h} \\ \mathbf{P_f} \end{pmatrix} = \mathbf{K}^T \mathbf{G}^{-1} \left(\mathbf{K} \begin{pmatrix} \mathbf{V} \\ \boldsymbol{\Omega} \end{pmatrix} + \dot{\mathbf{L}} \right). \tag{17}$$

This equation can be solved for $\mathbf{V}$ and $\boldsymbol{\Omega}$ to obtain

$$\begin{pmatrix} \mathbf{V} \\ \boldsymbol{\Omega} \end{pmatrix} = -\left(\mathbf{K}^T \mathbf{G}^{-1} \mathbf{K}\right)^{-1} \mathbf{K}^T \mathbf{G}^{-1} \dot{\mathbf{L}}, \tag{18}$$

where $\mathbf{M} = \left(\mathbf{K}^T \mathbf{G}^{-1} \mathbf{K}\right)^{-1}$ is the inverse of the resistance matrix, called the mobility matrix. In this scenario, the translational velocity $\mathbf{V}$ and the torque on the flagellum $\mathbf{N_f}$ are the outputs. To solve for the torque, we find $\mathbf{P_f}$ through Eq. (16) since $\mathbf{V}$ and $\boldsymbol{\Omega}$ are now known, giving

$$\mathbf{N_f} = \sum_{\alpha_2=1}^{N_2} \Delta \mathbf{r}^{\alpha_2} \times \mathbf{p_f^{\alpha_2}}. \tag{19}$$

C. Resistive force theory for swimmer with ellipsoidal head

We also examine the accuracy of resistive force theory for the case of the swimmer. In resistive force theory, long-range hydrodynamic interactions are ignored, so we treat the hydrodynamics of the flagellum and head separately through their resistance matrices. The resistance matrix of the ellipsoidal head $\mathbf{R_h}$ may be calculated from analytical results, e.g., as presented in the textbook of Kim and Karrila.[37] Resistive force theory is used to calculate the resistance matrix of the helix as follows. The local force per unit length on the filament is

$$\mathbf{f}_{\mathrm{RFT}} = \xi_\perp \mathbf{v}_{\mathrm{rel}} + \left(\xi_\parallel - \xi_\perp\right) \hat{\mathbf{t}}\hat{\mathbf{t}} \cdot \mathbf{v}_{\mathrm{rel}}, \tag{20}$$

where $\mathbf{v}_{\mathrm{rel}} = \mathbf{V} + \boldsymbol{\Omega} \times \mathbf{r}$, $\hat{\mathbf{t}}$ is the local unit tangent vector, and the coefficients $\xi_\parallel$ and $\xi_\perp$ are drag coefficients obtained by slender body analysis. For the theories of Gray and Hancock[21] and Lighthill,[20] these coefficients are

$$\xi_\parallel,\ \xi_\perp = \begin{cases} \dfrac{2\pi\mu}{\ln(2\tilde{p}/\tilde{a}) - 1/2},\ \dfrac{4\pi\mu}{\ln(2\tilde{p}/\tilde{a}) + 1/2} & \text{(Gray and Hancock)} \\ \dfrac{2\pi\mu}{\ln(0.18\tilde{p}/\tilde{a})},\ \dfrac{4\pi\mu}{\ln(0.18\tilde{p}/\tilde{a}) + 1/2} & \text{(Lighthill)} \end{cases}.$$

Note that in Lighthill's formula, we use the pitch as suggested by analysis of helical filaments.[38] The Lighthill coefficients might be expected to be more applicable since in a comparison of RFT and SBT for planar thin filaments, Johnson and Brokaw[10] found that the Lighthill coefficients adequately predicted local forces and torques on the filament, while the Gray and Hancock coefficients required ~35% adjustments to produce comparable accuracy. Integrating the force and torque $\mathbf{r} \times \mathbf{f}_{RFT}$ along the filament for various translational and rotational velocities yields the resistance matrix $\mathbf{R_f}$ of the flagellum. The origin of rotation for both $\mathbf{R_h}$ and $\mathbf{R_f}$ is the flagellum attachment point.

Given the resistance matrices, we require that the total force and torque be zero,

$$\mathbf{0} = \begin{pmatrix} \mathbf{F}_{\text{tot}} \\ \mathbf{N}_{\text{tot}} \end{pmatrix} = \begin{pmatrix} \mathbf{F_h} \\ \mathbf{N_h} \end{pmatrix} + \begin{pmatrix} \mathbf{F_f} \\ \mathbf{N_f} \end{pmatrix}, \tag{21}$$

and using Eq. (8), we may express the above equation as

$$\mathbf{0} = \mathbf{R_h} \begin{pmatrix} \mathbf{V} \\ \boldsymbol{\Omega} \end{pmatrix} + \mathbf{R_f} \begin{pmatrix} \mathbf{V} \\ \boldsymbol{\Omega} + \boldsymbol{\omega} \end{pmatrix}. \tag{22}$$

This equation is solved for $\mathbf{V}$ and $\boldsymbol{\Omega}$ to give

$$\begin{pmatrix} \mathbf{V} \\ \boldsymbol{\Omega} \end{pmatrix} = -(\mathbf{R_h} + \mathbf{R_f})^{-1} \mathbf{R_f} \begin{pmatrix} \mathbf{0} \\ \boldsymbol{\omega} \end{pmatrix}, \tag{23}$$

which gives us one of our outputs, the translational velocity $\mathbf{V}$. Using the relationship

$$\begin{pmatrix} \mathbf{F_f} \\ \mathbf{N_f} \end{pmatrix} = \mathbf{R_f} \begin{pmatrix} \mathbf{V} \\ \boldsymbol{\Omega} + \boldsymbol{\omega} \end{pmatrix}, \tag{24}$$

we find our second output, the torque on the flagellum $\mathbf{N_f}$.

D. Geometries

1. Filament

In each of the physical scenarios described in Section I, we consider a helical filament oriented in the positive x-direction of non-dimensional radius $\tilde{a}$ and non-dimensional helical pitch $\tilde{p}$ whose arclength is fixed at $\tilde{L} = L/R = 3\tilde{p}$. The filament centerline is described by

$$\mathbf{r_c}(s) = s\hat{\mathbf{x}} + \left(1 - e^{-s^2/k_E^2}\right)\left[\cos(2\pi s/\tilde{p})\hat{\mathbf{y}} + \sin(2\pi s/\tilde{p})\hat{\mathbf{z}}\right]. \tag{25}$$

The exponential term describes a tapering region near the attachment point, where $k_E = \tilde{p}/(2\pi)$ is the characteristic length of the tapering region.[14]

2. Helical swimmer

For the helical swimmer, we use an ellipsoidal cell body with semi-major and semi-minor axes which are $\tilde{a}_h = a_h/R = 10.204$ and $\tilde{b}_h = b_h/R = 5.102$, respectively. The major axis is placed along the x-axis, and a helical flagellum whose geometry is prescribed in Eq. (25) is attached at $x = 0$. The helix is translated away from the ellipsoid to create a gap between the head and flagellum in order to ensure accurate results for nearby moving surfaces.[14] An example of this geometry is seen in Fig. 2.

3. Filament above a no-slip plane

Here, we examine the rotation of a helical filament with its end at a distance of $\tilde{h} = 10\tilde{a}$ above a no-slip plane (Fig. 2). To model this scenario, we translate the centerline prescribed above by $\tilde{h}$ in the x-direction. This setup is inspired by pumping applications where pumping flows may be caused by the movement of filaments.

E. Numerical methods: Kernels and discretization

1. Method of regularized Stokeslets: Surface distribution

For the benchmark cases, we employ the method of regularized Stokeslets by distributing smoothed analogues of the classical Stokeslet on the filament surface or body.[31–33] In the following calculations, we make use of a standard smoothing function which depends on a "blob" parameter δ that describes the spread of the point forces and allows us to obtain non-singular numerical values for all calculations. A full description of the regularized Stokeslet is found in the literature,[31–33] and the kernel $\mathbf{g}^{\alpha,\beta}$ (defined in Section II) that we use for the method of regularized Stokeslets is given by Eq. (10*b*) in the work of Cortez *et al.*[33]

For discretization, the filament is divided into cross sections perpendicular to the centerline of the filament. We place n_c evenly spaced Stokeslets on the perimeter of each cross section, similar to the discretization described previously by Hyon *et al.*[14] The cross sections are spaced so that the distance between Stokeslets (Δs) on a given cross section is the same as the distance between successive cross sections. Therefore, $\Delta s = 2\tilde{a}\sin(\pi/n_c)$. This spacing means that the total number of Stokeslets increases rapidly as we increase the number of Stokeslets per cross section and as the filament radius decreases. For a given spacing, the blob parameter δ is set equal to the distance between Stokeslets, $\delta = \Delta s$.

For the discretization of the swimmer with an ellipsoidal head, each successive filament cross section is rotated by an angle π/n_c with respect to its normal axis in order to stagger the Stokeslets. Also, the ends of the filament are capped with hemispheres that are discretized using the grid method given by Cortez *et al.*[33] The ellipsoidal head is discretized by cutting into cross sections perpendicular to the major (fore-aft) axis. If we define Δs_h as the spacing between Stokeslets on the cell body and successive cross sections, the number of Stokeslets on each cross section depends on the radius of the cross section and is determined by $n_c = 2\pi r_h/\Delta s_h$, where $r_h = \tilde{b}_h\sqrt{1-(x/\tilde{a}_h)^2}$. Similarly to the flagellum, each successive cross section of the head is rotated by an angle $\Delta s_h/2r_h$ to stagger the Stokeslets on the cell body. For our investigation, $\Delta s_h = 0.1$ is the non-dimensional Stokeslet spacing on the head, and $N_1 = 750$ is the total number of regularized Stokeslets on the head.

The case of the filament rotating above a no-slip plane uses a slightly different discretization. The cross sections are not rotated about the normal axis of the filament, and there are no hemispherical caps added to the end of the filament. Most importantly, the kernel is modified to satisfy the no-slip boundary conditions at the planar boundary ($x = 0$). For the method of regularized Stokeslets, we employ a full regularized Blakeslet distribution which consists of the regularized Stokeslet and its corresponding image system mirrored about the $x = 0$ plane:[31] for a collocation point on the filament surface at $\mathbf{r}^\alpha = (h^\alpha, y^\alpha, z^\alpha)$, its image is located at a point $\mathbf{r}^\alpha_* = (-h^\alpha, y^\alpha, z^\alpha)$. In this scenario, the kernel $\mathbf{g}^{\alpha,\beta}$ is derived from Eq. (21) in the work of Ainley *et al.*[31]

2. Method of regularized Stokeslets: Centerline distribution

The flows around filaments have also been computed using a centerline distribution along the center of the filament instead of at the filament surface. For this method, we use the same kernels as in Section II E 1. For the swimmer, the head is always modelled using a surface distribution of regularized Stokeslets with spacing and blob size as defined in Sec. II E 1.

For both the swimmer and the pump, we discretize the filament centerline by placing regularized Stokeslets with blob size δ at equally spaced points along the filament centerline with spacing Δs. There is no *a priori* choice of Stokeslet spacing Δs or blob size δ, although physically the blob size is expected to be of the same order of magnitude as the filament radius. These parameters must be tuned for each geometry to obtain the most accurate result. We report the optimal parameter values for each geometry we study later; these provide starting points for studies determining the optimal parameter values for other geometries in future studies. Despite this, the positive aspects of this discretization are twofold. First, it still relies on the method of regularized Stokeslets, and so we may use the same kernels found in the works of Cortez *et al.*[33] and Ainley *et al.*,[31] which are relatively easy to implement. Second, the number of Stokeslets needed for the discretization is much lower than that of the surface distribution, increasing the computational efficiency of the method.

3. Slender body theory

In our investigation, we use the slender body theory outlined by Higdon[27] as a representative SBT. This method calculates the flow due to a distribution of classical Stokeslets and dipoles along the centerline of the filament. The force distribution $\mathbf{f}$ along the centerline is unknown, while the dipole strength $\mathbf{d} = -(\tilde{a}^2/4\mu)\mathbf{f}_\perp$ is specified to preserve no-slip boundary conditions on the surface of the filament. In Higdon's method, the filament centerline is discretized into small cylindrical segments of length $2q$, and the Stokeslet (and hence dipole strength) is assumed to be constant within each segment. The integral of the Stokeslet and dipole distribution along each segment can be evaluated analytically to yield the flow produced by each segment, which defines the kernel. The expression for the kernel we use can be found in Eq. (27) in the work of Higdon.[27] Similarly to the centerline distribution of regularized Stokeslets discussed in Sec. II E 2, the parameter q must be tuned to ensure the most accurate results, but the advantage is far fewer discretization elements than a surface discretization, especially for thin filaments.

For the swimmer, we always model the ellipsoidal head using the surface distribution of regularized Stokeslets described in Section II E 1. Therefore, the $\mathbf{G_{hh}}$ and $\mathbf{G_{fh}}$ submatrices in Eq. (16) are always formulated in terms of the regularized Stokeslet kernel discussed in Section II E 1. The other submatrices $\mathbf{G_{hf}}$ and $\mathbf{G_{ff}}$ are formulated using the kernel for the slender body theory.

For the case of a helical filament above a plane, we must include an image system to satisfy the no-slip condition on the plane. The singularities distributed along the centerline of the filament are Stokeslets *and* dipoles, and so the system is not simply a Blakeslet distribution since we must include the image system of the dipole.[25] To evaluate the contribution of the images, we integrate the contribution from each image segment numerically using Simpson's rule since they are non-singular at the collocation points on the filament centerline. The kernel for this method is defined by the sum of Eq. (27) in the work of Higdon[27] and the numerical integral of the Stokeslet and dipole image systems provided by Blake and Chwang.[25]

F. Error metric

In order to assess the accuracy of these methods, we examine an error metric which includes both output parameters, the swimming velocity $\mathbf{V}$ and torque on the filament $\mathbf{N_f}$ in the case of the swimmer, and the net force $\mathbf{F}$ and the angular velocity $\mathbf{\Omega}$ in the case of the pump,

$$E_{\text{swimmer}}\,(\%) = 100\sqrt{\left(\frac{|\mathbf{V}^b - \mathbf{V}|}{|\mathbf{V}^b|}\right)^2 + \left(\frac{|\mathbf{N_f}^b - \mathbf{N_f}|}{|\mathbf{N_f}^b|}\right)^2}, \tag{26}$$

$$E_{\text{pump}}\,(\%) = 100\sqrt{\left(\frac{|\mathbf{F}^b - \mathbf{F}|}{|\mathbf{F}^b|}\right)^2 + \left(\frac{|\mathbf{\Omega}^b - \mathbf{\Omega}|}{|\mathbf{\Omega}^b|}\right)^2}, \tag{27}$$

where we add the sum-squared error of each respective output. The "b" superscript denotes the output from the benchmark case using the surface distribution of regularized Stokeslets.

III. RESULTS

A. Convergence study for regularized Stokeslets on filament surface

In previous work,[14] we have shown that for geometries similar to those used here for swimming, the method of regularized Stokeslets agrees well with SBT and boundary element method results presented in the work of Phan-Thien *et al.*[11] For this study, we create benchmark results using the surface distribution of regularized Stokeslets and perform convergence studies for selected geometries for swimming and pumping. These sample cases correspond to $\tilde{p} = 20$ and $\tilde{a} = 0.05, 0.35, 0.65, 0.95$. For the swimmer, we examine the x-component of the non-dimensionalized translational velocity against the Stokeslet spacing Δs. For the pump, we examine the x-component of the non-dimensionalized force against Δs.

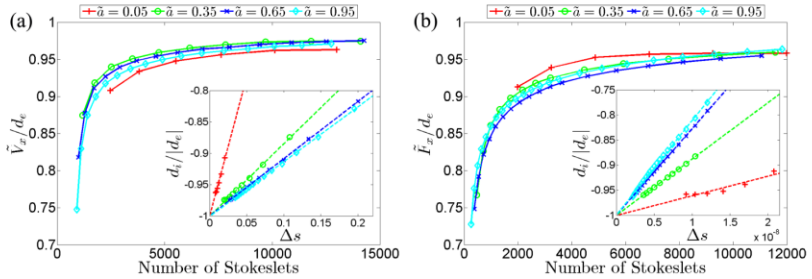

FIG. 3. Convergence studies for selected geometries of (a) swimmer (velocity normalized by extrapolant d_e) and (b) pump (force normalized by extrapolant d_e) using surface distribution of regularized Stokeslets. Inset in each figure is a plot of the data d_i normalized by the extrapolant against the Stokeslet spacing Δs with linear fit. As described in the text, the linear fit applies to each data set except for $\tilde{a} = 0.05$, for which it yields a conservative estimate of error. From these, we estimate that our results are converged to within 5% accuracy.

Fig. 3 presents the convergence studies for the swimmer and pump, respectively. In both cases, the quantity examined (either velocity or force) is normalized by a Richardson extrapolant obtained as described below, as a function of number of regularized Stokeslets used in the discretization. The extrapolant d_e for each case is obtained from the expectation that the error for each data point d_i obeys a power law relation to the discretization spacing Δs,

$$d_i - d_e = C\Delta s^{\gamma}, \tag{28}$$

where C and γ are constants. In each case, we examine the data for which γ is in the asymptotic range to obtain a fit for C and γ in the least-squared sense.

Ainley *et al*. find slightly greater than first order convergence when using a blob size $\delta \sim \Delta s^{0.9}$ for the problem of a sphere translating near a wall.[31] Since we use the similar $\delta = \Delta s$, we expect similar rates of convergence, and indeed in nearly all the cases, we find that $\gamma \approx 1$. To provide estimates of error, in the insets of Fig. 3, we show the fits to $d_i/|d_e|$ vs. Δs for $\gamma = 1$ over the asymptotic range. The swimming and pumping geometries with $\tilde{a} = 0.05$ (red crosses) display higher order behavior. In those cases, for consistency, we still find the extrapolant using $\gamma = 1$, which yields a conservative estimate of error. For the swimmer, the non-dimensionalized x-component of velocity for every geometry has converged to within 4% of the linear extrapolant. For the pump, the non-dimensionalized x-component of force has converged to within 5% of the linear extrapolant.

Based on these convergence studies, benchmark results for all the other geometries are generated using 8300 – 12 000 regularized Stokeslets for the swimmer and 10 000 – 12 500 regularized Stokeslets for the pump, for which we expect an error of less than 5%. These convergence studies also highlight the computational cost of this method and the motivation behind our investigation of other computationally cheaper numerical methods. The computational cost for all methods scales as N^3, where N is the total number of collocation points. As we will see in Secs. III B and III C, the method of regularized Stokeslets distributed on the filament centerline as well as the slender body theory provides a significant reduction in the total number of collocation points. This reduction comes at the cost of reduced accuracy, and so we examine the error due to each of these methods to assess their utility in various physical regimes.

B. Regularized Stokeslets distributed on the filament centerline

We now investigate the accuracy of the computationally cheaper methods outlined in Section II by comparing the results with the benchmarks obtained from calculations using the converged surface distribution of regularized Stokeslets. First, we present findings for the method of regularized Stokeslets distributed on the filament centerline. For each of the 50 filament geometries, we minimize the total percentage error metric E as defined in Section II F with respect to the blob parameter δ and the Stokeslet spacing Δs. Tables I and II report the value of these optimal parameters. From the tables, we see that for those geometries where the error can be made small (<10%), the optimal blob size is typically between $\tilde{a}$ and $3\tilde{a}$, while the spacing is similar to the blob size. In this regime

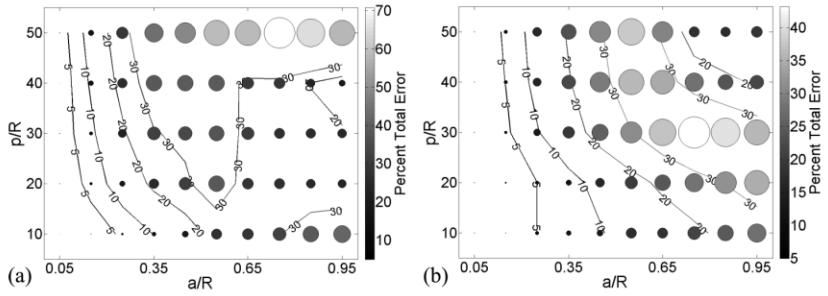

FIG. 4. Total error for (a) pump and (b) swimmer using centerline distribution of regularized Stokeslets. The size of circles at each investigated geometry is proportional to the total error (Eqs. (26) and (27)). Contour lines show interpolated errors.

of accuracy, both the optimal spacing and blob size tend to increase as $\tilde{p}$ increases. Our result for optimal blob size is consistent with the results of Bouzarth and Minion,[36] who found an optimal blob size of $1.43a$ for slender prolate ellipsoids with aspect ratios >10, which might be used to model straight rods.

Fig. 4 shows the total error for each geometry for pumping and swimming, respectively. In these figures, the circle size is scaled according to the percent error, and interpolated contour lines are drawn at 5, 10, 20, and 30 percent error in order to give a visual representation of the regions of accuracy. From the results, we make the following observations. First, the centerline distribution of regularized Stokeslets is more accurate for the swimmer than the pump. Second, this numerical method is most accurate for thin filaments (where $\tilde{a}$ is relatively small) and not accurate for the thickest filaments examined. For example, comparing to Fig. 1(b), this numerical method is quite accurate (with errors less than 5%) in the modeling of the flagella of bacteria such as *Salmonella* and *E. coli* as well as spermatozoa, but not accurate (with errors of approximately 25% in each scenario) for spirochetes such as *L. illini* and *B. burgdorferi*.

C. Slender body theory

We perform a similar investigation by comparing results for the slender body theory outlined in Section II to the benchmark results. In this numerical method, the total error is minimized with respect to the parameter q (recall that the length of the individual cylindrical segments is $2q$). Tables I and II report the optimal value of q for each geometry. From the tables, we see that accurate results are produced when both $q/\tilde{a} > 5$ (the segment length is at least 5 times the diameter) and $N \gtrsim 45$ ($\gtrsim$15 segments per turn). For slender body theory, we only report error values for the first 25 geometries since the error grows rapidly as a/R increases. This is consistent with expectations for this method: as the filament radius approaches the helical radius, the filament is less slender, and so it follows that a slender body theory approach would break down.

Fig. 5 shows the total error for each geometry for pumping and swimming, respectively. The total error in the slender body theory is within a tolerable range (<10%) only for $\tilde{a} \lesssim 0.10$. We note that the total error using the method of regularized Stokeslets on the filament centerline is also quite low for these particularly slender geometries, so in this range, we must make a judgement based on computational cost to compare the two methods.

D. Resistive force theory

Table III shows the results of RFT using the drag coefficients from the theories of Gray and Hancock[21] and Lighthill.[20] Throughout the whole range, neither gives accurate results; for the coefficients derived by Lighthill, the total percent error is minimal at $E_{\text{Total}} = 26\%$ and for the coefficients derived by Gray and Hancock, the total percent error is minimal at $E_{\text{Total}} = 33.6\%$, both for the geometry specified by $\tilde{a} = 0.05$ and $\tilde{p} = 50$.

Although the total error is large throughout the range tested, it is interesting to note that if one only considers the error in swimming speed (separately reported in Table III), the coefficients

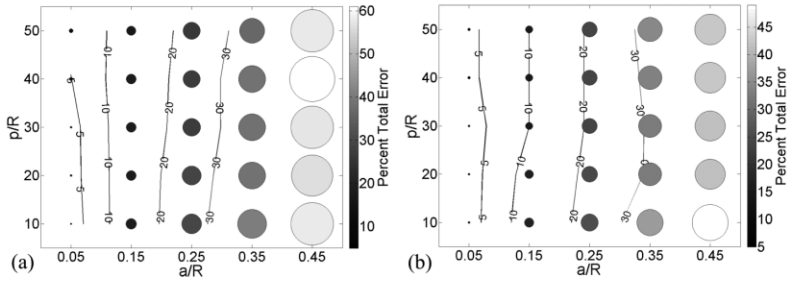

FIG. 5. Total error for (a) pump and (b) swimmer using slender body theory. The size of circles at each investigated geometry is proportional to the total error (Eqs. (26) and (27)). Contour lines show interpolated errors.

derived by Gray and Hancock produce accurate results for the swimming speed ($E_{\mathbf{V}} < 10\%$) for $\tilde{a} \leq 0.65$ and $\tilde{p} \geq 30$, a large range of geometries. In this regime, however, we find large errors in the filament torque. On the other hand, the theory of Lighthill produces accurate results for the filament torque for $\tilde{a} < 0.15$, but always gives large errors for the translational velocity. Thus, RFT may give accurate results for individual quantities, as has previously been observed in the literature, not only for swimming speeds but also for quantities such as distance traveled per revolution,[15] but does not accurately capture the full dynamics for any investigated geometry. Furthermore, without a more accurate benchmark comparison such as that performed here, it is difficult to know in advance if any particular quantity of interest will be accurately calculated using RFT.

IV. DISCUSSION

To summarize the results up to this point, based on a convergence study, we created benchmark results for swimming and pumping flows caused by helical filaments using a surface distribution of regularized Stokeslets. By comparison to the benchmark results, we found that resistive force theory does not give accurate results (in terms of total error) for any of the geometries studied. We also used the benchmark case to optimize the relevant parameters of a centerline distribution of regularized Stokeslets and slender body theory with respect to a total error metric and obtained regimes of accuracy for each numerical method. Together, Figs. 1, 4, and 5 allow us to make a judgement about which numerical method is appropriate for a wide variety of biological and artificial filament geometries. The regimes of accuracy for more cost efficient methods (SBT and centerline distributed regularized Stokeslets) overlap, so it is of interest to examine which numerical method will be optimal in terms of computational efficiency as well as total error. The computational cost of the numerical methods scales as N^3, where N is the number of collocation point. As noted before, a surface distribution of regularized Stokeslets (or any boundary element method) requires more and more collocation points as the filament becomes thinner since the spacing of the cross sections becomes smaller, but for slender filaments, SBT and centerline distributions of regularized Stokeslets are accurate and much cheaper computationally.

The overall choice for the cheapest numerical method which is still accurate can be summarized in Fig. 6. In this figure, we first choose an error threshold of 10% against the benchmarks obtained from the surface distribution of regularized Stokeslets. A contour is drawn for an interpolated 10% error threshold for each of the cheaper methods, which delineate three regions labeled near the bottom of each plot as "SBT" for the slender body theory, "CL" for the centerline distribution of regularized Stokeslets, and "SURFACE" for the surface distribution. These regions show the method which, given the 10% error threshold, is the most computationally efficient for a given geometry. Note that the regions are similar for the swimming and pumping scenarios, which suggests that these recommendations are broadly appropriate across many applications.

In order to provide information about the computational costs in each region, in Fig. 6, we also write the number of collocation points for each geometry tested. For the surface distribution region, we report the number of collocation points obtained by decreasing the number of collocation

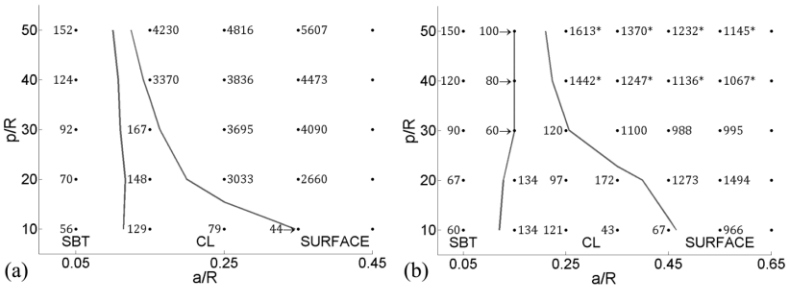

FIG. 6. Diagram of best choice of method (regions labeled above horizontal axis) to be used for 10% error in $\tilde{a}$-$\tilde{p}$ phase space for (a) pump and (b) swimmer based on computational efficiency. Note that the choice of method is broadly similar for both pumps and swimmers. Computational cost can be deduced from number at each geometry, which indicates optimal number of collocation points for the centerline distribution of regularized Stokeslets and slender body theory, and the number of collocation points needed to achieve 10% error for surface distribution of regularized Stokeslets.

points for each geometry by lowering the number of regularized Stokeslets per cross section n_c until we reach the error threshold of 10%. Points marked with an asterisk denote geometries for which the error of the surface distribution against the benchmark case was always less than 10%, even for the lowest number of regularized Stokeslets per cross section ($n_c = 3$). In these cases, the value of N using $n_c = 3$ is reported. This number allows us to compare to the costs required for the other methods. For the centerline distribution and SBT regions, we report the number of collocation points needed for the *optimal* accuracy parameters.

Within its regime of accuracy, we see that slender body theory requires approximately half as many collocation points as the centerline distribution of regularized Stokeslets. This means that the slender body theory may be up to ~10 times more computationally efficient in these regimes, which include more slender forms of bacterial flagella as well as spermatozoa. This result is consistent with the experimentally confirmed results of Rodenborn *et al.*[13] It should be noted that due to the addition of the dipole singularity (as well as the corresponding image system in the case of the pump), this method requires a larger initial investment for implementation than the method of regularized Stokeslets. Taking this into account, it becomes a value judgement in this regime as to whether the computational savings will be worth the initial effort in the long run.

For $0.15 < \tilde{a} < 0.40$, the centerline distribution of regularized Stokeslets provides a very efficient model for a wider range of physical examples. This range may include some bacterial flagella which are enveloped by a sheath, which makes them thicker than a bare flagellum, such as those of *H. pylori*[39] or *Vibrio* species.[40] Finally, as expected for the thickest filaments, such as the cell bodies of spirochetes or artificial helical microswimmers, the surface distribution of regularized Stokeslets is required for accurate results but increases the required number of collocation points by at least an order of magnitude.

In conclusion, the numerical methods tested — resistive force theory, slender body theory, and the method of regularized Stokeslets — have gained popularity due to their ease of implementation. We investigated their use throughout the range of geometries likely to be encountered in applications. In Tables I and II, we present optimized parameters for each method we study. Although in other geometries these precise parameters may not be optimal, they should provide useful starting points for tuning the parameters in other applications and geometries. For the case of a 10% accuracy threshold, Fig. 6 shows how an appropriate choice of method can be made for a wide range of filament geometries. Thus, our results provide necessary guidance for selection of computational method and should be useful for many future investigation involving filament induced flows.

ACKNOWLEDGMENTS

This work was supported by National Science Foundation Award Nos. DMR-1307497 and CBET-1252182.

APPENDIX: TABLES

TABLE I. Optimal parameters for centerline distribution and slender body theory, swimmer with head. For the slender body theory, only the first 25 entries are shown since error is large for all other (thick) geometries.

		Centerline				SBT		
$\tilde{a}$	$\tilde{p}$	$\Delta s/a$	δ/a	E_{swimmer} (%)	N	q/a	E_{swimmer} (%)	N
0.05	10	2.5	1.8	1.1	241	5	3	60
0.05	20	2.5	1.8	1.2	481	9	3	67
0.05	30	3.0	1.8	1.3	601	10	3	90
0.05	40	3.5	2.0	1.6	686	10	4	120
0.05	50	3.5	2.0	1.7	858	10	4	150
0.15	10	1.5	2.0	1.7	134	3	13	33
0.15	20	3.0	2.2	2.3	134	5	12	40
0.15	30	3.5	2.4	4.2	172	5	10	60
0.15	40	3.5	2.4	5.1	229	5	10	80
0.15	50	3.5	2.4	5.6	286	5	10	100
0.25	10	1.0	2.2	5.0	121	3	23	20
0.25	20	2.5	2.8	5.0	97	3	22	40
0.25	30	3.0	2.8	9.6	120	3	21	60
0.25	40	3.0	2.8	11.8	160	3	21	80
0.25	50	3.0	3.0	12.9	200	3	21	100
0.35	10	2.0	2.6	7.2	43	2	36	21
0.35	20	1.0	3.2	7.7	172	2	31	43
0.35	30	2.5	3.4	16.1	103	2	31	64
0.35	40	3.5	3.6	19.4	98	2	32	86
0.35	50	5.5	4.2	20.9	78	2	33	107
0.45	10	1.0	2.6	9.3	67	2	49	17
0.45	20	1.0	3.6	12.4	134	2	41	33
0.45	30	3.0	3.8	23.3	67	2	41	50
0.45	40	3.0	4.2	27.4	89	2	42	67
0.45	50	5.0	4.8	29.3	67	2	42	83
0.55	10	1.5	2.8	14.1	37			
0.55	20	1.0	3.8	17.0	110			
0.55	30	4.0	4.4	29.8	41			
0.55	40	3.0	4.4	35.3	73			
0.55	50	3.5	5.2	37.4	78			
0.65	10	1.5	3.0	14.9	31			
0.65	20	1.0	4.0	21.9	93			
0.65	30	4.5	4.6	36.7	31			
0.65	40	1.0	9.8	33.6	185			
0.65	50	1.0	10.0	28.5	231			
0.75	10	1.5	2.8	18.2	27			
0.75	20	1.0	4.0	26.1	81			
0.75	30	4.5	4.6	43.2	27			
0.75	40	1.0	9.4	25.8	161			
0.75	50	1.0	10.0	14.5	201			
0.85	10	2.0	3.0	22.3	18			
0.85	20	1.0	4.2	30.4	71			
0.85	30	1.0	7.8	40.1	106			
0.85	40	1.0	9.0	21.5	142			
0.85	50	1.0	9.6	13.5	177			
0.95	10	1.0	2.8	25.7	32			
0.95	20	1.0	4.2	34.0	64			
0.95	30	1.0	7.6	35.2	95			
0.95	40	1.0	8.6	19.1	127			
0.95	50	1.0	9.2	15.8	158			

TABLE II. Optimal parameters for centerline distribution and slender body theory, filament above no-slip surface. For the slender body theory, only the first 25 entries are shown since error is large for all other (thick) geometries.

		Centerline				SBT		
$\tilde{a}$	$\tilde{p}$	$\Delta s/a$	δ/a	E_{pump} (%)	N	q/a	E_{pump} (%)	N
0.05	10	0.91	2.01	0.95	562	5.3	2.6	56
0.05	20	1.01	2.27	1.66	1136	8.5	3.2	70
0.05	30	1.66	2.56	2.04	1063	9.7	3.3	92
0.05	40	1.36	2.74	1.46	1745	9.6	4.9	124
0.05	50	1.90	2.84	2.35	1568	9.9	6.1	152
0.15	10	1.33	2.27	2.79	129	3.1	14.2	32
0.15	20	2.60	2.75	6.35	148	4.8	14.0	41
0.15	30	3.54	3.22	8.67	167	5.1	14.1	58
0.15	40	4.37	3.74	10.85	182	5.3	13.8	75
0.15	50	5.28	4.24	12.58	189	5.3	12.7	94
0.25	10	1.31	2.57	5.64	79	3.0	27.0	19
0.25	20	3.10	3.46	13.72	75	3.2	26.3	37
0.25	30	4.10	4.42	18.69	87	3.2	24.1	56
0.25	40	4.20	5.37	23.02	114	3.3	23.8	72
0.25	50	3.61	6.25	26.47	166	3.3	23.2	90
0.35	10	1.70	2.76	10.20	44	1.9	38.9	22
0.35	20	1.95	4.10	21.86	85	2.0	36.6	42
0.35	30	2.19	5.60	29.44	116	2.0	36.4	64
0.35	40	2.37	7.28	36.29	144	2.0	36.8	85
0.35	50	2.56	8.82	41.82	168	2.0	34.3	107
0.45	10	1.78	2.89	14.43	33	1.8	58.0	18
0.45	20	0.46	4.86	28.57	278	1.8	56.1	37
0.45	30	0.73	8.05	31.93	270	1.8	57.4	55
0.45	40	0.90	9.36	36.83	294	1.9	61.0	70
0.45	50	0.85	9.65	47.54	391	1.9	57.8	87
0.55	10	1.34	2.93	24.23	36			
0.55	20	0.87	5.22	36.13	121			
0.55	30	1.04	8.54	35.09	156			
0.55	40	1.10	9.75	36.77	198			
0.55	50	1.10	10.05	58.54	248			
0.65	10	1.72	2.98	25.83	24			
0.65	20	0.45	5.16	25.91	197			
0.65	30	0.90	8.25	27.84	152			
0.65	40	0.96	9.35	27.22	192			
0.65	50	1.00	9.80	58.19	231			
0.75	10	1.81	3.01	29.52	20			
0.75	20	0.46	5.22	23.68	168			
0.75	30	0.92	7.96	23.77	129			
0.75	40	1.17	9.45	26.23	137			
0.75	50	1.47	10.54	70.87	138			
0.85	10	1.79	3.01	36.49	18			
0.85	20	0.46	5.05	21.13	148			
0.85	30	1.05	7.76	22.13	100			
0.85	40	1.18	9.18	19.71	120			
0.85	50	1.40	10.29	64.93	127			
0.95	10	1.51	2.95	39.67	19			
0.95	20	0.48	4.90	20.03	127			
0.95	30	1.12	7.63	21.04	84			
0.95	40	1.26	9.03	14.36	101			
0.95	50	1.35	10.00	57.54	118			

TABLE III. Resistive force theory results for swimmer computed using analytical resistance matrix for the ellipsoidal head. For the theories of Gray and Hancock, and Lighthill, we present the percent error in the translational velocity $\mathbf{V}$, filament torque $\mathbf{N_f}$, and the total percent error.

		Gray and Hancock			Lighthill		
$\tilde{a}$	$\tilde{p}$	$E_{\mathbf{V}}$ (%)	$E_{\mathbf{N_f}}$ (%)	E_{Total} (%)	$E_{\mathbf{V}}$ (%)	$E_{\mathbf{N_f}}$ (%)	E_{Total} (%)
0.05	10	26.95	35.95	44.9	69.80	5.54	70.0
0.05	20	16.77	36.32	40.0	51.90	5.82	52.2
0.05	30	9.89	34.88	36.3	41.58	6.14	42.0
0.05	40	7.45	34.17	35.0	32.21	6.80	32.9
0.05	50	6.03	33.09	33.6	25.11	6.56	26.0
0.15	10	28.18	47.39	55.1	70.94	10.19	71.7
0.15	20	15.40	46.23	48.7	54.92	12.89	56.4
0.15	30	7.40	44.75	45.4	42.42	14.04	44.7
0.15	40	7.18	43.60	44.2	32.16	14.56	35.3
0.15	50	8.05	42.55	43.3	24.69	14.67	28.7
0.25	10	31.00	56.10	64.1	69.80	16.92	71.8
0.25	20	15.04	54.58	56.6	57.35	21.94	61.4
0.25	30	6.12	53.11	53.5	44.18	23.49	50.0
0.25	40	6.46	52.09	52.5	33.50	24.35	41.4
0.25	50	8.18	51.26	51.9	25.87	24.85	35.9
0.35	10	31.04	62.86	70.1	65.59	23.45	69.7
0.35	20	14.74	61.52	63.3	59.44	30.64	66.9
0.35	30	6.00	60.51	60.8	46.15	33.09	56.8
0.35	40	6.95	59.63	60.0	35.44	34.17	49.2
0.35	50	8.53	58.96	59.6	27.93	34.89	44.7
0.45	10	34.97	68.73	77.1	61.24	30.46	68.4
0.45	20	15.70	67.46	69.3	62.46	38.85	73.6
0.45	30	5.93	66.48	66.7	49.07	41.34	64.2
0.45	40	7.62	65.84	66.3	38.21	42.75	57.3
0.45	50	9.10	65.30	65.9	30.94	43.60	53.5
0.55	10	36.49	73.24	81.8	53.97	36.04	64.9
0.55	20	16.47	72.16	74.0	64.75	45.65	79.2
0.55	30	7.25	71.36	71.7	52.40	48.41	71.3
0.55	40	8.06	70.78	71.2	41.70	49.83	65.0
0.55	50	8.45	70.26	70.8	34.73	50.62	61.4
0.65	10	39.06	76.92	86.3	45.78	40.77	61.3
0.65	20	18.03	75.97	78.1	67.66	51.40	85.0
0.65	30	9.20	75.27	75.8	55.89	54.26	77.9
0.65	40	9.00	74.68	75.2	45.79	55.57	72.0
0.65	50	9.54	74.19	74.8	39.39	56.32	68.7
0.75	10	40.88	79.85	89.7	35.97	44.49	57.2
0.75	20	19.99	78.98	81.5	70.74	56.04	90.2
0.75	30	11.38	78.33	79.1	60.19	58.92	84.2
0.75	40	11.16	77.77	78.6	50.74	60.19	78.7
0.75	50	11.71	77.27	78.2	44.78	60.85	75.6
0.85	10	41.96	82.21	92.3	27.42	47.31	54.7
0.85	20	22.69	81.44	84.5	74.45	59.90	95.6
0.85	30	14.18	80.79	82.0	64.97	62.72	90.3
0.85	40	13.96	80.23	81.4	56.20	63.90	85.1
0.85	50	14.98	79.69	81.1	51.11	64.45	82.3
0.95	10	44.65	84.18	95.3	33.16	49.55	59.6
0.95	20	25.65	83.45	87.3	78.24	63.11	100.5
0.95	30	17.62	82.79	84.6	70.29	65.84	96.3
0.95	40	17.83	82.21	84.1	62.33	66.93	91.5
0.95	50	19.53	81.64	83.9	58.13	67.35	89.0

[1] E. Lauga and T. R. Powers, "The hydrodynamics of swimming microorganisms," Rep. Prog. Phys. **72**, 096601 (2009).
[2] A. Ghosh and P. Fischer, "Controlled propulsion of artificial magnetic nanostructured propellers," Nano Lett. **9**, 2243–2245 (2009).
[3] A. Ghosh, D. Paria, H. J. Singh, P. L. Venugopalan, and A. Ghosh, "Dynamical configurations and bistability of helical nanostructures under external torque," Phys. Rev. E **86**, 031401 (2012).
[4] C. Peters, O. Ergeneman, B. J. Nelson, and C. Hierold, "Superparamagnetic swimming microrobots with adjusted magnetic anisotropy," in *2013 IEEE 26th International Conference on Micro Electro Mechanical Systems (MEMS)* (IEEE, 2013), pp. 564–567.
[5] K. E. Peyer, L. Zhang, B. E. Kratochvil, and B. J. Nelson, "Non-ideal swimming of artificial bacterial flagella near a surface," in *2010 IEEE International Conference on Robotics and Automation* (IEEE, 2010), pp. 96–101.
[6] S. Tottori *et al.*, "Assembly, disassembly, and anomoalous propulsion of microscopic helices," Nano Lett. **13**, 043705 (2013).
[7] Y. Ding, J. C. Nawroth, M. J. McFall-Ngai, and E. Kanso, "Mixing and transport by ciliary carpets: A numerical study," J. Fluid Mech. **743**, 124–140 (2014).
[8] H. Guo, J. Nawroth, Y. Ding, and E. Kanso, "Cilia beating patterns are not hydrodynamically optimal," Phys. Fluids **26**, 091901 (2014).
[9] M. J. Kim and K. S. Breuer, "Use of bacterial carpets to enhance mixing in microfluidic systems," J. Fluids Eng. **129**, 319–324 (2007).
[10] R. E. Johnson and C. J. Brokaw, "Flagellar hydrodynamics. A comparision between resistive-force theory and slender-body theory," Biophys. J. **25**, 113–127 (1979).
[11] N. Phan-Thien, T. Tran-Cong, and M. Ramia, "A boundary-element analysis of flagellar propulsion," J. Fluid Mech. **184**, 533–549 (1987).
[12] M. Ramia, D. L. Tullock, and N. Phan-Thien, "The role of hydrodynamic interaction in the locomotion of microorganisms," Biophys. J. **65**, 755–778 (1993).
[13] B. Rodenborn, C.-H. Chen, H. L. Swinney, B. Liu, and H. P. Zhang, "Propulsion of microorganisms by a helical flagellum," Proc. Natl. Acad. Sci. U. S. A. **110**, E338–E347 (2013), http://www.pnas.org/content/110/5/E338.full.pdf+html.
[14] Y. Hyon, Marcos, T. R. Powers, R. Stocker, and H. C. Fu, "The wiggling trajectories of bacteria," J. Fluid Mech. **705**, 58–76 (2012).
[15] H. C. Fu, M. Jabbarzadeh, and F. Meshkati, "Magnetization directions and geometries of helical microswimmers for linear velocity-frequency response," Phys. Rev. E **91**, 043011 (2015).
[16] N. Darnton and H. C. Berg, "Force-extension measurements on bacterial flagella: Triggering polymorphic transformations," Biophys. J. **92**, 2230 (2007).
[17] N. Darnton, L. Turner, S. Rojevsky, and H. C. Berg, "On torque and tumbling in swimming *Escherichia coli*," J. Bacteriol. **189**, 1756–1764 (2007).
[18] K. Hasegawa, I. Yamashita, and K. Namba, "Quasi- and nonequivalence in the structure of the bacterial flagellar filament," Biophys. J. **74**, 569–575 (1998).
[19] C. Brennen and H. Winet, "Fluid mechanics of propulsion by cilia and flagella," Annu. Rev. Fluid Mech. **9**, 339–398 (1977).
[20] J. Lighthill, "Flagellar hydrodynamics," SIAM Rev. **18**, 161–230 (1976).
[21] J. Gray and G. J. Hancock, "The propulsion of sea-urchin spermatozoa," J. Exp. Biol. **32**, 802–814 (1955).
[22] G. K. Batchelor, "Slender body theory for particles of arbitrary cross section in Stokes flow," J. Fluid Mech. **44**, 419 (1970).
[23] R. G. Cox, "The motion of long slender bodies in a viscous fluid. Part 1. General theory," J. Fluid Mech. **44**, 791–810 (1970).
[24] J. P. K. Tillett, "Axial and transverse Stokes flow past slender axisymmetric bodies," J. Fluid Mech. **44**, 401–417 (2001).
[25] J. R. Blake and A. T. Chwang, "Fundamental singularities of viscous flow. Part 1. Image systems in vicinity of a stationary no-slip boundary," J. Eng. Math. **8**, 23–29 (1974).
[26] R. Cortez and M. Nicholas, "Slender body theory for stokes flows with regularized stokeslets," Commun. Appl. Math. Comput. Sci. **7**, 33 (2012).
[27] J. L. L. Higdon, "A hydrodynamic analysis of flagellar propulsion," J. Fluid Mech. **90**, 685–711 (1979).
[28] S. Goldstein, K. Buttle, and N. Charon, "Structural analysis of the *Leptospiraceae* and *Borrelia burgdorferi* by high-voltage electron microscopy," J. Bacteriol. **178**, 6539–6545 (1996).
[29] A. Ghosh, P. Mandal, S. Karmakar, and A. Ghosh, "Analytical theory and stability analysis of an elongated nanoscale object under external torque," Phys. Chem. Chem. Phys. **15**, 10817–10823 (2013).
[30] C. Pozrikidis, *A Practical Guide to Boundary Element Methods with the Software Lirary BEMLIB* (Chapman and Hall/CRC, Boca Raton, FL, 2002).
[31] J. Ainley, S. Durkin, R. Embid, P. Boindala, and R. Cortez, "The method of images for regularized Stokeslets," J. Comput. Phys. **227**, 4600–4616 (2008).
[32] R. Cortez, "The method of regularized Stokeslets," SIAM J. Sci. Comput. **23**, 1204–1225 (2001).
[33] R. Cortez, L. Fauci, and A. Medovikov, "The method of regularized stokeslets in three dimensions: Analysis, validation, and application to helical swimming," Phys. Fluids **17**, 031504 (2005).
[34] S. Olson, S. Lim, and R. Cortez, "Modeling the dynamics of an elastic rod with intrinsic curvature and twist using a regularized stokes formulation," J. Comput. Phys. **238**, 169 (2013).
[35] S. D. Olson, S. S. Saurez, and L. J. Fauci, "Coupling biochemistry and hydrodynamics captures hyperactivated sperm motility in a simple flagellar model," J. Theor. Biol. **283**, 203–216 (2011).
[36] E. L. Bouzarth and M. L. Minion, "Modeling slender bodies with the method of regularized stokeslets," J. Comput. Phys. **230**, 3929–3947 (2011).
[37] S. Kim and S. J. Karrila, *Microhydrodynamics* (Dover, Mineola, New York, 2005).
[38] S. Childress, *Mechanics of Swimming and Flying* (Cambridge University Press, Cambridge, 1981).
[39] G. Geis, S. Sauerbaum, B. Forsthoff, H. Leying, and W. Opferkuch, "Ultrastructure and biochemical studies of the flagellar sheath of *Heliobacter pylori*," J. Med. Microbiol. **38**, 371–377 (1993).
[40] E. A. Follett and J. Gordon, "An electron microscope study of *Vibrio* flagella," J. Gen. Microbiol. **32**, 235–239 (1963).

CHAPTER 3

HELICAL AND ROD-SHAPED BACTERIA SWIM IN HELICAL TRAJECTORIES WITH LITTLE ADDITIONAL PROPULSION FROM HELICAL SHAPE

.

SCIENCE ADVANCES | RESEARCH ARTICLE

MICROBIOLOGY

Helical and rod-shaped bacteria swim in helical trajectories with little additional propulsion from helical shape

Maira A. Constantino,[1] Mehdi Jabbarzadeh,[2] Henry C. Fu,[2]* Rama Bansil[1]*

It has frequently been hypothesized that the helical body shapes of flagellated bacteria may yield some advantage in swimming ability. In particular, the helical-shaped pathogen *Helicobacter pylori* is often claimed to swim like a corkscrew through its harsh gastric habitat, but there has been no direct confirmation or quantification of such claims. Using fast time-resolution and high-magnification two-dimensional (2D) phase-contrast microscopy to simultaneously image and track individual bacteria in bacterial broth as well as mucin solutions, we show that both helical and rod-shaped *H. pylori* rotated as they swam, producing a helical trajectory. Cell shape analysis enabled us to determine shape as well as the rotational and translational speed for both forward and reverse motions, thereby inferring flagellar kinematics. Using the method of regularized Stokeslets, we directly compare observed speeds and trajectories to numerical calculations for both helical and rod-shaped bacteria in mucin and broth to validate the numerical model. Although experimental observations are limited to select cases, the model allows quantification of the effects of body helicity, length, and diameter. We find that due to relatively slow body rotation rates, the helical shape makes at most a 15% contribution to propulsive thrust. The effect of body shape on swimming speeds is instead dominated by variations in translational drag required to move the cell body. Because helical cells are one of the strongest candidates for propulsion arising from the cell body, our results imply that quite generally, swimming speeds of flagellated bacteria can only be increased a little by body propulsion.

INTRODUCTION

Bacteria come in a wide variety of shapes, and bacterial morphology affects selective adaptation (*1*). One important mechanism by which morphology could affect biological function is through motility (*2*); for example, cell length has been shown to affect the tumbling (*3*) and, hence, chemotactic ability in *Escherichia coli*. It is well known that the translational and rotational drag on the cell body depends on the shape and thus alters swimming speed (*4*, *5*). For swimming bacteria, it has also been of interest how the cell body can directly contribute toward propulsion, obviously for species that propel themselves by deforming or twisting their bodies such as spiroplasma (*6*, *7*) or spirochetes (*8*), but also for bacteria, which use a rotating flagellum or flagellar bundle like a propeller. For these flagella-propelled bacteria, Liu *et al.* (*9*) have recently shown that the counter-rotation and subsequent helical path of the cell body may contribute to swimming propulsion, but it is unclear how large this effect may be in general and how important it may be for adaptation. Here, we compare helical cells with their rod-shaped isogenic mutants to place quantitative bounds on the contribution of cell body shape to propulsion because a rotating helical cell body (like the helical flagellum) is well suited to provide maximal amounts of thrust; indeed, long ago, Berg and Turner (*10*) suggested that a helical cell shape would result in additional corkscrew-like propulsion for bacteria moving in viscous environments.

It has not been possible to draw firm conclusions from earlier studies addressing the role of helical cell shape on propulsion because many of these studies compare different species, which may have uncontrolled differences beyond cell morphology. Ferrero and Lee (*11*) compared the swimming speeds of the helical-shaped bacteria *Campylobacter jejuni* with rod-shaped bacteria, *Vibrio cholerae*, *Salmonella enteritidis*, and *E. coli*. They found that in viscous methylcellulose solutions, the helical-shaped *C. jejuni* were more motile than rod-shaped bacteria. Later work done by Karim *et al.* (*12*) compared the swimming speeds of the helical bacteria *Helicobacter pylori* and *C. jejuni* to rod-shaped *E. coli* bacteria, finding *C. jejuni* to be the fastest (median speed, 38 μm/s; range, 29 to 53 μm/s) compared to *H. pylori* (median speed, 25 μm/s; range, 12 to 29 μm/s), whereas the rod-shaped *E. coli* were the slowest (median speed, 12 μm/s; range, 8 to 18 μm/s). These studies seemed to indicate that helical cell shape resulted in increased swimming speed by factors of 2 to 3; however, because there are several other differences between these bacteria, it is unclear how much the observed differences in motility are due to cell body helicity. Furthermore, none of these studies measured the counter-rotational motion of the body of swimming bacteria nor did they measure speed and shape of individual bacteria to enable quantitative comparison between experiment and theoretical models.

Here, we use *H. pylori*, an important human pathogen that colonizes the epithelial surface of the gastric mucosa of the human stomach and is known to cause gastritis, gastric ulcers, and gastric cancer (*13*–*15*). Other *Helicobacters* with a larger number of helical turns [*Helicobacter heilmannii*, *Helicobacter suis*, *Helicobacter felis*, among others (*16*)] are also found in the gastric mucosa of humans, although they primarily infect other animals. As their name suggests, the helical shape of these bacteria is one of their most salient features and is purported to be an important factor in the ability of the bacterium to traverse the protective mucus barrier and colonize on the epithelial surface of the stomach mucosa. For example, it has been suggested that the helical shape enables the bacterium to bore its way like a corkscrew through the gastric mucus gel that covers the epithelial surface (*17*, *18*). This commonly held view was questioned by previous studies of ours, which show that *H. pylori* can rotate its flagella but does not swim in mucin gels buffered at acidic pH 2 to 4 comparable to the stomach (*19*), as well as gelatin gels at neutral pH (*20*). In the case

[1]Department of Physics, Boston University, Boston MA 02215, USA. [2]Department of Mechanical Engineering, University of Utah, Salt Lake City, UT 84112, USA. *Corresponding author. Email: henry.fu@utah.edu (H.C.F.); rb@bu.edu (R.B.)

of mucus, gelation is related to a liquid-to-gel transition of the glycoprotein mucin at pH 4 and below (*21*, *22*). We showed that *H. pylori* uses urease-mediated hydrolysis of urea to neutralize the pH of the mucin (*19*), enabling the non-acidophilic bacterium to not only survive in acidic conditions but also trigger a pH-dependent gel-to-liquid transition of mucin (*19*, *23*, *24*), enabling the bacterium to swim in a liquid environment. More recently, Mirbagheri and Fu (*25*) have developed a model that couples motility and diffusion to describe how *H. pylori* can swim as if in an unconfined medium by creating a moving pocket of fluid in a gel. However, it remains unknown to what extent the helical shape of the cell could be advantageous for swimming in a viscous fluid, which we address here.

To directly address the link between cell shape and motility, we use isogenic straight rod cell–shaped mutants of *H. pylori*, called Δ*csd6* (*26*), which lack the Csd6 peptidoglycan carboxypeptidase responsible for cell helicity (*27*). These isogenic mutants differ only in cell shape due to the single *csd6* gene mutation but are otherwise shown to have the same flagellation characteristics and motility as the wild type (WT) (*26*, *28*). Rod- or C-shaped mutants of *H. pylori* lacking helical shape were found to show decreased halo formation in soft agar and impaired stomach colonization in a mouse model (*26*, *27*); however, in these early studies, helical and straight rod bacteria were found to exhibit similar swimming speeds. Recently, we reported a detailed study on the relationship between *H. pylori* cell shape morphology and motility using live-cell microscopic imaging to track both helical and straight rod mutants of three different strains in several solutions (bacterial broth, gastric mucin, and methylcellulose) (*28*) and also measured the distribution of cell shapes and sizes from a separate microscopic imaging of bacteria fixed to a slide. The speed of individual bacteria was found to vary with time as well as due to the broad distribution of cell sizes (length, diameter, and pitch) and variation in the number of flagella among the bacteria population in the sample. Martinez *et al.* (*28*) concluded that, on average, helical bacteria had the same number of flagella and swam with a slightly increased median speed compared to their isogenic rod-shaped mutants, whereas other characteristics of the trajectories, such as linearity of tracks and frequency of reversals, were not significantly altered. They also noted that the effect of shape was larger in gastric mucin solutions than in culture broth or methylcellulose solutions, possibly due to specific interactions between *H. pylori* and mucin as well as viscoelasticity of mucin solutions. In that paper (*28*), resistive force theory (RFT) (*29*) was used to calculate the swimming speed using an average of all the cell shape measurements to define the bacterium. The RFT calculations overestimate the effect of shape, producing a significantly larger increase in the speed, ~30% for the helical bacterium relative to an elongated rod-like, ellipsoidal cell shape, as compared to the ~10% enhancement observed experimentally. However, crucially, Martinez *et al.* (*28*) found that variations in swimming speed are dominated by variations in the number of flagella and hence motor torque propelling the cells, meaning that the effect of body shape on swimming speed could be difficult to extract from population averages of bacteria differing not only in shape and size but also in number of flagella. By examining mutants with an average of one less flagella or one more flagella, they showed a direct correlation between the speed and number of flagella (*28*). In view of these variable factors of shape, size, and number of flagella within the population, it was not possible to clearly elucidate the relationship between cell body shape and swimming speed by comparing average speeds of rod-shaped mutants and helical WT bacteria.

Here, we take advantage of advances in high–frame rate digital tracking and image analysis (*30*) to design a study to directly address the question of shape and motility by simultaneously imaging and tracking individual cells as they rotate and translate. Whereas previous work to examine the rotational motion used a specialized, custom built three-dimensional (3D) tracking microscope (*9*), we use the more readily available 2D phase-contrast microscope to simultaneously measure both swimming properties and cell geometry for the same individual cell. Single-cell tracks in *H. pylori* have previously been reported (*28*, *31*), but they did not address or analyze rotational motion and propulsion of the cell body. Using the high-resolution geometric and kinematic measurements reported here, we can quantitatively validate numerical models of swimming propulsion and thrust, and then use those numerical models to perform properly controlled investigations of how helical body shapes change in swimming speed while keeping other quantities, such as motor torque, fixed, leading to a physical mechanistic understanding of the contribution of cell body shape to thrust. These investigations are not possible without the combination of our simultaneous high-resolution tracking and numerical models.

To summarize our results, we present simultaneous shape and tracking measurements of individual *H. pylori* and its rod-shaped mutant (Δ*csd6*) while swimming in mucin and broth solutions using 2D phase-contrast imaging at high magnification and at high frame rates. The helical shape of *H. pylori* enables direct visualization of corkscrew motion. These measurements enable us to determine the rotational speed of the bacterium while simultaneously measuring the translational speed and cell shape parameters of a single bacterium for both forward and reverse motions, as well as the change in direction of rotation after a reversal event, providing detailed kinematic information that allows deduction of flagellar kinematics. We were able to confirm the previous finding that, during swimming, *H. pylori*'s multiple flagellar bundle together, forming a single left-handed bundle (*19*, *28*). We used the measured geometry and the observed rotational rate to numerically calculate the swimming speed of both helical and rod-shaped bacteria moving forward as well as in reverse using the method of regularized Stokeslets (RSM) and find good quantitative agreement between theory and experiment for the swimming speed and the pitch of the trajectory. Using the observed rotation rate as an input, we circumvent the problems arising from not knowing the number of flagella in *H. pylori*, which as mentioned above is known to strongly affect the swimming speed (*28*). We find that because of the relatively slow counter-rotation rate of the cell body, the helical shape produces <15% extra propulsive thrust and <15% changes in swimming speeds as compared to the rod-shaped cell. Moreover, the accuracy of the theoretical model allows us to explore the influence of cell body shape on swimming speeds and enables us to predict how the speed depends on length, diameter, and helicity and to examine the effect of varying flagella geometry.

More generally, the helical shape might be considered a maximal case to produce thrust from cell body rotation. Thus, our result suggests that for flagellated bacteria, which usually have much slower cell body rotation rates than flagellar rotation rates, cell body shape has at most 10 to 15% effect on swimming speeds.

RESULTS

Helical trajectory

The swimming of bacteria can be easily visualized by time-resolved optical microscopy, and their trajectories can be obtained from frame-by-frame digital processing of movies to follow individual

bacteria as they swim (*30*, *32*). We use time-resolved phase-contrast microscopy to track the motion of live bacteria, although other types of microscopy have also been used in the literature (*29*, *30*, *32*). In our previous study (*28*), we tracked a hundred or more bacteria at a low–video frame rate [10 frames per second (fps)] to analyze the speed distributions of large populations of the WT helical *H. pylori* from three different strains and rod-shaped mutant Δ*csd6*. Here, we focus on imaging only a few bacteria from the LSH100 strain at higher magnification and faster frame rates to determine both the translational and rotational speeds of the swimmer and its relation to shape from a single trajectory. The experiments were done both in *Brucella* culture broth (BB10) and in porcine gastric mucin (PGM; 15 mg/ml solution at pH 6). This low concentration of PGM corresponds to the average concentration of mucin in the loose, nonadherent outer layer of mucus (*33*). At this concentration, PGM solutions in pH 6 buffer do not exhibit significant non–Newtonian effects (*28*, *34*, *35*). Movie S1 acquired at 100× with 200 fps shows a single helical bacterium swimming as a pusher in PGM at pH 6. An optical microscopic image from one frame of the movie shows the bacterium's cell body (see Fig. 1A, inset) along with the contour (blue), centerline (red), and flagellar junction localization (J). The shapes of the images were analyzed using CellTool (*36*), as described in Materials and Methods. The 2D projection of the helix centerline was fit to a sinusoidal shape to obtain the cell body parameters. Figure 1A shows images from every fifth frame (about four images per body revolution) of this movie obtained by analyzing movie S1. Overlaid on this image is the trajectory obtained by tracking the centroid of the images, as explained in Materials and Methods.

Figure 1B shows that the center point of the centerline and the axis of the body rotate as a function of time, and fig. S1 shows head and flagellar junction rotation independently. The rotation of the body causes the alignment angle between the body axis and the *x* axis of the image measured by CellTool (*36*) to oscillate in time. Measurement of the center point of the body (denoted by subscript b) and the alignment angle (denoted by subscript a) provide independent estimates of the rotation rates $\Omega_b = 10.3 \pm 0.9$ Hz and $\Omega_a = 10.4 \pm 0.9$ Hz, respectively. The 2D speed (V) during each revolution was calculated from the distance traveled on the image plane per revolution, as described in Materials and Methods. The rotation rate varies by ~9% during this run, whereas the speed varies about 12% with an average speed over the entire run of $V = 17 \pm 2$ μm/s. The fact that body rotation and alignment angle precession have the same period is consistent with "wiggling" trajectories caused by flagellar bundles with fixed orientation relative to the cell body (*37*). For these trajectories, the oscillation amplitude of the alignment angle is roughly twice the precession angle between the cell body axis and the average swimming direction. The data follow a positive linear correlation between V and Ω. The ratio V/Ω is a useful measure of the distance traveled in one revolution and should be independent of the motor torque and only weakly dependent on the thickness of the flagellar bundle. However, it depends on cell and flagellar size parameters as well as flagellar bundle orientation.

For this bacterium imaged at high resolution, it was also possible to visualize the flagellar rotation in some frames, as shown in movie S2 and Fig. 1C. The flagellar rotation rate is much faster than the body rotation, leading to an estimate of around 66 Hz, which is about three frames on the 200-fps camera and thus estimated with an uncertainty of 33%. In the images, the orientation of the flagella appears to change with respect to the body. The diffraction blur makes it hard to make a definitive evaluation of this angle, but it seems to range from 0° to 45°

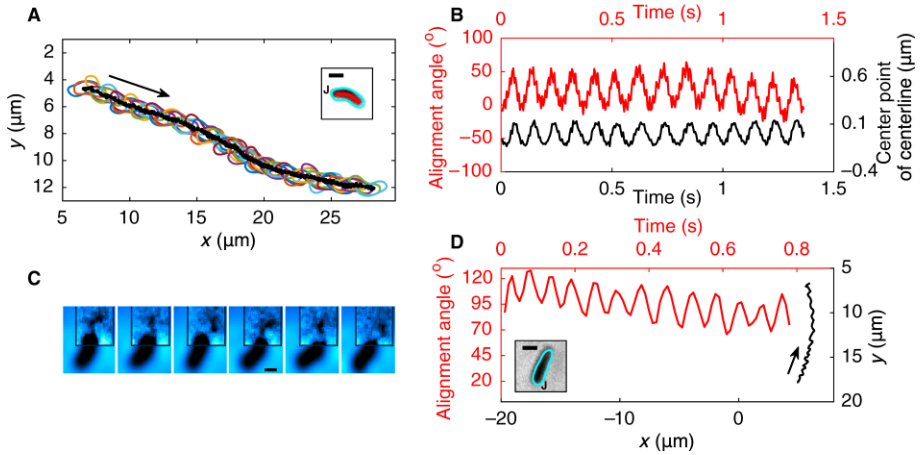

Fig. 1. Trajectory and body rotation of *H. pylori* LSH100 helical bacterium (WT) and rod-shaped mutant (Δ*csd6*) swimming in PGM (15 mg/ml at pH 6). (**A**) Trajectory of helical bacterium plotted as body contours of cells (colors) every five frames from movie S1. From this trajectory, we measured a mean trajectory pitch $P_T = 1.5 \pm 0.2$ μm (SD is based on the 13 full rotations observed in the entire movie S1). The inset shows the contour (blue), centerline of bacterium's cell body (red), and the flagellar junction (J). The flagellar bundle cannot be seen in this image because of low contrast. (**B**) Rotation of helical bacterium as measured by the change of the axis angle as a function of time (red) and by the motion of the center point of the centerline (black) (more details in Materials and Methods). (**C**) Image of the flagellar bundle of helical bacterium for consecutive frames, giving an estimated rotation rate of 66 Hz with an uncertainty of 33%. This image sequence is from the same movie used in (A) and (B), with images rotated for display and filtered to increase contrast (movie S2), especially around the flagellar junction. (**D**) Trajectory of the rod-shaped mutant from movie S3 plotted on the right side of graph in black (bottom and right axis) and rotation of bacterium as measured by change of the axis angle as a function of time plotted on top in red (top and left axis). The inset shows the contour (blue) of the bacterium cell body with the flagellar junction indicated by J. Scale bars, 1 μm; arrows indicate the swim direction.

from the body axis. Note that apparent changes in the flagellar orientation in these 2D images are also consistent with those of a bacterium with fixed flagellar orientation undergoing bodily rotation (*37*), although the observed slight temporal variation of swimming speeds, trajectories, rotation rates, and precession angles suggests that flagellar orientation may not be constant in time.

These direct observations of both body and flagellar rotation accompanied by a precession show that by tracking at high frame rate and high magnification, it is possible to directly observe the corkscrew motion of the bacterium as it swims. Additionally, because of the fact that as the flagellar bundle rotates the cell must counter-rotate to balance the flagellar torque, we can infer the sense of rotation of the flagella by imaging the rotation of the body. Flagellar rotation is very difficult to visualize, even under enhanced imaging conditions, because they are very thin and rotate much faster (~60 to 100 Hz), as well as by fluorescence microscopy, because the *Helicobacter* flagella are sheathed in the same cell membrane that covers the cell body. However, we have observed by looking at the movies that the end of the bacterium where the flagella are located (referred to as the junction J here) exhibits a more rapid variation in the contrast on the image as compared to the other end. Thus, we can identify the flagellar junction end even when the flagella cannot be imaged.

Comparison of helical with rod-shaped mutant

To address the question of how the shape affects swimming speed, we also tracked the rod-shaped mutant Δ*csd6* in PGM and compared it to the helical bacterium (see movies S1 and S3). Figure 1D shows the trajectory of the rod-shaped mutant, indicating that it also swims in a helical track. The cell body image, its contour, and flagella junction localization are shown in the inset. The precession of the rod axis angle can be observed by looking at the orientation of the cell as it moves along a helical trajectory (see Fig. 1D), and the variation of the axis orientation with time provides a measure of the rotation rate. Although the 2D images of the cell body remain rod-shaped as the bacterium rotates, the length of the image of the rod changes in an oscillatory fashion with the same period as the axis. We were also able to see the flagella of this rod-shaped bacterium in some frames, but because it was not seen clearly in all successive frames, we cannot evaluate the flagellar rotation rate.

We also compared the helical *H. pylori* and its rod-shaped mutant in BB10 (see movies S4 and S5 and Fig. 2, A to D). Figure 2A shows the trajectory of a helical bacterium (from movie S4, recorded at 200 fps and 100× magnification) whose cell body image is shown in the inset, and Fig. 2C shows the trajectory for the rod-shaped mutant (from movie S5, recorded at 30 fps and 40× magnification). Both trajectories show forward and reverse swimming. The rotation of the alignment angle is shown for both the forward and reverse motions, in Fig. 2B for the helical bacterium and in Fig. 2D for the rod-shaped mutant. The inset in Fig. 2C shows that the axial length X_B and the diameter of this rod-shaped bacterium are close to the contour length of the cell body centerline L_{arc} and to the diameter of the helical bacterium shown in Fig. 2A (see Table 1), that is, the two bacteria have similar cell volumes.

In Table 1, we list the observed speeds and also include the parameters V/Ω and $V/(\Omega\ X_B)$, which correspond to the distance traveled per rotation in dimensional and nondimensional units, respectively. A comparison of the observed speeds (Table 1) shows that the rod-shaped bacterium swims at a slower speed than the helical bacterium in both PGM and broth. We also observe that the relative change in speed of helical versus rod is larger in PGM than in broth, in agreement with the previous result reported by Martinez *et al.* (*28*) for the increase in median speed in viscous PGM as compared to broth. However, we cannot infer that this holds in general by comparing individual bacteria. The individual rod and helical bacteria examined here had different sizes as well as different rotation rates, which implies that they may have also differed in number of flagella in the bundle as well as flagellar geometry and orientation, features that we could not image.

Forward versus reverse motion

It is well known that bacteria change their swimming direction to explore their environment and respond to chemotactic gradients (*32*). In addition to the familiar run-tumble mechanism seen in many bacteria, such as *E. coli* (*32*), *H. pylori* also tends to reverse its swimming direction, which has been related to chemotactic sensing and quorum sensing in earlier works (*28*, *31*, *38*–*41*). Such run-reverse swimming has also been seen in several marine bacteria that swim in highly viscous environments (*42*–*45*) and in *Caulobacter crescentus* (*9*). We were able to observe reversal events in both the helical and rod-shaped bacteria tracks swimming in BB10, as shown in Fig. 2. We measured the average rotation rate before and after a reversal (see Table 1) and found that it increased by 40% for the rod-shaped mutant, whereas it decreased by 60% for the helical bacterium when swimming in reverse. The definition of forward/reverse relies on visualizing the rapid change in contrast at the flagella junction end further substantiated by actually seeing faint images of flagella in some frames (more details in the Supplementary Materials and movies S4 and S5). During the reverse run, the helical WT bacterium swims at $V_{WT,rev} = 10 \pm 2$ μm/s and the rod-shaped mutant at a similar speed, $V_{\Delta csd6,rev} = 11 \pm 2$ μm/s. Moreover, in the reverse run, this rod-shaped mutant swims at a similar rotation rate $\Omega_{\Delta csd6,rev} = 10 \pm 1$ Hz as compared to the helical one, $\Omega_{WT,rev} = 11 \pm 2$ Hz. Instead of comparing speeds for forward and reverse runs, it is better to measure distance traveled per rotation V/Ω [or the dimensionless quantity $V/(\Omega X_B)$], which are slightly larger during forward versus reverse swimming for both the helical and rod-shaped bacteria tracked here (see Table 1). However, using either V/Ω or $V/(\Omega X_B)$ to compare the swimming ability of rod-shaped and helical cell bodies in this context is problematic because one should compare cells with the same motor torque, cell body diameter, and flagellar orientation angle, all of which could vary from cell to cell. For example, variations in the swimming speed are dominated by variations in the number of flagellar motors per cell, which alters the total torque (*28*). As discussed later, our numerical model circumvents these problems to allow direct tests of the effect of cell body geometry on propulsion while keeping all other parameters fixed.

Simultaneous imaging of the trajectory and cell body allows us to determine the sense of rotation of the cell body by analyzing the phase of the rotation angle (more details in Materials and Methods). Because the body counter-rotates relative to the flagellum to balance torques, we thereby deduce the sense of flagellar rotation. Relative to the cell body, such an analysis shows that the sense of rotation of the flagellar bundle appears to reverse on a reversal event, implying that during both pushing (forward motion) and pulling (backward motion), the propulsive flagella have the same left-handed configuration.

In addition to the results on the 4 individual bacteria reported in detail above, we imaged and tracked 22 other bacteria (16 helical and 6 rod-shaped) in PGM and broth, all showing cells rotating while swimming along their trajectory. Although the speeds and rotation rates of individual bacteria vary because of different cell and flagella sizes, the overall rotation rates and swimming speeds are in a similar

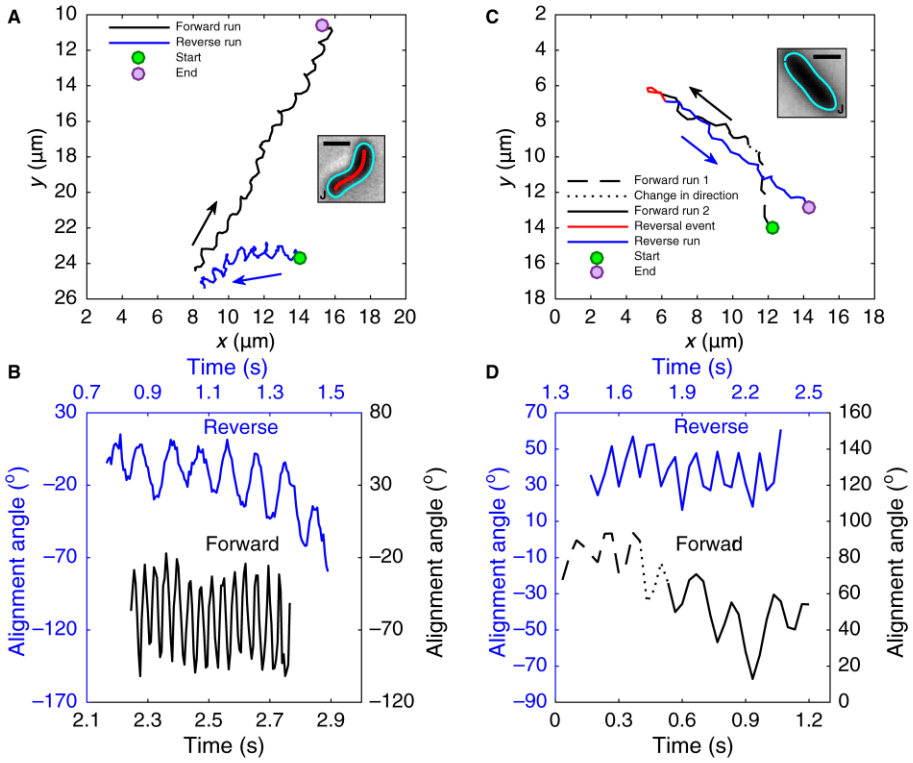

Fig. 2. Trajectory, body shape, and body rotation rate of *H. pylori* LSH100 helical WT and rod-shaped Δ*csd6* bacteria showing one reversal while swimming in BB10. (**A**) Trajectory of helical bacterium from movie S4 starting at the green point and ending at the purple point; arrows indicate swimming direction. The forward (black) and reversed (blue) trajectories are not connected because the tracking software could not track the bacterium during the reversal event as it left the field of view. However, movie S4 captures part of the bacterium's diffraction rings during the reversal event, confirming that it is the same bacterium for both tracks. The inset shows the contour (blue), centerline of cell (red), and the location of flagellar junction (J) of the helical bacterium; scale bar, 1 μm. (**B**) Rotation of helical bacterium measured by change of the axis angle with time for both runs, color-coded as in the track in (A). (**C**) Trajectory of rod-shaped mutant obtained from movie S5. The forward (black) and reversed (blue) trajectories are connected by the reversal event (red). The different lines in the forward run show changes in the direction of the trajectory and not from the reversals. The inset shows the contour (blue), centerline of cell (red), and the location of flagellar junction (J) of the rod-shaped bacterium; scale bar, 1 μm. (**D**) Rotation of rod-shaped mutant measured by change of the axis angle with time for both runs, color-coded as in the track in (C).

range to those displayed in Figs. 1 and 2. Although the numbers are not large enough to do a detailed statistical analysis, we note that the average of both V/Ω and $V/(\Omega\ X_B)$ are larger for the helical versus rod-shaped mutant, irrespective of the swimming medium. The values we obtained for the dimensionless ratio $V/(\Omega\ X_B)$ are 0.5 for helical versus 0.4 for the rod in PGM, and 0.6 for helical versus 0.5 for rod in BB10, implying about 25% extra propulsion for the helical shape in PGM and 20% in broth.

Calculation of trajectory using RSM

We used RSM (*46*, *47*) to calculate swimming trajectories and speeds of *H. pylori* with the same cell body shape, as shown in the inset in Fig. 1A. The bacterial geometry is specified by the helical pitch, helical radius, length, and cell body diameter, and the flagellar bundle is modeled as a single helix rotating around its helical axis at a fixed orientation relative to the cell body (Fig. 3A). Once the geometry is defined, all swimming kinematics are determined by a single input, the body rotation rate, which can be directly measured by experiment. This single input parameter incorporates the effects of varying flagella number, as well as any effects of medium viscosity on the rotation rate. Details of the numerical method, including convergence studies, are given in the Supplementary Materials, and the numerical parameters for both cell body and flagellum geometry are provided in Tables 1 and 2. The calculated trajectory for a particular choice of flagella geometry (as discussed later) shown in Fig. 3B is in reasonable agreement with the experimentally observed trajectory of Fig. 1A. The average velocity is the component of instantaneous velocity along the rotation direction, which is equivalent to the net translation over a revolution divided by the period of revolution.

Quantitative comparison between model and experiment

Figure 3C shows the predicted average speed as a function of cell body rotation frequency for the bacterium in Fig. 1. The error bars correspond to the propagated uncertainty from the measurements

Table 1. Cell body shape parameters, translation, and rotation speeds of helical- and rod-shaped mutants of *H. pylori* in PGM and BB10. NA, not applicable.

Medium		PGM (15 mg/ml)		BB10	
Bacterium shape		**Helical**	**Rod**	**Helical**	**Rod**
Cell shape parameters	X_B (μm)*	2.51 ± 0.09	2.74 ± 0.09	2.33 ± 0.09	2.6 ± 0.1
	L_{arc} (μm)*	2.69 ± 0.09	2.74 ± 0.09	2.53 ± 0.09	2.6 ± 0.09
	d_B (μm)*	0.83 ± 0.09	0.61 ± 0.09	0.61 ± 0.09	0.7 ± 0.1
	P_B (μm)*	2.43 ± 0.09	—	2.32 ± 0.09	—
	R_B (μm)*	0.15 ± 0.09	—	0.17 ± 0.09	—
Forward run	V (μm/s)†	17 ± 2	15 ± 4	31 ± 4	10 ± 2
	Ω (Hz)†	10.3 ± 0.9	17 ± 2	28 ± 3	7 ± 2
	V/Ω (μm) (measured)	1.6 ± 0.2	0.9 ± 0.3	1.2 ± 0.2	1.5 ± 0.4
	V/Ω (μm) (modeled)	1.66 ± 0.26	0.88 ± 0.15	1.13 ± 0.26	1.33 ± 0.12
	$V/\Omega X_B$ (measured)	0.67 ± 0.08	0.3 ± 0.1	0.50 ± 0.07	0.6 ± 0.1
Reverse run	V (μm/s)†	NA	NA	10 ± 2	11 ± 2
	Ω (Hz)†	NA	NA	11 ± 2	10 ± 1
	V/Ω (μm) (measured)	NA	NA	0.8 ± 0.2	1.1 ± 0.2
	V/Ω (μm) (modeled)	NA	NA	0.82 ± 0.25	1.14 ± 0.13
	$V/\Omega X_B$ (measured)	NA	NA	0.35 ± 0.09	0.44 ± 0.06

*The errors are given by $2^{1/2}$ (pixel size of image). †Averaged over the entire run; error is the SD for the run.

of cell body parameters (Table 1). The geometry and orientation of the bundle can affect the result, but flagellar geometry is difficult to measure precisely because it is difficult to visualize the flagella. Therefore, we investigate the effect of flagellar geometry by finding the range of swimming speeds possible for the observed cell body shape. Each of the different lines in Fig. 3C corresponds to different bundle geometries and orientations (pictorially represented beside the lines; see Table 2 for specific flagella geometrical parameters). The range of calculated speeds nearly spans all observed speeds: the minimum swimming speeds obtained for the bundle geometry F_{min} are below those observed in this experiment, whereas the maximum swimming speeds obtained for the bundle geometry F_{max} encompass the upper end of experimental measurements. The variation in swimming speed between the different bundle geometries is most strongly affected by the orientation angle. The flagellar configuration corresponding to the average flagellum geometry measured by Martinez *et al.* (*28*) using transmission electron microscopy (TEM) (Table 2) and bundle orientation parallel to the cell body helical axis (F_0) gives calculated swimming speeds smaller than the observed speeds. However, the geometry with the flagellum oriented at 40° from the helical axis (F_{fit}) yields swimming speeds that match experiments well. Note that a 40° orientation is consistent with the images in Fig. 1C.

We also investigated the dependence of trajectory on the flagellar bundle geometry. In Fig. 3D, the horizontal lines show the calculated trajectory pitch for the F_{min}, F_0, F_{fit}, and F_{max} bundle geometries. The F_{fit} geometry produces trajectories that have the most commonly observed trajectory pitch, calculated as V/Ω, further supporting the quantitative agreement between our model and experiment. The calculated overlay of images from trajectory for the flagellar geometry F_{fit} shown in Fig. 3B is comparable to the observed trajectory in Fig. 1A.

In addition to the helical bacterium shown in Fig. 1A, we also performed quantitative modeling of the rod-shaped mutant in PGM (Fig. 1D) as well as the helical bacterium and the rod-shaped mutant in BB10 (Fig. 2, A and B, respectively). We used the measured body parameters in Table 1 in combination with a range of flagellar bundle geometries as previously described (see Table 2 for specific geometric parameters). As in the previous case, the observed swimming speeds lie within the minimum and maximum values obtained by varying flagellar geometries. For the rod-shaped mutant in PGM (Fig. 3E), the best fit to observed speeds is obtained with the flagellar bundle at 30° from the body axis. For the bacteria in BB10 (Fig. 4), the best fits to observed speeds are obtained with the flagella at 50° and 40° from the helical axis for the rod-shaped bacterium swimming as a pusher (forward) and puller (reverse), and 30° and 5° for the helical bacterium swimming as a pusher and puller, respectively. Error bars for the calculated swimming speeds are the propagated uncertainty from errors in measured body parameters in Table 1. Note that the large errors in experimental frequencies for the Δ*csd6* bacterium arise from the slower frame rate of the videos in that case. The slopes of the fitted lines in Figs. 3 (C and E) and 4 (A and B) correspond to V/Ω and can be used to compare swimming speeds at the same rotation rates. In our calculations, we assume that the flagellar bundle has a fixed orientation relative to the cell body during swimming, which results in a linear relationship between V and Ω. Deviations from linearity in the experimental data indicate that the flagellar bundle orientation relative to the cell body may vary in time along the trajectory.

Effect of body helicity on swimming speeds

The above results provide quantitative validation of the numerical model, so we next use the numerical model to explore the effect of body helicity on swimming speeds. Although our experimental observations must only focus on individual examples, the numerical model allows us to continuously vary geometries. Numerical modeling circumvents the experimental difficulty of ensuring that flagellar geometries and cell body diameters are the same in comparison to helical and rod-shaped bacteria. To test the propulsive effect of the helical cell body, we first compare the swimming speed of helical and rod-shaped *H. pylori* cells with fixed flagellar geometry. In the following, we report speeds and angular velocities in nondimensional units by normalizing by $T/(\mu X_f^2)$ and $T/(\mu R X_f^2)$, respectively, where T is the motor torque, R is the flagellar helical radius, and X_f is the flagellar axial length. This choice of normalization amounts to keeping torque constant, as appropriate for flagellar motors under normal operating conditions, and provides a way to directly evaluate the effect of cell body shape on

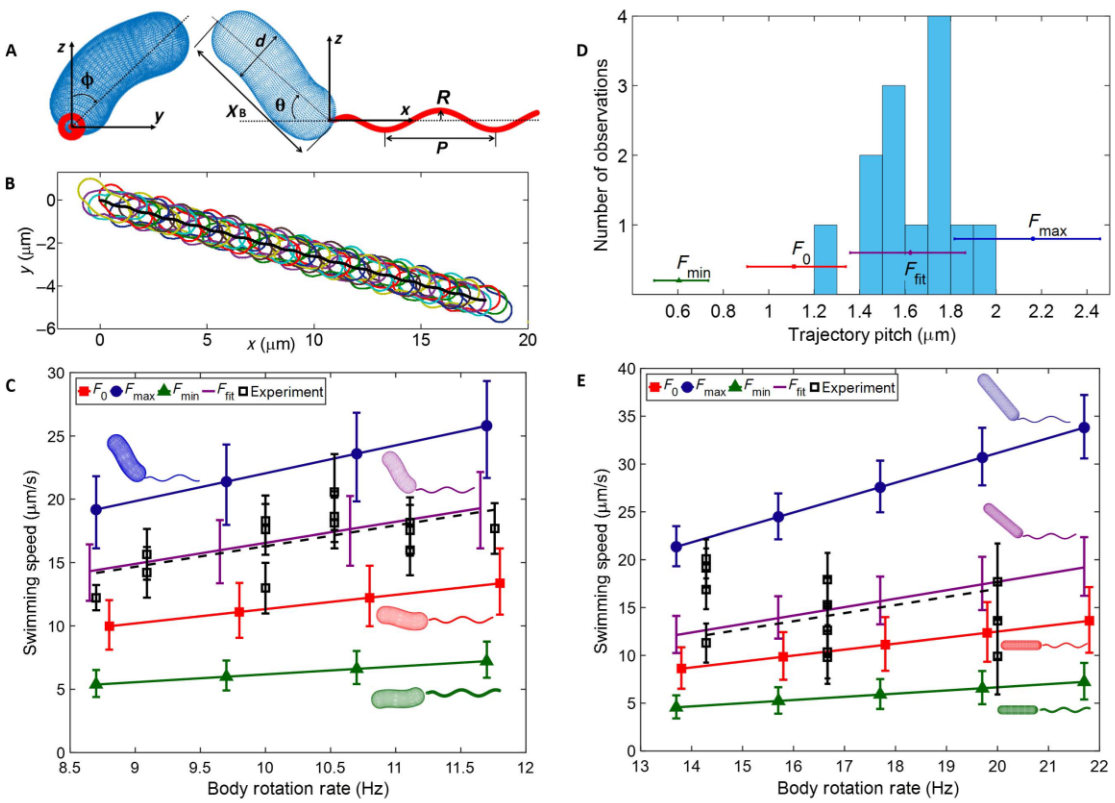

Fig. 3. Comparison of numerical model to experiment for bacteria in PGM. (**A**) Discretized geometry used for numerical calculations. Cell body geometry is parameterized by diameter *d* and axial length X_B, and flagellar bundle geometry is parameterized by pitch *P* and helical radius *R*. Orientation of the helical centerline of the cell body with respect to the centerline of the flagellum is determined by angles θ and φ. (**B**) Calculated trajectory of the cell body with geometry measured from Fig. 1 and flagellar parameters F_{fit} (see text and Tables 1 and 2). Frame interval is the same as in Fig. 1A, and trajectory pitch is 1.62 ± 0.3 μm. (**C**) Swimming speed observed from Fig. 1B (helical WT) compared to those numerically calculated for different flagellar geometries, which are shown next to each line. (**D**) Histogram of the trajectory pitch observed in experiments and numerically modeled trajectory pitch for the same flagellar geometries as in (C). (**E**) Swimming speed observed from Fig. 1D (rod-shaped mutant Δ*csd6*) compared to those numerically calculated for different flagellar geometries, which are shown next to each line. Vertical error bars in (C) and (E) and horizontal error bars in (D) correspond to propagated uncertainty from experimental cell body measurements.

swimming speeds. In addition, the length scale X_f is derived from the flagellum and so remains constant as cell body geometry is altered.

To investigate the effect of cell body helicity on swimming speed, we compare three scenarios (Fig. 5A, inset): (i) the actual geometry with left-handed flagellum and right-handed cell body, (ii) a geometry with left-handed flagellum and left-handed cell body, and (iii) a geometry with left-handed flagellum and rod-shaped (nonhelical) cell body. For the helical cell body, we use the mean value of the helical radius (0.22 μm), pitch (2.4 μm), and body diameter (0.58 μm) (*28*). For the rod-shaped cell body, the pitch is 0 and other geometrical values are the same as the helical cell body. Figure 5A shows the swimming speed as a function of varying cell body axial length for these three scenarios. As expected, right-handed cell bodies have faster swimming speeds. The difference between swimming speeds for the left- and right-handed cell bodies is always less than 30%, whereas the swimming speed of the cylindrical cell body is usually between them. The inset in Fig. 5A shows the percent difference between the swimming speeds of left- and right-handed cell bodies. Typically, the cylindrical cell body has a swimming speed closer to that of the right-handed cell body (<10% difference) and further from that of the left-handed cell body (<20% difference). Note that because the geometry of the flagellum remains constant for all three cases, there is no overall symmetry relation between the left- and right-handed cell body scenarios, and the swimming speed of the ellipsoidal cell body is not expected to lie exactly in between that of the left- and right-handed cell bodies. These results support the idea that the effect of the body helicity on propulsion is quite small relative to a cell with a nonhelical geometry.

In addition to the direct comparison between the helical and rod-shaped bacterium presented above, we also examine our calculations relative to previous results comparing speed distributions for rod-shaped Δ*csd6* and helical WT populations of the LSH100 strain (*28*). The measured speed distributions indicate that the rod-shaped mutants swim with an average swimming speed of ~10% slower,

Table 2. Flagellar bundle parameters. Flagellar geometry parameters following Martinez *et al.* (*28*) are inputs for our numerical calculations.

		PGM (15 mg/ml)		BB10	
		Helical	**Rod**	**Helical**	**Rod**
Flagella (F_0)	X_f (μm)*	2.97	2.97	2.97	2.97
	d_f (μm)†	0.07	0.07	0.07	0.07
	P (μm)‡	1.58	1.58	1.58	1.58
	R (μm)‡	0.14	0.14	0.14	0.14
	Ω_f (Hz)	66§	—	—	—
Flagella (F_{fit})	Θ_{fwd} (°)	40	30	30	50
	Φ_{fwd} (°)	0	0	0	0
	Θ_{rev} (°)	NA	NA	5	40
	Φ_{rev} (°)	0	0	0	0
Flagella (F_{min})	d_f (μm)	0.14	0.14	0.14	0.14
	Θ (°)	15	0	15	0
	Φ (°)	180	0	225	0
Flagella (F_{max})	d_f (μm)	0.035	0.035	0.035	0.035
	Θ (°)	45	50	45	50
	Φ (°)	0	0	0	0

*The end-to-end length X_f of the flagellum is calculated from a helical length of 3.4 μm following Martinez *et al.* (*28*) and was the same for the helical- and rod-shaped cells. †The thickness of the flagellar bundle d_f is taken the same way as that used in the RFT calculation of Martinez *et al.* (*28*) for the F_0 and F_{fit} geometries and then varied for F_{min} and F_{max} geometries. ‡The flagella pitch P and helical radius R are taken the same way as that used by Martinez *et al.* (*28*), which are based on the values used for *Vibrio alginolyticus* (*29*). §Flagellar rotation is estimated from only three frames per rotation (see Fig. 1C), and thus, the error would be about 33%.

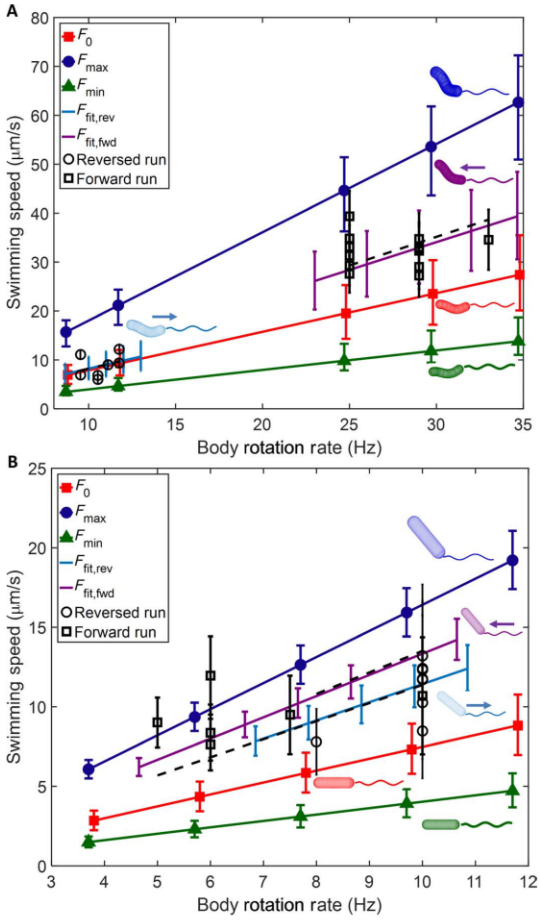

Fig. 4. Comparison of numerical model to experiment for bacteria in broth. (**A**) Swimming speed calculated for LSH100 helical WT trajectory from Fig. 2A using measured cell body geometry and different flagellar geometries, which are shown next to each line. Isolated symbols are experimental observations from trajectory. (**B**) Swimming speed calculated for LSH100 rod-shaped mutant Δ*csd6* trajectory from Fig. 2B using measured cell body geometry and different flagellar geometries, which are shown next to each line. Isolated symbols are experimental observations from trajectory. All parameters used for these models are described in Tables 1 and 2.

which is not too far from the result shown in Fig. 5A where the cylindrical body swimming speed is about 6% lower than that of a helical cell with a right-handed body. Because the swimming speed variation in the populations would be more strongly affected by variations in the number of flagella, this suggests that both the rod-shaped mutant and helical WT populations have similar distributions of number of flagella, as was confirmed from TEM measurements in (*28*). In addition, Martinez *et al.* (*28*) used RFT to calculate speed and found that the speed monotonically decreases with increasing length and increasing helical radius, whereas it showed a nonmonotonic dependence on pitch, increasing at low values of pitch and decreasing slightly for high pitch. These trends are the same as obtained here for the RSM calculation (Fig. 5, A and D, for constant contour length). However, the RFT predicted a much larger effect of helicity on speed, with the helical cell swimming about 40% faster than the rod [modeled as an ellipsoid (*20*)]. In contrast, RSM results are quite close to the observed speed increase of 10% for helix versus rod.

Little thrust produced by slowly rotating cell body

Physically, the small amount of cell body propulsion can be explained by the relatively small rotational speed of the cell body as compared to the flagella. Figure 5B shows the rotation rate for both the flagella and cell body for the scenarios in Fig. 5A. In all cases, the cell body rotation rate is less than $^1/_{10}$ of the flagellar rotation rate (comparable within errors to the experimentally observed ratio of cell body to flagellar rotation rate shown in Fig. 1), implying that there is limited ability for the cell body to generate thrust. Because of hydrodynamic interactions between the cell body and flagellum, it is not possible to clearly define which portion of the total thrust arises from the cell body and flagellum separately. However, thrust and drag can be estimated from a model that ignores the hydrodynamic interactions between the cell body and

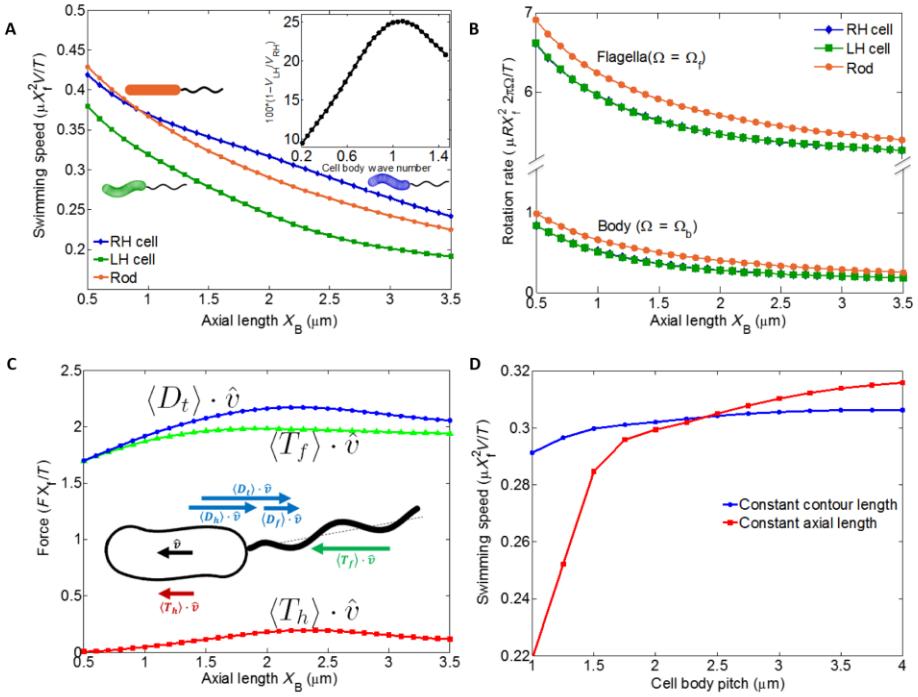

Fig. 5. Effect of body helicity on propulsion. (**A**) Nondimensional swimming speed versus axial length for constant torque. Comparison between cell bodies of opposite helicity [blue/diamonds, right-handed (RH); green/square, left-handed (LH)] and a rod-shaped cell body (orange/circles) reveals the effect of helicity on swimming speed. Inset: Percent difference between swimming speeds for left- and right-handed cell bodies. (**B**) Nondimensional cell body rotation rate for different axial lengths. The body rotation rate is an order of magnitude slower than the flagellar rotation rate. Both rotation rates are virtually the same for RH and LH cells, as seen by the overlapping blue and green symbols. (**C**) Average swimming direction component of total drag and estimated thrusts from cell body and flagella. (**D**) Nondimensional swimming speed as a function of cell body pitch, which varies the helicity of the cell body. In the two curves, either cell body contour length or cell body axial length is kept fixed.

flagellar bundle. We calculate the force and torque on the body and flagellar bundle separately using the RSM to calculate resistance matrices that express the forces and torques in terms of their linear and rotational velocities (*48*). Imposing the kinematic constraint of a fixed bundle-cell orientation and net force and torque balance yields swimming velocities and body rotations that are qualitatively in agreement to the full RSM calculations (see the Supplementary Materials for details).

In Fig. 5C, we plot the components of estimated total drag, flagellar thrust, and cell body thrust in the swimming direction as a function of axial length for the case of right-handed cell body and left-handed flagellum. In accord with the expectations arising from the smaller rotation rates of the cell body compared to the flagellum, the cell body thrust is estimated to be only about 15% of the flagellar thrust. Because of the net force constraint, the sum of the thrust from the cell body and flagellar bundle equals the total drag. Thus, the helicity of the cell body (which leads to thrust) should not affect swimming speeds through propulsion by more than that percentage.

Drag-dominated effect of cell body geometry on swimming speed

If the cell body shape does not affect the swimming speed through propulsion, then what dominates the changes in swimming speeds observed in Fig. 5A? In Fig. 5A, the dominant trend is that swimming speed decreases (by a factor of about 2) as the axial length increases. The trend in swimming speed can be explained by the following: for constant prescribed motor torque, the flagellar rotation rate should be relatively constant, yielding an approximately constant flagellar thrust and, hence, nearly constant total thrust, as apparent in Fig. 5 (B and C). The velocity is set by balancing the total thrust against the total drag, both of which are linearly related to the swimming velocity (Eq. 7 in the Supplementary Material). Thus, changes in the swimming speed are primarily due to changes in the translational resistance of the cell body, which increases with increasing axial length of the helix for fixed pitch, consistent with the results of Fig. 5A. Having the cell body affect swimming speeds through drag is the most commonly considered situation for bacteria as well as for sperm (*4*, *49*, *50*).

In addition to investigating the effect of cell body helicity by comparing left-handed, right-handed, and rod-shaped cell bodies, we can change the helical character of the cell body by varying the helical pitch: a small pitch yields a very tight helix, whereas a large pitch yields a loose helix. The resulting swimming speeds are shown in Fig. 5D. The blue curve (circle symbols) is the swimming speed versus pitch for constant arc length; the swimming speed increases by less than 5% as the pitch varies by a factor of 4. The small change in

swimming speed suggests that helicity does not appreciably affect swimming speed. On the other hand, if the axial length of the helix is kept fixed instead of keeping the arc length of the helical cell body fixed (red curve, square symbols), the swimming speed increases by nearly 50% over the same range of pitches. However, changing the pitch changes not only the helical character of the geometry but also the quantities, such as rotational and translational drag of the cell body. Our results are consistent with the hypothesis that changes in drag are the dominant contributors to changes in swimming speed: translational drag increases with increasing contour length of the cell body, which increases with decreasing pitch for fixed axial length (red curve), whereas translational drag is relatively constant with pitch for fixed contour length of the cell body (blue curve).

Martinez *et al.* (*28*) also studied three different helical strains varying in shape parameters and found that some strains differed in average swimming speed by as much as a factor of 2. However, these observations cannot be directly compared to our calculation of dependence of speed on length or pitch of helical bacteria because these strains not only varied in their morphological parameters but also had a different number of flagella, which varied within each population as well. In accord with our investigation here, we believe that the latter may have a larger effect than variation in shape/size, as was observed in the experiments of Martinez *et al.* (*28*) by examining mutants with varying numbers of flagella. Such observations highlight the complicated variations within populations of a given bacterium and differences among strains, which make direct experimental evaluation of the changes in swimming speed due to cell body shape difficult. Even measures such as V/Ω should not be used to definitively compare swimming efficacy. Indeed, although Table 1 shows that V/Ω of the forward-swimming helical cell is equal within experimental error to that of the rod-shaped mutant bacteria in broth and that V/Ω of the forward-swimming helical cell is faster than that of the rod-shaped mutant in PGM, when we performed apple-to-apple comparisons by calculating swimming speeds of a rod-shaped bacterium with the same body diameter, length, and flagellar orientation as the helical bacterium (or vice versa), we found up to 50% differences in V/Ω. However, examining the constant-torque swimming speed between each rod-shaped/helical pair revealed less than 15% differences, in agreement with the calculations presented above.

Comparison to other bacteria species

The effect of propulsion arising from cell body rotation was also recently examined for the curved bacterium *C. crescentus* by Liu *et al.* (*9*). In that paper, the relative orientation of the cell body to the swimming trajectory is shown to affect swimming speeds, and it is hypothesized that tilted cell bodies significantly contribute to propulsive thrust. In contrast, our results suggest that helical cell bodies produce little propulsive thrust. Because helical cell bodies would be expected to have more propulsive thrust than the slightly curved cell bodies of *C. crescentus*, we reexamined the model of Liu *et al.*, which presents a decoupled model treating the cell body as a rod-shaped body tilted from the flagellar axis by an angle θ. The resistance matrix for the cell body depends on the tilt angle θ and contains an off-diagonal term ϵ_c, which is nonzero when $\theta \neq 0$, describing cell body propulsion arising from rotation, and diagonal terms σ_c and τ_c, describing the cell body rotational drag arising from rotation or cell body translational drag arising from translation, respectively. In Fig. 6, we regenerate Liu *et al.*'s (*9*) Figure 4 for cell mobility versus precession angle, plotting the speed normalized by cell body rotation rate and cell body length, $[K = V/(\Omega L) = (b\tau_c + \epsilon_c)/(\sigma_c + c + b\epsilon_c)]$, which is Eq. 4 in the work of Liu *et al.* (*9*). The precise parameters we used are the following: $L = 2\,\mu\text{m}$, $b = 1.1\,\mu\text{m}^{-1}$, $c = 0.65\,\mu m \times 4\pi\mu$, $\frac{c_\perp}{c_\parallel} = 1.4$, $C_s = 4\pi\mu$, and $2R = L\sin(\theta)$.

In Fig. 6, we examine the relative contribution of cell body propulsion by also plotting $K_{\tau c} = b\tau_c/(\sigma_c + c)$, which ignores the contribution of the cell body propulsion by setting $\epsilon_c = 0$. It is apparent that the dependence of swimming speed on tilt angle is largely captured even without considering cell body propulsion. Furthermore, we also plot $K_{\epsilon c} = \epsilon_c/(\sigma_c + c + b\epsilon_c)$, which isolates the contribution of the cell body propulsion by setting $\tau_c = 0$. This yields only a small variation of swimming speed, in accord with our results for *H. pylori*.

DISCUSSION

Our overall conclusion is that helical shape adds only a small advantage in motility. The results reported here and the earlier studies of Liu *et al.* (*9*) are consistent with the interpretation that cell bodies affect swimming speeds primarily through changes in rotational and translational drag rather than through changes in the cell body propulsion. This general statement should hold true when the propulsive thrust is largely generated by an external flagellum or flagellar bundle; on the other hand, in cases where propulsion is generated by cell body deformations, such as *Spiroplasma* or *Spirochete* bacteria, clearly the helicity of the cell body will play a dominant role in thrust. Likewise, the helicity of artificial swimmers where rotation rates can be controlled by external fields also plays a large role in thrust (*51*–*54*). In this manuscript, we have so far focused on swimming speed rather than efficiency because bacteria that live in the digestive tract are likely not limited by the power output needed for locomotion. However, for bacteria in other environments, such as marine bacteria, nutrient scarcity and higher swimming speeds may select for efficiency rather than speed. In the Supplementary Materials, we show the efficiencies of bacteria (defined as work done to translate the cell body divided by total power expended; Eq. 12 in the Supplementary Material) with the right-handed, left-handed, and rod-shaped cell bodies examined in Fig. 5A. We find that changes in efficiency are well-accounted for by the change in swimming speed, rather than changed resistance or changed power expended as the geometry varies. Because the work to translate the cell body scales as speed squared, one may expect that the 10% changes in swimming speed between rod and helical cell bodies would lead to larger changes in efficiency of a factor of ~1.2 ($= 1.1^2$), and 30% changes in swimming speed between left- and right-handed cell bodies would lead to changes in efficiency of a factor of ~1.7, which may be enough to play an important role in those bacteria that optimize efficiency and perhaps gain a fitness advantage in evolutionary terms. Furthermore, relatively small changes in swimming speeds may have large effects on chemotactability (*1*, *2*, *55*), which could be another way that the effects of body shape could be selected for.

To summarize, we have performed experiments and modeling to answer how much additional propulsion can be added by cell body shape, obtaining both quantitative results for *H. pylori* as well as a mechanistic, physical understanding of the dominant effects of cell body shape on propulsion. We show that bacteria rotation rates can be determined using readily available 2D microscopy tracking methods with fast time-resolution and high magnification (100×) phase-contrast microscopy along with a shape analysis program. More specialized 3D tracking microscopes are not essential, although they enable observation of longer tracks. We observed that the alignment

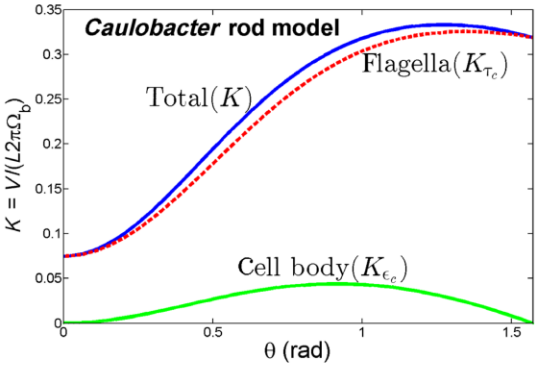

Fig. 6. Nondimensional swimming speed for *C. crescentus* predicted from flagellar thrust only (red) and cell body thrust only (green) compared to swimming speed predicted by model in Liu *et al.* (9).

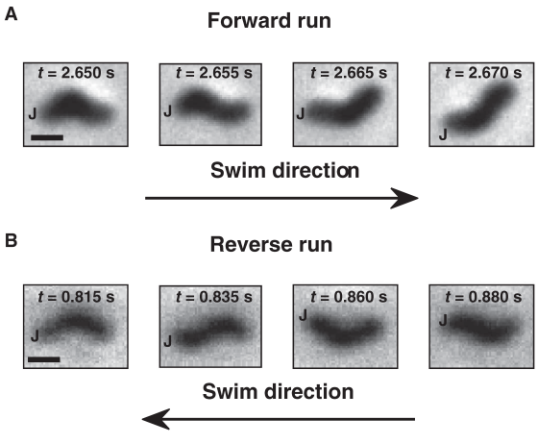

Fig. 7. Method to obtain the sense of rotation of helical body of the bacterium. (**A**) Forward run: Sequence of shape projections, a few frames apart, of the right-handed helical body rotating one way. (**B**) Reverse run: Sequence of shape projections, a few frames apart, of the right-handed helical body rotating the opposite way. Both sequences are obtained from the same bacterium before and after reversal, swimming in BB10 (from movie S4, same as Fig. 2A). The position of the flagellar junction is marked as J. Scale bars, 1 μm.

angle of the 2D image of the cell precesses as the cell rotates about an axis aligned at a nonzero angle relative to the flagella, producing a helical trajectory, that is, proving that *Helicobacters* do indeed swim in a corkscrew fashion in a solution. However, this type of motion is not unique to the helical cell; rod-shaped cells also precess as they swim, in agreement with previous observations of other bacteria, such as *E. coli* (56) and *Bacillus subtilis* (37). The images of the helical-shaped bacterium change in shape and those of the rod-shaped bacterium change in length, further enabling us to visualize the rotation of the cell body.

We were also able to image the rotation of the flagellar bundle in a few bacteria in PGM and directly show that the rotation of the cell body is considerably slower than that of the flagella; the body rotation rate was one-sixth of the flagellar rotation rate for the bacterium swimming in PGM solution at pH 6. As the flagella rotate to provide thrust, the right-handed cell body counter-rotates in the opposite direction to produce net zero torque at the flagellar pole. Because the direction of the thrust is opposite for the right- and left-handed helices rotating in the same sense, it has been suggested that the helix of the cell body is right-handed rather than left-handed to provide additional propulsive thrust in the swimming direction. The sense of rotation of the flagella and cell body reverses on a reversal, implying that during both pushing (forward motion) and pulling (backwards motion), the propulsive flagella have the same left-handedness. Similar run-reverse motion and precession of the cell could also be seen for the rod-shaped Δ*csd6* mutant, implying that this type of motion is not unique to helical bacteria, but rather it is similar to the motion previously observed in *C. crescentus* using a 3D tracking microscope.

Our quantitative measurements of the shape and speed of individual bacteria enable direct comparison and validation of theoretical models; previous experiments only provided indirect comparisons based on separate measurements of shape and speed distributions from a large population of bacteria. With the validated model, we were able to predict the effects of varying body helicity, length, and diameter, as well as flagellar configuration on swimming speeds and trajectories. Because of the relatively slow rotation of the cell body compared to flagella, we found that the body shape makes a small contribution to propulsive thrust—in agreement with our experimental observations—and swimming speed variations due to body shape are dominated by changes in translational drag due to length and diameter variations. Because helical cell bodies might be considered the strongest candidate for propulsion due to cell body, our results imply that quite generally, swimming speeds of flagellated bacteria are little affected by body geometry.

MATERIALS AND METHODS

H. pylori culturing

All experiments reported in this paper were done on the LSH100 strain of *H. pylori*, a derivative of the human clinical isolate G27 (38, 57) and its isogenic mutant with a straight rod shape, LSH100 Δ*csd6* (26, 28). The culture procedure was identical to that used by Martinez *et al.* (28) and is described briefly here. Frozen aliquots of bacteria were grown on *Brucella* agar plates with 5% horse blood (BD Biosciences) for 2 days, after which, they were restreaked onto new plates. After 2 to 5 days, the grown cells were transferred into BB10 containing *Brucella* broth (BD Biosciences) with 10% heat-inactivated fetal bovine serum (GIBCO) and left to grow overnight under constant agitation. Both cultures in agar plate and BB10 were kept in an incubator at 37°C under microaerophilic conditions (6 to 16% oxygen and 2 to 10% carbon dioxide; BD Biosciences GasPak EZ Campy Container System Sachets).

Preparation of PGM

PGM was isolated from mucosal scrapings of pig stomach epithelium and purified by Sepharose CL-2B column chromatography followed by density gradient ultracentrifugation, as described by Celli *et al.* (19). Lyophilized PGM was weighed, and the appropriate amount of PGM was dissolved in sterile H_2O to prepare a solution (15 mg/ml). PGM solution was allowed to hydrate and equilibrate for 48 hours at 4°C, and an appropriate amount of 0.1 M phosphate-succinate buffer (pH 6) was added before use. A more detailed procedure is in the work of Martinez *et al.* (28).

Bacterial suspension in different media

Bacteria were removed from liquid culture during the exponential phase of growth (0.4 to 0.7 optical density at 600 nm) and diluted in BB10 or PGM solution (with buffer at pH 6) to produce 10% bacteria mixture by volume. To get adapted to the new environment, the bacteria in PGM were left in the incubator at 37°C for 45 min and used immediately. A more detailed procedure is in the work of Martinez *et al.* (*28*).

Microscopy and imaging

Bacteria samples were pipetted onto standard microscope slides with a 9-mm-diameter, 120-μm thick secure spacer (SecureSeal Imaging Spacers, Sigma-Aldrich) and sealed with a coverslip. The bacteria were imaged at room temperature using an Olympus IX70 inverted microscope. We were careful to focus in the center of the spacer to avoid swimming surface effects (*58*). We used a 100× phase-contrast lens with a numerical aperture (NA) of 1.25 and with Zyla 5.5 sCMOS Andor camera (6.5 μm per pixel) at 200 or 100 fps for most of the measurements. One series of measurements for the rod-shaped mutant in BB10 was done using a 40× phase-contrast lens with an NA of 0.65 and with QImaging Rolera CMOS camera (3.63 μm per pixel) at 30 fps. The 40× and 30-fps imaging conditions enabled us to track the bacterium for a longer time but with smaller spatial and temporal resolution than the 100× at 200 or 100 fps.

Cell shape analysis

The selected supplementary movies were individually and manually cropped to contain only one bacterium using ImageJ. The shape (which includes the cell body contour, diameter, and cell centerline) of each bacterium was extracted and aligned using the software program CellTool (*36*). The end-to-end axial length was measured as the distance between the front and back contour points of the aligned bacterium contour. For helical bacteria, the aligned centerline was imported to MATLAB v8.3.0.532 and fitted using a sine function, $y = R_b\left(\frac{2\pi}{P_b}x + \delta\right)$, from which the body helical pitch (P_b) and body helical radius (R_b) were obtained (*28*). Here, δ is a parameter that allows the sine function to have a phase shift. The cell shape parameters, reported in Table 1, are from the most in-plane image, and the errors were calculated as $\sqrt{2}\left(\frac{\text{pixel size of camera}}{\text{lens magnification}}\right)$.

Body rotation rate and sense of rotation

The body rotation rate for the helical bacterium was measured using CellTool to monitor the vertical change in the center point of the centerline of the aligned bacterium contour over time. CellTool saves the alignment angle of each aligned contour, so an independent measure of the body rotation rate was also obtained by monitoring the change in the alignment angle of the bacterium. Only the alignment angle method was used for determining the body rotation rate of the rod-shaped bacteria. The periodicity in both methods was obtained by measuring the time between two maximum points and showed consistent results. In addition to monitoring the alignment angle and change in vertical position of the center point, we also tracked a point at the head of the bacterium and one at the flagella junction pole, as shown in fig. S1. These points also give the same period of rotation. The rotation rate reported in Table 1 is an average of the rotation rates of each revolution during one run, and the error is the SD. At 30 fps, it was not possible to estimate the SD of the body rotation rate of fast rotating bacteria because the time resolution was not large enough to obtain the small variations in rotation rate over the duration of the track.

The sense of rotation can be obtained because of the helical shape of the body. Depending on the sense of rotation, the 2D projections over one revolution will go through a different sequence of shapes, analogous to a sinusoidal phase shift. When the bacterium is swimming as a pusher, its right-handed body rotates and the 2D shape projection sequence is given by Fig. 7A, and when it swims as a puller, the shape projection sequence is given by Fig. 7B.

The flagellar bundle handedness of both pusher/puller cases can be inferred if one knows the localization of the flagellar bundle, sense of body rotation, and swim direction. To swim in the direction shown in Fig. 7 (A or B), the flagella have to generate a thrust in that same swimming direction. This thrust can be accomplished by a right-handed flagellar bundle rotating in the same sense as the body rotates or by a left-handed flagellar bundle rotating in the opposite direction of the body rotation. As mentioned before, the flagellar bundle has to rotate in the opposite direction of the body to balance torque. Consequently, the flagellar bundle has to be left-handed in both pusher and puller cases.

Tracking of bacteria and measuring 2D speed

The centroid of the bacterium obtained using CellTool for all frames provided the position over time of the swimmer and therefore was used for generating the tracks (shown in Fig. 1D). The same bacterium was also tracked using PolyParticleTracker (*59*), which generates tracks, as shown in Fig. 1B. Both methods show consistent results. Even though the bacterium is free to swim in a 3D volume, the supplementary movies only capture the bacterium swimming on a horizontal plane and thus measure the 2D speed. The distance traveled during one revolution was divided by the period of rotation to obtain the speed for each full revolution. The speed reported in Table 1 is given by the average of the speed per revolution during the run, and the error is the SD. The programs also give the instantaneous speed of the bacterium calculated from the displacement between successive frames.

SUPPLEMENTARY MATERIALS

Supplementary material for this article is available at http://advances.sciencemag.org/cgi/content/full/2/11/e1601661/DC1

movie S1. Motility of LSH100 WT (helical) *H. pylori* swimming in PGM (15 mg/ml) imaged with 100× lens, 200 fps.

movie S2. Flagellar bundle visualization.

movie S3. Motility of LSH100 Δ*csd6* (rod mutant) *H. pylori* swimming in PGM (15 mg/ml) imaged with 100× lens, 100 fps.

movie S4. Motility of LSH100 WT (helical) *H. pylori* swimming in BB10 imaged with 100× lens, 200 fps.

movie S5. Motility of LSH100 Δ*csd6* (rod mutant) *H. pylori* swimming in BB10 imaged with 40× lens, 30 fps.

fig. S1. Head and flagellar junction trajectories of LSH100 helical *H. pylori* swimming in PGM (15 mg/ml) (movie S1).

fig. S2. Swimming speed versus axial length, calculated by decoupled model.

fig. S3. Swimming power versus axial length for right- and left-handed helical cells and rod-shaped cell body.

Numerical calculation methods

References (*60*, *61*)

REFERENCES AND NOTES

1. K. D. Young, Bacterial morphology: Why have different shapes? *Curr. Opin. Microbiol.* **10**, 596–600 (2007).
2. J. G. Mitchell, The energetics and scaling of search strategies in bacteria. *Am. Nat.* **160**, 727–740 (2002).
3. N. Maki, J. E. Gestwicki, E. M. Lake, L. L. Kiessling, J. Adler, Motility and chemotaxis of filamentous cells of *Escherichia coli*. *J. Bacteriol.* **182**, 4337–4342 (2000).

4. S. Cooper, M. W. Denny, A conjecture on the relationship of bacterial shape to motility in rod-shaped bacteria. *FEMS Microbiol. Lett.* **148**, 227–231 (1997).
5. D. B. Dusenbery, Fitness landscapes for effects of shape on chemotaxis and other behaviors of bacteria. *J. Bacteriol.* **180**, 5978–5983 (1998).
6. J. W. Shaevitz, J. Y. Lee, D. A. Fletcher, *Spiroplasma* swim by a processive change in body helicity. *Cell* **122**, 941–945 (2005).
7. J. Yang, C. W. Wolgemuth, G. Huber, Kinematics of the swimming of *Spiroplasma*. *Phys. Rev. Lett.* **102**, 218102 (2009).
8. D. K. Vig, C. W. Wolgemuth, Swimming dynamics of the Lyme disease spirochete. *Phys. Rev. Lett.* **109**, 218104 (2012).
9. B. Liu, M. Gulino, M. Morse , J. X. Tang, T. R. Powers, K. S. Breuer, Helical motion of the cell body enhances *Caulobacter crescentus* motility. *Proc. Natl. Acad. Sci. U.S.A.* **111**, 11252–11256 (2014).
10. H. C. Berg, L. Turner, Movement of microorganisms in viscous environments. *Nature* **278**, 349–351 (1979).
11. R. L. Ferrero, A. Lee, Motility of *Campylobacter jejuni* in a viscous environment: Comparison with conventional rod-shaped bacteria. *J. Gen. Microbiol.* **134**, 53–59 (1988).
12. Q. N. Karim, R. P. Logan, J. Puels, A. Karnholz, M. L. Worku, Measurement of motility of *Helicobacter pylori*, *Campylobacter jejuni*, and *Escherichia coli* by real time computer tracking using the Hobson BacTracker. *J. Clin. Pathol.* **51**, 623–638 (1998).
13. B. J. Marshall, J. A. Armstrong, D. B. McGechie, R. J. Glancy, Attempt to fulfil Koch's postulates for pyloric Campylobacter. *Med. J. Aust.* **142**, 436–439 (1985).
14. R. M. Peek Jr., J. E. Crabtree, *Helicobacter* infection and gastric neoplasia. *J. Pathol.* **208**, 233–248 (2006).
15. H. L. T. Mobley, G. L. Mendz, S. L. Hazell, *Helicobacter pylori: Physiology Genetics* (ASM Press, 2001).
16. K. Van den Bulck, A. Decostere, M. Baele, A. Driessen, J.-C. Debongnie, A. Burette, M. Stolte, R. Ducatelle, F. Haesebrouck, Identification of non-*Helicobacter pylori* spiral organisms in gastric samples from humans, dogs, and cats. *J. Clin. Microbiol.* **43**, 2256–2260 (2005).
17. C. Montecucco, R. Rappuoli, Living dangerously: How *Helicobacter pylori* survives in the human stomach. *Nat. Rev. Mol. Cell Biol.* **2**, 457–466 (2001).
18. H. Yoshiyama, T. Nakazawa, Unique mechanism of *Helicobacter pylori* for colonizing the gastric mucus. *Microbes Infect.* **2**, 55–60 (2000).
19. J. P. Celli, B. S. Turner, N. H. Afdhal, S. Keates, I. Ghiran, C. P. Kelly, R. H. Ewoldt, G. H. McKinley, P. So, S. Erramilli, R. Bansil, *Helicobacter pylori* moves through mucus by reducing mucin viscoelasticity. *Proc. Natl. Acad. Sci. U.S.A.* **106**, 14321–14326 (2009).
20. J. M. Hardcastle, thesis, Boston University (2016).
21. R. Bansil, J. P. Celli, J. M. Hardcastle, B. S. Turner, The influence of mucus microstructure and rheology in *Helicobacter pylori* infection. *Front. Immunol.* **4**, 310 (2013).
22. R. Bansil, B. S. Turner, Mucin structure, aggregation, physiological functions and biomedical applications. *Curr. Opin. Colloid Interface Sci.* **11**, 164–170 (2006).
23. J. P. Celli, B. S. Turner, N. H. Afdhal, R. H. Ewoldt, G. H. McKinley, R. Bansil, S. Erramilli, Rheology of gastric mucin exhibits a pH-dependent sol–gel transition. *Biomacromolecules* **8**, 1580–1586 (2007).
24. X. Cao, R. Bansil, K. R. Bhaskar, B. S. Turner, J. T. LaMont, N. Niu, N. H. Afdhal, pH-dependent conformational change of gastric mucin leads to sol-gel transition. *Biophys. J.* **76**, 1250–1258 (1999).
25. S. A. Mirbagheri, H. C. Fu, *Helicobacter pylori* couples motility and diffusion to actively create a heterogeneous complex medium in gastric mucus. *Phys. Rev. Lett.* **116**, 198101 (2016).
26. L. K. Sycuro, C. S. Rule, T. W. Petersen, T. J. Wyckoff, T. Sessler, D. B. Nagarkar, F. Khalid, Z. Pincus, J. Biboy, W. Vollmer, N. R. Salama, Flow cytometry-based enrichment for cell shape mutants identifies multiple genes that influence *Helicobacter pylori* morphology. *Mol. Microbiol.* **90**, 869–883 (2013).
27. L. K. Sycuro, Z. Pincus, K. D. Gutierrez, J. Biboy, C. A. Stern, W. Vollmer, N. R. Salama, Peptidoglycan crosslinking relaxation promotes *Helicobacter pylori*'s helical shape and stomach colonization. *Cell* **141**, 822–833 (2010).
28. L. E. Martínez, J. M. Hardcastle, J. Wang, Z. Pincus, J. Tsang, T. R. Hoover, R. Bansil, N. R. Salama, *Helicobacter pylori* strains vary cell shape and flagellum number to maintain robust motility in viscous environments. *Mol. Microbiol.* **99**, 88–110 (2016).
29. Y. Magariyama, S. Sugiyama, K. Muramoto, I. Kawagishi, Y. Imae, S. Kudo, Simultaneous measurement of bacterial flagellar rotation rate and swimming speed. *Biophys. J.* **69**, 2154–2162 (1995).
30. K. Son, D. R. Brumley, R. Stocker, Live from under the lens: Exploring microbial motility with dynamic imaging and microfluidics. *Nat. Rev. Microbiol.* **13**, 761–775 (2015).
31. M. R. Howitt, J. Y. Lee, P. Lertsethtakarn, R. Vogelmann, L. M. Joubert, K. M. Ottemann, M. R. Amieva, ChePep controls *Helicobacter pylori* infection of the gastric glands and chemotaxis in the *Epsilonproteobacteria*. *MBio* **2**, e00098–11 (2011).
32. H. C. Berg, *E. coli* in Motion (Springer-Verlag, 2004), 134 pp.
33. C. Taylor, A. Allen, P. W. Dettmar, J. P. Pearson, Two rheologically different gastric mucus secretions with different putative functions. *Biochim. Biophys. Acta* **1674**, 131–138 (2004).
34. P. Georgiades, P. D. A. Pudney, D. J. Thornton, T. A. Waigh, Particle tracking microrheology of purified gastrointestinal mucins. *Biopolymers* **101**, 366–377 (2014).
35. R. Bansil, J. M. Hardcastle, M. A. Constantino, Microrheology of mucin: Tracking particles and Helicobacter pylori bacteria. *Epitoanyag J. Silicate Based Composite Mater.* **67**, 150–154 (2015).
36. Z. Pincus, J. Theriot, Comparison of quantitative methods for cell-shape analysis. *J. Microsc.* **227**, 140–156 (2007).
37. Y. Hyon, T. R. Powers, R. Stocker, H. C. Fu, The wiggling trajectories of bacteria. *J. Fluid Mech.* **705**, 58–76 (2012).
38. A. C. Lowenthal, M. Hill, L. K. Sycuro, K. Mehmood, N. R. Salama, K. M. Ottemann, Functional analysis of the *Helicobacter pylori* flagellar switch proteins. *J. Bacteriol.* **191**, 7147–7156 (2009).
39. A. S. Rolig, J. Shanks, J. E. Carter, K. M. Ottemann, *Helicobacter pylori* requires TlpD-driven chemotaxis to proliferate in the antrum. *Infect. Immun.* **80**, 3713–3720 (2012).
40. P. Lertsethtakarn, M. R. Howitt, J. Castellon, M. R. Amieva, K. M. Ottemann, *Helicobacter pylori* $CheZ_{HP}$ and ChePep form a novel chemotaxis-regulatory complex distinct from the core chemotaxis signaling proteins and the flagellar motor. *Mol. Microbiol.* **97**, 1063–1078 (2015).
41. D. Keilberg, K. M. Ottemann, How *Helicobacter pylori* senses, targets and interacts with the gastric epithelium. *Environ. Microbiol.* **18**, 791–806 (2016).
42. J. G. Mitchell, L. Pearson, S. Dillon, Clustering of marine bacteria in seawater enrichments. *Appl. Environ. Microbiol.* **62**, 3716–3721 (1996).
43. J. E. Johansen, J. Pinhassi, N. Blackburn, U. L. Zweifel, A. Hagström, Variability in motility characteristics among marine bacteria. *Aquat. Microb. Ecol.* **28**, 229–237 (2002).
44. R. Stocker, J. R. Seymour, A. Samadani, D. E. Hunt, M. F. Polz, Rapid chemotactic response enables marine bacteria to exploit ephemeral microscale nutrient patches. *Proc. Natl. Acad. Sci. U.S.A.* **105**, 4209–4214 (2008).
45. G. M. Barbara, J. G. Mitchell, Marine bacterial organisation around point-like sources of amino acids. *FEMS Microbiol. Ecol.* **43**, 99–109 (2003).
46. R. Cortez, The method of regularized Stokeslets. *SIAM J. Sci. Comput.* **23**, 1204–1225 (2001).
47. R. Cortez, L. Fauci, A. Medovikov, The method of regularized Stokeslets in three dimensions: Analysis, validation, and application to helical swimming. *Phys. Fluids* **17**, 031504 (1994).
48. J. D. Martindale, M. Jabbarzadeh, H. C. Fu, Choice of computational method for swimming and pumping with nonslender helical filaments at low Reynolds number. *Phys. Fluids* **28**, 021901 (2016).
49. J. Gray, G. J. Hancock, The propulsion of sea-urchin spermatozoa. *J. Exp. Biol.* **32**, 802–814 (1955).
50. S. Humphries, J. P. Evans, L. W. Simmons, Sperm competition: Linking form to function. *BMC Evol. Biol.* **8**, 319 (2008).
51. A. Ghosh, P. Fischer, Controlled propulsion of artificial magnetic nanostructured propellers. *Nano Lett.* **9**, 2243–2245 (2009).
52. L. Zhang, J. J. Abbott, L. Dong, B. E. Kratochvil, D. Bell, B. J. Nelson, Artificial bacterial flagella: Fabrication and magnetic control. *Appl. Phys. Lett.* **94**, 064107 (2009).
53. F. Meshkati, H. C. Fu, Modeling rigid magnetically rotated microswimmers: Rotation axes, bistability, and controllability. *Phys. Rev. E. Stat. Nonlin. Soft Matter Phys.* **90**, 063006 (2014).
54. D. Walker, B. T. Käsdorf, H.-H Jeong, O. Lieleg, P. Fischer, Enzymatically active biomimetic micropropellers for the penetration of mucin gels. *Sci. Adv.* **1**, e1500501 (2015).
55. K. D. Young, The selective value of bacterial shape. *Microbiol. Mol. Biol. Rev.* **70**, 660–730 (2006).
56. H. C. Berg, D. A. Brown, Chemotaxis in *Escherichia coli* analyzed by three-dimensional tracking. *Nature* **239**, 500–504 (1972).
57. D. A. Baltrus, M. R. Amieva, A. Covacci, T. M. Lowe, D. S. Merrell, K. M. Ottemann, M. Stein, N. R. Salama, K. Guillemin, The complete genome sequence of *Helicobacter pylori* strain G27. *J. Bacteriol.* **191**, 447–448 (2009).
58. P. D. Frymier, R. M. Ford, H. C. Berg, P. T. Cummings, Three-dimensional tracking of motile bacteria near a solid planar surface. *Proc. Natl. Acad. Sci. U.S.A.* **92**, 6195–6199 (1995).
59. S. S. Rogers, T. A. Waigh, X. Zhao, J. R. Lu, Precise particle tracking against a complicated background: polynomial fitting with Gaussian weight. *Phys. Biol.* **4**, 220–227 (2007).
60. N. Phan-Thien, T. Tran-Cong, M. Ramia, A boundary-element analysis of flagellar propulsion. *J. Fluid Mech.* **184**, 533–549 (1987).
61. M. Ramia, D. L. Tullock, N. Phan-Thien, The role of hydrodynamic interaction in the locomotion of microorganisms. *Biophys. J.* **65**, 755 (1993).

Acknowledgments: We thank J. Hardcastle for helpful discussions regarding his work on *H. pylori* motility and for training M.A.C. in the early stages of this work; B. Turner for very

helpful discussions regarding mucin and providing purified PGM; N. Salama for providing the parent culture of LSH100 and its rod-shaped mutant Δ*csd6*, as well as for discussions on *H. pylori* motility and critically reading this manuscript; and L. Martinez for helpful discussions about bacterial culture and making samples. **Funding:** This work was supported by the NSF awards PHY 1410798 (R.B.) and CBET 1252182 (H.C.F.). The funders have no role in the study design, data collection, and interpretation or in the decision to submit the work for publication. The contents are solely the responsibilities of the authors and do not necessarily represent the official views of these funding agencies. **Author contributions:** R.B. and H.C.F. designed the research; M.A.C. performed the experiments and data analysis; M.J. performed the theoretical calculations; R.B., M.A.C., H.C.F., and M.J. analyzed and interpreted the results and wrote the paper. **Competing interests:** The authors declare that they have no competing interests. **Data availability:** All data needed to evaluate the conclusions in the paper are present in the paper and/or the Supplementary Materials. Additional data available from authors upon request.

Submitted 19 July 2016
Accepted 12 October 2016
Published 16 November 2016
10.1126/sciadv.1601661

Citation: M. A. Constantino, M. Jabbarzadeh, H. C. Fu, R. Bansil, Helical and rod-shaped bacteria swim in helical trajectories with little additional propulsion from helical shape. *Sci. Adv.* **2**, e1601661 (2016).

Science Advances
AAAS

advances.sciencemag.org/cgi/content/full/2/11/e1601661/DC1

Supplementary Materials for

Helical and rod-shaped bacteria swim in helical trajectories with little additional propulsion from helical shape

Maira A. Constantino, Mehdi Jabbarzadeh, Henry C. Fu, Rama Bansil

Published 16 November 2016, *Sci. Adv.* **2**, e1601661 (2016)
DOI: 10.1126/sciadv.1601661

The PDF file includes:

Other Supplementary Material for this manuscript includes the following:
(available at advances.sciencemag.org/cgi/content/full/2/11/e1601661/DC1)

- movie S1 (.mov format). Motility of LSH100 WT (helical) *H. pylori* swimming in PGM (15 mg/ml) imaged with 100× lens, 200 fps.
- movie S2 (.mov format). Flagellar bundle visualization.
- movie S3 (.mov format). Motility of LSH100 Δ*csd6* (rod mutant) *H. pylori* swimming in PGM (15 mg/ml) imaged with 100× lens, 100 fps.
- movie S4 (.mov format). Motility of LSH100 WT (helical) *H. pylori* swimming in BB10 imaged with 100× lens, 200 fps.
- movie S5 (.mov format). Motility of LSH100 Δ*csd6* (rod mutant) *H. pylori* swimming in BB10 imaged with 40× lens, 30 fps.

Supplementary Materials

movie S1. Motility of LSH100 WT (helical) *H. pylori* swimming in PGM (15 mg/ml) imaged with 100× lens, 200 fps.

movie S2. Flagellar bundle visualization. This is movie S1 with increased contrast.

movie S3. Motility of LSH100 Δ*csd6* (rod mutant) *H. pylori* swimming in PGM (15 mg/ml) imaged with 100× lens, 100 fps.

movie S4. Motility of LSH100 WT (helical) *H. pylori* swimming in BB10 imaged with 100× lens, 200 fps. Flagellar junction can be identified as more rapid changes in contrast at one end than the other during the time interval 2.500s to 2.700s. The end with the more rapid change in contrast is identified as the flagellar junction, and in some frames a very faint outline of flagella can be seen.

movie S5. Motility of LSH100 Δ*csd6* (rod mutant) *H. pylori* swimming in BB10 imaged with 40× lens, 30 fps. Flagellar junction can be identified as more rapid changes in contrast at one end than the other during the time interval 0.198s to 1.089s.

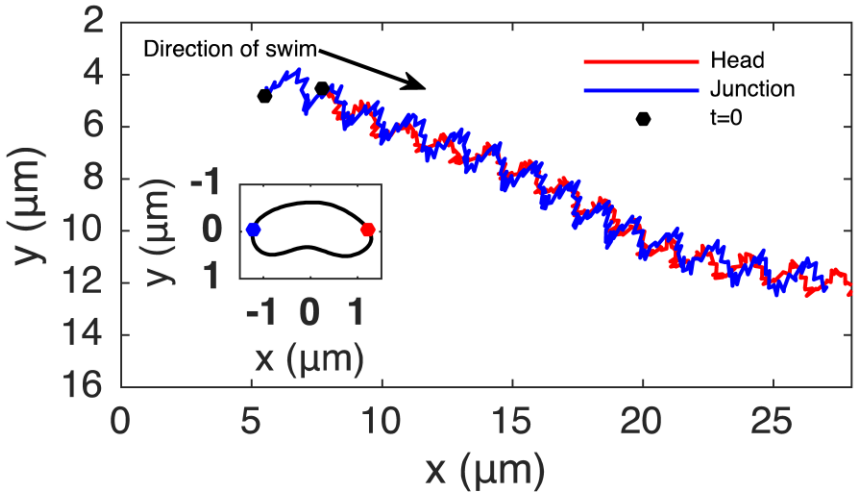

fig. S1. Head and flagellar junction trajectories of LSH100 helical *H. pylori* swimming in PGM (15 mg/ml) (movie S1). Red line is the trajectory of head point and blue line of the flagellar junction point. The trajectory pitch was obtained for both head and flagellar junction trajectories by de-trending the trajectories and measuring the distance between peaks for the entire track. As expected, the head and flagellar junction pitches are the same, $P_T = 1.5 \pm 0.2$ µm (the pitch is the average of the entire run and the error is the standard deviation). The trajectory radius is obtained by measuring the distance between the top and bottom envelope functions, $R_{head} = 0.45 \pm 0.03$ µm, $R_{junction} = 0.55 \pm 0.06$ µm (the radius is the average of the entire run and the error is the standard deviation). Inset: Example of definition of head and flagellar junction points. The head and flagellar junction points have to be defined for every frame because there is not a marker or feature in the bacterium's images. The contour of the body (in black) was aligned and centered with CellTool [36]. The head (red) and flagellar junction points (blue) were defined as the contour points intercepting the line y = 0. CellTool [36] saves the original alignment angle and localization of center point thus the trajectory can be reconstructed.

Numerical calculation methods

Regularized Stokeslets. To investigate the swimming properties of a helical cell body driven by rotating helical flagella, we use the method of regularized Stokeslets (RSM) [46, 47]. The flagellar bundle is modeled as a single helical flagellum, so for convenience we refer to it as the flagellum in the rest of the Supplementary Materials. In this method the surface of the cell body and flagellum is discretized by regularized Stokeslets which are fundamental solutions to the Stokes equation for applied localized force distributions $\phi_\epsilon(\mathbf{r}) = 15\epsilon^4\mathbf{f}/\left[8\pi(r^2+\epsilon^2)^{7/2}\right]$ that are smooth approximation for delta function. The small parameter ϵ controls the size of the distribution. The total flow velocity is

$$\mathbf{v}(\mathbf{r}) = \sum_{j=1}^{N} \mathbf{S}(\mathbf{r}-\mathbf{r}_j)\mathbf{f}_j \tag{1}$$

where $\mathbf{f}$ is the vector of localized force of each regularized Stokeslet, $\mathbf{r}$ is the position at which velocity is being calculated $\mathbf{r}_j$ is the position of the Stokeslet, and $S_{ij}(\mathbf{x}) = \frac{1}{8\pi\mu}\left(\frac{\delta_{ij}(x^2+2\epsilon^2)+x_i x_j}{(x^2+\epsilon^2)^{\frac{3}{2}}}\right)$ is the regularized Stokeslet which depends on cutoff parameter ϵ.

To solve equation (1), we need to find localized forces of Stokeslets on the surface of the cell and flagellum. Using no-slip boundary conditions on the surface it is convenient to express the velocity at each point of the surface to the swimming velocity and rotation in body-fixed-frame of the swimmer. This relation can be written as

$$\mathbf{v}(\mathbf{r}_j) = \mathbf{V} + \boldsymbol{\Omega} \times \mathbf{r}_j + \dot{\mathbf{L}}_j \tag{2}$$

where $\mathbf{V}$ and $\boldsymbol{\Omega}$ are swimming velocity and rotation vector respectively, $\mathbf{r_j}$ are the Stokeslet positions placed on material points of the surfaces in the body-fixed-frame, and $\dot{\mathbf{L}}_\mathbf{j}$ are the velocity of the Stokeslets with respect to the body-fixed-frame. In our case, the flagellum is rotating relative to the cell body with relative rotational velocity of $\boldsymbol{\Omega}$, so $\mathbf{r_j}$ is fixed for the positions on the cell body, but rotates for the flagellum. Thus $\dot{\mathbf{L}}_\mathbf{j}$ is the rotational velocity ($\dot{\mathbf{L}}_\mathbf{j} = \boldsymbol{\Omega} \times \mathbf{r_j}$) of the flagellum and zero for the cell body. To find the six unknowns (components of velocity and rotation of the swimmer) in equation (2), we apply zero total force and torque conditions for a free swimmer in the fluid, $\sum_j \mathbf{f_j} = 0$, and $\sum_j \mathbf{r_j} \times \mathbf{f_j} = 0$, which yields a linear system of equations in the body-fixed-frame that can be solved at each time step of flagellum rotation.

We use as the origin of the body-fixed-frame the junction point of the body and flagellum, with x-axis along the center-line of the flagellum (Fig. 1). The flagellum rotates along this axis with constant rotational velocity $\boldsymbol{\Omega}$. Similar to work done by Hyon et al. [37], we only solve for one rotation of flagellum and record velocities and rotations in the local frame, because after one full rotation of the flagellum in the local frame its position with respect to the cell body will be same as the initial state and we can use results for first rotation of the flagellum to reproduce results for many other revolutions. By converting these data to the lab frame and integrating velocities we find the position of the swimmer in the lab frame, which traces a helical trajectory. Unless otherwise specified, we report the average swimming speed, which is the component of the instantaneous velocity along the direction of the rotation, $V_s = \mathbf{V}.\widehat{\boldsymbol{\Omega}}_b$.

Geometry used in calculations. The cell body is modeled as a standard helix with its centerline positions given by

$$\mathbf{r}(x) = x\hat{\mathbf{x}} + R_B \cos(kx)\,\hat{\mathbf{y}} + R_B \sin(kx)\,\hat{\mathbf{z}} \qquad (3)$$

where $k = 2\pi/P_B$ is the wave number, R_B is the helical radius and P_B is the pitch of the cell body. The surface of the helix can be represented by the coordinates $(x + H(x,\phi), R_B \cos(kx) + M(x,\phi), R_B \sin(kx) + N(x,\phi))$ where $0 \le \phi \le 2\pi$ is the polar coordinate for the body's cross section orthogonal to the center-line at point x and H, M and N are some functions of x and ϕ [60]. We discretize the helical surface by choosing points at intervals Δx and $\Delta\phi$ in x and ϕ, respectively, such that the spacing between points (ΔS_b) for the cross section and longitudinal directions of the helix is uniform. We also use two hemispherical caps for the ends of the helix to generate a closed body. To discretize the caps, we try to keep uniform spacing in circular cross sections and radial direction of the hemispheres close to the cell body spacing ΔS_b. For the cell body geometry, we use the mean values for the pitch and helical radius while varying axial length, or mean values for the helical radius and axial length while varying pitch. The mean values are obtained from histogram of helical parameters previously obtained by Martinez et al. [28] using the cell outline software CellTool [36].

H. Pylori has multiple flagella at one end that bundle form a flagellar bundle during propulsion. In our model we treat this flagellar bundle as a single helix. We taper the bundle's helical radius near the cell body [60, 61] and assume the centerline of the bundle is along the **x** axis so the equation of the centerline could be described by

$$\mathbf{r}(x) = x\hat{\mathbf{x}} + \left(1 - e^{-\left(x/k_e\right)^2}\right) R\left(\cos\left(\frac{2\pi}{P}x\right)\hat{\mathbf{y}} + \sin\left(\frac{2\pi}{P}x\right)\hat{\mathbf{z}}\right) \quad (4)$$

Here P is the pitch of the bundle and k_e is the characteristic length of the tapering region and considered to be equal to $k_e = P/2\pi$. To discretize the bundle surface, we first a discretize circular cross section with spacing ΔS_f then sweep along the center-line creating discretized cross sections at the same spacing to place points on the entire surface. Finally, we add two discretized hemispherical caps to the ends of the flagellum. The helical properties of the flagellum are given in Table (2).

Satisfying observed body rotation or constant torque constraints. The calculations are performed by prescribing a constant angular velocity of the flagellum relative to the cell body. Given this relative rotation rate, both the cell body and flagellum rotation rate relative to the lab frame are determined by torque balance. All three rotation rates are proportional to each other as well as to the swimming velocities. To achieve an observed body rotation rate, we scale all the rotation rates and velocities by the same amount. Equivalently, we can present the calculated swimming speed result as the ratio V/Ω_b as in Table 1. For comparisons of swimming speeds between different cell body geometries, it is more realistic to consider that the flagellar motor is likely operating in the constant-torque regime of its angular velocity-torque curve. Thus, to present results for constant flagellar torque, all the results reported here are nondimensionalized using the flagellar torque, which can be obtained from the forces and positions of the regularized Stokeslets.

Convergence. We performed convergence tests using regularized Stokeslets to validate the results. More Stokeslets on the surface results in more accuracy, but at the cost of computational

efficiency. So we aim to use a reasonable number of Stokeslets to reduce costs while achieving acceptable accuracy for calculations. In our convergence tests, we separately discretize the body and flagellum with different number of Stokeslets on each surface (N_{body}, $N_{flagella}$, respectively). We checked that swimming speeds converged as N_{body}, $N_{flagella}$ are increased. In the reported results, we use $N_{flagella}$ = 4312 and N_{body} about 2000, for which the difference in results from our most accurate calculations using the largest numbers of Stokeslets is about 1.4%.

Estimates of cell-body and flagellar thrust from a hydrodynamically decoupled model. In this model, we calculate resistance matrices for the head and flagellum separately using the RSM. The force and torque on the body ($\mathbf{F_b}$ and $\mathbf{N_b}$) and flagellum ($\mathbf{F_f}$ and $\mathbf{N_f}$) are expressed in terms of the resistance matrices as

$$\begin{pmatrix}\mathbf{F_f}\\ \mathbf{N_f}\end{pmatrix} = \mathbf{R}_f \begin{pmatrix}\mathbf{V}\\ \mathbf{\Omega}_f\end{pmatrix} \tag{5}$$

$$\begin{pmatrix}\mathbf{F_b}\\ \mathbf{N_b}\end{pmatrix} = \mathbf{R}_b \begin{pmatrix}\mathbf{V}\\ \mathbf{\Omega}_b\end{pmatrix} \tag{6}$$

The origin for the resistance matrices is chosen to be the attachment point of the flagellum on the cell body, so $\mathbf{V}$ is the translational velocity of the attachment point, and $\mathbf{\Omega_b}$ and $\mathbf{\Omega_f}$ are the angular velocities of the cell body and flagellum, respectively, about the attachment point. Total hydrodynamic forces and torques are calculated by summing the forces and torques resulting from these resistance matrices

$$\begin{pmatrix}\mathbf{F}\\ \mathbf{N}\end{pmatrix} = \mathbf{R}_b \begin{pmatrix}\mathbf{V}\\ \mathbf{\Omega_b}\end{pmatrix} + \mathbf{R}_f \begin{pmatrix}\mathbf{V}\\ \mathbf{\Omega_b} + \mathbf{\Omega}\end{pmatrix} \tag{7}$$

which ignores interactions between the flagellum and cell body. Applying the constant relative rotation rate between the flagellum and body yields $\boldsymbol{\Omega}_f = \boldsymbol{\Omega}_b + \boldsymbol{\Omega}$, and by enforcing the force- and torque-free constraints for the swimmer, we calculate the instantaneous velocity and body rotation rate

$$\begin{pmatrix} \mathbf{V} \\ \boldsymbol{\Omega}_b \end{pmatrix} = -(\mathbf{R}_f + \mathbf{R}_b)^{-1}\mathbf{R}_f \begin{pmatrix} \mathbf{0} \\ \boldsymbol{\Omega} \end{pmatrix} \tag{8}$$

As in the numerical calculations, the average swimming velocity is $V_s = \mathbf{V}.\widehat{\boldsymbol{\Omega}}_b$. To assess the accuracy of this model, we first compare the swimming velocity calculated by the decoupled model to the numerical results including all hydrodynamic interactions previously presented in Figure 3A. Figure S2 shows the swimming speeds as a function of axial length for all three scenarios presented in Figure 3A, while the inset shows the error in swimming speed relative to the results of Figure 3A. The trends in swimming speeds are similar, and the decoupled model is within 20% accuracy for shorter helical cell bodies (axial length < 1 μm), and always within 30% for the biological scenario of a right-handed cell body. Thus, although the decoupled model is not quantitatively accurate it is likely to capture the qualitative trends in swimming speeds.

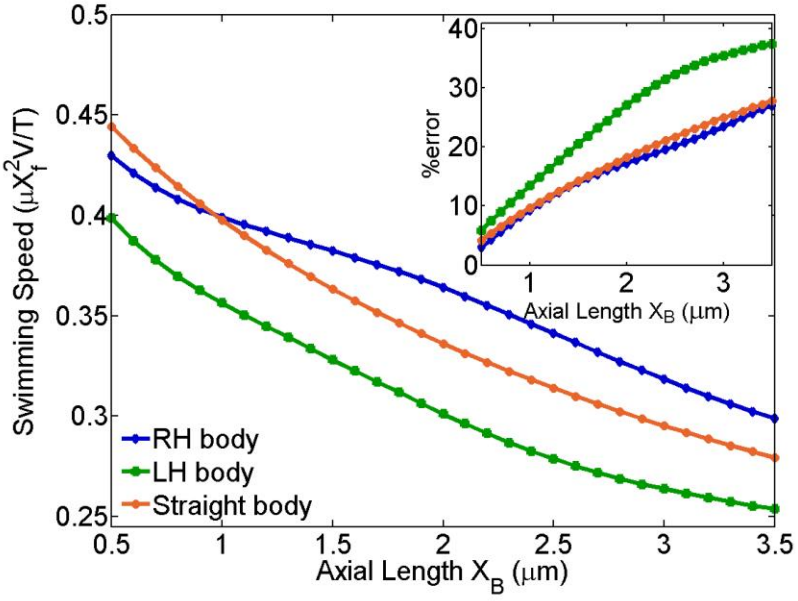

fig. S2. Swimming speed versus axial length, calculated by decoupled model. Comparison to the results of Fig. 3A reveals the accuracy of the decoupled model. Inset: Percent error of the decoupled model relative to the results of Fig. 3A.

Using the decoupled model, it is possible to estimate the total drag (D_T), and the thrust from the cell body (T_b) and flagellum (T_f) separately

$$\mathbf{D_T} = (\mathbf{R_b} + \mathbf{R_f}) \begin{pmatrix} \mathbf{V} \\ \mathbf{0} \end{pmatrix} \tag{9}$$

$$\mathbf{T_b} = \mathbf{R_b} \begin{pmatrix} \mathbf{0} \\ \boldsymbol{\Omega}_b \end{pmatrix} \tag{10}$$

$$\mathbf{T_f} = \mathbf{R_f} \begin{pmatrix} \mathbf{0} \\ \boldsymbol{\Omega}_b + \boldsymbol{\Omega} \end{pmatrix} \tag{11}$$

Power and efficiency. Figure S3 shows the power ($P = N\,\boldsymbol{\Omega}$) expended by the bacterial geometries explored in Fig. 3A. Note the scale of the vertical axis implies that the helicity of the body has little (<3%) effect on power expended. From the power, we can calculate the swimming efficiency

$$\eta = \frac{V^2 R_{trans}}{P} \tag{12}$$

where P is the total power, and V and R_{trans} are the swimming velocity and translational resistance of the cell body in the swimming direction. The resulting efficiency for the geometries in Fig. 3A are shown in the inset to fig. S3. Comparing the left-handed, right-handed and rod-shaped cell bodies at any fixed axial length, and keeping in mind that the power is little affected by the cell body geometry (fig. S3), we find that most of the change in swimming efficiency is accounted for by the corresponding difference in swimming velocities in Fig. 3A; for example, if the right-handed body is 10% faster than the straight body, then the efficiency is approximately a factor of $1.21 = 1.1^2$ higher.

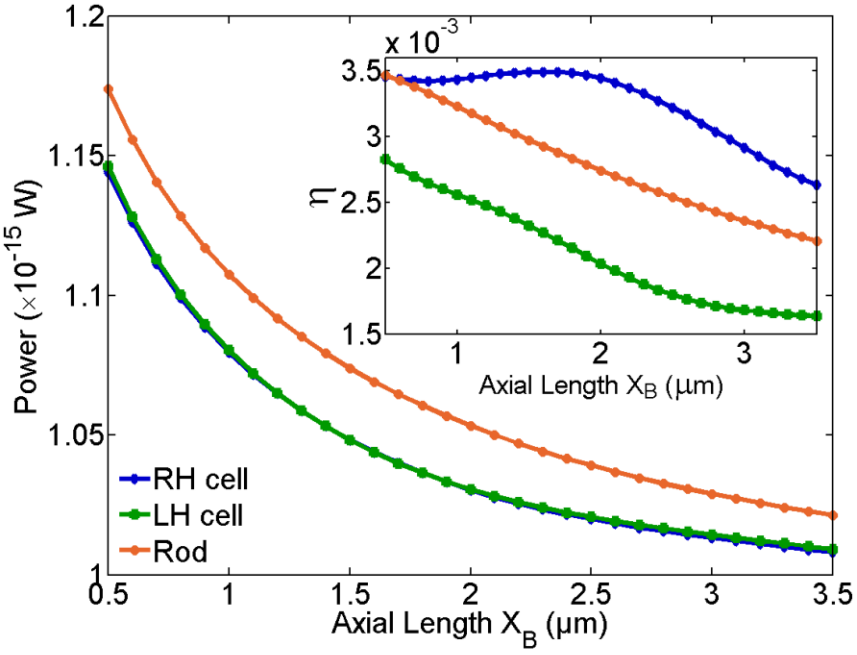

fig. S3. Swimming power versus axial length for right- and left-handed helical cells and rod-shaped cell body. Inset: Swimming efficiency vs axial length for RH and LH helical cells and rod-shaped cell body.

CHAPTER 4

DYNAMIC INSTABILITY IN THE HOOK-FLAGELLUM SYSTEM THAT TRIGGERS BACTERIAL FLICKS

PHYSICAL REVIEW E **97**, 012402 (2018)

Dynamic instability in the hook-flagellum system that triggers bacterial flicks

Mehdi Jabbarzadeh and Henry Chien Fu*
Department of Mechanical Engineering, University of Utah, Salt Lake City, Utah 84112, USA

(Received 18 August 2017; published 11 January 2018)

Dynamical bending, buckling, and polymorphic transformations of the flagellum are known to affect bacterial motility, but run-reverse-flick motility of monotrichous bacteria also involves the even more flexible hook connecting the flagellum to its rotary motor. Although flick initiation has been hypothesized to involve either static Euler buckling or dynamic bending of the hook, the precise mechanism of flick initiation remains unknown. Here, we find that flicks initiate via a dynamic instability requiring flexibility in both the hook and flagellum. We obtain accurate estimates of forces and torques on the hook that suggest that flicks occur for stresses below the (static) Euler buckling criterion, then provide a mechanistic model for flick initiation that requires combined bending of the hook and flagellum. We calculate the triggering torque-stiffness ratio and find that our predicted onset of dynamic instability corresponds well with experimental observations.

DOI: 10.1103/PhysRevE.97.012402

I. INTRODUCTION

The deformations of rotating filaments play an important role in bacterial motility. The dynamical bending of rotating rods and helices and its effect on swimming has been extensively investigated [1–6], including in the context of flagellar extension [7–12], polymorphic transitions [11,13–17], bundling [18–24], and wrapping around the cell body [25]. Dynamical configurations of rotating filaments have also been considered for microrobotic propulsion [26,27]. Here, we concentrate on monotrichous bacteria such as *Vibrio alginolyticus* that swim by rotating a single helical flagellar filament and display the ubiquitous run-reverse-flick motility [28], in which straight forward and backward runs are interspersed with reorienting flicks caused by deformation of the flagellum up to 90° [29] off-axis.

Rotary motion of the flagellum is driven by a motor embedded in the cell body that is connected to the flagellar filament by a structure called the hook, which plays a crucial role in flicks. The hook is much shorter and more flexible than the flagellum. As thin filaments, their resistance to bending is measured by a bending stiffness [EI, where E is the Young's modulus and I is a second moment of the cross-sectional area; see Eq. (1)]. Hook lengths are $L_H = 100$ nm and bending stiffnesses are $EI \approx 10^{-25}$ Nm^2, while flagellum arc lengths are $L \approx 5$ μm and stiffnesses are $EI \approx 10^{-23}$ Nm^2. The events before and after the flick are summarized in the inset to Fig. 1. Key to this paper are the preflick forward run (B) in which compressive forces and torques build up to trigger the flick (C), and the postflick forward run (D) in which the flagellum has returned to an on-axis orientation. The difference between the two is that preflick, clockwise rotation during backward swimming (A) unwinds the hook leading to a smaller bending stiffness ($EI_u = 3.6 \pm 0.4 \times 10^{-26}$ Nm^2), while postflick, counterclockwise rotation winds the hook leading to a larger bending stiffness ($EI_w = 2.2 \pm 0.4 \times 10^{-25}$ Nm^2) [29].

The mechanism triggering flicks remains imprecisely understood. Flicks have been proposed to involve buckling of the hook in static Euler buckling [29]. Buckling of the flagellum during swimming has been investigated [5,15], but only a few recent studies explicitly consider the role of the hook, and in flicks always in the case of effectively rigid flagellum. For free swimmers, Shum *et al.* used a boundary element method to model hydrodynamic interactions of the cell body and a rigid flagellum connected by a hook modeled as an inextensible Kirchoff rod [30]. They did not address flicks and due to computational expense provided detailed results for only a few geometry and hook stiffness scenarios. Modeling the hook as a torsional spring connected to a rigid flagellum, Nguyen *et al.* [31] described a transition from straight hook and straight trajectories to bent hook and helical trajectories as hook stiffness decreased. Park *et al.* [32] modeled flicks using a time-dependent decrease in hook stiffness and flagellum stiff enough not to bend, but their model could be at most qualitative since the bacteria were not free swimming. While their model showed off-axis motion, it did not lead to hook bending with deflections more than 25°, and they did not compare predictions for the onset of flick behavior to experimental observations. Flagellar precession due to hook bending has also been observed and modeled for surface-attached bacteria [33].

Here, we combine theoretical modeling with experimental data to determine the mechanism of flick initiation. We show that the flick is triggered by a dynamic buckling requiring both hook and flagellum bending, and find good agreement between predicted torque-stiffness ratios required to trigger flicks and experimental observations. Flicks are a biological example of how failure of compliant structures can be used constructively, a potential design paradigm for soft robotics. For any design application, predictive models yielding quantitative criteria for failure are necessary; our work provides an example of such a predictive model.

*henry.fu@utah.edu

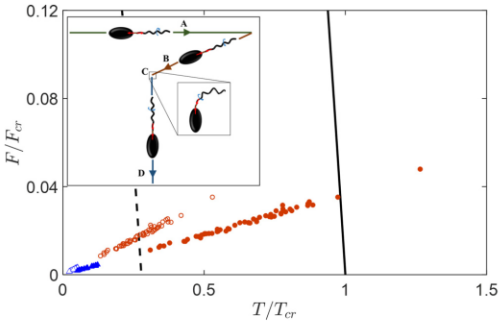

FIG. 1. Axial torques and forces on hook during preflick (flick-triggering, red circles, EI_u) and postflick (non-flick-triggering, blue triangles, EI_w) runs of different bacteria, estimated by Son *et al.*'s [29] 1D model (open symbols) and our full hydrodynamic model (filled symbols). The solid line is the static Euler buckling criterion, while the dashed line is the Euler buckling criterion if $EI = 1 \times 10^{-26}$ Nm^2 (see text). Inset: After swimming backwards (A) with clockwise flagellar rotation, which unwinds the hook and decreases its stiffness to EI_u, reversal of the flagellar motor leads to a short preflick forward run (B) that increases loading on the hook and causes a flick (C) in which the flagellum deforms off-axis and turns the bacteria. Postflick, the wound hook with increased bending stiffness EI_w returns the flagellum on-axis for a forward run (D).

A. Critical torques and forces for flick initiation suggest a dynamical, not static, buckling mechanism

The torque (**M**) and force (**F**) on the hook required to cause flicks provide clues to the mechanism of flick initiation. To quantify the forces and torques needed to initiate flicks, Son *et al.* [29] imaged swimming cell body geometries and velocities [34] during preflick as well as postflick forward runs. They calculated the motor torque and axial hook force using a one-dimensional (1D) model [29] that used the known drag coefficients for ellipsoidal cell bodies with the imaged dimensions, and drag coefficients and rotation-torque coupling coefficients for the flagellum (geometry in Table I) obtained from resistive force theory. Their results are plotted in Fig. 1 (open symbols). In this plot, values are scaled by the critical force $F_{cr} = \pi^2 EI/L_H^2$ and critical torque $M_{cr} = 2\pi EI/L_H$, using the measured [29] bending stiffnesses EI_u for preflick runs and EI_w for postflick runs. Son *et al.* noted that the average force and torque of preflick runs just exceed the Euler buckling criterion $F/F_{cr} + (M/M_{cr})^2 > 1$ if it were calculated using a smaller $EI = 1.0 \times 10^{-26}$ Nm^2 (dashed line in Fig. 1, plotted using EI_u for F_{cr} and T_{cr} in the axes normalization), which is of the same order of magnitude but outside the error of the measured EI_u, and they suggested that the flick initiation is caused by a static Euler buckling of the hook.

We reanalyzed the data from pre- and postflick runs using our previously described implementation [36–38] of the method of regularized Stokeslets [39,40]. The method of regularized Stokeslets is a well-established numerical technique that calculates fluid velocity fields, swimming speeds, and trajectories for bacteria; it can handle complex geometries and accounts for all hydrodynamic interactions and is therefore expected to be significantly more accurate [37] than the 1D model. The cell body is modeled as a prolate ellipsoid with major axis $2a$ and minor axis $2b$. The flagellum is modeled as a rigid helical filament with filament radius r, helical radius R, and helical pitch P, specified in Table I, and a taper that ensures the filament is normal to the cell body at the attachment (see Supplemental Material [41]). We prescribe a fixed rotation rate for a flagellum orientation along the x direction for forward runs. For a given body geometry, due to the linearity of Stokes equations the swimming speed, force, and torque on the hook are proportional to the rotation rate (ω) of the flagellum. Therefore, choosing ω to match the swimming speed with its experimental value also determines the force and torque on the hook.

Our results are plotted (filled symbols) in Fig. 1. The x components of forces (0.4–1.7 pN) and torques (700–2860 pN nm) are approximately 1.3 and 2.4 times larger than forces (0.3–1.3 pN) and torques (300–1200 pN nm) estimated by the 1D model (full results are given in Table S1 of the Supplemental Material [41]). It is evident that the forces and torques are not large enough to exceed the static Euler buckling criterion of the hook (black line). Therefore, in this paper we explore the possibility that the flick mechanism involves dynamical buckling of the hook.

B. Outline

To investigate the role of hook and flagellar bending in flicks, we first study the response of a hook modeled as an inextensible Kirchoff rod to forces and torques exerted by the cell body and flagellum and show that the response can accurately be linearized (but not as a simple torsional spring) in the biologically relevant regime. Then, we take advantage of the computational advantages of such linearization to explore flagellum orientation dynamics in a model of a swimming bacterium with rigid flagellum connected to the cell body by

TABLE I. Dimensions of the flagellar filament and cell body for *V. alginolyticus*. (All values are taken from [29], except values for EA and GA which are taken from [4,35].)

Flagellar filament								Cell body	
Flagellar pitch	Filament radius	Helix radius	Contour length	Bending stiffness	Torsional stiffness	Stretch stiffness	Shear stiffness	Head length	Head width
P (μm)	r (μm)	R (μm)	L (μm)	EI (Nm^2)	GJ (Nm^2)	EA (N)	GA (N)	$2a$ (μm)	$2b$ (μm)
1.49 ± 0.02	0.016	0.14 ± 0.02	4.59 ± 1	10^{-23}	10^{-23}	8×10^{-10}	8×10^{-10}	3.2 ± 0.5	1.2 ± 0.1

the linearized hook. As hook stiffness decreases, there is a transition from on-axis flagellar rotation to off-axis flagellar precession. However, precession alone cannot explain the large ($>60^\circ$) flagellar reorientations observed during flicks. We show that precession is not realized since forces during precession lead to the significant flagellar bending seen during flicks, by treating the flagellum as an extensible Kirchoff rod coupled to hydrodynamic forces. Thus, we establish the mechanism by which the combined flexibility of hook and flagellum initiates flicks. Finally, we calculate triggering torque-stiffness ratios for different cell sizes and find that the predicted onset of dynamic instability corresponds well with experimental observations.

II. METHODS

A. Inextensible Kirchoff-rod model of hook

Since the radius of the hook is only 10 nm, following [30] we treat it as a slender inextensible Kirchoff rod which resists bending due to elastic material response. During motion, hydrodynamic forces and torques arise on the cell body and flagellum, but we ignore hydrodynamic forces on the hook itself due to its short length.

This model is described in detail in [30], but briefly, the undeformed hook of length L_H is straight and in the x direction (Fig. 2). As a function of the arc length $s \in [0, L_H]$, the position $\mathbf{x}(s)$ defines the deformed centerline of the rod with an associated orthonormal triad $\{\mathbf{d_1}(s), \mathbf{d_2}(s), \mathbf{d_3}(s)\}$. $\mathbf{d_1}(s)$ and $\mathbf{d_2}(s)$ specify the orientations of material cross sections of the rod and $\mathbf{d_3}(s) = \mathbf{d_1}(s) \times \mathbf{d_2}(s) = \partial \mathbf{x}/\partial s$ is tangent to the centerline. At each cross section, a force $\mathbf{F}$ and moment $\mathbf{M}$ are exerted by the material with greater s on the material with lesser s. The constitutive law for the moment is

$$\mathbf{M} = EI(\kappa_1 \mathbf{d}_1 + \kappa_2 \mathbf{d}_2) + GJ\kappa_3 \mathbf{d}_3, \tag{1}$$

where the twist vector $\boldsymbol{\kappa} = \kappa_i(s)\mathbf{d}_i(s)$ measures the local curvature of the rod via $\partial_s \mathbf{d}_i = \boldsymbol{\kappa} \times \mathbf{d}_i$, EI is the bending stiffness related to Young's modulus E, and GJ is the torsional stiffness of the rod related to shear modulus G. I and J are second moments of the cross-sectional area about the bending or twisting axis, respectively.

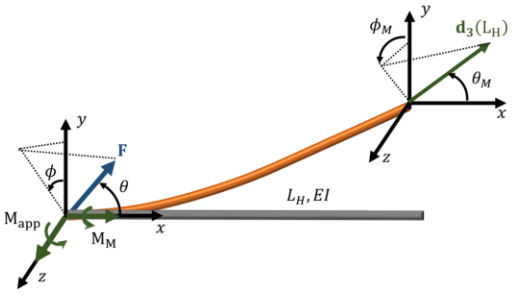

FIG. 2. Forces $\mathbf{F}$, motor (M_M), and perpendicular (M_{app}) torques at one end of a hook deform it from a straight rest position in the x direction so that the tangent direction at the other end is $\mathbf{d}_3(L_H)$, described by polar angles (θ_M, ϕ_M).

The Kirchhoff equations,

$$\partial_s \mathbf{F} = 0, \quad \partial_s \mathbf{M} + \mathbf{d}_3 \times \mathbf{F} = 0, \tag{2}$$

express local force and moment balance on rod elements in the absence of external (hydrodynamic) forces and torques, and together with Eq. (1) yield a system of ordinary differential equations (ODEs) that can be solved given initial conditions at $s = 0$ (the cell body). Nondimensionalizing to tilde variables by using L_H as the unit of length and EI/L_H^2 as the unit of force, the ODEs are

$$\begin{aligned} \mathbf{d}_i' &= \tilde{\kappa} \times \mathbf{d}_i, \\ \tilde{\kappa}_1' &= (\tilde{\mathbf{F}} \cdot \mathbf{d}_2) - \tilde{\kappa_2}\tilde{\kappa_3}(\Gamma - 1), \\ \tilde{\kappa}_2' &= -(\tilde{\mathbf{F}} \cdot \mathbf{d}_1) + \tilde{\kappa_1}\tilde{\kappa_3}(\Gamma - 1), \\ \tilde{\kappa}_3' &= 0, \\ \tilde{\mathbf{x}}' &= \mathbf{d}_3, \end{aligned} \tag{3}$$

where $(\cdot)' = \partial(\cdot)/\partial\tilde{s}$, and $\Gamma = GJ/EI$ is the ratio of the torsional to bending stiffness. We solve these using a fourth-order Runge-Kutta scheme.

B. Linearization of hook response

In the zero-Reynolds-number limit appropriate for bacteria [42], the forces (and torques) exerted by the hook on the flagellum and cell body are equal and opposite. The shape that the hook takes under these applied torques determines the relative orientation of the flagellum and cell body. Equations (3) are solved by imposing boundary conditions at the hook-cell body junction ($s = 0$). The boundary conditions are determined by considering that the flagellar motor keeps the attached end of the hook normal to the cell body surface and applies a nearly constant motor torque [43] in the x direction. To keep the end of the hook normal to and translating with the cell body, there are also constraint torques in the y and z directions and constraint forces applied to the hook by the cell body. Thus we study the deformations of the hook while varying the torque $\mathbf{M}_0$ (with motor x-component M_M) and force $\mathbf{F}_0$, defined as applied on the cell body by the hook. The dominant influence of the hook on swimming dynamics is due to change in the orientation of the flagellum relative to the cell body [30]; we ignore displacements of the hook endpoint since it is much shorter than the flagellum or cell body. The orientation of the flagellum is determined by the direction of the hook's end, $\mathbf{d}_3(s = L_H)$.

Without loss of generality, we consider the case where $M_{\text{app}} > 0$, the nonmotor component of $\mathbf{M}_0$, is in the z direction (Fig. 2) and calculate $\mathbf{x}(s)$. The orientation of $\mathbf{d}_3(L_H)$ is specified by angles (θ_M, ϕ_M). Dimensional analysis implies that both of these angles are functions of $\{GJ/EI, k_H = |EI/L_H M_M|, M_{\text{app}}/M_M, \mathbf{F}_0 L_H^2/EI\}$. In Appendix A, we show that the effects of typical $\mathbf{F}_0$ on $\mathbf{d}_3(L_H)$ are $< 4\%$ of the effects of typical $\mathbf{M}_0$. Furthermore, GJ/EI has little influence on swimming dynamics [30] so we always use $GJ = EI$. Thus, we seek to model the orientation of $\mathbf{d}_3$ as a function of only k_H and M_{app}/M_M. For a given k_H, we find that (θ_M, ϕ_M) are well approximated by linear functions of M_{app}/M_M in much of the regime experienced by V.

alginolyticus [$1000 < M_M < 4000$ pN nm [44], $0.1 < k_H < 2$ [29], $0.1 < M_{\rm app}/M_M < 0.5$ [45]]:

$$\theta_M = \alpha_\theta |M_{\rm app}/M_M|, \tag{4}$$

$$\phi_M = [\alpha_\phi |M_{\rm app}/M_M| + \beta_\phi]{\rm sgn}(M_M), \tag{5}$$

where α_θ, α_ϕ, and β_ϕ are functions of k_H. Appendix A contains details of the linearization and interpolations of α_θ, α_ϕ, and β_ϕ as a function of k_H. Heuristically, θ_M is proportional to the perpendicular torque $M_{\rm app}$, while ϕ_M is an odd roughly linear function of motor torque M_M, with a small dependence on $M_{\rm app}$. We find that this model has $< 4\%$ error relative to the Kirchoff-rod calculation of (θ_M,ϕ_M) for the ranges $0 < 1/k_H < 3$ and $0 \leqslant M_{\rm app}/M_M \leqslant 0.5$, corresponding to $0 \leqslant \theta_M \leqslant 55^\circ$ and $0 \leqslant \phi_M \leqslant 100^\circ$.

C. Calculation of swimming velocities, trajectories, and flagellum dynamics

Using the linearized hook response and assuming a rigid flagellum, it is possible to efficiently calculate instantaneous swimming translational and rotational velocities, changes in flagellum orientation, and hence swimming trajectories and flagellum dynamics. In the low-Reynolds-number limit appropriate to swimming bacteria [42], the translational and angular velocities of a rigid body are linearly related to the force and torque applied to the body. In our calculation, applied forces and torques are determined from the hook configuration, and then used to calculate the dynamics of connected cell body and flagellum. Given the flagellum orientation, the torque applied by the hook on the cell body is determined using the linearized model as

$$\mathbf{M}_c = M_M \hat{\mathbf{x}} + M_{\rm app}\hat{\mathbf{n}}, \tag{6}$$

where $M_{\rm app} = |M_M|\theta/\alpha_\theta$, and $\hat{\mathbf{n}}$ is the unit vector in the direction of $\hat{\mathbf{x}} \times \hat{\mathbf{r}}$ rotated by an angle $-\phi_M(M_{\rm app}/M_M)$ about the x axis. Then we calculate the velocity of the attachment point ($\mathbf{V}$) and the angular velocities of the cell body (Ω_c) and flagellum (Ω_f) about the attachment point as follows. By force and torque balance on the bacterium, the force and torque on the flagellum are $-\mathbf{F}_c$ and $-\mathbf{M}_c$, where $\mathbf{F}_c$ is the (unknown) force exerted by the hook on the cell body. We treat the hydrodynamics of the cell body and flagellum separately and ignore their hydrodynamic interactions, so

$$\begin{pmatrix}\mathbf{F}_c\\ \mathbf{M}_c\end{pmatrix} = \mathbf{R}_c\begin{pmatrix}\mathbf{V}\\ \Omega_c\end{pmatrix}, \quad \begin{pmatrix}-\mathbf{F}_c\\ -\mathbf{M}_c\end{pmatrix} = \mathbf{R}_f\begin{pmatrix}\mathbf{V}\\ \Omega_f\end{pmatrix}, \tag{7}$$

where $\mathbf{R}_c$ and $\mathbf{R}_f$ are the resistance matrices for the cell body and flagellum, calculated using our previously reported implementation [36–38] of the method of regularized Stokeslets [39,40]. Equation (7) gives 12 linear equations which can be solved for the 12 unknown components of $\mathbf{V}$, Ω_c, Ω_f, and $\mathbf{F_c}$.

For an instantaneous orientation $\hat{\mathbf{r}}$ of the flagellum defined by (θ,ϕ), the swimming velocity $\mathbf{V}$, and body and flagellum angular velocities (Ω_c,Ω_f) are found in the body coordinate system. The rate of change of flagellum orientation is specified by $(\dot\theta,\dot\phi,\dot\gamma)$ [see Fig. 3(a)], which is obtained from the relative angular velocity $\Omega = \Omega_f - \Omega_c$ and the geometric constraint $\dot{\hat{\mathbf{r}}} = \Omega \times \hat{\mathbf{r}}$, as

$$\begin{aligned}\dot\theta &= \Omega_z\cos(\phi) - \Omega_y\sin(\phi),\\ \dot\phi &= \Omega_x - \cot(\theta)[\Omega_y\cos(\phi) + \Omega_z\sin(\phi)],\\ \dot\gamma &= \Omega_{\mathbf{f}}\cdot\hat{\mathbf{r}},\end{aligned} \tag{8}$$

where $\dot\gamma$ is the rotation rate of the flagellar filament along its centerline axis. We numerically integrate in time to obtain the trajectory of the flagellum orientation.

D. Extensible Kirchoff rod coupled to hydrodynamic forces

To study how off-axis motion leads to bending of the flagellum, we must consider the deformations of a Kirchoff rod (representing the flagellum) under the influence of hydrodynamic forces. It is more convenient to couple external hydrodynamic forces into models of extensible, rather than inextensible Kirchoff rods [4,23,32,35]. Flagella are nearly inextensible, but in this model inextensibility is approximately enforced by adding a stiff extensional modulus that can be thought of as a penalty for filament extension.

We adopt the method used by Olson *et al.* [4] to study the dynamics of an elastic rod interacting with an incompressible viscous fluid. Here, the filament represented by the Kirchoff rod is the flagellum, not the hook, so the curve $\mathbf{x}(s,t)$ describes the filament centerline of the flagellum, where $s \in [0,L]$ is a parametrization of the material arc length along the filament. As in the inextensible Kirchoff model, material frames are tracked by the orthonormal triad $\{\mathbf{d}_1(s,t),\mathbf{d}_2(s,t),\mathbf{d}_3(s,t)\}$. However, the inextensibility condition $|\partial_s\mathbf{x}(s,t)| = 1$ does not hold; in the undeformed state, the unit vector $\mathbf{d}_3(s,t=0)$ is equal to the tangent vector to the filament centerline $[\partial_s\mathbf{x}(s,t)]$, but in general they are not equal.

Kirchoff-rod theory relates the cross-sectional force $\mathbf{F}(s,t)$ and moment $\mathbf{M}(s,t)$ to the external per unit length force $\mathbf{f}(s,t)$ and external per unit length moment $\mathbf{m}(s,t)$ applied by fluid on the filament,

$$0 = \partial_s\mathbf{F} + \mathbf{f}, \tag{9}$$

$$0 = \partial_s\mathbf{M} + (\partial_s\mathbf{x}\times\mathbf{F}) + \mathbf{m}. \tag{10}$$

The constitutive relations for the extensible Kirchhoff rod are

$$\begin{aligned}\mathbf{F} = {}& GA(\mathbf{d}_1\cdot\partial_s\mathbf{x})\mathbf{d}_1 + GA(\mathbf{d}_2\cdot\partial_s\mathbf{x})\mathbf{d}_2\\ &+EA(\mathbf{d}_3\cdot\partial_s\mathbf{x}-1)\mathbf{d}_3,\end{aligned} \tag{11}$$

$$\mathbf{M} = EI(\kappa_1-\tau_1)\mathbf{d}_1 + EI\kappa_2\mathbf{d}_2 + GJ(\kappa_3-\tau_3)\mathbf{d}_3, \tag{12}$$

where EI and GJ are the bending and twist stiffnesses, respectively, while GA and EA allow extensibility of the rod. In the stiffnesses E and G are the Young's modulus and shear modulus, and A is the cross-sectional area of the filament. The values of GA and EA used in our calculations are listed in Table I, and taken from [4] and [35]. As for the inextensible rod, the twist vector $\boldsymbol{\kappa}(s,t)$ is related to the local material frames by $\partial_s\mathbf{d}_i = \boldsymbol{\kappa}\times\mathbf{d}_i$. The initial shape of the flagellar filament is set to be a tapered helix with centerline described in the Supplemental Material [41], and τ_1 and τ_3 are reference curvatures chosen so that in the initial configuration, $\mathbf{M} = 0$.

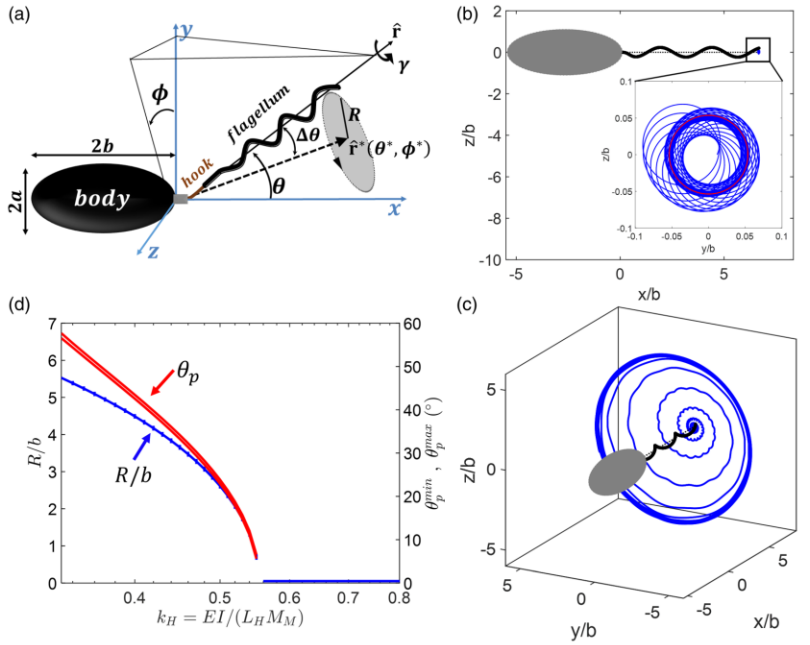

FIG. 3. (a) Orientation of flagellum along $\hat{\mathbf{r}}$ described by angles (θ,ϕ) traces a nearly circular trajectory (dashed line) around average orientation $\hat{\mathbf{r}}^*$. (b),(c) Examples of the flagellar orientation trajectories during free swimming with linearized hook dynamics. The flagellum is initially oriented in the x direction and, after a transient motion, settles into either orbits or precession. The blue trace is the motion of the flagellum endpoint relative to the cell body for motor moment of $M_M = 2000$ pN nm. (b) For $k_H = 1 > k_H^*$, the long-time motion is a small orbit, shown as a red circle. One orbit traversal takes one flagellar rotation. (c) For $k_H = 0.36 < k_H^*$, the long-time motion is precession closely following the largest circular paths. One traversal around the path takes multiple flagellar rotations. (d) Trajectory size measured by minimum ($\theta_p^{\min}$) and maximum ($\theta_p^{\max}$) deflection angles (red lines) or radius of endpoint motion (R, blue line). In the model with rigid flagellum, as stiffness parameter k_H decreases, flagellum trajectories transition from small orbits to large precession at k_H^*.

Given a current configuration of the filament $\mathbf{x}(s)$, the time evolution of $\mathbf{x}(s,t)$ and $\mathbf{d}_i(s,t)$ is numerically obtained by using Eqs. (9)–(12) to determine the hydrodynamic force $\mathbf{f}$ and moment $\mathbf{m}$ on discretized segments of the filament. Since hydrodynamic forces and torques on the filament are equal and opposite to the forces and torques applied by the filament on the fluid, we can use the forces and torques in the method of regularized Stokeslets to calculate the fluid flow fields everywhere, and hence by the no-slip boundary condition the translational and rotational velocities of filament segments. Time integration of the velocities yields the configuration of the filament as a function of time. Details of our numerical implementation are in Appendix B. For our choices of stiffness parameters and motions, the arc length changes by at most 0.2% so the flagellum remains nearly inextensible.

III. RESULTS

A. Flagellar orbits and precession

Linearizing the hook makes calculation of the time-dependent swimming behavior of a bacterium with a flexible hook but rigid cell body and rigid flagellum significantly less computationally expensive, allowing investigation of a wide enough range of body geometries and hook stiffnesses to connect to experiments. In this and the next section, the cell body is an ellipsoid with the mean geometry listed in Table I, and the same flagellum geometry as above. Neglecting the hook length, the flagellum is attached at the pole of the cell body and instantaneously oriented along $\hat{\mathbf{r}} = \cos(\theta)\hat{\mathbf{x}} + \sin(\theta)\cos(\phi)\hat{\mathbf{y}} + \sin(\theta)\sin(\phi)\hat{\mathbf{z}}$. A constant negative motor torque M_M is applied to give counterclockwise rotation. We compute the trajectory of flagellum orientation (θ,ϕ) during swimming. If the helical centerline of the flagellum is initially oriented in the x direction, after a transient it moves around a central direction $\mathbf{r}^*$ [at (θ^*,ϕ^*)] such that the endpoint of the centerline nearly traces a circle [dashed circle in Fig. 3(a); example trajectories in Figs. 3(b) and 3(c)].

For stiff hooks ($k_H > k_H^* \approx 0.552$), a stable orbit around $\mathbf{r}^*$ occurs for each motor revolution and the deflection angle $\Delta\theta$ between the flagellum orientation $\mathbf{r}$ and $\mathbf{r}^*$ is small. In Fig. 3(b), we show a typical trajectory of the flagellum orientation in this regime. Initially the flagellum is in the x direction, but, after a transient, stabilizes in a nearly circular trajectory. The deflection angle of the hook is quite small throughout. Stable

orbits were identified by direct time evolution. Orbits can also be identified as the fixed points (modulo 2π) of the discrete map,

$$\mathcal{F}:(\theta_i,\phi_i)\mapsto\left(\theta_i+\int_0^{2\pi}\theta'd\gamma,\phi_i+\int_0^{2\pi}\phi'd\gamma\right)=(\theta_f,\phi_f), \tag{13}$$

where $(\theta',\phi')=(d\theta/d\gamma,d\phi/d\gamma)=(\dot{\theta}/\dot{\gamma},\dot{\phi}/\dot{\gamma})$. The stability of an orbit was evaluated by constructing a Poincaré map on a local line in (θ,ϕ) space transverse to the orbit: if ζ is a coordinate along the line such that $\zeta=0$ is on the orbit, then the Poincaré map takes ζ_n to $\zeta_{n+1}=g(\zeta_n)$, which is the next intersection of the orientation trajectory with the line. Linearizing around $\zeta=0$, $g(\zeta)\approx\tilde{g}\zeta$, and orbits are asymptotically stable if $|\tilde{g}|<1$. Stable orbits identified using this metric matched stable orbits identified by direct time evolution of the dynamics.

For less stiff hooks or greater motor torques ($k_H<k_H^*$), orbits become unstable and instead the flagellum precesses, taking multiple flagellar revolutions to circle around $\mathbf{r}^*$. During precession, typical deflection angles $\Delta\theta$ are much larger than during orbits. In Fig. 3(c), we show a typical orientation trajectory in this regime. After a transient, the precessional behavior can be seen in which $\hat{\mathbf{r}}$ wiggles as it traces out the circle, staying between two angles $\theta^{\min}$ and $\theta^{\max}$ as it precesses. Each small loop in the transient or wiggle in the outer precessional circle corresponds to a single motor revolution. Because the precession angle is large, the transient takes many ($\approx$20) motor revolutions. Figure 3(d) shows how $\Delta\theta$ and the radius of the circle traced by the flagellum endpoint increase as k_H decreases and orbits transition to precession.

For both orbiting and precession, the center of the orbit or precession remains quite close ($\theta^*<0.01^\circ$) to the x axis for all values of k_H investigated.

Our results are consistent with the precessionlike behavior robustly observed across a variety of systems with flexible hooks and rigid flagella. Reference [30] found orbits which became unstable as hooks became less stiff, and precession was observed and modeled [33] for bacteria stuck to a slide. However, precession itself cannot explain flick initiation; for a simple torsional spring [31] as well as in our more realistic linearization, precession would lead to helical swimming trajectories [31], not flicks. Even supposing that the flick is just a portion of a helical trajectory lasting until hook stiffness increases, experimental movies [29] show $\approx$90° flagellar deflection during flicks, while in our model we find θ significantly less than 60° for a wide range of $k_H<k_H^*$.

B. Flicks require flagellar bending

Buckling of the hook alone leads to precession and helical trajectories with too small deflection angles to explain flicks. In the above, the flagellum was assumed to be rigid, but large precessional rotations introduce significant forces on the flagellum which may cause it to bend. Bending of both the flagellum and hook is thus essential for understanding flicks. To determine whether precessional orbits lead to the bending observed in flicks, we prescribe that the base of the flagellum translates and rotates its orientation exactly as predicted by the rigid model above, and ignore the hydrodynamic interactions with the cell body and hook. The flexible flagellum is started with the same configuration as a rigid flagellum then allowed to evolve in time. If the model shows little flagellar bending, the rigid flagellum assumption is valid and precessional orbits are predicted, but if it shows significant flagellar bending, the actual (uncalculated) dynamics will be strongly affected by both hook and flagellum bending. We use this approach rather than directly simulating the full swimming dynamics incorporating hook and flagellum flexibility since the extensible Kirchoff-rod model is computationally expensive, and due to long transients we could not reliably identify long-time flagellar behavior under full swimming dynamics.

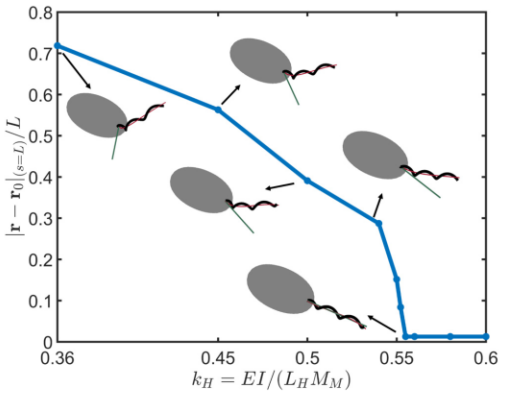

FIG. 4. Adding flagellum flexibility, for $k_H>k_H^*$ flagellum remains nearly unbent and on-axis, while for $k_H<k_H^*$ stresses from precession lead to large deformations from rigid flagellum (straight gray line), as measured by endpoint displacement between bent and rigid flagellum, $|\mathbf{r}-\mathbf{r}_0|_{(s=L)}$.

Movies S1–S5 (see Supplemental Material [41]) show the resulting flexible flagellar motion for k_H above and below the critical value, along with fits of the deformed centerline of the flagellum (red line) and, for comparison, the location of the rigid flagellum. For orbits with small $\Delta\theta$ ($k_H>k_H^*$), deflections of the flexible flagellum are small. On the other hand, for precessional motion ($k_H<k_H^*$), flagellar deflections are large. We quantify deflections via the displacement between the endpoint of the deformed centerline and the rigid centerline at a time corresponding to half of a precessional rotation (Fig. 4). The bending displacement is significant even for $k_H=0.55$, nearly immediately below k_H^*. Thus after accounting for flagellum flexibility, for $k_H<k_H^*$ precession is not observed; instead significant flagellar bending alters the dynamics. Thus, together with hook bending, the flagellar bending apparent in movies of flicks [29] is necessary for flick initiation.

By comparison, the only previous simulations of flicks [32] choose flagellar stiffness such that the flagellum hardly bends, and find deflections of, at most, 25°. These simulations do not quantitatively predict the critical stiffness for the onset of flicks, possibly since the flagellum base is fixed in position rather than free swimming, or since the spatial resolution of short hooks was limited.

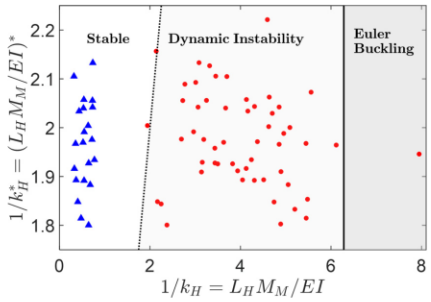

FIG. 5. Calculated $1/k_H$ values of postflick (blue triangles) runs lie in the stable regime to the left of the critical value (dashed line) predicted by the dynamic buckling instability, while those of preflick runs (red circles) lie in the unstable regime. Nearly all preflick runs do not exceed the static Euler buckling criterion (solid line).

C. Comparison to experiments and discussion

The results above imply that flicks are initiated by the dynamic buckling instability when $k_H = EI/M_M L_H < k_H^*$. The critical k_H^* depends on body and flagellum geometry. To compare with experimentally observed runs (Table S1 of Supplemental Material [41]), we calculate k_H^* for the body geometry of each run, and in Fig. 5 plot $1/k_H^*$ against $1/k_H = M_M L_H/EI$ obtained from the regularized Stokeslet calculation of the torque, $L_H = 100$ nm, EI_u for preflick runs and EI_w for postflick runs. The dotted line is $1/k_H^* = 1/k_H$, so stable orbits are predicted to the left and above the dotted line, while dynamical buckling is predicted to the right and below, in good agreement with the distribution of post- and preflick runs. Notably, only one preflick run exceeds the Euler buckling condition (solid line) [46] in addition to our dynamic instability condition. Figure 5 strongly supports the claim that flicks are initiated by the dynamic instability of the hook and flagellum that we have identified rather than static Euler buckling of the hook. Although our models and the experiments are specific to *Vibrio alginolyticus*, we expect that the physical conclusions arising from flexible filaments are robust. In particular, as torque increases, our dynamical transition occurs before the static Euler buckling condition is met, especially since as noted above the orbit-precession transition for hook-mediated rotation is robust across models.

Our calculations ignored displacement of the hook endpoint and hydrodynamic interactions between the flagellum, hook, and cell body, which we expect to result in 15–20% errors, in the same range as the uncertainty of the measured EI_u. We have not calculated the full swimming and bending dynamics during the flick, only determined the mechanism of flick initiation. To model the full kinematics of a flick requires knowledge of the time- and winding-dependent stiffness of the hook and treating a fully flexible flagellum and hook for a swimming bacterium with full hydrodynamic interactions, which is computationally expensive if one wishes to model multiple cell body geometries. For hook deflections within its range of validity, our linearized model could aid in this goal, especially since other models of flexible hooks and flagella may be limited by insufficient resolution of the hook [32], which is an order of magnitude shorter than the flagellum. Our results indicate that dynamical instabilities must be accounted for in designs incorporating slender filaments since they can occur before static failure, although we expect any instabilities to be highly dependent on the details of system geometries and actuation.

ACKNOWLEDGMENTS

We thank K. Son, J. Guasto, and R. Stocker for sharing and allowing us to publish the original data from [29]. This work was supported by National Science Foundation Award No. CBET-1651031 to HCF.

APPENDIX A: DETAILS FOR LINEARIZATION OF HOOK

As described in Sec. II B, we apply a motor torque (M_M) in the x direction and a torque M_{app} in the z direction, and calculate the orientation at the endpoint [$\mathbf{d}_3(s = L_H)$] expressed in terms of the polar coordinates (θ,ϕ) (see Fig. 2). The results calculated for $M_M = 2000$ pN nm and $L_H = 100$ nm are shown in Fig. 6. We vary EI to select a fixed value of $k_H = EI/M_M L_H$, then plot the angles (θ, ϕ) as a function of varying M_{app}. It is evident that θ is nearly linear in M_{app} and ϕ has only a slight dependence on M_{app} in the investigated range. For each k_H, we perform a linear fit of the angle as a

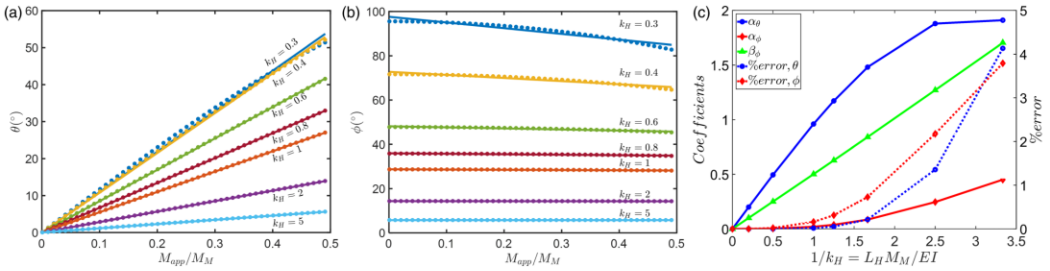

FIG. 6. The linear response of hook deflection angles to applied moments. (a),(b) Dots are the response of deflection angles (θ,ϕ) for the exact Kirchhoff-rod model, while lines are the linear interpolations for different relative stiffnesses k_H. The coefficients plotted in (c) are the intercepts and slopes of these linear interpolations. (c) The linearization coefficients for the orientation angles (θ,ϕ) and associated errors. The corresponding relations are Eqs. (4) and (5).

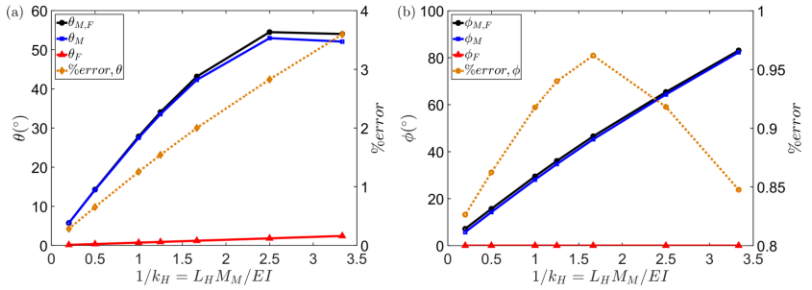

FIG. 7. The effects of applied force on the deflection angles. (a) $\theta_{M,F}$ is the deflection angle due to applying a typical moment and upper bound for the force, while θ_M and θ_F are the deflection angles when applying only the moment or force, respectively. The dashed line represents the percentage change in the deflection due to the force compared to the moment. (b) Similar quantities for the torsional deflection ϕ due to applied moment and force.

function of M_{app}/M_M, then numerically interpolate those as a function of k_H to find the linear fit reported in the main text with coefficients

$$\alpha_\theta = 0.0024/k_H^4 - 0.05/k_H^3 + 0.013/k_H^2 + 1/k_H,$$
$$\alpha_\phi = 0.05/k_H^2 - 0.031/k_H, \tag{A1}$$
$$\beta_\phi = 0.5/k_H.$$

Figure 6(c) shows the coefficients and percent error in the fits as a function of $1/k_H$. By comparing this range ($0 \leqslant M_{\text{app}}/M_M \leqslant 0.5$) to those in Figs. 6(a) and 6(b), one can see that the linear fits have less than 5% error as long as $\theta < 55^\circ$ and $\phi < 100^\circ$. Finally, we repeated the procedure for motor torques $M_M = \{500, 1000, 4000, 6000\}$ pN nm and found that the coefficients have the same dependence on k_H for all the motor torques.

In the above, the force $\mathbf{F}_0 = 0$. To investigate the effect of $\mathbf{F}_0$ on the orientation of the endpoint, we considered the case with $M_M = 2000$ pN nm and $M_{\text{app}}/M_M = 0.5$, which are typical values for the torque. Since a typical force magnitude due to flagellar propulsion is 1 pN, to be conservative we applied a force with $(F_{0,x}, F_{0,z}) = (1, 0.8)$ pN. The latter value corresponds to the z component of flagellar force when the deflection angle $\theta = 55^\circ$. The results are plotted for varying stiffnesses in Fig. 7. The error due to ignoring the contribution of force to the deflection angles is always less than 4%. Finally, we also measure the magnitude of the displacement of the hook at the end of the hook ($s = L_H$) and find that for typical forces and torques, the end of the hook can be displaced by up to about $0.5L_H$. While this is a large fraction of the hook length, in the context of the bacterium it only amounts to 50 nm, which is an order of magnitude smaller than the length of the flagellum; hence we ignore the effects of hook displacements for bacterial dynamics.

APPENDIX B: NUMERICAL IMPLEMENTATION OF EXTENSIBLE KIRCHOFF ROD

We couple the extensible Kirchhoff-rod model [Eqs. (9)–(12)] with hydrodynamic forces calculated by using surface distributions of regularized Stokeslets [39]. We uniformly discretize the centerline of the filament along the arc length into N segments of length Δs. There are $N + 1$ cross sections at points $s_p = p\Delta s$, for $p = 0, 1, \ldots, N + 1$. The center of segment p is at the half-integer-indexed point $s_{p+1/2}$. We represent each segment as a cylinder undergoing rigid body dynamics, and uniformly discretize the surface of each cylinder using N_s regularized Stokeslets, as shown in Fig. 8. Note that since the segment has finite extent, torques can result from the force distribution on the segment and there is no need to include rotlet singularities.

The position of each segment of the filament determines the position $\mathbf{x}(s_{p+1/2})$, and the orientation of each segment determines the frame $\mathbf{d}_i(s_{p+1/2})$ at each center point $p + 1/2$. The discretized versions of the Kirchoff equations for force

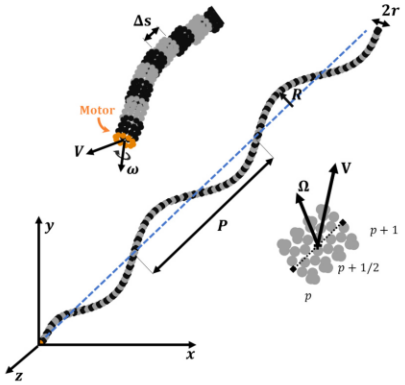

FIG. 8. The regularized Stokeslet method is coupled with an extensible Kirchhoff-rod model to model a flexible flagellum. The flagellum is discretized into cylindrical segments of length Δs. Cross sections between the segments are labeled by integers p, while segment centers are labeled by half integers $p + 1/2$. Each segment is treated as a rigid body with translational and angular velocities $\mathbf{V}$ and Ω. The elastic forces from deformation are calculated from the relative motion of segments. Points show regularized Stokeslets on the surface of each segment. A prescribed velocity and rotation rate are applied to the cell end of the flagellum ($s = 0$) and then the time-dependent deflections of the flagellum are calculated.

and moment balance [Eqs. (9) and (10)] for segment $p+1/2$ are

$$0 = \mathbf{F}_{p+1} - \mathbf{F}_p + \sum\nolimits_i \mathbf{f_i}, \tag{B1}$$

$$0 = \mathbf{M}_{p+1} - \mathbf{M}_p + 0.5[(\partial_s \mathbf{x} \times \mathbf{F})_{p+1} - (\partial_s \mathbf{x} \times \mathbf{F})_p] + \sum\nolimits_i [\mathbf{r}_i - \mathbf{x}(s_{p+1/2}, t)] \times \mathbf{f_i}, \tag{B2}$$

where $\sum_i \mathbf{f_i}$ is the total force from regularized Stokeslets on the surface of the segment (i.e., the force from the interaction of a rigid segment and the fluid), $\mathbf{r}_i$ is the position vector of the points on the surface of the segment, and $(\partial_s \mathbf{x})_p = [\mathbf{x}(s_{p+1/2}) - \mathbf{x}(s_{p-1/2})]/\Delta s$. Given the current configuration, Eqs. (11) and (12) determine $(\mathbf{F}_p, \mathbf{M}_p)$, and hence (B1) and (B2) determine the total hydrodynamic force $(\sum_i \mathbf{f_i})$ and torque $(\sum_i [\mathbf{r}_i - \mathbf{x}(s_{p+1/2}, t)] \times \mathbf{f_i})$ on each segment, which acts as a constraint on each segment. In Eqs. (11) and (12), the frame $\mathbf{d}_i(s_p)$ is interpolated between $\mathbf{d}_i(s_{p-1/2})$ and $\mathbf{d}_i(s_{p+1/2})$ [35]. Assuming rigid body motion of each segment, the method of regularized Stokeslets is then used to find translational and angular velocities $(\mathbf{u}_{p+1/2}, \Omega_{p+1/2})$ of each segment that satisfy the force and torque constraints and no-slip boundary conditions on all surfaces. This is accomplished using the same method as for swimming bacterium in [37], except here each segment has a separate force constraint, instead of just the flagellum and cell body having separate force constraints. From these velocities, we compute

$$\partial_t \mathbf{x}(s_{p+1/2}) = \mathbf{u}_{p+1/2}, \tag{B3}$$

$$\partial_t \mathbf{d}_i(s_{p+1/2}) = \Omega_{p+1/2} \times \mathbf{d}_i(s_{p+1/2}), \tag{B4}$$

at each time step and numerically integrate in time to evolve the shape of the flexible flagellum.

[1] C. H. Wiggins and R. E. Goldstein, Phys. Rev. Lett. **80**, 3879 (1998).
[2] C. W. Wolgemuth, T. R. Powers, and R. E. Goldstein, Phys. Rev. Lett. **84**, 1623 (2000).
[3] B. Qian, T. R. Powers, and K. S. Breuer, Phys. Rev. Lett. **100**, 078101 (2008).
[4] S. D. Olson, S. Lim, and R. Cortez, J. Comput. Phys. **238**, 169 (2013).
[5] M. K. Jawed, N. K. Khouri, F. Da, E. Grinspun, and P. M. Reis, Phys. Rev. Lett. **115**, 168101 (2015).
[6] M. K. Jawed and P. M. Reis, Phys. Rev. Fluids **2**, 034101 (2017).
[7] Y. Takano and T. Goto, JSME Int. J., Ser. C **46**, 1234 (2003).
[8] H. Hoshikawa, Biophys. Chem. **17**, 105 (1983).
[9] H. Hoshikawa and R. Kamiya, Biophys. Chem. **22**, 159 (1985).
[10] M. J. Kim and T. R. Powers, Phys. Rev. E **71**, 021914 (2005).
[11] N. C. Darnton and H. C. Berg, Biophys. J. **92**, 2230 (2007).
[12] M. K. Jawed and P. M. Reis, Soft Matter **12**, 1898 (2016).
[13] Y. Takano, K. Yoshida, S. Kudo, M. Nishitoba, and Y. Magariyama, JSME Int. J., Ser. C **46**, 1241 (2003).
[14] T. C. Adhyapak and H. Stark, Soft Matter **12**, 5621 (2016).
[15] R. Vogel and H. Stark, Eur. Phys. J. E: Soft Matter Biol. Phys. **35**, 1 (2012).
[16] S. Trachtenberg and I. Hammel, J. Struct. Biol. **109**, 18 (1992).
[17] T. C. Flynn and J. Ma, Biophys. J. **86**, 3204 (2004).
[18] M. Kim, J. C. Bird, A. J. Van Parys, K. S. Breuer, and T. R. Powers, Proc. Natl. Acad. Sci. USA **100**, 15481 (2003).
[19] H. Flores, E. Lobaton, S. Méndez-Diez, S. Tlupova, and R. Cortez, Bull. Math. Biol. **67**, 137 (2005).
[20] N. Watari and R. G. Larson, Biophys. J. **98**, 12 (2010).
[21] P. J. A. Janssen and M. D. Graham, Phys. Rev. E **84**, 011910 (2011).
[22] S. Y. Reigh, R. G. Winkler, and G. Gompper, PLoS One **8**, e70868 (2013).
[23] S. Lim and C. S. Peskin, Phys. Rev. E **85**, 036307 (2012).
[24] T. C. Adhyapak and H. Stark, Phys. Rev. E **92**, 052701 (2015).
[25] M. J. Kühn, F. K. Schmidt, B. Eckhardt, and K. M. Thormann, Proc. Natl. Acad. Sci. USA **114**, 6340 (2017).
[26] M. Manghi, X. Schlagberger, and R. R. Netz, Phys. Rev. Lett. **96**, 068101 (2006).
[27] N. Coq, O. Du Roure, J. Marthelot, D. Bartolo, and M. Fermigier, Phys. Fluids **20**, 051703 (2008).
[28] L. Xie, T. Altindal, S. Chattopadhyay, and X.-L. Wu, Proc. Natl. Acad. Sci. USA **108**, 2246 (2011).
[29] K. Son, J. S. Guasto, and R. Stocker, Nat. Phys. **9**, 494 (2013).
[30] H. Shum and E. Gaffney, Phys. Fluids **24**, 061901 (2012).
[31] F. T. Nguyen and M. D. Graham, Biophys. J. **112**, 1010 (2017).
[32] Y. Park, Y. Kim, W. Ko, and S. Lim, Phys. Rev. E **95**, 022410 (2017).
[33] Y. Shimogonya, Y. Sawano, H. Wakebe, Y. Inoue, A. Ishijima, and T. Ishikawa, Sci. Rep. **5**, 18488 (2015).
[34] The data were originally taken and analyzed in Ref. [29] using the methods described therein. In [29], only the 1D model estimates of force and torque were reported; Table S1 of the Supplemental Material [41] has previously unpublished data of cell body geometries and swimming speeds for each imaged run.
[35] S. Lim, A. Ferent, X. S. Wang, and C. S. Peskin, SIAM J. Sci. Comput. **31**, 273 (2008).
[36] Y. Hyon, T. R. Powers, R. Stocker, H. C. Fu *et al.*, J. Fluid Mech. **705**, 58 (2012).
[37] J. Martindale, M. Jabbarzadeh, and H. Fu, Phys. Fluids **28**, 021901 (2016).
[38] M. A. Constantino, M. Jabbarzadeh, H. C. Fu, and R. Bansil, Sci. Adv. **2**, e1601661 (2016).
[39] R. Cortez, SIAM J. Sci. Comput. **23**, 1204 (2001).
[40] R. Cortez, L. Fauci, and A. Medovikov, Phys. Fluids **17**, 031504 (2005).
[41] See Supplemental Material at http://link.aps.org/supplemental/10.1103/PhysRevE.97.012402 for details of the flagellum geometry.
[42] E. M. Purcell, Am. J. Phys. **45**, 3 (1977).
[43] H. C. Berg, Annu. Rev. Biochem. **72**, 19 (2003).
[44] Y. Sowa, H. Hotta, M. Homma, and A. Ishijima, J. Mol. Biol. **327**, 1043 (2003).
[45] The range of M_{app} is obtained from the hydrodynamic model of swimming used for Fig. 1.
[46] Calculated assuming a typical axial force $F = 0.83$ pN and EI_u.

Supplemental Material for "The dynamic instability in the hook/flagellum system that triggers bacterial flicks"

Mehdi Jabbarzadeh[1] and Henry Chien Fu[1,*]

[1] *Department of Mechanical Engineering, University of Utah, Salt Lake City, UT 84112 USA*

(Dated: November 17, 2017)

Estimation of forces and torques using method of regularized Stokeslets. We use the method of regularized Stokeslets [S1, S2] in which the surface of the cell body and flagellar filament are discretized by a distribution of regularized point forces on the surface. Our implementation was previously described in [S3]. We consider a rigid helical filament with filament radius r, helical radius R, and helical pitch P (numerical values in Table 1), oriented in positive x-direction. The path of the flagellum filament is described by

$$\mathbf{r_c}(l) = l\hat{\mathbf{x}} + R(1 - e^{-(2\pi l/P)^2})[\cos(2\pi l/P)\hat{\mathbf{y}} - \sin(2\pi l/P))\hat{\mathbf{z}}], \tag{S1}$$

where l varies from 0 to a value chosen such that the total contour length is L. The radius has an exponential taper at the end connecting to the cell body so that the filament is normal to the cell body at the attachment, as used in many previous models[S4**? ?**]. The cell body is modeled as an ellipsoid with semi-major and minor axis of a and b, respectively. We prescribe the relative rotation rate between the cell body and flagellum and then calculate swimming speed, cell body rotation rate, and forces and torques on the cell body and flagellum [S3] for the cell body geometry of each run reported in Table S1. Since all these calculated quantities are proportional to the rotation rate, for each run we scale the rotation rate so that the swimming speed matches the observed value, and report the axial force and torque exerted by the flagellum in Table S1.

Movies of flexible flagella during swimming. Movies S1-5 show the deformations of flagella during swimmiing when the swimming translational and rotational velocities as well as the orientation of the flagellar base are imposed from the calculations for the swimming bacterium with linearized hook and rigid cell body and flagellum.

MOVIE S1. Deformation of flagellum for motion corresponding to $k_H = 0.6$. Simulation time is 6 motor revolutions.
MOVIE S2. Deformation of flagellum for motion corresponding to $k_H = 0.54$. Simulation time is 10.1 motor revolutions, or half of precessional period.
MOVIE S3. Deformation of flagellum for motion corresponding to $k_H = 0.50$. Simulation time is 8.8 motor revolutions, or half of precessional period.
MOVIE S4. Deformation of flagellum for motion corresponding to $k_H = 0.45$. Simulation time is 7 motor revolutions, or half of precessional period.
MOVIE S5. Deformation of flagellum for motion corresponding to $k_H = 0.36$. Simulation time is 3.1 motor revolutions, or half of precessional period.

* henry.fu@utah.edu

[S1] R. Cortez, SIAM Journal on Scientific Computing **23**, 1204 (2001).
[S2] R. Cortez, L. Fauci, and A. Medovikov, Physics of Fluids **17**, 031504 (2005).
[S3] J. Martindale, M. Jabbarzadeh, and H. Fu, Physics of Fluids **28**, 021901 (2016).
[S4] Y. Hyon, T. R. Powers, R. Stocker, H. C. Fu, *et al.*, Journal of Fluid Mechanics **705**, 58 (2012).

TABLE S1. Cell body dimensions, swimming speeds, calculated forces and torques, and critical nondimensional stiffness parameters for *V. alginolyticus* imaged by Son *et al.*

Pre-flick run					
Head length	Head width	Swimming velocity	Force (model)	Torque (model)	Critical k_H^*
$2a(\mu m)$	$2b(\mu m)$	$V(\mu m/s)$	F(pN)	T(pN nm)	
3.05	0.48	73.64	0.88	1551	0.529
2.69	0.61	55.86	0.73	1238	0.519
2.42	0.60	50.84	0.62	1068	0.502
3.03	0.53	83.06	1.06	1821	0.531
2.03	0.56	69.48	0.73	1333	0.475
3.41	0.45	37.30	0.46	810	0.542
2.04	0.61	54.44	0.61	1085	0.478
2.78	0.60	63.90	0.84	1418	0.523
2.48	0.57	55.04	0.66	1149	0.506
3.57	0.48	86.83	1.14	1964	0.551
1.89	0.65	55.32	0.64	1112	0.469
3.21	0.60	72.48	1.03	1708	0.541
2.26	0.52	80.09	0.85	1553	0.489
2.51	0.62	72.88	0.92	1576	0.507
2.31	0.53	85.97	0.94	1694	0.493
2.05	0.61	49.90	0.57	999	0.479
2.23	0.57	66.38	0.74	1323	0.490
2.63	0.44	68.01	0.70	1307	0.508
2.80	0.55	64.16	0.80	1378	0.519
3.40	0.49	83.86	1.09	1873	0.546
2.47	0.55	87.06	1.01	1785	0.503
2.95	0.55	66.50	0.85	1457	0.528
3.50	0.72	66.28	1.12	1761	0.555
2.11	0.58	101.5	1.12	2003	0.483
2.83	0.53	59.17	0.72	1260	0.519
2.00	0.59	63.54	0.70	1244	0.475
3.71	0.53	35.98	0.51	856	0.555
3.15	0.58	85.83	1.17	1974	0.540
2.16	0.55	85.33	0.93	1670	0.485
2.37	0.62	78.53	0.97	1666	0.500
2.76	0.57	52.52	0.66	1137	0.518
3.21	0.55	34.27	0.46	781	0.541
2.58	0.54	106.7	1.25	2203	0.509
2.16	0.59	58.35	0.66	1171	0.486
2.22	0.59	86.54	0.99	1748	0.490
2.56	0.49	48.92	0.54	971	0.506
2.70	0.60	69.77	0.90	1528	0.517
2.27	0.54	76.28	0.83	1500	0.492
2.59	0.64	128.8	1.70	2862	0.514
2.31	0.48	58.56	0.59	1104	0.490
2.57	0.54	94.95	1.11	1962	0.508
2.60	0.51	60.95	0.69	1237	0.511
1.66	0.65	85.62	0.94	1655	0.450
2.23	0.51	51.19	0.54	982	0.487
2.59	0.51	86.27	0.98	1748	0.509
2.39	0.55	91.00	1.03	1834	0.500
1.95	0.58	61.92	0.66	1195	0.470
2.87	0.49	71.45	0.84	1486	0.522
2.93	0.56	73.80	0.95	1626	0.528
2.85	0.54	52.64	0.65	1131	0.524
2.74	0.64	77.33	1.06	1763	0.524
2.39	0.56	34.55	0.40	701	0.499
1.82	0.65	38.72	0.44	771	0.464
2.18	0.58	74.67	0.84	1488	0.486

Post-flick run				
Head length	Head width	Swimming velocity	Force (model)	Torque (model)
$2a(\mu m)$	$2b(\mu m)$	$V(\mu m/s)$	F(pN)	T(pN nm)
3.05	0.48	56.77	0.68	1196
2.69	0.61	64.07	0.84	1420
2.42	0.60	57.28	0.69	1203
3.03	0.53	68.16	0.87	1494
2.48	0.57	75.74	0.91	1581
3.57	0.48	46.38	0.61	1049
1.89	0.65	80.65	0.93	1620
2.23	0.57	58.49	0.65	1166
2.63	0.44	59.67	0.62	1147
2.95	0.55	36.86	0.47	808
2.00	0.59	35.89	0.39	703
3.71	0.53	59.52	0.85	1416
3.21	0.55	39.11	0.53	891
2.16	0.59	79.91	0.91	1603
2.70	0.60	77.60	1.00	1700
2.27	0.54	48.50	0.53	953
2.31	0.48	85.40	0.86	1610
2.57	0.54	37.83	0.44	782
2.87	0.49	34.83	0.41	725
2.39	0.56	68.75	0.79	1395
2.18	0.58	59.51	0.67	1186

CHAPTER 5

SWIMMING FLUCTUATIONS OF MICRO-ORGANISMS DUE TO HETEROGENEOUS MICROSTRUCTURE

PHYSICAL REVIEW E **90**, 043021 (2014)

Swimming fluctuations of micro-organisms due to heterogeneous microstructure

Mehdi Jabbarzadeh,[1,*] YunKyong Hyon,[2,*] and Henry C. Fu[1,†]
[1]*Department of Mechanical Engineering, University of Nevada at Reno, Reno, Nevada 89557 USA*
[2]*Division of Computational Sciences in Mathematics, National Institute for Mathematical Sciences, Daejeon, Republic of Korea 305-811*
(Received 4 April 2014; revised manuscript received 29 July 2014; published 31 October 2014)

Swimming microorganisms in biological complex fluids may be greatly influenced by heterogeneous media and microstructure with length scales comparable to the organisms. A fundamental effect of swimming in a heterogeneous rather than homogeneous medium is that variations in local environments lead to swimming velocity fluctuations. Here we examine long-range hydrodynamic contributions to these fluctuations using a Najafi-Golestanian swimmer near spherical and filamentous obstacles. We find that forces on microstructures determine changes in swimming speed. For macroscopically isotropic networks, we also show how the variance of the fluctuations in swimming speeds are related to density and orientational correlations in the medium.

DOI: 10.1103/PhysRevE.90.043021 PACS number(s): 47.15.G−, 87.16.Qp

I. INTRODUCTION

The locomotion of microorganisms such as bacteria and sperm that swim in the viscosity-dominated Stokes flow regime has received significant attention [1] and remains an active topic of research. Here, we focus on situations when microorganisms swim through complex biological environments. For instance, *Helicobacter pylori* swims through gastric mucus by changing the rheological properties of the mucus [2], and mammalian sperm swim through mucus in the female reproductive tract [3,4]. The effect of complex media on swimming has recently been actively investigated in experiments as well as modeling and theory [5–17], particularly for viscoelastic media [2,3,8,18–36].

So far, most theoretical efforts have focused on constitutive models of complex fluids that incorporate non-Newtonian behavior through a homogeneous, continuum description [10,17,19–29,31,34,36], and most experiments in synthetic media with controlled material properties have involved fluids [3,8,18,27,30,32,35] or gels [37], which are homogeneous on the scale of swimming organisms since their micro- or nanostructural lengthscales are much smaller than the organisms. Due to this focus, even studies involving complex biomaterials are typically interpreted in terms of continuum phases of complex media [2].

However, many biological environments, including the common examples of mucus above, are heterogeneous on the scale of microorganisms. For example, cervical mucus contains a network of glycoprotein fibers with diameters around 100 nm, and network pore sizes ranging from hundreds of nanometers to 25 μm [38,39], so that the features of the mucus microstructure have lengthscales comparable to sperm, which have ∼5-μm cell bodies and ∼40-μm flagella. In these situations, the complete effects of the microstructure cannot be captured using homogeneous, continuum models of the complex medium.

A swimmer in an environment with comparably sized microstructural features has significantly richer physics than in a homogeneous medium. Fundamentally, the heterogeneiety means that the organism encounters different local environments as it traverses the medium. While a swimmer moving with a periodic stroke in a homogeneous medium has a constant stroke-averaged velocity, the same swimmer in a heterogeneous medium has a fluctuating swimming velocity. Thus, in the biologically relevant scenarios when media are heterogeneous on swimmer lengthscales, velocity fluctuations are a physically important quantity incapable of being addressed by previous homogeneous frameworks. Fluctuations can also arise from stochasticity in the propulsive machinery of microorganisms [40] (such as that seen in run-and-tumble chemotaxis and flagellates [41–43]), or transient adhesions to the medium [44], but here we show that even in the absence of stochasticity, fluctuations can arise from long-range hydrodynamic interactions with heterogeneous microstructure.

A number of previous works have explicitly mentioned the role of heterogeneity in swimming. Chrispell *et al.* [45] considered how a swimming sheet is affected by another nearby sheet, while Fu *et al.* [46] pointed out that local details of interaction with heterogeneous microstructure affect the boundary conditions used in continuum representations of complex media. Ledesma-Aguilar and Yeomans [47] studied a finite swimmer within confining rigid and elastic tubes, and Leshansky [48] examined how an explicit representation of random heterogeneous obstacles can be modeled as a Brinkmann fluid. However, all of these focused on averaged properties such as average swimming speed and power rather than fluctuations in swimming properties. Fluctuations in swimming velocity due to heterogeneity have been reported in two systems. In a combined experimental and numerical investigation of *Caenorhabditis elegans* swimming in an array of ordered posts, Majmudar *et al.* [49] reported fluctuations in swimming speed due to temporal switching between different gaits induced by mechanical interactions with the ordered obstacles. For spirochetes in gelatin models of tissue, Harman *et al.* [44] found that fluctuations in swimming speed arise from temporal switching between different modes of locomotion corresponding to levels of adhesion to the gelatin substrate.

*Mehdi Jabbarzadeh and YunKyong Hyon contributed equally to this work.
†hfu@unr.edu

In contrast to focusing on the averaged quantities, which are accessible in continuum models, in this manuscript we focus on fluctuations in swimming velocities caused by heterogeneity. Rather than fluctuations arising from close-range interactions, we investigate how the long-range hydrodynamic interactions with an unordered microstructure contributes to fluctuations as a swimmer moves through different local environments, even as the gait of the swimmer is unaffected. By using a simplified model, we are able to directly connect the variance of the fluctuations to information about the structure of the medium.

II. SWIMMER MODEL

To capture the spatially dependent effects of heterogeneity, it is necessary to use a finite length swimmer. We use the simplest possible representations of microstructure, immobile spherical particles [48], and immobile rigid rods. Although immobile microstructures ignore the effects of compliance, they are the simplest models that demonstrate how heterogeneous structure can hydrodynamically lead to fluctuations in swimming speed. How the results might be affected by compliance is addressed in the discussion.

For the work here we use the Najafi-Golestanian swimmer [50,51] with spheres of radius d and prescribed distances L_1 between spheres 1 and 2 and L_3 between spheres 2 and 3 (Fig. 1) given by $L_1 = 10d + 2.5d\cos(\omega t)$ and $L_3 = 10d + 2.5d\cos(\omega t + \pi/4)$.

We start by examining the effect of a single spherical obstacle (also of radius d), which allows us to establish a physical interpretation of the interaction between the swimmer and heterogeneity. While the topology of this obstacle is different from that of a microstructural network, this simple representation illuminates important features of more realistic systems. To find the swimming speed of the swimmer, we treat the hydrodynamic interactions between the swimmer and obstacle spheres using the Stokeslet (S_{ij}) [50,51], which is appropriate when spheres remain separated by distances much larger than their radii.

Therefore, in all the work reported in this paper, we only consider configurations where the obstacle (or later, filaments) are further than $17.5d$ from the center of the swimmer. The

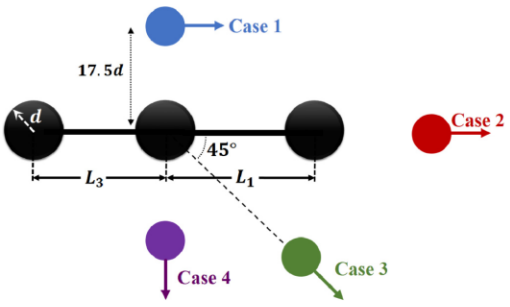

FIG. 1. (Color online) Najafi-Golestanian three-sphere swimmer near obstacles and rods. The isolated circles and arrows show cuts of positions for obstacles, or for the center of rods extending perpendicularly out of the plane, investigated in Figs. 2 and 4, respectively.

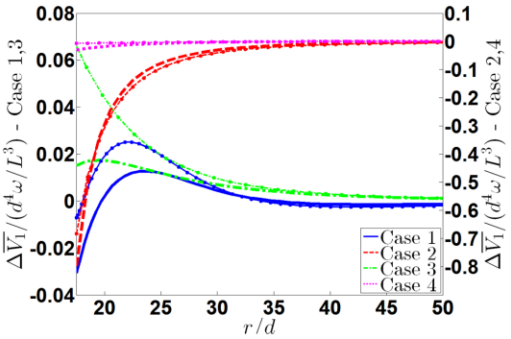

FIG. 2. (Color online) Change in velocity $[\Delta\overline{V}_1/(d^4\omega/L^3)$, thick lines] of swimmer due to single obstacle placed along cuts 1, 2, 3, and 4 [blue (solid), red (dashes), green (dash-dots), magenta (dots)] in Fig. 1. Comparison to $\frac{1}{3}\sum_\alpha 1/(8\pi\mu)\{\overline{[(\mathbb{I}+\mathbf{rr}/r^2)/r]\mathbf{f}}\}_1/(d^4\omega/L^3)$ (thin lines), and $\frac{1}{3}\sum_\alpha 1/(8\pi\mu)\{\overline{[(\mathbb{I}+\mathbf{rr}/r^2)/r]}(-6\pi\mu d\overline{\mathbf{v}_0})\}_1/(d^4\omega/L^3)$ (circles on thin lines) corroborates Eqs. (3) and (4).

resulting velocity field at the swimmer sphere positions $\mathbf{x}^\alpha$ ($\alpha = 1,2,3$) and obstacle position $\mathbf{x}^4$ is given by

$$v_i^\alpha(\mathbf{x}^\alpha) = \frac{f_i^\alpha}{6\pi\mu d} + \sum_{\beta\neq\alpha}^{3} S_{ij}^{\alpha\beta} f_j^\beta + S_{ij}^{\alpha 4} f_j^4, \quad (1)$$

$$v_i^4(\mathbf{x}^4) = \frac{f_i^4}{6\pi\mu d} + \sum_{\beta=1}^{3} S_{ij}^{4\beta} f_j^\beta, \quad (2)$$

where μ is the viscosity, $\mathbf{S}_{ij}^{ab} = \frac{1}{8\pi\mu}(\frac{\delta_{ij}}{x^{ab}} + \frac{x_i^{ab}x_j^{ab}}{(x^{ab})^3})$, $\mathbf{x}^{ab} = \mathbf{x}^a - \mathbf{x}^b$, and $\mathbf{f}^a$ is the force on the ath sphere.

The no-slip boundary conditions on the sphere surfaces are approximately satisfied by setting the obstacle velocities $\mathbf{v}^a(\mathbf{x}^a) = 0$ and the swimmer sphere velocities $\mathbf{v}(\mathbf{x}^\alpha) = \mathbf{V}_C + \mathbf{\Omega}_C \times \Delta\mathbf{x}^\alpha + \Delta\mathbf{v}^\alpha(\dot{L}_1, \dot{L}_3)$, where $\mathbf{V}_C$ and $\mathbf{\Omega}_C$ are the centroid velocity and the angular velocity of the swimmer, respectively, $\Delta\mathbf{x}^\alpha$ are the sphere positions relative to the centroid, and $\Delta\mathbf{v}^\alpha$ are the sphere velocities relative to the centroid induced by changes in $L_1(t)$ and $L_3(t)$.

The six unknown components of $\mathbf{V}_C$ and $\mathbf{\Omega}_C$ are the numerical solutions to the linear system obtained by applying the zero net force and torque conditions appropriate for the zero-Reynolds-number limit ($\sum_{\alpha=1}^3 \mathbf{f}^\alpha = 0$ and $\sum_{\alpha=1}^3 \Delta\mathbf{x}^\alpha \times \mathbf{f}^\alpha = 0$) and the boundary conditions to Eqs. (1) and (2). Integrating these instantaneous velocities yields swimming trajectories, and the averages (denoted by a bar) reported here are obtained over two periods of swimmer deformations.

In Fig. 2, we plot the change in the first component (in the direction aligned with the swimmer spheres) of the swimming velocity ($\Delta\overline{V_1}$) for a variety of obstacle positions corresponding to the cuts shown in Fig. 1.

III. FORCES ON MICROSTRUCTURE DETERMINE THE CHANGE IN SWIMMING VELOCITY

We provide a physical interpretation of these results by connecting the change in swimming speed to the force exerted

by the obstacle on the fluid. If the swimming velocity in the absence of obstacles is $\mathbf{V}_0$, consider the change of swimming speed due to the presence of the obstacle, $\Delta\mathbf{V} = \mathbf{V}_C - \mathbf{V}_0$. From Eq. (1), it can be seen that upon addition of an obstacle, $\mathbf{V}_C = \frac{1}{3}\sum_\alpha \mathbf{v}^\alpha$ changes due to either changes in the swimmer forces $\mathbf{f}^\alpha$, or changes in the flow due to obstacle force $\mathbf{f}^4$. In the following, we argue that for a single obstacle the magnitude of velocity changes due to the latter dominate over changes due to the former. Let $\mathbf{r}$ be the displacement of $\mathbf{x}^4$ from the swimmer centroid. Suppose $L = 10d$ is the typical separation between swimmer spheres, $\xi = 2.5d$ is the amplitude of sphere displacements, $\dot{L} = \xi\omega = 2.5d\omega$ is the typical speed of prescribed swimmer sphere displacements, and the obstacle is a distance $r \gg L$ from the swimmer.

We can estimate the magnitude of instantaneous swimmer forces as $f^\alpha \sim \mu d\dot{L}$. The average velocity induced by the swimmer at the obstacle is approximately $\sum_\alpha \overline{\mathbf{S}^{4\alpha}\mathbf{f}^\alpha}$, and given by Eq. (2) of [52], which finds that the time-averaged flow of a Najafi-Golestanian swimmer is quadrupolar rather than dipolar in nature. In terms of our variables, their equation yields that the induced velocity scales as $\xi^2 d^2\omega/r^3 \sim d^2\xi\dot{L}/r^3$. Using this in Eq. (2) implies that the magnitude of $\overline{f^4} \sim \mu d^3\xi\dot{L}/r^3$. Thus, the magnitude of flows (hence changes in swimmer speed) induced at the swimmer due to the obstacle force is $\overline{\mathbf{S}^{\alpha 4}\mathbf{f}^4} \sim d^3\xi\dot{L}/r^4$. Furthermore, from Eq. (1) the magnitude of changes in the swimmer forces will be $\Delta\overline{f}^\alpha \sim d\mu\overline{\mathbf{S}^{\alpha 4}\mathbf{f}^4} \sim \mu d^4\xi\dot{L}/r^4$. On the other hand, since force balance implies that changes to the swimmer forces change $V_C = \frac{1}{3}\sum_\alpha \mathbf{v}^\alpha$ only through the second term of Eq. (1), the magnitude of changes in the swimming speed will be $\Delta\overline{f^\alpha}/(\mu L) \sim d^4\dot{L}\xi/(r^4 L)$, which is smaller than the flows induced by the obstacle force by a factor of d/L.

Therefore, the change in swimming velocity should be dominated by the effect of the obstacle-induced flow,

$$\overline{\Delta V_i} \approx \frac{1}{3}\sum_\alpha \overline{S_{ij}^{\alpha 4} f_j^4}. \tag{3}$$

We verify this relation in Fig. 2 by comparing the numerically calculated swimming velocities to $\frac{1}{3}\sum_\alpha 1/(8\pi\mu)[\{(\mathbb{I} + \overline{\mathbf{r}^{\alpha 4}\mathbf{r}^{\alpha 4}/(r^{\alpha 4})^2)/r^{\alpha 4}}\}\overline{\mathbf{f}^4}]_1$, which shows that Eq. (3) holds quite well. To scale these quantities by a quantity that does not vary as r is changed, we take the estimates above and replace r by L, leading to the velocity scale $2.5^2 d^5\omega/L^4 \approx d^4\omega/L^3$, an overestimate of the velocity changes. The relation breaks down when the obstacle approaches the swimmer within a distance comparable to the length of the swimmer, 20–25d.

Since the obstacle force provides a way to interpret the effect of heterogeneity on swimmers, it is helpful to have a way to understand the force. Equation (2) and the estimate that swimmer forces are (to leading order) unchanged by the presence of the obstacle mean that the obstacle force is approximately the pinning force resisting the Stokes drag on the obstacle in the flow $\mathbf{v}_0$ of a free swimmer,

$$\overline{\mathbf{f}^4} \approx -6\pi\mu d\overline{\mathbf{v}_0(\mathbf{x}^a)}. \tag{4}$$

In Fig. 2, Eq. (4) is verified by comparing the change in velocity induced by the obstacle force given by Eq. (4),

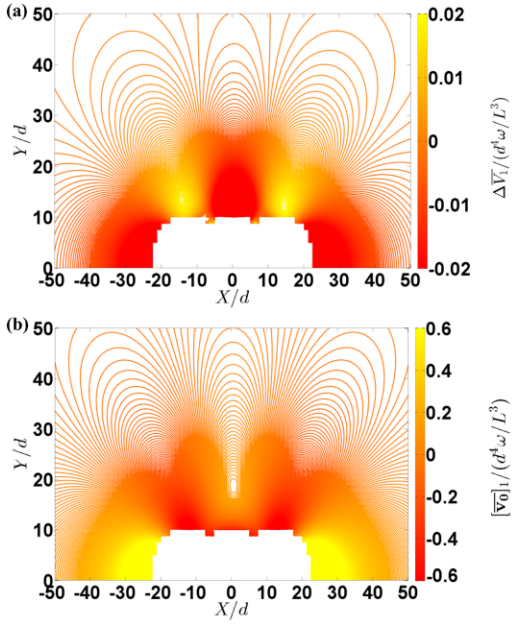

FIG. 3. (Color online) For a swimmer at the origin, contour plots of (a) change in first component of swimmer velocity (ΔV_1) due to obstacle at various positions relative to the swimmer, and (b) first component of swimmer's velocity field in the absence of obstacle ($v_{0,1}$). Positive (negative) regions of (a) correlate with the negative (positive) regions of (b). In the whited-out regions within $10d$ of the swimmer spheres, we do not plot results since there the far-field approximations are not valid.

$\frac{1}{3}\sum_\alpha 1/(8\pi\mu)(\{\overline{[\mathbb{I} + \mathbf{r}^{\alpha 4}\mathbf{r}^{\alpha 4}/(r^{\alpha 4})^2]/r^{\alpha 4}}\}(-6\pi\mu d\overline{\mathbf{v}_0}))_1$, to $\Delta\overline{V}_1$ and the flow induced by the actual obstacle force, $\frac{1}{3}\sum_\alpha 1/(8\pi\mu)(\overline{\{[\mathbb{I} + \mathbf{r}^{\alpha 4}\mathbf{r}^{\alpha 4}/(r^{\alpha 4})^2]/r^{\alpha 4}\}\mathbf{f}^4})_1$. Note that Fig. 2 and Eq. (4) imply that it is the *average*, not instantaneous, velocity at the obstacle that determines the effect on swimming, likely because the swimmer does not move much during one period of its stroke. Finally, note that if the obstacle is interpreted as a section of the microstructure attached to other elements of the microstructure, Eq. (4) holds for sufficiently stiff microstructure.

To illustrate how Eqs. (3) and (4) explain why swimming speeds can increase or decrease depending on the position of the obstacle relative to the swimmer, in Fig. 3(a) we plot the change in the first component of the swimming velocity (ΔV_1) as a function of the position of the obstacle, and in Fig. 3(b) we plot the first component of the free swimming velocity ($v_{0,1}$). In both panels, the swimmer is centered at the origin, and we do not plot the region closest to the swimmer where the far-field approximation fails. Equations (3) and (4) imply that where $v_{0,1}$ is negative, the first component of the obstacle force is positive, and the obstacle-induced flow ΔV_1 is positive, and vice versa. Thus, the positive (negative) sectors of Fig. 3(a) correlate with the negative (positive) sectors of

Fig. 3(b), providing a heuristic picture of the locations where an obstacle will speed up or slow down the swimmer based on the swimmer's velocity field in the absence of obstacles.

IV. INTERACTION WITH FILAMENTS

Consider the effect of many obstacles representing an entire microstructure. For the swimmer in a sparse microstructure, the effect on the swimming velocity can be obtained by adding up contributions like Eq. (3) for each obstacle: the sum over volume converges since in Eq. (4) the quadrupolar $\overline{\mathbf{v}_0}$ decays as $1/r^3$ and the Stokeslet decays as $1/r$. This convergence also implies that for sparse enough obstacles, the velocity field at one obstacle is not altered much from the free velocity field, and thus the approximation made in Eq. (4) is self-consistent. In the discussion we address the effect of denser microstructure or dipolar swimmers.

The above provides a physical way to interpret the interaction between swimmers and sparse pointlike heterogeneities. However, microorganisms often encounter filamentous networks, such as in mucus, which correspond to a (linearly) dense system of pointlike obstacles. Does the physical interpretation of Eqs. (3) and (4) apply to filaments? To address this, we study the interaction between the simple swimmer and cylindrical rod-shaped filaments. To describe flows around these slender filaments, we use Higdon's slender-body theory [53]. The filament of radius d_f is discretized into N segments of length $2q$ and constant force along each segment. The velocity field at the swimmer sphere locations ($\alpha = 1,2,3$) and rod segment locations $\mathbf{x}^a$ are

$$v_i^\alpha(\mathbf{x}^\alpha) = \frac{f_i^\alpha}{6\pi\mu d} + \sum_{\beta\neq\alpha}^{3} S_{ij}^{\alpha\beta} f_j^\beta + \sum_{b=1}^{N} G_{ij}^{\alpha b} f_j^b, \quad (5)$$

$$v_i^a(\mathbf{x}^a) = \sum_{\beta=1}^{3} S_{ij}^{a\beta} f_j^\beta + \sum_{b=1}^{N} G_{ij}^{ab} f_j^b, \quad (6)$$

where the G_{ij}^{ab} is the flow velocity at $\mathbf{x}^a$ in the ith direction due to a segment at $\mathbf{x}^b$ with force in the jth direction. [See Appendix for details on slender-body theory (SBT).] As before, Eq. (6) expresses approximate no-slip boundary conditions for the spheres and filament, and by applying the zero net force and torque conditions, Eqs. (5) and (6) can be solved for the forces and velocities, including the swimmer velocity.

Investigating the interaction between a swimmer and a single rod shows that the physical interpretation deduced from spherical obstacles applies to filaments, with a slight modification. Far enough from each segment the segment's flow contribution is dominated by its Stokeslet contributions. As in the case of spherical obstacles, the change in swimming velocity results from advection in the flow caused by the forces on the rod. We verify this by calculating the swimming velocity for a range of rod-swimmer configurations with a rod of length $125d$ perpendicular to the swimmer plane and its center varying in position along the cuts shown in Fig. 1. Figure 4 shows that the change in velocity relative to the free swimmer ($\Delta\overline{V_1}$) compares well to the advecting Stokeslet contribution summed over all rod elements, $\frac{1}{3}\sum_{\alpha,a}[\overline{\mathbf{S}^{\alpha a}\mathbf{f}^a}]_1$.

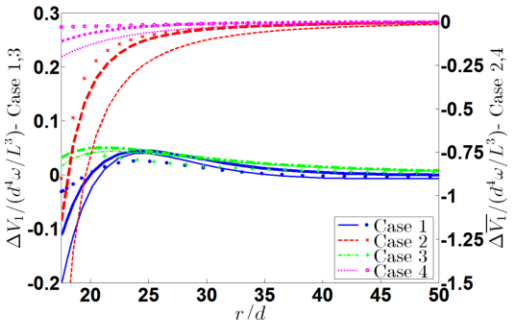

FIG. 4. (Color online) Change in velocity $[\Delta\overline{V}_1/(d^4\omega/L^3)$, thick lines] of swimmer due to rod placed along cuts 1, 2, 3, and 4 [blue (solid), red (dashes), green (dash-dots), magenta(dots)] in Fig. 1. Comparison to $\frac{1}{3}\sum_{\alpha,a}[\overline{\mathbf{S}^{\alpha a}\mathbf{f}^a}]_1/(d^4\omega/L^3)$ (thin lines) and $\frac{1}{3}\sum_{\alpha,a}[\overline{\mathbf{S}^{\alpha a}\mathbf{R}^{\mathrm{RFT},a}\mathbf{v}_0^a}]_1/(d^4\omega/L^3)$ (symbols) corroborates Eq. (3), interpreted as additive contributions from each segment of the rod, and Eq. (7).

Thus, the change in swimming velocity due to a filament is qualitatively related to $\mathbf{f}^a$, the numerically obtained force on each element. Figure 4 also shows that an estimate of $\mathbf{f}^a$ can be obtained using resistive force theory [54] (see Appendix for details), which gives

$$\mathbf{f}^a/(2q) = -[\zeta_\parallel\hat{\mathbf{n}}\hat{\mathbf{n}} + \zeta_\perp(\mathbb{I} - \hat{\mathbf{n}}\hat{\mathbf{n}})]\mathbf{v}_0(\mathbf{x}^a) \equiv \mathbf{R}^{\mathrm{RFT},a}\mathbf{v}_0^a, \quad (7)$$

where $\hat{\mathbf{n}}$ is the unit vector tangent to the segment a of the filament. Note that as in the case of spherical obstacles, it is the average rather than instantaneous velocity that determines the change in average swimming speed.

V. INTERACTION WITH FILAMENTOUS NETWORKS

Finally, consider the implications of the effect of rods on swimmers for a network of many filaments. Based on the interaction with rods, the total change in the swimming velocity $\Delta\overline{\mathbf{V}^t}$ is the sum of contributions of advective flows from all filaments, $\Delta\overline{\mathbf{V}^t} = \int d^3\mathbf{x}\,\overline{\mathbf{Sf}(\mathbf{x})}n(\mathbf{x})$, where $n(\mathbf{x}) = \sum_a \delta^3(\mathbf{x} - \mathbf{x}^a)$ is the density function for the microstructural filaments. Hence, using resistive force theory the change in velocity can be written

$$\Delta\overline{\mathbf{V}^t} = \int d^3\mathbf{x}\left[\left(\frac{2}{3}\zeta_\parallel + \frac{1}{3}\zeta_\perp\right)\mathbb{I} + (\zeta_\parallel - \zeta_\perp)\mathbf{Q}\right]\overline{\mathbf{v}_0}n(\mathbf{x}), \quad (8)$$

where the first term in the brackets only depends on the density, and the second term in the brackets depends on the orientational order parameter of the filament, $\mathbf{Q} = \hat{\mathbf{n}}\hat{\mathbf{n}} - \mathbb{I}/3$.

Now consider a swimmer in a macroscopically homogeneous and isotropic system moving over a trajectory long enough to average over heterogeneity, or a population large enough to average over heterogeneity. Denoting this trajectory or population average by $\langle\cdot\rangle$, $\langle n(\mathbf{x})\rangle = \rho$, a constant, and $\langle\mathbf{Q}\rangle = 0$, so the average change in velocity only depends on the density:

$$\langle\Delta\overline{\mathbf{V}^t}\rangle = \rho\int d^3\mathbf{r}\left(\frac{2}{3}\xi_\parallel + \frac{1}{3}\xi_\perp\right)\overline{\mathbf{Sv}_0}. \quad (9)$$

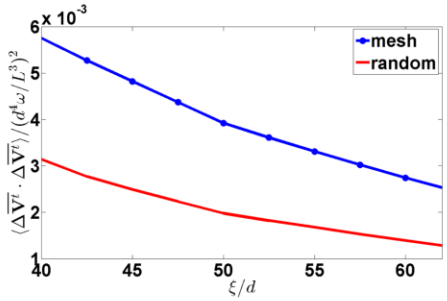

FIG. 5. (Color online) Variance of swimming velocity calculated from Eq. (10) for isotropically averaged structured mesh as a function of mesh size and random obstacles with equivalent density.

However, if we consider the variance in the change in swimming velocity it can be written in terms of two functions that only depend on the properties of the free swimmer, $F^1(\mathbf{x},\mathbf{x}') = (\overline{\mathbf{S}\mathbf{v}_0})|_{\mathbf{x}} \cdot (\overline{\mathbf{S}\mathbf{v}_0})|_{\mathbf{x}'}$ and $F^2_{jklm}(\mathbf{x},\mathbf{x}') = \overline{S_{ij}(\mathbf{x})v_{0,k}(\mathbf{x})}\ \overline{S_{il}(\mathbf{x}')v_{0,m}(\mathbf{x}')}$:

$$\langle \Delta\overline{\mathbf{V}^t} \cdot \Delta\overline{\mathbf{V}^t} \rangle = \int d^3\mathbf{x} d^3\mathbf{x}' \left\{ \left(\frac{2}{3}\zeta_\parallel + \frac{1}{3}\zeta_\perp \right)^2 \langle n(\mathbf{x}) n(\mathbf{x}') \rangle F^1(\mathbf{x},\mathbf{x}') + (\zeta_\parallel - \zeta_\perp)^2 \langle n(\mathbf{x}) Q_{jk} n(\mathbf{x}') Q_{lm} \rangle F^2_{jklm}(\mathbf{x},\mathbf{x}') \right\}. \quad (10)$$

Thus, the density and orientational correlations in the microstructure leave signatures in the velocity fluctuations of swimming microorganisms that are not accessible through continuum approaches.

We finish with an example of how variance of the swimming velocity reflects microstructural correlations. First consider a cubic mesh of straight rods with radius $d_f = d/40$ and mesh size ξ, averaged over mesh orientations and positions to represent a macroscopically isotropic medium. Since the density depends on mesh size, we compare it to a field of random spherical obstacles with density equal to the segment density for each mesh size. For each case, we calculate $\langle \Delta\overline{\mathbf{V}^t} \rangle$ and $\langle \Delta\overline{\mathbf{V}^t} \cdot \Delta\overline{\mathbf{V}^t} \rangle$ through correlation functions as in Eqs. (9) and (10). Since this letter focuses on the long-range hydrodynamic contributions to velocity changes, we impose a short-range cutoff in these calculations, ignoring any obstacles or segments closer than $25d$ to the swimmer; this is consistent with the range of validity of Eq. (3). As expected, $\langle \Delta\overline{\mathbf{V}^t} \rangle$ is the same for both cases. For the random case, the variance can be calculated explicitly as $\rho(\frac{2}{3}\xi_\parallel + \frac{1}{3}\xi_\perp)^2 \int d^3\mathbf{x}(\overline{\mathbf{S}\mathbf{v}_0} \cdot \overline{\mathbf{S}\mathbf{v}_0})$. Figure 5 shows that $\langle \Delta\overline{\mathbf{V}^t} \cdot \Delta\overline{\mathbf{V}^t} \rangle$ as a function of mesh size is nonzero, in contrast to homogeneous media. Furthermore, the mesh has more fluctuations than random obstacles, primarily due to additional density-density correlations.

VI. DISCUSSION

Using a simple model, we have demonstrated how fluctuations in swimming velocities can arise from the interaction of swimmers with spatially varying microstructural heterogeneity, and that the forces on microstructure are physically related to changes in swimming velocities. Hydrodynamic interactions with the heterogeneities leads to variances in swimming velocities that depend on correlations in density and orientation, which reflect the structure of filamentous networks. Thus, observations of swimming fluctuations may provide a way to probe microstructural features. These fluctuations are inaccessible via homogeneous, continuum treatments of complex media.

We used the Najafi-Golestanian swimmer since its tractability eases the handling of hydrodynamic interactions with microstructure. Our analysis was also possible because the swimmer is a quadrupolar swimmer, hence the effects of many obstacles on the swimmer and each other remains bounded for sparse enough networks. Thus, the specific results [e.g., Eq. (10)] we obtained are only valid for quadrupolar swimmers in very sparse networks. However, for denser networks and more realistic dipolar swimmers (or asymmetric three-sphere swimmers), we expect that our physical point still holds: swimming through an environment with disordered spatial heterogeneity at swimmer lengthscales leads to fluctuations in swimming velocities. To see that this is plausible, consider hydrodynamic interactions in the limit of a dense network or for a dipolar swimmer. In that case, Leshansky [48] has shown that the long-range flows can be described as those in a damped Brinkmann fluid. However, even in such a medium, if the local environment varies, one could represent the situation as a background homogeneous Brinkmann fluid with local defects or variations near the swimmer. The local defects would again lead to fluctuations in swimming velocities, and there could be analogues to Eqs. (3) and (4) that involve the flow due to a point force in a Brinkmann fluid, and the drag on a sphere in a Brinkmann fluid, respectively. In the biologically relevant case of mucus, which could be neither extremely sparse nor extremely dense, due to the alteration in long-distance flows the precise relation between fluctuations, microstructure, and free-swimmer properties depend on nontrivial solutions where local variations in the medium mean that neither Newtonian nor Brinkmann solutions are valid near the swimmer. Nonetheless we expect that heterogeneity leads to fluctuations, which reflect the structure of the medium.

In addition to hydrodynamic interactions, for denser networks close-range interactions (such as near-field hydrodynamics, mechanical contact, screened electrostatic, chemical bonding, or van der Waals interactions) become important if the swimmer frequently closely approaches microstructure. These contribute additional fluctuations in the swimming speed inaccessible within the scope of the current calculation. For example, the previously mentioned fluctuations in swimming velocities of spirochetes [44] and nematodes [49] originate in interactions dominated by chemical interactions and mechanical contact, respectively. Even in those cases the physical mechanism we elucidate still applies: if the swimmer encounters locally varying environments as it passes through the medium, they will lead to additional fluctuations in swimming speed that reflect the local variation.

Our work suggests a number of future directions. We ignored the role of compliance, even though many biological

networks may deform in response to swimmers. For compliant networks, a relation like Eq. (3) would still hold, but due to the possibility of filament motion the force on obstacles would not be given by Eq. (4). In calculating the variance of fluctuations, we also assumed that the medium was macroscopically isotropic, but recent experiments suggest that it may be interesting to look at cases where the medium is anisotropic as well [55]. Last, we focused on changes in swimming speed in this manuscript, but rotations caused by interactions with heterogeneity could alter the persistence length of swimming trajectories, leading to enhanced diffusion or spreading. Note that since net displacements depend on the entire orientational history of the trajectory, infrequent close range encounters with obstacles would have a larger effect on persistence lengths than on the fluctuations in speed examined here.

ACKNOWLEDGMENTS

M.J. and H.C.F. are supported by NSF Award No. CBET-1252182-CAREER to H.C.F. Y.H. is supported by KRCF Research Fellowship for Young Scientists and National Institute for Mathematical Sciences in Korea.

APPENDIX A: SLENDER-BODY THEORY

Around a slender object with circular cross section, the no-slip boundary conditions can be satisfied by a distribution of Stokeslets and dipoles along the centerline. Following Higdon's slender-body theory, the filament is discretized into straight segments of length $2q$ as shown in Fig. 6 for a filament of radius d_f. The velocity at the point $\mathbf{x^L}$ due to the singularities in the small interval $(-q,q)$, which is centered at $\mathbf{X^L}$, is

$$v_i^L(\mathbf{x^L}) = \int_{-q}^{+q} \left[S_{ij}(\mathbf{x^L},\mathbf{X^L}+s\hat{\mathbf{n}})\frac{f_{ij}^a(\mathbf{X^L})}{8\pi\mu} - \frac{d_f^2}{4} D_{ij}(\mathbf{x^L},\mathbf{X^L}+s\hat{\mathbf{n}})\frac{f_{\perp ij}^a(\mathbf{X^L})}{4\pi\mu}\right] ds. \quad \text{(A1)}$$

$$S_{ij}(\mathbf{x},\mathbf{X}) = \frac{\delta_{ij}}{r} + \frac{(x_i - X_j)(x_j - X_j)}{r^3} \quad \text{(A2)}$$

$$D_{ij}(\mathbf{x},\mathbf{X}) = -\frac{\delta_{ij}}{r^3} + \frac{3(x_i - X_j)(x_j - X_j)}{r^5}, \quad \text{(A3)}$$

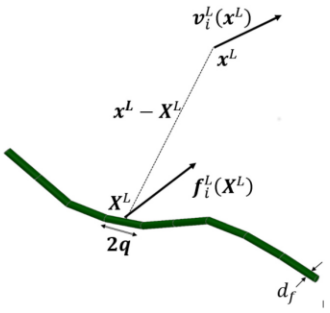

FIG. 6. (Color online) Configuration for slender-body theory.

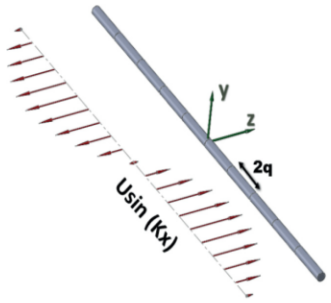

FIG. 7. (Color online) Straight rod with varying background flow.

where $\hat{\mathbf{n}}$ is the unit tangent vector to the segment, $\mathbf{f}^a$ is a force density assumed to be constant over this short interval, and $\mathbf{f}_\perp^a = (\mathbb{I} - \hat{\mathbf{n}}\hat{\mathbf{n}})\mathbf{f}^a$. Equation (A1) is integrated to yield

$$v_i^L(\mathbf{x^L}) = G_{ij}(\mathbf{x^L},\mathbf{X^L}) f_j^a, \quad \text{(A4)}$$

where explicit expressions for G_{ij} can be found in Higdon [53].

The accuracy of slender-body theory requires that the ratio between segment length and diameter (q/d_f) is small.

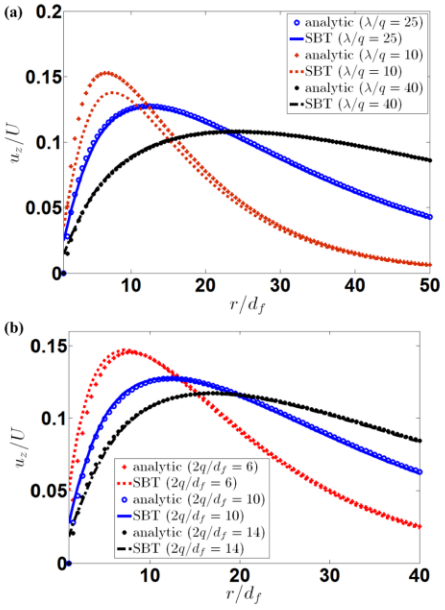

FIG. 8. (Color online) Comparison of the z component of the velocity at positions along the z axis passing through the middle of the long rod. In (a) the background wavelength λ and rod radius $d_f = 0.01\lambda$ are fixed and the segment length $2q$ is varied. In (b) the wavelength λ and segment length $2q$ are fixed, and the rod radius d_f is varied.

For interactions between rod-shaped filaments and swimmer, the rod is in a nonuniform background flow. Thus, to validate our approach, we compare our SBT results to a scenario of a rod in a spatially varying background flow that has an analytical solution. In this scenario, the background flow is sinusoidal and perpendicular to the rod (see Fig. 7), $v_z = U\sin(Kx)$ sufficiently far from the rod, and the analytic solution can be found in Happel and Brenner [56].

For example, in Fig. 8 we compare the z component of the velocity at positions along the z axis passing through the middle of the long rod for a specific case with fixed $\lambda = 2\pi/K$, U, and total rod length 40 λ. In Fig. 8(a), the rod radius $d_f = 0.01\lambda$ and we vary the segment length $2q$ to show that as long as $\lambda/q > 25$, the numerical results are accurate (average percentage errors from analytic results are 27%, 2.94%, and 0.16% for $\lambda/q = 10$, 25, and 40, respectively). In Fig. 8(b), we keep $q = 25\lambda$ fixed and vary the rod radius d_f to show that the numerical results are accurate as long as the segment length $2q$ is greater than $10d_f$ (average percentage errors from analytic results are 17.9%, 2.94%, and 0.96% for $2q/d_f = 6$, 10, and 14, respectively). Through this comparison, we determine that the SBT results are accurate so long as $\lambda/q > 25$ and $q/d_f > 5$. Physically, this means that the segments must be short compared to the wavelength in order to resolve spatial variations in the flow, yet still slender enough to apply Higdon's method. For the results presented in the main text, these conditions are satisfied if λ is taken to be the lengthscale of variation in the swimmer's free velocity field at the location of the rod.

APPENDIX B: RESISTIVE FORCE THEORY ESTIMATES THE FORCES ON RODS

For filaments, the force on each segment is not given by the Stokes drag as it is for spherical obstacles. Instead, the force $\mathbf{f}^q$ on each segment is better expressed by resistive force theory, which has anisotropic local drag coefficients for parallel and perpendicular background flow, as in Eq. (7). In Eq. (7), $\hat{\mathbf{n}}$ is tangent to the filament, $\zeta_\parallel$ and $\zeta_\perp$ are parallel and perpendicular drag coefficients, and $\mathbf{v}_0(\mathbf{r})$ is the free velocity field due to the swimmer at the position of the filament.

To estimate the drag coefficients, we place single rods in different positions and orientations relative to the swimmer and compute the instantaneous force on each segment of the filament throughout a swimming stroke. Then we find values for $\zeta_\parallel$ and $\zeta_\perp$, which provide the best fit (measured by the sum of squared residuals) for the entire set of position- and time-dependent forces. The best-fit coefficients are $\zeta_\perp = 1.77\mu$ and $\zeta_\parallel = 1.02\mu$. To see that these values are reasonable, we compare with the results of Gray and Hancock [57], which state that

$$\zeta_\perp^{\mathrm{GH}} = \frac{4\pi\mu}{\ln(2\times 0.09\Lambda/d_f) + 0.5}, \tag{B1}$$

$$\zeta_\parallel^{\mathrm{GH}} = \frac{2\pi\mu}{\ln(2\times 0.09\Lambda/d_f) - 0.5}. \tag{B2}$$

In these equations, if the lengthscale Λ is chosen to be $100d$, which is the approximate lengthscale of variations in the free swimmer field at the locations of the rods, then $\zeta_\perp^{\mathrm{GH}} = 1.77\mu$ and $\zeta_\parallel^{\mathrm{GH}} = 1.03\mu$.

[1] E. Lauga and T. R. Powers, Rep. Prog. Phys. **72**, 096601 (2009).
[2] J. P. Celli, B. S. Turner, N. H. Afdhal, S. Keates, I. Ghiran, C. P. Kelly, R. H. Ewoldt, G. H. McKinley, P. So, S. Erramilli, and R. Bansil, Proc. Natl. Acad. Sci. USA **106**, 14321 (2009).
[3] S. Suarez and H.-C. Ho, Reprod. Dom. Anim. **38**, 119 (2003).
[4] S. S. Suarez and A. A. Pacey, Human Reprod. Update **12**, 23 (2006).
[5] G. E. Kaiser and R. N. Doetsch, Nature **255**, 656 (1975).
[6] W. R. Schneider and R. N. Doetsch, J. Bacteriol. **117**, 696 (1974).
[7] E. P. Greenberg and E. Canale-Parola, J. Bacteriol. **131**, 960 (1977).
[8] H. C. Berg and L. Turner, Nature **278**, 349 (1979).
[9] T. K. Chaudhury, J. Fluid Mech. **95**, 189 (1979).
[10] Y. Magariyama and S. Kudo, Biophys. J. **83**, 733 (2002).
[11] A. M. Siddiqui and A. R. Ansari, J. Porous Media **6**, 235 (2003).
[12] R. Gilad, A. Porat, and S. Trachtenberg, Mol. Microbiol. **47**, 657 (2003).
[13] M. J. Daniels, J. M. Longland, and J. Gilbart, J. Gen. Microbiol. **118**, 429 (1980).
[14] J. W. Shaevitz, J. R. Lee, and D. A. Fletcher, Cell **122**, 941 (2005).
[15] G. Juarez, K. Lu, J. Sznitman, and P. E. Arratia, Europhys. Lett. **92**, 44002 (2010).
[16] S. Jung, Phys. Fluids **22**, 031903 (2010).
[17] J. R. Vélez-Cordero and E. Lauga, J. Non-Newtonian Fluid Mech. **199**, 37 (2013).
[18] R. B. Kimsey and A. Spielman, J. Infect. Disease **162**, 1205 (1990).
[19] G. R. Fulford, D. F. Katz, and R. L. Powell, Biorheology **35**, 295 (1998).
[20] E. Lauga, Phys. Fluids **19**, 083104 (2007).
[21] H. C. Fu, T. R. Powers, and C. W. Wolgemuth, Phys. Rev. Lett. **99**, 258101 (2007).
[22] H. C. Fu, C. W. Wolgemuth, and T. R. Powers, Phys. Rev. E **78**, 041913 (2008).
[23] T. Normand and E. Lauga, Phys. Rev. E **78**, 061907 (2008).
[24] H. C. Fu, C. W. Wolgemuth, and T. R. Powers, Phys. Fluids **21**, 033102 (2009).
[25] E. Lauga, Europhys. Lett. **86**, 64001 (2009).
[26] J. Teran, L. Fauci, and M. Shelley, Phys. Rev. Lett. **104**, 038101 (2010).
[27] D. Smith, E. A. Gaffney, H. Gadelha, N. Kapur, and J. C. Kirkman-Brown, Cell. Motil. Cytoskel. **66**, 220 (2009).
[28] O. S. Pak, T. Normand, and E. Lauga, Phys. Rev. E **81**, 036312 (2010).
[29] G. Elfring, O. S. Pak, and E. Lauga, J. Fluid Mech. **646**, 505 (2010).
[30] X. N. Shen and P. E. Arratia, Phys. Rev. Lett. **106**, 208101 (2011).
[31] L. Zhu, M. Do-Quang, E. Lauga, and L. Brandt, Phys. Rev. E **83**, 011901 (2011).

[32] B. Liu, T. R. Powers, and K. S. Breuer, Proc. Natl. Acad. Sci. USA **108**, 19516 (2011).
[33] Y. Bozorgi and P. T. Underhill, Phys. Rev. E **84**, 061901 (2011).
[34] M. P. Curtis and E. A. Gaffney, Phys. Rev. E **87**, 043006 (2013).
[35] M. Dasgupta, B. Liu, H. C. Fu, M. Berhanu, K. S. Breuer, T. R. Powers, and A. Kudrolli, Phys. Rev. E **87**, 013015 (2013).
[36] S. E. Spagnolie, B. Liu, and T. R. Powers, Phys. Rev. Lett. **111**, 068101 (2013).
[37] D. A. Gagnon, X. N. Shen, and P. E. Arratia, Europhys. Lett. **104**, 14004 (2013).
[38] J. Ruttlant, M. López-Béjar, and F. López-Gatius, Reprod. Dom. Anim. **40**, 79 (2005).
[39] S. K. Lai, Y.-Y. Wang, D. Wirtz, and J. Hanes, Adv. Drug Delivery Rev. **61**, 86 (2009).
[40] P. Olla, Phys. Rev. E **89**, 032136 (2014).
[41] R. E. Goldstein, M. Polin, and I. Tuval, Phys. Rev. Lett. **103**, 168103 (2009).
[42] R. Ma, G. S. Klindt, I. H. Riedel-Kruse, F. Jülicher, and B. M. Friedrich, Phys. Rev. Lett. **113**, 048101 (2014).
[43] K. Y. Wan and R. E. Goldstein (2014), arXiv:1406.3725.
[44] M. Harman, S. M. Dunhams-Ems, M. J. Caimano, A. Belperron, L. Bockenstedt, H. Fu, J. D. Radolf, and C. W. Wolgemuth, Proc. Natl. Acad. Sci. USA **109**, 3059 (2012).
[45] J. C. Chrispell, L. J. Fauci, and M. Shelley, Phys. Fluids **25**, 013103 (2013).
[46] H. C. Fu, V. B. Shenoy, and T. R. Powers, Euro. Phys. Lett. **91**, 24002 (2010).
[47] R. Ledesma-Aguilar and J. M. Yeomans, Phys. Rev. Lett. **111**, 138101 (2013).
[48] A. M. Leshansky, Phys. Rev. E **80**, 051911 (2009).
[49] T. Majmudar, E. E. Keaveny, J. Zhang, and M. J. Shelley, J. R. Soc. Interface **9**, 1809 (2012).
[50] A. Najafi and R. Golestanian, Phys. Rev. E **69**, 062901 (2004).
[51] R. Golestanian and A. Ajdari, Phys. Rev. E **77**, 036308 (2008).
[52] C. M. Pooley, G. P. Alexander, and J. M. Yeomans, Phys. Rev. Lett. **99**, 228103 (2007).
[53] J. J. L. Higdon, J. Fluid Mech. **90**, 685 (1979).
[54] S. Childress, *Mechanics of Swimming and Flying* (Cambridge University Press, Cambridge, 1981).
[55] S. Zhou, A. Sokolov, O. D. Lavrentovich, and I. S. Aranson, Proc. Natl. Acad. Sci. USA **111**, 1265 (2013).
[56] J. Happel and H. Brenner, *Low Reynolds Number Hydrodynamics* (Noordhoff, Leyden, 1973).
[57] J. Gray and G. Hancock, J. Exp. Biol. **32**, 802 (1955).

CHAPTER 6

VISCOUS CONSTRAINTS ON MICROORGANISM APPROACH AND INTERACTION [*]

6.1 Abstract

Microorganisms must approach other suspended organisms or particles in order to interact with them during a host of life processes including feeding and mating. These interactions happen at low Reynolds number where viscosity dominates and strongly affects the hydrodynamics of the swimmer and nearby cells and objects. Viscous hydrodynamics makes it difficult for two surfaces to approach closely at low Reynolds number. Nonetheless, it is observed that microorganisms in fluid are still able to approach closely enough to interact with each other or suspended particles. Here, we study how the physical constraints provided by viscous hydrodynamics affect the feasibility of direct approach of flagellated and ciliated microorganisms to targets of different sizes. We find that it is feasible for singly flagellated swimmers to approach targets that are the same size or bigger. On the other hand, for squirmers, pullers can approach any size of targets by generating a current toward the swimmer, but pushers generate a current away from the

[*] The following sections have been submitted to be published in Journal of Fluid Mechanics as a paper. As such, it is to be treated as a stand-alone paper with its own references, sections, and equations. Coauthors of this paper are Mehdi Jabbarzadeh and Henry C. Fu.

swimmer and the strength of the current and hence feasibility of approach depends on the squirmer parameter.

6.2 Introduction

Microorganisms live in viscous environments in which they interact with other organisms for genetic exchange, mating, and colonization, as well as interact with other nearby passive and active particles that are prey or nutrient sources [1]. These interactions are crucial for enhancing populations, establishing a community during colonization, biofilm formation, and microbe-host interactions [2]. Many of these interactions require inducing near-contact between the microorganism and target (either another microorganism or a particle) in a viscous flow, and can involve a wide range of swimmer and target particle sizes. For example, during feeding, the size of prey is generally much smaller than the predator [3]–[8]. However, during bacterial conjugation [9], zooplankton mating [10], [11], or colonization, an organism approaches another member of the same species of similar size. Approach to larger targets also occurs during fertilization of an egg by sperm [12] or when bacteria find new habitats by approaching marine snow, small biological debris which provides a local nutrient source and habitat in the ocean [13], [14].

The microorganisms we study live at low Reynolds number ($10^{-5} - 10^{-1}$) where there is a thick boundary layer of fluid that moves together with their moving body or appendages. This hydrodynamic boundary layer plays an important role in the hydrodynamic interactions of a swimmer and other particles, and makes it difficult to closely approach target particles. For example, when a copepod feeds on a particle, the movements of its appendages induce hydrodynamic flows that tend to push or pull the

particle in concert with the appendage [15], and due to the kinematic reversibility of flows at low Reynolds number, it is difficult for the copepod to easily move the particle closer to its mouth.

Small target particles near a swimming microorganism are often assumed to follow streamlines of the flow induced by the swimmer in the absence of other particles. However, understanding approach to similarly- or larger-sized particles, or understanding very close approach to particles of any size, requires incorporating the hydrodynamic interactions between the microorganism and target. Although microorganisms (including their appendages) and targets can have complex shapes, physical insight into their hydrodynamic interactions can be gained by considering analytically tractable geometries such as approaching spheres. The exact solution for the motion of two spheres translating with the same velocity along their common diameter was first developed by [16]. The special case of a sphere approaching a solid plane was extensively studied [17], [18] for both large separations and close to contact. Later, [19] analytically calculated the interaction of two spherical "squirmer" swimmers, both in the limit of small separation using lubrication theory, and in the limit of large separation using a multipole expansion, then compared their results with numerical (boundary element method) simulations. Potomkin *et al.* [20] discuss the collision (i.e., physical contact) of microswimmers with different boundary conditions in a viscous fluid. They show that with no-slip boundary conditions, collisions between two swimmers are impossible in finite collision times, while with slip boundaries, collisions can occur within finite times. More recently, Papavassiliou and Alexander [21] found an exact solution for the hydrodynamic interactions of two squirmers. They also provide exact solution for specific cases when the squirmer sphere is

close to a solid or free surface to study hydrodynamic interactions of swimmers in confined boundaries.

In this paper, we investigate the physical constraints placed by viscous hydrodynamics on organisms approaching passive target particles. We first review the exact solution for two spheres with no-slip boundaries in a bispherical coordinate system described in [16]. As a simple example of hydrodynamic constraints on approach, in section 6.3, we modify this solution for the case when the two spheres have different velocities and a constant, localized propulsion force towards the other sphere pushes one sphere, which is a neutrally buoyant (force-free) target. To show that the physical insights from this model also apply to swimmers, in section 6.3.2, we validate a numerical method for studying close approach and use it to study a singly-flagellated swimmer with spherical cell body approaching a spherical target. For both of these cases with localized propulsion, we find that approach is feasible when the target is of similar or larger size than the swimmer, but infeasible for smaller size targets. Finally, to study organisms with distributed propulsion, in section 6.4, we present an exact solution for a spherical squirmer approaching a no-slip target sphere in the bispherical coordinate system. We find that swimmers with distributed propulsion mechanisms can generate currents during swimming that allow them to approach smaller as well as larger targets, with differences in the currents and approach feasibility controlled by whether the squirmer is a pusher- or puller-type swimmer.

6.3 Approach with localized propulsion

6.3.1 Analytical model for approaching spheres – localized propulsion

We developed an analytical model for the approach of two spheres along their centerline in Stokes flow. The spherical swimmer is assumed to be pushed toward a force-free suspended spherical target particle by a constant force F along their common centerline (Figure 6.1b). Although swimming microorganisms should be considered force free, as we show in section 6.3.2, this simple model has similar qualitative features to a force-free swimmer with a single localized propulsion element, with the constant force corresponding to the localized thrust on the body provided by the element. Note that the "swimming" sphere could also be a model for an appendage or a portion of an organism, in which case the constant force would describe the force exerted on it by the rest of the organism. Also, note that a number of real organisms do have roughly spherical geometries, such as *Opalina* and *Volvox* [19].

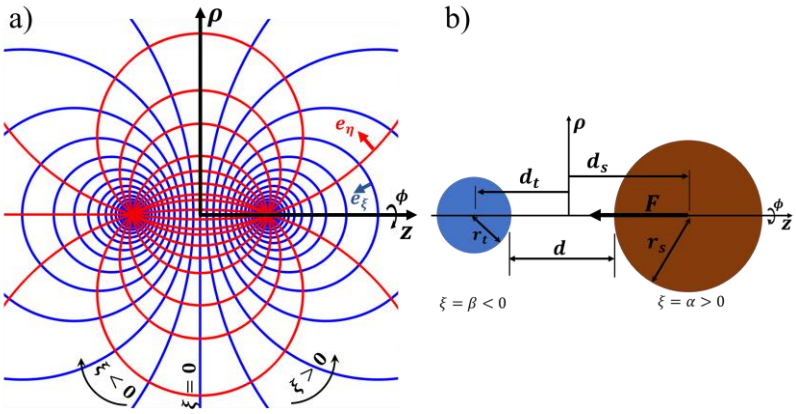

Figure 6.1. a) Relation between the bispherical coordinate system (ξ, η, ϕ) and cylindrical coordinate system (z, ρ, ϕ). The axisymmetric ϕ coordinate is rotation about the z-axis. b) Spherical swimmer with radius r_s is pushed by a constant force $\boldsymbol{F}$ toward a force-free spherical target particle with radius r_t. The surface-to-surface separation distance of the swimmer and particle is d and surfaces with constant ξ describe spheres in bispherical coordinate system for the swimmer ($\xi = \alpha > 0$) and target ($\xi = \beta < 0$).

Our solution is based on finding the Stokes' stream function in the bispherical coordinate system (Figure 6.1a) for an axisymmetric Stokes flow around the spheres. For Stokes flow, the flow velocity field can be described as the curl of a vectorial stream function $\boldsymbol{\psi}$ that satisfies the biharmonic equation, $\nabla^4 \boldsymbol{\psi} = 0$. For a flow axisymmetric in the angular coordinate ϕ (corresponding to rotation angle about the z axis), $\boldsymbol{\psi}$ can be expressed in terms of a scalar ψ, as $\boldsymbol{\psi} = \psi\, \boldsymbol{e}_\phi$, and the components of the velocity field in the cylindrical coordinate system are

$$u_\rho = \frac{1}{\rho}\frac{\partial \psi}{\partial z}, \tag{6.1}$$

$$u_z = -\frac{1}{\rho}\frac{\partial \psi}{\partial \rho}. \tag{6.2}$$

For two interacting spheres, it is convenient to use the bispherical coordinate system (ξ, η, ϕ) (Figure 6.1a), for which the general solution was given by [16] as

$$\psi = (\cosh\xi - \mu)^{-3/2} X, \tag{6.3}$$

$$X = \sum_{n=1}^{\infty} U_n(\xi) V_n(\mu), \tag{6.4}$$

$$\begin{aligned} U_n(\xi) = {} & A_n \cosh\big((n-1/2)\xi\big) + B_n \sinh\big((n-1/2)\xi\big) \\ & + C_n \cosh\big((n+3/2)\xi\big) + D_n \sinh\big((n+3/2)\xi\big) \end{aligned} \tag{6.5}$$

where $\mu = \cos\eta$ and A_n, B_n, C_n, and D_n are real constants determined by boundary conditions. The notation $V_n(\mu) = P_{n-1}(\mu) - P_{n+1}(\mu)$ is used for combinations of Legendre functions $P_n(\mu)$ that satisfy the differential equation

$$(1-\mu^2)\frac{d^2 V_n}{d\mu^2} + n(n+1)V_n = 0. \tag{6.6}$$

The relations between the cylindrical coordinates (ρ, z, ϕ) and bispherical

coordinates (ξ, η, ϕ) are (Figure 6.1a) ,

$$\rho = \frac{c \sin \eta}{\cosh(\xi) - \mu}, \qquad z = \frac{c \sinh \xi}{\cosh(\xi) - \mu} \tag{6.7}$$

where c is a real positive constant and surfaces of constant ξ are nonintersecting spheres centered at $z = c \coth \xi$ with radius $a = c\,|\mathrm{csch}\,\xi|$. We assume that the swimmer with $\xi = \alpha > 0$ and radius r_s is approaching the target particle with $\xi = \beta < 0$ and radius r_t as shown in Figure 6.1b. Using the above, consider two spheres centered at $d_s = c \coth \alpha$ and $d_t = c \coth \beta$ with surfaces defined by $\left(z - d_{s,t}\right)^2 + \rho^2 = r_{s,t}^2$ in cylindrical coordinates. If the sphere surfaces are separated by d, then

$$r_s = c\,\mathrm{csch}\,\alpha, \tag{6.8}$$

$$r_t = -c\,\mathrm{csch}\,\beta, \tag{6.9}$$

$$d = c\,(\coth \alpha - \coth \beta) - (r_s + r_t). \tag{6.10}$$

Defining the target:swimmer size ratio by $r = r_t/r_s$ and $x = 1 + d/r_s$, equations 6.35 can be solved for α, β, and c,

$$\alpha = \cosh^{-1}\left(\frac{(x+r)^2 - (r^2-1)}{2(x+r)}\right), \tag{6.11}$$

$$\beta = -\cosh^{-1}\left(\left|\frac{(x+r)^2 + (r^2-1)}{2r(x+r)}\right|\right), \tag{6.12}$$

$$\frac{c}{r_s} = \sqrt{\left(\frac{(x+r)^2 - (r^2-1)}{2(x+r)}\right)^2 - 1}. \tag{6.13}$$

Stimson and Jeffery studied the translation of two spheres moving along their common centerline with the same velocity. Here, we present analogous results for two spheres translating along their common diameter (in the z-direction) with arbitrary velocities V_s and V_t for the swimmer and target, respectively. In cylindrical coordinates,

the no-slip boundary conditions at the surface of the spheres are

$$\frac{\partial \psi}{\partial z} = 0, \qquad \frac{\partial \psi}{\partial \rho} = -\rho V_s \tag{6.14}$$

on the swimmer, and

$$\frac{\partial \psi}{\partial z} = 0, \qquad \frac{\partial \psi}{\partial \rho} = -\rho V_t \tag{6.15}$$

on the target. These boundary conditions can be rewritten in a bispherical coordinate system as [16]

$$\psi + \frac{1}{2}\rho^2 V_s = 0, \qquad \frac{\partial}{\partial \rho}\left(\psi + \frac{1}{2}\rho^2 V_s\right) = 0 \tag{6.16}$$

on the swimmer, and

$$\psi + \frac{1}{2}\rho^2 V_t = 0, \qquad \frac{\partial}{\partial \rho}\left(\psi + \frac{1}{2}\rho^2 V_t\right) = 0 \tag{6.17}$$

on the target. Using these four equations (6.16 and 6.17) for the boundary conditions at the surface of the spheres ($\xi = \alpha$ and $\xi = \beta$) and evaluating the stream function (6.3) at the surface of spheres, one can determine the unknown coefficients $A_n, B_n, C_n,$ and D_n. For each n by solving the system of linear equations

$$\begin{aligned} A_n \cosh\left(n - \frac{1}{2}\right)\alpha + B_n \sinh\left(n - \frac{1}{2}\right)\alpha + C_n \cosh\left(n + \frac{3}{2}\right)\alpha \\ + D_n \sinh\left(n + \frac{3}{2}\right)\alpha \\ = -kV_s\left[(2n+3)e^{\left(n-\frac{1}{2}\right)\alpha} - (2n-1)e^{\left(n+\frac{3}{2}\right)\alpha}\right] \end{aligned} \tag{6.18}$$

$$(2n-1)\left[A_n \sinh\left(n-\frac{1}{2}\right)\alpha + B_n \cosh\left(n-\frac{1}{2}\right)\alpha\right] + (2n+3)\left[C_n \sinh\left(n+\frac{3}{2}\right)\alpha + D_n \cosh\left(n+\frac{3}{2}\right)\alpha\right] = -kV_s(2n-1)(2n+3)\left[e^{\left(n-\frac{1}{2}\right)\alpha} - e^{\left(n+\frac{3}{2}\right)\alpha}\right] \tag{6.19}$$

$$A_n \cosh\left(n-\frac{1}{2}\right)\beta + B_n \sinh\left(n-\frac{1}{2}\right)\beta + C_n \cosh\left(n+\frac{3}{2}\right)\beta + D_n \sinh\left(n+\frac{3}{2}\right)\beta = -kV_t\left[(2n+3)e^{\left(n-\frac{1}{2}\right)\beta} - (2n-1)e^{\left(n+\frac{3}{2}\right)\beta}\right] \tag{6.20}$$

$$(2n-1)\left[A_n \sinh\left(n-\frac{1}{2}\right)\beta + B_n \cosh\left(n-\frac{1}{2}\right)\beta\right] + (2n+3)\left[C_n \sinh\left(n+\frac{3}{2}\right)\beta + D_n \cosh\left(n+\frac{3}{2}\right)\beta\right] = -kV_t(2n-1)(2n+3)\left[e^{\left(n-\frac{1}{2}\right)\beta} - e^{\left(n+\frac{3}{2}\right)\beta}\right] \tag{6.21}$$

$$k = \frac{c^2 n(n+1)}{\sqrt{2}(2n-1)(2n+1)(2n+3)} \tag{6.22}$$

Forces on the swimmer (F_s) and target particle (F_t) are determined by integrating the stress tensor over the surface of the spheres which, as shown by [16], results in

$$F_s = -\kappa \frac{2\pi\sqrt{2}}{c}\sum_{n=1}^{\infty}(2n+1)(A_n + B_n + C_n + D_n) \tag{6.23}$$

$$F_t = -\kappa \frac{2\pi\sqrt{2}}{c}\sum_{n=1}^{\infty}(2n+1)(A_n - B_n + C_n - D_n). \tag{6.24}$$

where κ is the viscosity of the fluid.

Coefficients $A_n, B_n, C_n,$ and D_n are linear in the velocities V_s and V_t in equations

6.18-6.22. Therefore, we can find a 2×2 resistance matrix ($\boldsymbol{R}$) that relates forces on the swimmer and target spheres to their velocities, $[F_s; F_t] = \boldsymbol{R}[V_s; V_t]$. Note that for given sphere sizes, the resistance matrix $\boldsymbol{R}$ depends on the separation of spheres and must be recalculated at each time during their approach. We are interested in the approach dynamics when the swimmer is pushed by a constant propulsion force ($F_s = -F$) towards the target, and the target has zero force ($F_t = 0$). Inverting $\boldsymbol{R}$, we use these to solve for the sphere velocities at each time step, and integrate to find sphere trajectories assuming an initial separation d_0.

Coefficients $A_n, B_n, C_n,$ and D_n decay exponentially in α and β and the sums in equations 6.23 and 6.24 converge rapidly for large separations. However, as the separation decreases, more terms are required [18] to achieve accurate results. For our numerical evaluations, we continue to calculate terms until the last term is less than 10^{-15} of the sums for the forces.

The *no-collision paradox* indicates that it would take infinite time for the swimmer to physically contact the target particle in a viscous flow [20]. However, since organisms *can* get close enough to interact, rather than using a criterion of physical contact ($d = 0$), we arbitratrily choose a cut-off and deem a separation of a hundredth of the swimmer radius ($d = 0.01\, r_s$) as "close enough" approach. Physically, the idea is that at shorter distances (e.g., $0.01\, r_s \approx 10\, nm$ for a bacterium), non-hydrodynamic interactions such as electrostatic, van der Waals, or biochemical bonding will become important and take over to enable physiological interaction. Typical approach trajectories, separations, and velocities are shown in Figures 6.2a,b for the same size of the swimmer and target particle ($r = 1$). We set the initial separation of the swimmer and target spheres to be 10 times of

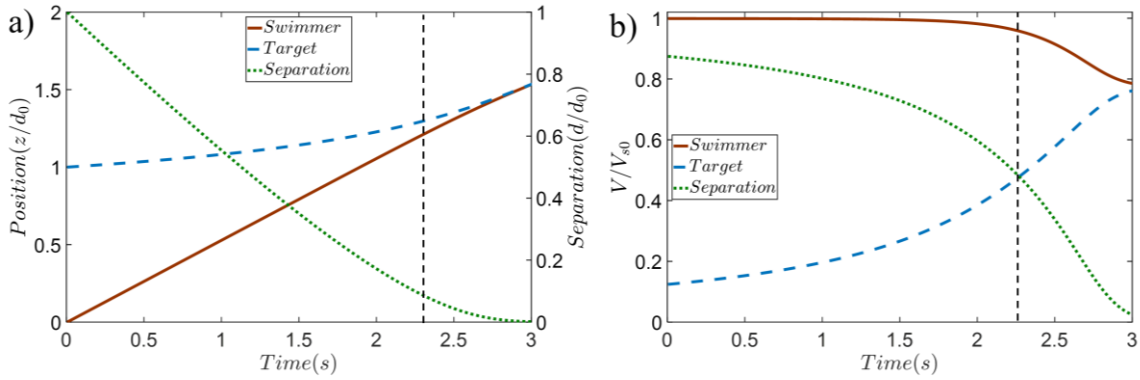

Figure 6.2. a) Typical trajectory and separation of the swimmer and target particle over time for $r_s/r_t = 1$. b) Velocities of the swimmer and target particle and the rate of change of the separation. The particle starts to move with small velocity. At the initial separation of $d_0 = 10r_s$, the target moves with small velocity, but when the separation is less than about the swimmer size (vertical dashed line), hydrodynamic interactions cause the target to move away from the swimmer, so the rate of change of separation decreases.

the swimmer radius for all calculations ($d_0 = 10r_s$). For large separations (i.e., at early times), the swimmer easily gets closer to the target particle at a rate corresponding to its interaction-free swimming speed $F/(6\pi\,\mu\,r_s)$ (given by the Stokes drag formula for a isolated sphere), but when the swimmer gets closer to the target, hydrodynamic interactions push the target away from the swimmer and the target velocity approaches the swimmer velocity as the separation decreases. Accordingly, the rate of decrease of the separation distance d also decreases. We can delineate a highly interacting regime when the approach velocity is less than half the initial value (dotted vertical line in Figure 6.2), which starts to occur at a separation distance of approximately the size of the swimmer.

To characterize the feasibility of approach, we measure the total distance ΔS necessary for the swimmer to travel before approaching within the cutoff separation ($d = 0.01r_s$). The results are shown in Figure 6.3b for different target:swimmer size ratios. For target particles of similar size or larger than the swimmer, the swimmer does not have to travel much more than the initial distance d_0 (for $r_t/r_s = 10, \Delta S = 1.04\,d_0$ and for

$r_t/r_s = 1, \Delta S = 1.53\ d_0$) since the target does not move much, and approach is feasible. On the other hand, for smaller targets, the target is pushed away by a significant amount and the swimmer has to travel farther (up to about 8 × the initial separation distance), so approach is infeasible.

These results suggest that swimmers using localized propulsion can directly approach similarly sized objects, which happens when mating or conjugation. In addition, such swimmers can approach much bigger particles, which happens when bacteria approach marine snow to find new environments, or sperm fertilize an egg. However, they may have trouble directly approaching or manipulating particles that are small compared to the swimmer size, which happens in feeding processes. If appendages are used to approach a target, those appendages should be of similar size or smaller than the target.

6.3.2 Numerical model for flagellated microswimmers – localized propulsion

The results of the previous section suggest how hydrodynamic interactions may place constraints on the ability of microorganisms to closely approach other particles. However, unlike real microswimmers, the swimmer model we used was not force- and torque-free. In this section, we numerically examine the approach of a singly-flagellated force- and torque-free microswimmer toward a suspended target particle to confirm that the physical conclusions from the simple model remain valid.

We model hydrodynamic contributions of the spherical cell body and target particle by the boundary element method (BEM) [22], [23], and model hydrodynamic contributions of the slender flagellum by slender body theory (SBT) [24]. We assume a rigid helical flagellar filament with filament radius a_f, helical radius R_f, and helical pitch P_f (numerical

values in Table 6.1), oriented in z-direction. The centerline of the flagellar filament is a helix with a taper such that it smoothly attaches to the hook [23], [25] given by

$$\boldsymbol{r_c}(s) = R_f\left(1 - e^{-\left(2\pi s/P_f\right)^2}\right)\left[\cos\left(2\pi s/P_f\right)\hat{\boldsymbol{x}} + \sin\left(2\pi s/P_f\right)\hat{\boldsymbol{y}}\right] + s\hat{\boldsymbol{z}} \tag{6.25}$$

The Stokes flow field external to the surface of the cell body, target particle, and flagellar filament is expressed in integral form by

$$\begin{aligned}\boldsymbol{u}(\boldsymbol{x}) = &\sum_{m=\{c,t\}}\int_{A_m}\boldsymbol{S}(\boldsymbol{x}-\boldsymbol{x}')\cdot\boldsymbol{q}(\boldsymbol{x}')\,dA_m(\boldsymbol{x}') \\ &-\sum_{m=\{c,t\}}\int_{A_m}\boldsymbol{H}(\boldsymbol{x}-\boldsymbol{x}')\cdot\boldsymbol{u}(\boldsymbol{x}')\,dA_m(\boldsymbol{x}') \\ &+\int_{C_f}\left[\boldsymbol{S}(\boldsymbol{x}-\boldsymbol{x}')\boldsymbol{f}_f - a_f^2\boldsymbol{D}(\boldsymbol{x}-\boldsymbol{x}')(\boldsymbol{I}-\boldsymbol{tt})\cdot\boldsymbol{f}_f\right]dx'\end{aligned} \tag{6.26}$$

Indices $c, t,$ and f stand for the cell body, target sphere, and flagellar filament, respectively. The first two terms on the RHS of equation 6.26 are BEM contributions to the velocity from the surfaces of the cell body A_c) and target (A_t) spheres, where $\boldsymbol{u}$ and $\boldsymbol{q}$\$ are the velocity field and traction force of the flow, respectively, $\boldsymbol{S}(\boldsymbol{x}-\boldsymbol{x}') = \frac{1}{8\pi\kappa}\left(\frac{\boldsymbol{I}}{|\boldsymbol{x}-\boldsymbol{x}'|}+\frac{(\boldsymbol{x}-\boldsymbol{x}')(\boldsymbol{x}-\boldsymbol{x}')}{|\boldsymbol{x}-\boldsymbol{x}'|^3}\right)$ is the Oseen tensor for a Stokeslet flow, and $\boldsymbol{H}(\boldsymbol{x}-\boldsymbol{x}') = \frac{-3}{8\pi\kappa}\frac{(\boldsymbol{x}-\boldsymbol{x}')(\boldsymbol{x}-\boldsymbol{x}')}{|\boldsymbol{x}-\boldsymbol{x}'|^5}(\boldsymbol{x}-\boldsymbol{x}')\cdot\boldsymbol{n}$ is its associated traction field for a surface with unit outward normal $\boldsymbol{n}$. $\boldsymbol{I}$ is the identity matrix. The last term on the RHS of equation 6.26 is the SBT contribution to the flow coming from the centerline of the flagellar filament C_f with filament radius a_f, where $\boldsymbol{D}$ is the Stokeslet dipole, $\boldsymbol{f}_f$ is the force distribution on C_f, and $(\boldsymbol{I}-\boldsymbol{tt})\cdot\boldsymbol{f}_f$is the component of the force perpendicular to the tangent of the centerline $\boldsymbol{t}$.

Table 6.1. Dimensions of the flagellar lament used for numerical simulations [30]

Flagellar $P_f(\mu m)$	Filament radius $a_f(\mu m)$	Helix radius $R_f(\mu m)$	Axial length $L_f(\mu m)$
1.58	0.035	0.14	2.97

The total forces $\boldsymbol{F}_m$ and torques $\boldsymbol{T}_m$ on the cell body and target sphere ($m = \{c, t\}$), and the total force $\boldsymbol{F}_f$ and torque $\boldsymbol{T}_f$ on the flagellar filament, are

$$\boldsymbol{F}_m = \int_{A_m} \boldsymbol{q}(\boldsymbol{x})\, dA_m, \quad \boldsymbol{T}_m = \int_{A_m} (\boldsymbol{x} - \boldsymbol{x}_m) \times \boldsymbol{q}(\boldsymbol{x})\, dA_m, \quad m \in (c, t) \tag{6.27}$$

$$\boldsymbol{F}_f = \int_{C_f} \boldsymbol{f}_f(\boldsymbol{x})\, dx', \qquad \boldsymbol{T}_f = \int_{C_f} (\boldsymbol{x} - \boldsymbol{x}_c) \times \boldsymbol{f}_f(\boldsymbol{x})\, dx',. \tag{6.28}$$

The boundary conditions are given by

$$\boldsymbol{u}(\boldsymbol{x}) = \boldsymbol{V}_m + \boldsymbol{\Omega}_m \times (\boldsymbol{x} - \boldsymbol{x}_m), \qquad \forall \boldsymbol{x} \in A_m, m \in (c, t) \tag{6.29}$$

$$\boldsymbol{u}(\boldsymbol{x}) = \boldsymbol{V}_c + \left(\boldsymbol{\Omega}_c + \boldsymbol{\omega}_f\right) \times (\boldsymbol{x} - \boldsymbol{x}_c), \quad \forall \boldsymbol{x} \in C_f. \tag{6.30}$$

where $\boldsymbol{V}_m$ and $\boldsymbol{\Omega}_m$ are the translational and rotational velocities of the cell body or target sphere identified by index m, $\boldsymbol{\omega}_f$ is the relative rotational velocities of the flagellar filament with respect to the cell body, and $\boldsymbol{x}_m$ are the centers of the cell body or target sphere.

To evaluate the first two terms of the RHS of 6.3.15, we discretize the surface of the cell body and target sphere into M_c andM_t, respectively, distinct triangular surface elements. Assuming a constant traction $\boldsymbol{q}$ or velocity $\boldsymbol{u}$ on each element, the integrals in 6.315 are numerically evaluated using 27 Gaussian quadrature points [26] for nonsingular elements. We use an analytical approach to remove the singularity in the integrand of 6.3.15 when points $\boldsymbol{x}$ and $\boldsymbol{x}'$ are on the same triangular element [27]. To evaluate the last term in equation 6.26, we discretize the slender flagellar filament into M_f straight rods of

length δs and assume constant force $\boldsymbol{f}_f$ over each segment [24]. For one segment, the result of the integral can be evaluated analytically (see equation 13 of [24]).

We evaluate equation 6.26 at collocation points at the centroid of areal elements or segments, so that there are a total of $M_c + M_t + M_f$ collocation points. The result is a $3(M_c + M_t + M_f)$ system of linear algebraic equations written in matrix form as

$$\begin{bmatrix} \boldsymbol{I_{cc}} + \boldsymbol{H_{cc}} & \boldsymbol{0_{cf}} & \boldsymbol{H_{ct}} \\ \boldsymbol{H_{fc}} & \boldsymbol{I_{ff}} & \boldsymbol{H_{ft}} \\ \boldsymbol{H_{tc}} & \boldsymbol{0_{tf}} & \boldsymbol{I_{tt}} + \boldsymbol{H_{tt}} \end{bmatrix} \begin{Bmatrix} \boldsymbol{u}_c \\ \boldsymbol{u}_f \\ \boldsymbol{u}_t \end{Bmatrix} = \begin{bmatrix} \boldsymbol{S_{cc}} & \boldsymbol{K_{cf}} & \boldsymbol{S_{ct}} \\ \boldsymbol{S_{fc}} & \boldsymbol{K_{ff}} & \boldsymbol{S_{ft}} \\ \boldsymbol{S_{tc}} & \boldsymbol{K_{tf}} & \boldsymbol{S_{tt}} \end{bmatrix} \begin{Bmatrix} \boldsymbol{f}_c \\ \boldsymbol{f}_f \\ \boldsymbol{f}_t \end{Bmatrix}. \tag{6.31}$$

where $\boldsymbol{I}, \boldsymbol{0}$ are identity and zero matrices. Here we use a compact notation such that (for example) $\boldsymbol{u}_c$ and $\boldsymbol{f}_c$ are $3M_c$-vectors containing all 3 components of the velocity or force at each of the M_c collocation points on the cell body. The matrices $\boldsymbol{S_{mn}}$ $(m = \{c, t, f\}, n = \{t, c\})$ are each a $M_m \times M_n$ block matrix of 3×3 submatrices where each submatrix comes from the evaluation of the integral $(1/A) \int_A \boldsymbol{S}(\boldsymbol{x} - \boldsymbol{x}')\, dA(\boldsymbol{x}')$ contributing to the velocity at a collocation point on sphere or filament m due to an element on sphere or filament n with area A. The matrices $\boldsymbol{H_{mn}}$ $(m = \{t, c, f\}, n = \{t, c\})$ are each a $M_m \times M_n$ block matrix of 3×3 submatrices, where each submatrix comes from the evaluation of the integral $(1/A) \int_A \boldsymbol{H}(\boldsymbol{x} - \boldsymbol{x}')\, dA(\boldsymbol{x}')$ contributing to the velocity at a collocation point on sphere or filament m due to an element on sphere n with area A. The matrices $\boldsymbol{K_{mf}}$ $(m = \{t, c, f\})$ are each a $M_m \times M_f$ block matrix of 3×3 submatrices, where each submatrix comes from the evaluation of the integral $(1/\delta s) \int_{\delta s} \boldsymbol{S}(\boldsymbol{x} - \boldsymbol{x}') - a_f^2 \boldsymbol{D}(\boldsymbol{x} - \boldsymbol{x}')(\boldsymbol{I} - \boldsymbol{tt})\, dA(\boldsymbol{x}')$ contributing to the velocity at a collocation point on sphere or filament m due to a segment of the filament n with length δs.

We consider a force-free swimmer with prescribed relative rotation rate for the

flagellum ($\boldsymbol{\omega}_f$) approaching a force-free target sphere. Thus, the force and torque conditions of the swimmer and target particle are

$$\boldsymbol{F}_c + \boldsymbol{F}_f = \boldsymbol{0}, \quad \boldsymbol{T}_c + \boldsymbol{T}_f = \boldsymbol{0}, \quad \boldsymbol{F}_t = \boldsymbol{0}, \quad \boldsymbol{T}_t = \boldsymbol{0}. \tag{6.32}$$

The velocity boundary conditions 6.3.17 and force conditions 6.319 can also be written in matrix form [28],

$$\begin{Bmatrix} \boldsymbol{u}_c \\ \boldsymbol{u}_f \\ \boldsymbol{u}_t \end{Bmatrix} = \boldsymbol{L} \begin{Bmatrix} \boldsymbol{V}_c \\ \boldsymbol{\Omega}_f \\ \boldsymbol{V}_t \\ \boldsymbol{\Omega}_t \end{Bmatrix} + \begin{Bmatrix} \boldsymbol{0} \\ \boldsymbol{\omega}_f \times (\boldsymbol{x} - \boldsymbol{x_c}) \\ \boldsymbol{0} \end{Bmatrix}. \tag{6.33}$$

$$\begin{Bmatrix} \boldsymbol{F}_c \\ \boldsymbol{T}_c \\ \boldsymbol{F}_t \\ \boldsymbol{T}_c \end{Bmatrix} = \boldsymbol{L}^T \begin{Bmatrix} \boldsymbol{f}_c \\ \boldsymbol{f}_f \\ \boldsymbol{f}_t \end{Bmatrix} \quad . \tag{6.34}$$

where $\boldsymbol{L}$ is a $6 \times 3(M_c + M_f + M_t)$ matrix as described in [28] which allows us to represent the velocity at the collocation points on the surfaces in terms of the translational and rotational velocities. In the last term, $\boldsymbol{\omega}_f \times (\boldsymbol{x} - \boldsymbol{x_c})$ is the prescribed rotation of collocation points on the flagellum.

The force and torque conditions (6.3.19) give 12 equations to be solved for 12 unknown components of the translational and rotational velocities $\boldsymbol{V}_c, \boldsymbol{\Omega}_c, \boldsymbol{V}_t, \boldsymbol{\Omega}_t$ in equations 6.34. To allow direct comparison with the analytical model, at each time step the prescribed rotation rate is adjusted so that the magnitude of $\boldsymbol{F}_f$ is equal to the propulsion force F in 6.3. Integrating these velocities using a fourth-order Runge-Kutta method yields trajectories of the swimmer and target particle.

The accuracy of the SBT depends on the slenderness parameter and total number of segments on the flagellar filament as described in [28], [29]. We discretize the flagellar filament into 140 segments with slenderness parameter $\delta s/a_f = 10$. In addition, we use

adaptive discretization for the surface of the cell body and target particle to accurately capture hydrodynamic interactions when spheres are close or the size ratio is small (Figure 6.3a). For separations $d/r_s > 0.5$, the surface of the swimmer and target sphere is divided into 284 nearly equal-size triangles. When $\frac{d}{r_s} \leq 0.5$, the elements near the contact region are refined to smaller triangular elements such that the gap distance is always 5 times greater than the smallest element on the surfaces as shown in Figure 6.3a. The maximum number of surface elements on each sphere used in this study is 3521 for the minimum separation of $d/r_s = 0.01$.

To validate our numerical method, we compare numerical results for a sphere pushed by an external force *without a flagellum* towards a target sphere with the analytical solutions from section 6.31 (Figure 6.3b). We find 1% average errors for the numerics relative to the exact solutions. The error is less than 2% for the size ratios bigger than 0.01, while it is about 7% for the smallest size ratio of 0.001.

We compare the travel distance needed for the swimmer to approach within the cutoff distance $d = 0.01\, r_s$ of the target particle for the single-flagellated swimmer and constant force case in Figure 6.3b. The comparison shows that both cases have qualitatively the same trend – for small target spheres, a swimmer must move very far to catch the target particle, but for similar size or larger targets, the swimmer does not need to move much farther than the initial separation distance. Quantitatively speaking, the difference between these two cases is an approximately constant factor of 10-15% in traveled distance for the swimmer. Thus, for the purposes of approach, one can model a flagellated swimmer with localized propulsion as a body pushed by constant force.

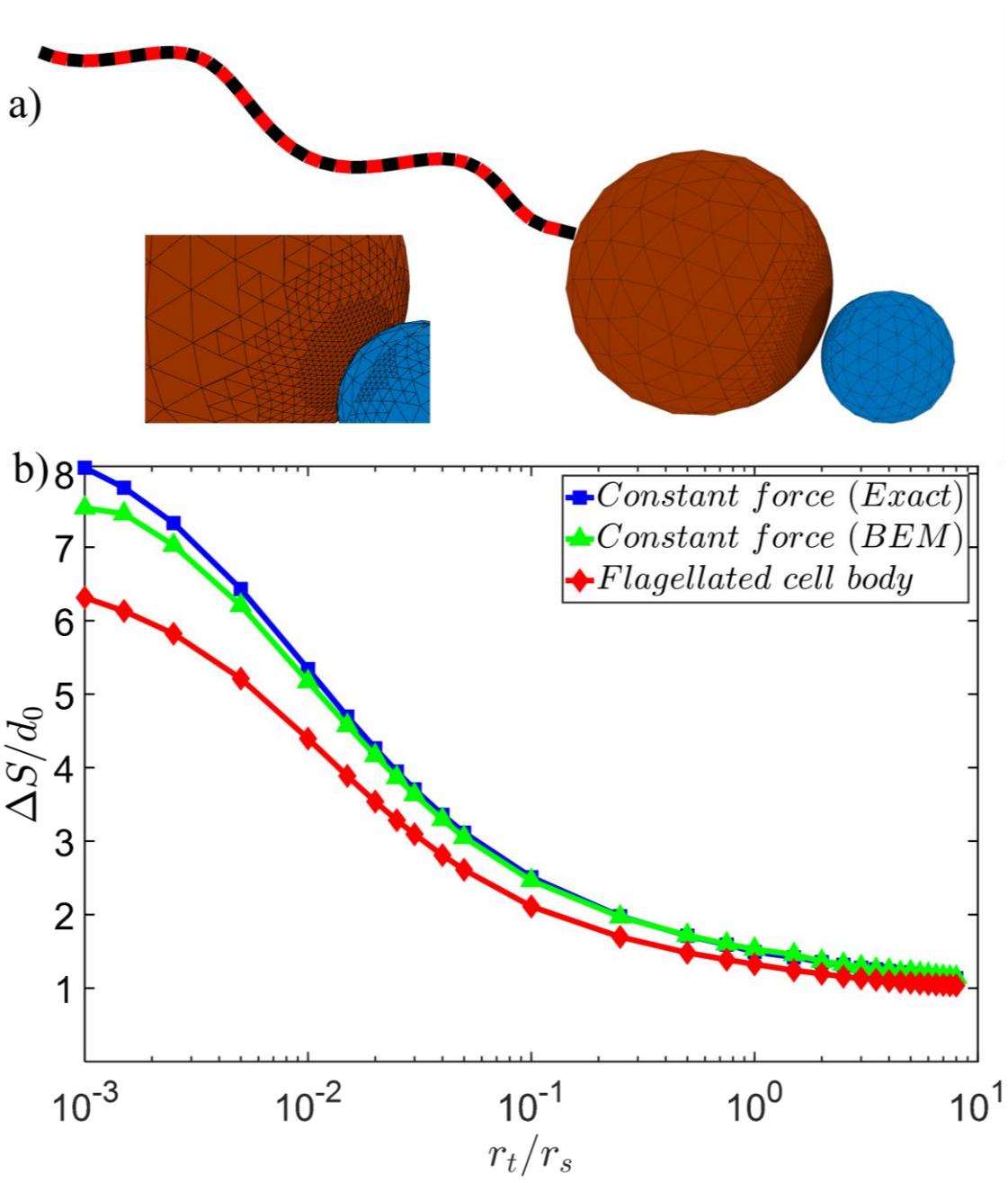

Figure 6.3. a) Adaptive discretization of the swimmer cell body and target particle with surface triangular elements used for boundary element method (BEM), and discretization for the swimmer flagellum used for slender body theory (SBT). b) Total traveled distance ΔS required for the swimmer to approach within $0.01r_s$ of the target after starting from initial separation of $10r_s$, as a function of target:swimmer size ratios. Analytical solution (blue diamonds) for two spheres (as in section 6.3.1) validates numerical results for the same situation obtained by BEM (green triangles). BEM results for the single-flagellated model (red squares) are qualitatively similar to the constant force case.

6.4. Approach with distributed propulsion

The previous results model microorganisms that swim using localized propulsion methods, such as a single flagellum, and suggest that approach towards smaller target particles such as prey is infeasible. However, many zooplankton use distributed propulsion generated by numerous appendages or cilia, and these organisms have been observed to feed by capturing prey using feeding currents. For instance, paramecia use beating cilia to capture food particles and transport these particles to their mouths [31]. This suggests that the use of distributed flow sources such as cilia provide a way for microorganisms to evade the viscous constraint on direct approach seen for localized thrust. Thus, we next investigate the approach towards target particles by microoganisms propelled by cilia, which might be viewed as the limit of maximally distributed propulsion.

6.4.1 Analytical model for approaching spheres – distributed propulsion

The swimmer and target particle are assumed to be spheres, but to model the ciliated microorganisms, we use a *squirmer model* in which cilia are replaced by a progressive waving envelope. The velocity boundary condition on the surface of the sphere can be defined by an infinite series of Legendre functions [32], but here we employ simplified boundary conditions, used by many researchers (e.g., [19], [33]) that neglect radial displacement of the boundary and consider only two modes in the tangential velocity of the boundary of the squirmer sphere. In spherical coordinates (when the origin of the coordinate system is in the center of the sphere) the tangential velocity at the surface is

$$\boldsymbol{u}_\theta = B_1 \sin\theta + B_2 \sin(2\theta)\,/2. \tag{6.35}$$

while u_r and u_ϕ are both zero. The parameters B_1 and B_2 determine the properties of the

swimmer. The parameter B_1 determines the swimming velocity of the isolated squirmer given by $U = 2B_1/3$. The second parameter B_2 is associated with the stresslet around the swimmer [19], [34]. The squirmer parameter $\gamma = B_1/B_2$ determines whether the swimmer is a pusher ($\gamma < 0$) or puller ($\gamma > 0$). The flow field around isolated squirmers are plotted in Figure 6.4 for the pusher and puller types.

We assume that a spherical squirmer with radius r_s is approaching a spherical target particle with radius r_t as shown in Figure 6.5. Including translational swimming speed U in the z-direction, velocity boundary conditions for a symmetric spherical squirmer mode in the lab frame are [32],

$$u_r = U\cos\theta, \tag{6.36}$$

$$u_\theta = (-U + B_1)\sin\theta + B_2\sin(2\theta)\,/2. \tag{6.37}$$

where θ is the angle between the swimming direction z and any point on the surface of the sphere in the coordinate system with origin at the squirmer center (Figure 6.5). These equations can be expressed in a cylindrical coordinate system,

$$u_z = u_r\cos\theta - u_\theta\sin\theta, \tag{6.38}$$

$$u_\rho = u_r\sin\theta + u_\theta\cos(\theta). \tag{6.39}$$

where $\cos\theta = (z - d_s)/r_s$, $\sin\theta = \rho/r_s$, and d_s is distance of the center of the swimmer sphere from the origin of the cylindrical coordinate system.

We solve this problem in the bispherical coordinate system using the same stream function approach as in section 6.3.1. Now the coefficients $A_n, B_n, C_n,$ and D_n in 6.5 are determined by the new boundary conditions described in equations 6.38 and 6.39. The boundary condition on the swimmer can be expressed in terms of the Stokes stream function in bispherical coordinate using equations 6.36 - 6.39 as:

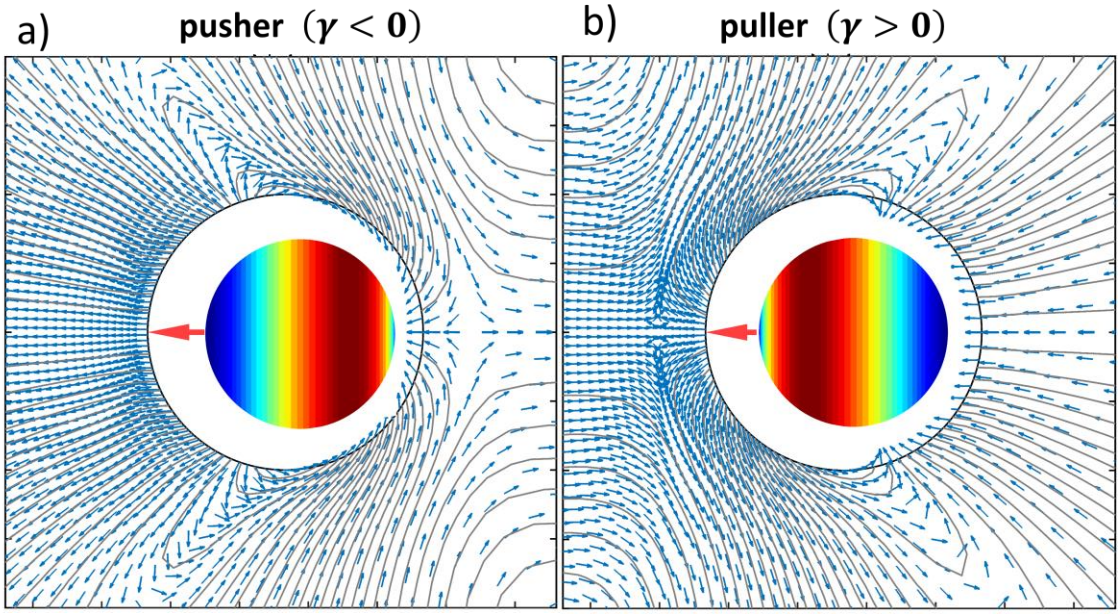

Figure 6.4. The flow field around and streamlines for different types of spherical squirmers. a) Pushers ($\gamma < 0$) push the flow in the swimming direction during their motions. b) Pullers ($\gamma > 0$) generate flow toward their body against their swimming direction. The color on the spherical surface shows the tangential velocity component u_θ (equation 6.35) of the surface boundary condition.

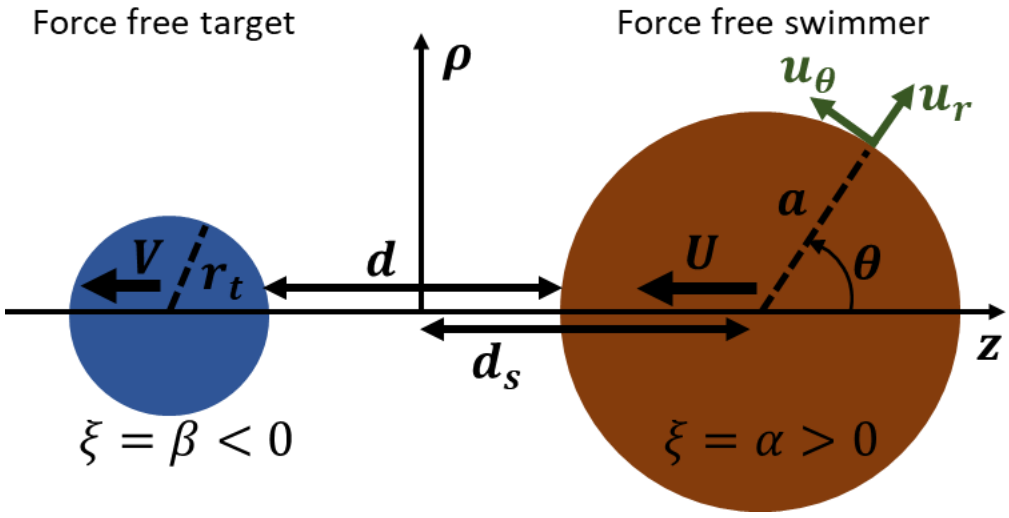

Figure 6.5. The force-free spherical swimmer "squirmer model" (right sphere) with radius r_s approaching a force-free spherical target (left sphere) with radius r_t. For the target sphere, no-slip boundary conditions are imposed. For the squirmer sphere, tangential velocity u_θ is imposed and $u_r = 0$.

$$\frac{\partial \psi}{\partial \xi} = -u_\theta \frac{\rho z r_s}{c}, \qquad \frac{\partial \psi}{\partial \eta} = -u_r \frac{\rho z r_s}{c} \tag{6.40}$$

We can also use equations 6.40 to obtain derivatives of the stream function.

$$\frac{\partial \psi}{\partial \xi} = \left[-\frac{3}{2}\sinh(\xi)\, X + (\cosh(\xi) - \mu)\frac{\partial X}{\partial \xi}\right](\cosh(\xi) - \mu)^{-\frac{5}{2}},$$

$$\frac{\partial \psi}{\partial \eta} = \left[-\frac{3}{2} X - (\cosh(\xi) - \mu)\frac{\partial X}{\partial \mu}\right]\frac{\rho}{c}(\cosh(\xi) - \mu)^{-\frac{3}{2}}. \tag{6.41}$$

Combining equations 6.40, 6.41, and applying the recurrence relations for Legendre functions,

$$(2n+1)\mu P_n(\mu) = (n+1)P_{n+1}(\mu) - nP_{n-1}(\mu), \tag{6.42}$$

$$\mu V_n(\mu) = \frac{n-1}{2n-1} V_{n-1}(\mu) + \frac{n+2}{2n+3} V_{n+1}(\mu). \tag{6.43}$$

we have

$$\begin{aligned} &\sum_{n=1}^{\infty}\left[\frac{3}{2}\sinh(\xi)\, U_n - \cosh(\xi)\, U_n' + \frac{n}{2n+1} U_{n+1}' + \frac{n+1}{2n+1} U_{n-1}'\right] V_n(\mu) \\ &\qquad = \left[-U + B_1 + B_2\left(\frac{\mu\cosh(\xi) - 1}{\cosh(\xi) - \mu}\right)\right]\frac{c^2 \sinh(\xi)\,(1-\mu^2)}{(\cosh(\xi) - \mu)^{\frac{1}{2}}}, \end{aligned} \tag{6.44}$$

$$\begin{aligned} &\sum_{n=1}^{\infty}\left[\left(n + \frac{5}{2}\right) U_{n+1} + \left(n - \frac{3}{2}\right) U_{n-1} - \cosh(\xi)\,(2n+1) U_n\right] P_n(\mu) \\ &\qquad = U\left(\frac{\mu\cosh(\xi) - 1}{\cosh(\xi) - \mu}\right) c^2 (\cosh(\xi) - \mu)^{\frac{1}{2}}. \end{aligned} \tag{6.45}$$

To solve this, we perform Taylor-Legendre expansions on the RHS of 6.44 and 6.45 as

$$\sum_{n=1}^{\infty} E_n(\xi)\, V_n(\mu) \equiv \left[-U + B_1 + B_2\left(\frac{\mu\cosh(\xi) - 1}{\cosh(\xi) - \mu}\right)\right]\frac{c^2 \sinh(\xi)\,(1-\mu^2)}{(\cosh(\xi) - \mu)^{\frac{1}{2}}}, \tag{6.46}$$

$$\sum_{n=0}^{\infty} F_n(\xi)\, P_n(\mu) = U\left(\frac{\mu\cosh(\xi)-1}{\cosh(\xi)-\mu}\right) c^2(\cosh(\xi)-\mu)^{\frac{1}{2}}. \tag{6.47}$$

In a Taylor-Legendre expansion, any piecewise smooth function $f(x)$ on $[-1,1]$ can be expressed as a series in $P_n(\xi)$ and $V_n(\xi)$

$$f(x) = \sum_{n=1}^{\infty} a_n\, P_n(x), \tag{6.48}$$

with a_n determined by

$$a_n = \frac{2n+1}{2}\int_{-1}^{1} f(x)\, P_n(x)\, dx. \tag{6.49}$$

Thus, to find E_n and F_n, we must evaluate equation 6.49 using the following relations

$$\int_{-1}^{1} \frac{V_n\, d\mu}{(\cosh(\xi)-\mu)^{\frac{1}{2}}} = 2\sqrt{2}\left[\frac{e^{\mp\left(n-\frac{1}{2}\right)\xi}}{2n-1} - \frac{e^{\mp\left(n+\frac{3}{2}\right)\xi}}{2n+3}\right], \tag{6.50}$$

$$xf(x) = \sum_{n=0}^{\infty}\left[\frac{n}{2n-1}a_{n-1} + \frac{n+1}{2n+3}a_{n+1}\right]P_n(x), \tag{6.51}$$

$$(1-x^2)f(x) = \sum_{n=0}^{\infty}\frac{n(n+1)}{2n+1}\left[\frac{a_{n-1}}{2n-1} + \frac{a_{n+1}}{2n+3}\right]V_n(x), \tag{6.52}$$

$$\begin{aligned} x(1-x^2)f(x) &= \sum_{n=0}^{\infty}\frac{n(n+1)}{2n+1}\left[\frac{(n-1)a_{n-1}}{(2n-1)(2n-3)} + \frac{a_{n+1}}{(2n-1)(2n+3)}\right. \\ &\left. - \frac{(n+2)a_{n+2}}{(2n+5)(2n+3)}\right]V_n(x), \end{aligned} \tag{6.53}$$

$$(1-x^2)P_n(x) = \frac{(n+1)(n+2)}{(2n+1)(2n+3)}V_{n+1} - \frac{n(n-1)}{(2n+1)(2n-1)}V_{n-1}. \tag{6.54}$$

We find E_n and F_n as,

$$F_n(\xi) = \sqrt{2}c^2\left(\cosh\xi\left[\frac{2}{2n-1}e^{-\left(n-\frac{1}{2}\right)\xi} + \frac{n+1}{2n+3}e^{-\left(n+\frac{3}{2}\right)\xi}\right] - e^{-\left(n+\frac{1}{2}\right)\xi}\right), \tag{6.55}$$

$$E_n(\xi) = -\sqrt{2}c^2(U-B_1)\sinh\xi\,\frac{n(n+1)}{2n+1}\left[\frac{e^{-\left(n-\frac{1}{2}\right)\xi}}{2n-1} - \frac{e^{-\left(n+\frac{3}{2}\right)\xi}}{2n+3}\right]$$

$$+\sqrt{2}c^2B_2\,\frac{n(n+1)}{2n+1}\left[\cosh\xi\left(\frac{e^{-\left(n-\frac{3}{2}\right)\xi}}{2n-1} - \frac{(2n+1)e^{-\left(n+\frac{1}{2}\right)\xi}}{(2n+3)(2n+5)}\right.\right. \tag{6.56}$$

$$\left.\left. - \frac{e^{-\left(n-\frac{5}{2}\right)\xi}}{2n+5}\right) - \left(e^{-\left(n-\frac{1}{2}\right)\xi} - e^{-\left(n+\frac{3}{2}\right)\xi}\right)\right].$$

Equations 6.48 and 6.49 then yield recurrence relations for U_n and U_n',

$$\frac{3}{2}\sinh(\xi)\,U_n - \cosh(\xi)\,U_n' + \frac{n}{2n+1}U_{n+1}' + \frac{n+1}{2n+1}U_{n-1}' = E_n(\xi)\,, \tag{6.57}$$

$$\left(n+\frac{5}{2}\right)U_{n+1} + \left(n-\frac{3}{2}\right)U_{n-1} - \cosh(\xi)\,(2n+1)U_n = F_n(\xi). \tag{6.58}$$

We calculate $U_n(\xi)$ and $U_n'(\xi)$ from 6.57 and 6.58, and after some simplification, can write

$$U_n = -kU\left[(2n+3)e^{-\left(n-\frac{1}{2}\right)\alpha} - (2n-1)e^{-\left(n+\frac{3}{2}\right)\alpha}\right], \tag{6.59}$$

$$U_n' = U\,H_n(\alpha) + G_n(\alpha). \tag{6.60}$$

where the expressions $H_n(\alpha)$ and $G_n(\alpha)$ can be found from recurrence relation 6.57 but are not illuminating to write down explicity.

Therefore, equations 6.20 and 6.21 that determine the coefficients A_n, B_n, C_n, D_n are altered, with equation 6.19 and 6.20 replaced by

$$A_n \cosh\left(n-\frac{1}{2}\right)\alpha + B_n \sinh\left(n-\frac{1}{2}\right)\alpha + C_n \cosh\left(n+\frac{3}{2}\right)\alpha + D_n \sinh\left(n+\frac{3}{2}\right)\alpha = -kU\left[(2n+3)e^{\left(n-\frac{1}{2}\right)\alpha} - (2n-1)e^{\left(n+\frac{3}{2}\right)\alpha}\right] \quad (6.61)$$

$$(2n-1)\left[A_n \sinh\left(n-\frac{1}{2}\right)\alpha + B_n \cosh\left(n-\frac{1}{2}\right)\alpha\right] + (2n+3)\left[C_n \sinh\left(n+\frac{3}{2}\right)\alpha + D_n \cosh\left(n+\frac{3}{2}\right)\alpha\right] = H_n(\alpha) + G_n(\alpha) \quad (6.62)$$

while equations 6.20 and 6.21 remain unaltered. Equations 6.61 and 6.62 describe the motion of the squirmer with translational swimming speed U, while equations 6.20 and 6.21 describe the motion of the target sphere with no-slip boundary conditions on the surface translating with velocity V_t. As before, the force (F_s) on the swimmer ($\xi = \alpha > 0$) and force (F_t) on the target sphere can be calculated by equations 6.23 and 6.24.

Given sphere radii r_s and r_t and their separation d, the quantities c, α, and β in the bispherical coordinate system are obtained using equations 6.8-6.10. Specification of the problem is completed by the squirmer mode strengths B_1 andB_2. So that we can compare results with the scenario in which the swimmer sphere pushed by a constant force *F* (section 6.3), we choose the mode strengths such that the power of the isolated squirmer ($P = 8\pi\ \kappa\ r_s\ B_1^2(1 + \gamma\text{^}2/3)$ [32]) is the same as the power required to push the isolated sphere by the constant force ($P = F^2/(6\pi\ \kappa\ r_s)$). Thus for a given *squirmer parameter* ($\gamma = B_1/B_2$), we find $B_1 = \frac{F}{12\pi\kappa r_s}\frac{1}{\sqrt{3+\gamma^2}}$. The swimmer and target sphere are both assumed to be force free ($F_s = 0$ and $F_t = 0$).

Equations 6.61 and 6.62 are linear in the translational velocities U and V and parameters B_1 and B_2 for the swimmer and target sphere. Therefore, we can relate the forces to the velocities and parameters via

$$\begin{bmatrix} F_s \\ F_t \end{bmatrix} = \boldsymbol{R} \begin{bmatrix} U \\ V_t \end{bmatrix} + \boldsymbol{B} \begin{bmatrix} B_1 \\ B_2 \end{bmatrix}. \tag{6.63}$$

where $\boldsymbol{R}$ and $\boldsymbol{B}$ are 2×2 matrices that depend on the separation d between spheres (in addition to the sphere sizes). For given mode strengths B_1 and B_2, we solve equation 6.63 under the force-free conditions to obtain the translational velocities U and V_t, then integrate them to find the trajectories of the spheres starting from an initial separation d_0.

In Figure 6.6, we plot the total distance (ΔS) that the swimmer needs to travel before approach to within $0.01r_s$ of the target particle starting from an initial separation of $10r_s$. For comparison, we include the results for the swimmer sphere pushed by constant force from Figure 6.3b. The results show that for pullers ($\gamma > 0$), the swimmer must travel at most 1.18 (for $r_t/r_s = 0.001, \gamma = 0$) times the initial separation, and often less than the initial separation for larger γ. Therefore, approach by pullers to target particles is feasible no matter the target size. Pushers with $-0.5 \leq \gamma < 0$ show similar behavior. However, pushers with $\gamma \leq -1$ must travel more than three times the initial separation distance, with stronger pushers traveling larger distances to approach the target closely. Therefore, in the context of approach, the behavior of pusher-type squirmers depends on the strength of the squirmer parameter. Weak pushers ($0 > \gamma > -1$) can approach any size target particles, while stronger pusher-type squirmers ($\gamma < -1$) can have difficulty approaching smaller target particles. In fact, as shown in Figure 6.6b, for strong enough pushers, ($\gamma < -2$), the minimum approach distance d_{min} remains larger than the cutoff $d = 0.01\, r_s$ even for targets that are larger than the swimmer; hence approach is infeasible for strong pushers.

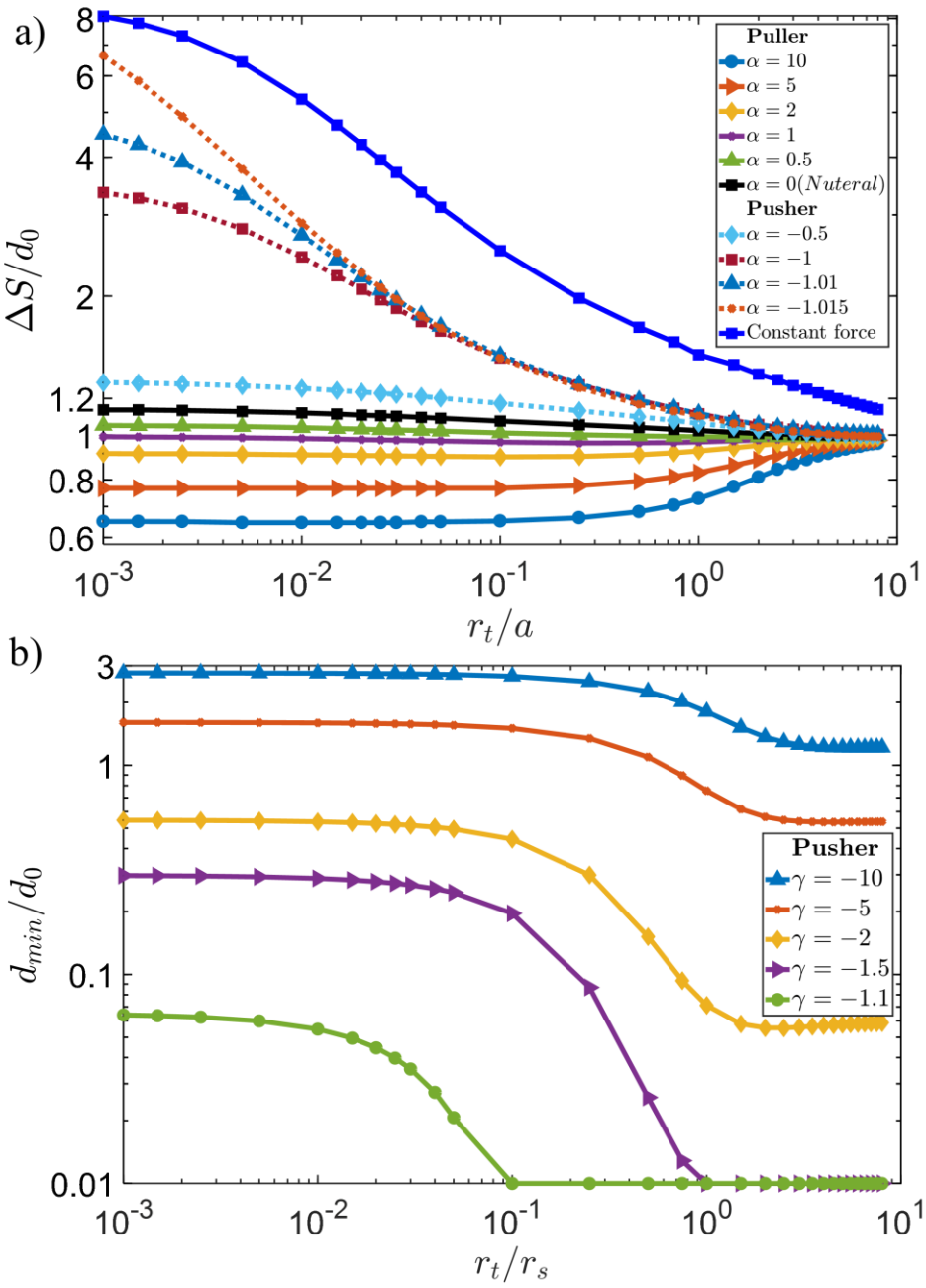

Figure 6.6. Approach to a target by a squirmer with distributed propulsions. Total traveled distance ΔS required for the squirmer to approach within $0.01r_s$ of the target after starting from initial separation $d_0 = 10r_s$, as a function of target:swimmer size ratio r_t/r_s. For comparison, results for the flagellated swimmer are plotted as dark blue diamonds. a) Pusher-type squirmers ($\gamma < 0$) can approach smaller target particles only when if the currents that move away from the swimmer (Figure 6.7a) are weak ($\gamma > -1$). Puller-type squirmers ($\gamma > 0$) can feasibly approach any size targets due to currents that move toward the swimmer (Figure 6.7b). b) Minimum separation d_{min} between the pusher-type squirmer and target. For strong pushers ($\gamma < -1$), the squirmer cannot approach even large targets with $r_t/r_s > 1$.

These results for squirmers can be understood in terms of the flow fields generated while swimming. Pullers generate currents that advect particles in front of the swimmer inwards similar to *feeding currents*. A typical flow field around a puller and target particle is shown in Figure 6.7b. The strength of these currents is controlled by the squirmer parameter (γ) and total traveled distances are smaller for the strong currents produced by larger values of γ. On the other hand, pushers tend to generate currents that advect particles in front of the swimmer away from the swimmer, hindering approach. A typical flow field for a pusher with $\gamma = -1$ and a target particle is shown in Figure 6.7a. Whether or not the current overcomes the swimming translation of the squirmer depends on the magnitude of the (negative) squirmer parameter γ.

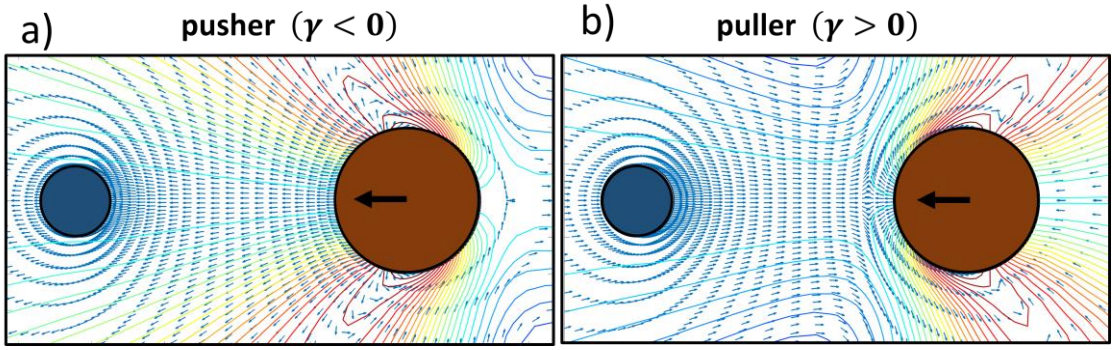

Figure 6.7. Typical flow fields around a squirmer interacting with a target sphere. a) A pusher ($\gamma < 0$) generates a current that move the target away from the swimmer, hindering the approach process, while b) a puller generates a current that moves the target toward the swimmer, helping the approach process. The strength of the current for both cases depends on the value of the squirmer parameter (γ).

6.5 Discussion

We have studied the approach of spheres to understand the viscous constraints on the approach of microorganisms to target particles. The swimmer starts at a separation of 10 swimmer radii ($d_0 = 10r_s$) from the target. As a metric, we calculated the total distance traveled by the swimmer until it approaches within a hundredth of the swimmer radius of the target ($d = 0.01r_s$). We use this finite cutoff since due to the no-collision paradox, in many situations, actual physical contact would require infinite time, and we expect that at small distances, non-continuum-hydrodynamic physics would take over to allow interaction between swimmer and target.

First, we modified the exact solution for two spheres with no-slip boundary conditions in bispherical coordinates obtained by [16] to investigate a "swimmer" sphere pushed by constant force towards a target sphere. We found that hydrodynamic constraints prevent the approach of swimmers to smaller target particles, but allow approach to similar- and larger-sized targets. Qualitatively similar results were obtained for a more realistic numerical model of a force-free spherical cell pushed by a rotating flagellum. The similarity between these results arises from the fact that in both cases, the propulsion is localized.

These hydrodynamic constraints on approach can be evaded by microorganisms using distributed modes of propulsion. To demonstrate this, we investigated the maximally distributed propulsion of squirmer-type swimmers. For a spherical squirmer approaching a spherical target, analytic results for approach can be obtained using bispherical coordinates. The results show that for these models, the feasibility of approach depends on the *squirmer parameter,* which determines the type and strength of the squirmer. We find that puller-

type squirmers generate feeding currents that pull particles towards the swimmer, and make approach to any size target particle feasible. On the other hand, strong-enough pusher-type squirmers can only approach similar- or larger-sized targets.

Our results are broadly consistent with biological observations. Feasibility of the direct approach for bigger or similar sizes of the target particles even for localized propulsion is demonstrated by bacterial conjugation, mating, and fertilization of an egg by sperm. On the other hand, direct approach to smaller prey particles by localized propulsion is difficult, and in these cases, microorganisms use other strategies to capturing small food particles. Our squirmer results indicate the importance of feeding currents for prey capture, and point out that feeding currents can be generated by propulsive strokes as well as via non-locomotory behavior. In addition to feeding currents, our results also shed light on the use of appendages or filters to manipulate or capture smaller target particles [8]. An appendage or filtration element could be viewed as an object pushed by an external force (exerted by the rest of the organism) towards a target; thus manipulation or filtration can be successful only if the appendage or filtration element is similar in size or smaller than the target particles.

Our models were limited to relatively simple spherical geometries and head-on approach. Future work could address issues arising from relaxing these conditions. Even though some organisms are quite close to spherical ciliated organisms [19], there are a wide variety of organisms with nonspherical ciliated geometries. For instance, *Opalina* and *Paramecium* are more likely to be ellipsoidal than spheres [1] and employing an ellipsoidal squirmer model can describe their behavior more appropriately [35]. Distributed propulsion is not isolated to ciliates. Organisms such as copepods can use multiple

appendages to generate propulsion as well as currents to pull and manipulate small particles [36]. Numerical analyses similar to ours could be suitable for studying approach and interactions with more complicated geometries or from different directions, including rotational motions [37]. Finally, understanding the hydrodynamics of near-contact interactions with swimmers is important for understanding the enhanced diffusion of particles in suspensions of active swimmers [38], which can depend on close approach.

6.6 References

[1] E. Lauga and T. R. Powers, "The hydrodynamics of swimming microorganisms," *Reports Prog. Phys.*, vol. 72, no. 9, p. 96601, 2009.

[2] R. M. Braga, M. N. Dourado, and W. L. Araújo, "Microbial interactions: ecology in a molecular perspective," *brazilian J. Microbiol.*, vol. 47, pp. 86–98, 2016.

[3] B. Hansen, P. K. Bjornsen, and P. J. Hansen, "The size ratio between planktonic predators and their prey," *Limnol. Oceanogr.*, vol. 39, no. 2, pp. 395–403, 1994.

[4] U. Sommer, E. Charalampous, S. Genitsaris, and M. Moustaka-Gouni, "Benefits, costs and taxonomic distribution of marine phytoplankton body size," *J. Plankton Res.*, vol. 39, no. 3, pp. 494–508, 2017.

[5] J. Johnke, J. Boenigk, H. Harms, and A. Chatzinotas, "Killing the killer: predation between protists and predatory bacteria," *FEMS Microbiol. Lett.*, vol. 364, no. 9, p. fnx089-fnx089, 2017.

[6] T. Kiørboe, "Fluid dynamic constraints on resource acquisition in small pelagic organisms," *Eur. Phys. J. Spec. Top.*, vol. 225, no. 4, pp. 669–683, 2016.

[7] T. Kiørboe, A. Andersen, V. J. Langlois, H. H. Jakobsen, and T. Bohr, "Mechanisms and feasibility of prey capture in ambush-feeding zooplankton," *Proc. Natl. Acad. Sci.*, vol. 106, no. 30, pp. 12394–12399, 2009.

[8] H. U. Riisgård and P. S. Larsen, "Particle capture mechanisms in suspension-feeding invertebrates," *Mar. Ecol. Prog. Ser.*, vol. 418, pp. 255–293, 2010.

[9] A. J. F. Griffiths, J. H. Miller, D. T. Suzuki, R. C. Lewontin, W. M. Gelbart, and others, "Transcription: an overview of gene regulation in eukaryotes," *An Introd. to Genet. Anal. 7th Ed. WH Free. Company, New York*, 2000.

[10] T. Kiørboe, “Mate finding, mating, and population dynamics in a planktonic copepod Oithona davisae: there are too few males,” *Limnol. Oceanogr.*, vol. 52, no. 4, pp. 1511–1522, 2007.

[11] J. R. Strickler, “Observing free-swimming copepods mating,” *Philos. Trans. R. Soc. London B Biol. Sci.*, vol. 353, no. 1369, pp. 671–680, 1998.

[12] R. D. Moreno, A. Laserre, C. Barros, and others, “Protease activity involvement in the passage of mammalian sperm through the zona pellucida,” *Biol. Res.*, vol. 44, no. 2, pp. 145–150, 2011.

[13] T. Kiørboe, K. Tang, H.-P. Grossart, and H. Ploug, “Dynamics of microbial communities on marine snow aggregates: colonization, growth, detachment, and grazing mortality of attached bacteria,” *Appl. Environ. Microbiol.*, vol. 69, no. 6, pp. 3036–3047, 2003.

[14] H. P. Grossart, T. Kiørboe, K. W. Tang, M. Allgaier, E. M. Yam, and H. Ploug, “Interactions between marine snow and heterotrophic bacteria: aggregate formation and microbial dynamics.,” *Aquat. Microb. Ecol.*, vol. 42, pp. 19–26, 2006.

[15] M. A. R. Koehl and J. R. Strickier, “Copepod feeding currents: food capture at low Reynolds number,” *Limnol. Oceanogr.*, vol. 26, no. 6, pp. 1062–1073, 1981.

[16] M. Stimson and G. B. Jeffery, “The motion of two spheres in a viscous fluid,” *Proc. R. Soc. London. Ser. A, Contain. Pap. a Math. Phys. Character*, vol. 111, no. 757, pp. 110–116, 1926.

[17] H. Brenner, “The slow motion of a sphere through a viscous fluid towards a plane surface,” *Chem. Eng. Sci.*, vol. 16, no. 3–4, pp. 242–251, 1961.

[18] R. G. Cox and H. Brenner, “The slow motion of a sphere through a viscous fluid towards a plane surface—II Small gap widths, including inertial effects,” *Chem. Eng. Sci.*, vol. 22, no. 12, pp. 1753–1777, 1967.

[19] T. Ishikawa, M. P. Simmonds, and T. J. Pedley, “Hydrodynamic interaction of two swimming model micro-organisms,” *J. Fluid Mech.*, vol. 568, pp. 119–160, 2006.

[20] M. Potomkin, V. Gyrya, I. Aranson, and L. Berlyand, “Collision of microswimmers in a viscous fluid,” *Phys. Rev. E*, vol. 87, no. 5, p. 53005, 2013.

[21] D. Papavassiliou and G. P. Alexander, “Exact solutions for hydrodynamic interactions of two squirming spheres,” *J. Fluid Mech.*, vol. 813, pp. 618–646, 2017.

[22] N. Phan-Thien, T. Tran-Cong, and M. Ramia, “A boundary-element analysis of flagellar propulsion,” *J. Fluid Mech.*, vol. 184, pp. 533–549, 1987.

[23] M. Ramia, D. L. Tullock, and N. Phan-Thien, “The role of hydrodynamic interaction in the locomotion of microorganisms,” *Biophys. J.*, vol. 65, no. 2, pp. 755–778, 1993.

[24] J. J. L. Higdon, “A hydrodynamic analysis of flagellar propulsion,” *J. Fluid Mech.*, vol. 90, no. 4, pp. 685–711, 1979.

[25] Y. Hyon, T. R. Powers, R. Stocker, H. C. Fu, and others, “The wiggling trajectories of bacteria,” *J. Fluid Mech.*, vol. 705, pp. 58–76, 2012.

[26] D. A. Dunavant, “High degree efficient symmetrical Gaussian quadrature rules for the triangle,” *Int. J. Numer. Methods Eng.*, vol. 21, no. 6, pp. 1129–1148, 1985.

[27] C. Pozrikidis, *A practical guide to boundary element methods with the software library BEMLIB*. CRC Press , 2002.

[28] J. D. Martindale, M. Jabbarzadeh, and H. C. Fu, “Choice of computational method for swimming and pumping with nonslender helical filaments at low Reynolds number,” *Phys. Fluids*, vol. 28, no. 2, p. 21901, 2016.

[29] M. Jabbarzadeh, Y. Hyon, and H. C. Fu, “Swimming fluctuations of micro-organisms due to heterogeneous microstructure,” *Phys. Rev. E*, vol. 90, no. 4, p. 43021, 2014.

[30] M. A. Constantino, M. Jabbarzadeh, H. C. Fu, and R. Bansil, “Helical and rod-shaped bacteria swim in helical trajectories with little additional propulsion from helical shape,” *Sci. Adv.*, vol. 2, no. 11, pp. e1601661–e1601661, 2016.

[31] A. C. Balazs, A. Bhattacharya, A. Tripathi, and H. Shum, “Designing bioinspired artificial cilia to regulate particle--surface interactions,” *J. Phys. Chem. Lett.*, vol. 5, no. 10, pp. 1691–1700, 2014.

[32] J. R. Blake, “A spherical envelope approach to ciliary propulsion,” *J. Fluid Mech.*, vol. 46, no. 1, pp. 199–208, 1971.

[33] J. J. Molina, Y. Nakayama, and R. Yamamoto, “Hydrodynamic interactions of self-propelled swimmers,” *Soft Matter*, vol. 9, no. 19, pp. 4923–4936, 2013.

[34] G. K. Batchelor, “The stress system in a suspension of force-free particles,” *J. Fluid Mech.*, vol. 41, no. 3, pp. 545–570, 1970.

[35] M. Theers, E. Westphal, G. Gompper, and R. G. Winkler, “Modeling a spheroidal microswimmer and cooperative swimming in a narrow slit,” *Soft Matter*, vol. 12, no. 35, pp. 7372–7385, 2016.

[36] T. Kiørboe, H. Jiang, R. J. Gonçalves, L. T. Nielsen, and N. Wadhwa, “Flow

disturbances generated by feeding and swimming zooplankton," *Proc. Natl. Acad. Sci.*, vol. 111, no. 32, pp. 11738–11743, 2014.

[37] K. Ishimoto, J. Cosson, and E. A. Gaffney, "A simulation study of sperm motility hydrodynamics near fish eggs and spheres," *J. Theor. Biol.*, vol. 389, pp. 187–197, 2016.

[38] R. Jeanneret, D. O. Pushkin, V. Kantsler, and M. Polin, "Entrainment dominates the interaction of microalgae with micron-sized objects," *Nat. Commun.*, vol. 7, 2016.

CHAPTER 7

SUMMARY AND CONCLUSIONS

The motion of bacteria and hydrodynamic interaction with microstructures in the fluid and other passive particles at low Reynolds number were discussed in this dissertation. The main results of this research and recommendations for future work are provided hereafter.

In Chapter 2, we reviewed different numerical approaches that were used to model the flagellated swimmers and pumping in Stokes flow. We created a benchmark model using a surface distributed regularized Stokeslets for the swimming and pumping flows. By comparison to the benchmark results, we calculated total errors corresponding to the other numerical methods (resistive force theory, slender body theory, and centerline distribution of regularized Stokeslets) for a wide range of flagellum helices. We also optimized the centerline distribution of Stokeslets and slender body theory by tuning the relevant parameters compared to the benchmark results. We concluded with providing a tabular guideline with errors and optimum relevant parameters for the centerline distribution of Stokeslets and slender body theory for selection of computational method for a wide and possible range of helices of the real and artificial swimmers.

In Chapter 3, we studied the effect of helical cell bodies on the swimming speed

and trajectory by direct comparison of the numerics to the observations. To validate our model, we compared our numerical model to the experiments from high-frame-rate digital tracking and image analysis for the helical (*H. pylori*) and its straight rod-shaped mutants swimming in mucin and broth solutions. Then, we used our models to explore the propulsive thrusts from the cell body and flagellum, respectively. Comparing helical body shapes to the rod-shaped geometries of the cell body, we calculated additive portion of the thrust due to the helicity of the cell body and found <15% extra propulsive thrust and <15% change in swimming speeds due to slower rotation rates of the cell body compared to the flagellum rotation rate.

Our calculations show that helical cell bodies add little additional propulsive thrust to increase the swimming velocity of the bacteria. These helical shapes can be considered as an upper bound for the propulsive thrust generated by the cell bodies. While microorganisms can be found in many different shapes of the cell body, the propulsion generated by the cell bodies is less than helical shapes for comparable geometries. These small changes in swimming velocity may affect chemotactability of bacteria ([1], [2]), which is not considered here and could be done in future work.

In Chapter 4, we showed that single-flagellated bacterial flicks are initiated by a dynamic instability during run-reverse-flick motility. It was believed that the static Euler buckling of the hook causes flicks in reorienting bacteria during its forward run. Our calculations show that the dynamic instabilities in the hook/flagellum system initiate the flicks and then the flexibility of the flagellar filament plays an important role in reorientation of the swimmer. We developed an efficient linear model for the hook that allows us to study a wide range of cell body geometries and hook stiffness of the dynamics

of a single-flagellated swimmer. Then we added the flexibility of the flagellum and found significant deformations of the flagellar filament.

Considering the full hydrodynamic interactions of the cell body with a flexible hook and flagellar filament is computationally expensive and we ignored interactions between the cell body and flexible flagellar filament. However, it is necessary for some cases to consider hydrodynamics interactions and flagellum flexibility that could be a direction for future work. With our new flexible model of the flagellum, we are able to study these kinds of interesting dynamics that can be considered in future researches. The flexibility of the flagellar filament can decrease effective viscosity to overcome local forces between molecules [3]–[5]. In addition, it can help bacteria to escape from trapping near objects and solid walls or some bacteria wraps and rotates the flagellum around its cell body and still is able to generate propulsive thrust to escape from trapping in narrow spacing [3], [6], [7].

In Chapter 5, we directly investigated the hydrodynamic interactions of a simple swimmer with microstructure in a complex biological fluid. This microstructure was assumed to have spherical or filamentous shapes with comparable size of the swimmer in different positions with respect to the swimmer. We calculated change in swimming fluctuations due to these different shapes and locations. We also considered contributions of random distributed spherical obstacles and networks of filamentous obstacles around the swimmer in changing the swimming speed compared to an unbounded fluid domain. We showed that the change in swimming velocity is closely related to the shape and location of a single obstacle and depends on the correlations in density and orientation of the network of obstacles.

We only treated long-range hydrodynamic interactions and prevented close

interactions and contact of the swimmer with obstacles during swimming. In most cases, the swimmer would closely interact with randomly oriented microstructure heterogeneities and it would be useful to investigate these interactions for more realistic swimmers as future work. For very close surfaces in microscale, other types of physicochemical interactions that are possible including Van der Waals, electrostatic, and chemical forces might be necessary to be considered in bacterial close interactions.

Many biological networks are flexible and can deform due to hydrodynamic forces and interactions with microorganisms. These elastic deformations may alter velocity fluctuations of the swimmer, which is not considered here and can be considered in future directions. In addition, we assumed uniform distribution of microstructures, which suggests microscopically isotropic medias, but recent experiments show many complex biological environments are anisotropic [8] and it would be interesting to study velocity fluctuations in an anisotropic medium.

In Chapter 6, we presented the approach of organisms with passive suspended particles in viscous fluid. We provide exact solutions assuming spherical shapes for the swimmer are driven by a constant force and the force-free target particle. Results from this model suggests that the approach for similar or bigger targets particle (compared to the swimmer size) can feasibly happen in mating or colonizing in real organisms' life. Then, we developed a numerical method for the approach of flagellated swimmers and see qualitatively similar results with the constant force driven case, such that approach is infeasible to smaller target particles.

Finally, we obtained exact solution for a force-free spherical squirmer approaching a force-free target sphere. Exploring the results for pushers and pullers, we found that

pullers can approach any size of targets, while for pushers, feasibility of approach depends on the current generate by the organism defined by the *squirmer parameter*.

Our exact solutions are designed to analyze the approach of spherical shapes translating along their centerline while microorganism are in very different shapes and approach each other or passive particles from different sides. Future work could resolve limitations in this work and expand it to microorganisms that are more realistic. The ellipsoidal squirmer model can describe the behavior of many ciliated microorganisms (i.e., *Opalina* and *Paramecium* [9], [10]) and analytical solutions could be obtained for the ellipsoidal swimmers' interactions with other spherical or ellipsoidal particles. Distributed propulsions are not limited to the ciliated microorganisms. In fact, the squirmer model is the limit for maximally distributed propulsion and many copepods use multiple appendages for their swimming and to manipulate particles around their cell bodies [11]. Finally, we only considered translational swimming velocity because of the geometries and approach is symmetric for two spheres translating along their common diameter while the rotations of the swimmer and target particles can be important for the side approaches and arbitrary shape of the microorganisms. Finding exact solutions is difficult for any arbitrary shapes, propulsion systems, and full hydrodynamic interactions, but numerical methods similar to ours can be useful for exploring more realistic and complicated geometries of swimmers and targets.

For this dissertation, I have considered three different aspects of locomotion at low Reynolds number, which were the effect of cell bodies on the swimming speed, the flexibility in the hook/flagellum system, and hydrodynamic interactions with complex environments and other passive particles in the fluid. Also, some future directions were

given separately for each chapter, which could be done in the context of that subject. Here, I discuss future directions of works that can be done in the context of what I have learned through this dissertation.

In Chapter 3, we find little additive propulsion coming from helical cell bodies of *H. pylori*, but still the question about "why they have helical cells?" remains unanswered. To find scientific explanations for this question, a first step could be investigation of motility and diffusion of *H. pylori* in a complex environment and gel. Swimming dynamics of *H. pylori* is greatly affected by acidic pH swimming in mucin gels [12]. For acidic pH 2 to 4, it can rotate its flagellar filament without any swimming speed in this range of pH, which is comparable to the stomach. To be able to swim, *H. pylori* needs to release urea around itself to neutralize the pH of the mucin to reduce mucin viscoelasticity [13]. More recently, Mirbagheri and Fu [14] have used a simple model to describe motility and diffusion of *H. pylori* and they found that it creates a moving pocket of fluid around the cell body and its swimming behavior is like in unconfined media. It would be useful to couple motility and diffusion equations for the helical cell bodies to study this problem more accurately. In addition, it would be interesting to study swimming dynamics of the helical cells in confined medias and their hydrodynamic interactions to the heterogeneity and immersed obstacles in the fluids like what we did in Chapter 5.

Development of artificial microswimmers has been a topic of research in the last decade due to the capability for drug delivery, microsurgery, and environmental sensing [15]–[20]. A wide variety of artificial microswimmers were designed, fabricated, and analyzed with biological inspiration [20]. Most of these micromachines are considered to be rigid in analytical and numerical analysis of their swimming dynamics, stability, and

controllability under external propulsive thrusts [15], [19]–[21]. However, a few reports that considering the flexibility in artificial microswimmers show that the stability and swimming dynamics could be different from rigid models [17], [20], [22]. In addition, some micromachines were fabricated using flexible flagella or cilia extracted from real organisms [18], [20], [23], which need to be considered as flexible parts in analyzing their dynamics and behaviors in viscous flow. For future directions, using our results and the more accurate numerical approach developed in Chapter 5 to simulate hydrodynamic interactions and flexibility of filaments can help us to understand the role of the flexibility in stability, controllability, and dynamics of artificial microswimmers.

7.1 References

[1] K. D. Young, "The selective value of bacterial shape," *Microbiol. Mol. Biol. Rev.*, vol. 70, no. 3, pp. 660–703, 2006.

[2] K. D. Young, "Bacterial morphology: why have different shapes?," *Current Opinion in Microbiology*, vol. 10, no. 6. pp. 596–600, 2007.

[3] M. Potomkin, M. Tournus, L. V Berlyand, and I. S. Aranson, "Flagella bending affects macroscopic properties of bacterial suspensions," *J. R. Soc. Interface*, vol. 14, no. 130, p. 20161031, 2017.

[4] J. Gachelin, G. Miño, H. Berthet, A. Lindner, A. Rousselet, and É. Clément, "Non-newtonian viscosity of escherichia coli suspensions," *Phys. Rev. Lett.*, vol. 110, no. 26, 2013.

[5] A. Sokolov and I. S. Aranson, "Reduction of viscosity in suspension of swimming bacteria," *Phys. Rev. Lett.*, vol. 103, no. 14, 2009.

[6] M. J. Kühn, F. K. Schmidt, B. Eckhardt, and K. M. Thormann, "Bacteria exploit a polymorphic instability of the flagellar filament to escape from traps," *Proc. Natl. Acad. Sci.*, vol. 114, no. 24, pp. 6340–6345, 2017.

[7] M. Hintsche *et al.*, "A polar bundle of flagella can drive bacterial swimming by pushing, pulling, or coiling around the cell body," *Sci. Rep.*, vol. 7, no. 1, 2017.

[8] S. Zhou, A. Sokolov, O. D. Lavrentovich, and I. S. Aranson, “Living liquid crystals,” *Proc. Natl. Acad. Sci.*, vol. 111, no. 4, pp. 1265–1270, 2014.

[9] E. Lauga and T. R. Powers, “The hydrodynamics of swimming microorganisms,” *Reports Prog. Phys.*, vol. 72, no. 9, p. 96601, 2009.

[10] M. Theers, E. Westphal, G. Gompper, and R. G. Winkler, “Modeling a spheroidal microswimmer and cooperative swimming in a narrow slit,” *Soft Matter*, vol. 12, no. 35, pp. 7372–7385, 2016.

[11] T. Kiørboe, H. Jiang, R. J. Gonçalves, L. T. Nielsen, and N. Wadhwa, “Flow disturbances generated by feeding and swimming zooplankton,” *Proc. Natl. Acad. Sci.*, vol. 111, no. 32, pp. 11738–11743, 2014.

[12] M. A. Constantino, M. Jabbarzadeh, H. C. Fu, and R. Bansil, “Helical and rod-shaped bacteria swim in helical trajectories with little additional propulsion from helical shape,” *Sci. Adv.*, vol. 2, no. 11, pp. e1601661–e1601661, 2016.

[13] J. P. Celli *et al.*, “Helicobacter pylori moves through mucus by reducing mucin viscoelasticity,” *Proc. Natl. Acad. Sci.*, vol. 106, no. 34, pp. 14321–14326, 2009.

[14] S. A. Mirbagheri and H. C. Fu, “Helicobacter pylori couples motility and diffusion to actively create a heterogeneous complex medium in gastric mucus,” *Phys. Rev. Lett.*, vol. 116, no. 19, 2016.

[15] A. Ghosh, D. Dasgupta, M. Pal, K. I. Morozov, A. M. Leshansky, and A. Ghosh, “Helical nanomachines as mobile viscometers,” *Adv. Funct. Mater.*, p. 1705687, 2018.

[16] J. Ali, U. K. Cheang, J. D. Martindale, M. Jabbarzadeh, H. C. Fu, and M. Jun Kim, “Bacteria-inspired nanorobots with flagellar polymorphic transformations and bundling,” *Sci. Rep.*, vol. 7, no. 1, 2017.

[17] U. K. Cheang, F. Meshkati, H. Kim, K. Lee, H. C. Fu, and M. J. Kim, “Versatile microrobotics using simple modular subunits,” *Sci. Rep.*, vol. 6, 2016.

[18] J. D. Martindale and H. C. Fu, “Autonomously responsive pumping by a bacterial flagellar forest: a mean-field approach,” *Phys. Rev. E*, vol. 96, no. 3, 2017.

[19] H. C. Fu, M. Jabbarzadeh, and F. Meshkati, “Magnetization directions and geometries of helical microswimmers for linear velocity-frequency response,” *Phys. Rev. E - Stat. Nonlinear, Soft Matter Phys.*, vol. 91, no. 4, 2015.

[20] M. Kim, A. Agung Julius, and E. Steager, *Microbiorobotics: biologically inspired microscale robotic systems*. 2012.

[21] F. Meshkati and H. C. Fu, “Modeling rigid magnetically rotated microswimmers: rotation axes, bistability, and controllability,” *Phys. Rev. E - Stat. Nonlinear, Soft Matter Phys.*, vol. 90, no. 6, 2014.

[22] U. K. Cheang, F. Meshkati, D. Kim, M. J. Kim, and H. C. Fu, “Minimal geometric requirements for micropropulsion via magnetic rotation,” *Phys. Rev. E - Stat. Nonlinear, Soft Matter Phys.*, vol. 90, no. 3, 2014.

[23] J. Ali, U. K. Cheang, J. D. Martindale, M. Jabbarzadeh, H. C. Fu, and M. Jun Kim, “Bacteria-inspired nanorobots with flagellar polymorphic transformations and bundling,” *Sci. Rep.*, vol. 7, no. 1, 2017.

APPENDIX

COPMUTER CODE (C++) FOR THE METHOD OF REGULARIZED STOKESLET TO CALCULATE BACTERIAL MOTION IN VISCOUS FLUIDS

```
#include <stdio.h>
#include <stdlib.h>
#include <string.h>
#include <ctype.h>
#include <assert.h>

#include <cuda_runtime.h>

#include "cublas_v2.h"
#include "cusolverDn.h"
#include "helper_cuda.h"

#include "helper_cusolver.h"

#define PI 3.14159265358979323846

*  solve A*x = b by LU with partial pivoting
int linearSolverLU(
       cusolverDnHandle_t handle, int n, double *A, int lda, double *b, int
nrhs)
{
       int bufferSize = 0;
       int *info = NULL;
       double *buffer = NULL;
       int *ipiv = NULL; // pivoting sequence
       int h_info = 0;

       checkCudaErrors(cusolverDnDgetrf_bufferSize(handle, n, n, (double*)A,
       lda, &bufferSize));

       checkCudaErrors(cudaMalloc(&info, sizeof(int)));
       checkCudaErrors(cudaMalloc(&buffer, sizeof(double)*bufferSize));
       checkCudaErrors(cudaMalloc(&ipiv, sizeof(int)*n));

       checkCudaErrors(cudaMemset(info, 0, sizeof(int)));

       checkCudaErrors(cusolverDnDgetrf(handle, n, n, A, lda, buffer, ipiv,
       info));
       checkCudaErrors(cudaMemcpy(&h_info, info, sizeof(int),
       cudaMemcpyDeviceToHost));

       if ( 0 != h_info ){fprintf(stderr, "Error: LU factorization failed\n");}
              checkCudaErrors(cusolverDnDgetrs(handle, CUBLAS_OP_N, n, nrhs, A,
       lda, ipiv, b, n, info));
       checkCudaErrors(cudaDeviceSynchronize());

       if (info  ) { checkCudaErrors(cudaFree(info  )); }
       if (buffer) { checkCudaErrors(cudaFree(buffer)); }
       if (A     ) { checkCudaErrors(cudaFree(A)); }
       if (ipiv  ) { checkCudaErrors(cudaFree(ipiv));}

       return 0;
}
```

```
int main (int argc, char *argv[])
{
struct testOpts opts;
cusolverDnHandle_t handle = NULL;
cusolverStatus_t cusolver_status = CUSOLVER_STATUS_SUCCESS;
cublasHandle_t cublasHandle = NULL;
cudaStream_t stream = NULL;

double **cTemp = NULL, **c = NULL, start, stop, time_solve;

int i, j, k, m, n, numStokesletsTail, numStokesletsHead, Ntotal, Ntime, it,
index=0 lwork = 0, ii,jj,numC;
double vis = 1e-3, WH = 0, WT = 2*PI*340,stokesletradiushead = 0,
stokesletradiustail = 0.010053/3,xcm = 0, ycm = 0, zcm = 0, dt = 1.000/340/50,
Time = 50*dt, Shh, xmn, ymn, zmn, rmn, angle,normO, OMEGA[3], theta, Ld1, Ld2,
Ld3, Fxh = 0, Fyh = 0, Fzh = 0, Txh = 0, Tyh = 0, Tzh = 0, q0, q1, q2, q3,
tail1, tail2, tail3, **tailTemp = NULL, **headTemp = NULL,**head = NULL,
**tail = NULL, *d_work = NULL;

const double eye[3][3] = {{1, 0, 0},{0, 1, 0},{0, 0, 1}};
double irx[3][3] = {0, 0, 0, 0, 0, 0, 0, 0, 0};

const double zero = 0.0, one = 1.0;

char *hname[100] = {"HeadRK1.txt"}, *tname[100] = {"TailLK.txt"};
char *OP[100] = {"OUTKK.txt"};

char *HNAME,*TNAME,*OUTP;

FILE *fidc;

cTemp = (double**)malloc(1000*sizeof(double*));
for(i=0; i<1000; i++)
       cTemp[i] = (double*)malloc(3*sizeof(double));
fidc = fopen("DSh.txt","r");
j = 0;
while(fscanf(fidc,"%lf", &cTemp[j][0]) != EOF)
       ++j;   fclose(fidc);
numC = j;

double *d_G = NULL, *d_Ld = NULL, *d_IRX = NULL, *d_IRXT = NULL, *d_IRXLd =
NULL, *d_invGIRX= NULL, *d_invGLd = NULL, *d_MB = NULL, *d_M = NULL, *d_B =
NULL, *d_Vcm1  = NULL, *GHH = NULL, *GHT = NULL, *GTH = NULL, *GTT = NULL, *G
= NULL, *Ld = NULL, *IRX = NULL, *IRXT = NULL, *IRXLd = NULL, *invGIRX= NULL,
*invGLd = NULL, *MB = NULL, *M = NULL, *B = NULL, *Vcm1 = NULL, *BB = NULL,
*Vcm = NULL;

int *IPIV = NULL, *ipiv = NULL, *devInfo = NULL, info_gpu = 0;
FILE *fid;
numStokesletsTail = 10000;numStokesletsHead = 4000; Ntotal = 14000;

printf("Allocating Matrices\n");
GHH  =
(double*)malloc(3*numStokesletsHead*3*numStokesletsHead*sizeof(double));
```

```
GHT  =
(double*)malloc(3*numStokesletsHead*3*numStokesletsTail*sizeof(double));
GTH  =
(double*)malloc(3*numStokesletsTail*3*numStokesletsHead*sizeof(double));
GTT  =
(double*)malloc(3*numStokesletsTail*3*numStokesletsTail*sizeof(double));
G    = (double*)malloc(3*Ntotal*3*Ntotal*sizeof(double));
IPIV = (int*)malloc(Ntotal*sizeof(int));
Ld   = (double*)malloc(3*Ntotal*sizeof(double));
IRX  = (double*)malloc(3*Ntotal*6*sizeof(double));
IRXT = (double*)malloc(6*3*Ntotal*sizeof(double));
IRXLd= (double*)malloc(3*Ntotal*7*sizeof(double));
invGIRX= (double*)malloc(3*Ntotal*6*sizeof(double));
invGLd = (double*)malloc(3*Ntotal*1*sizeof(double));
MB   = (double*)malloc(6*7*sizeof(double));
M    = (double*)malloc(6*6*sizeof(double));
B    = (double*)malloc(6*1*sizeof(double));
Vcm1 = (double*)malloc(7*1*sizeof(double));
BB   = (double*)malloc(6*1*sizeof(double));
Vcm  = (double*)malloc(6*1*sizeof(double));

for(ii=0;ii<100;ii++){
       stokesletradiushead = 1.000/3.000 * cTemp[ii][0];
       HNAME = hname[ii];   TNAME = tname[ii];     OUTP = OP[ii];

tailTemp = (double**)malloc(10000*sizeof(double*));
for(i=0; i<10000; i++)
       tailTemp[i] = (double*)malloc(3*sizeof(double));

headTemp = (double**)malloc(10000*sizeof(double*));
for(i=0; i<10000; i++)
       headTemp[i] = (double*)malloc(3*sizeof(double));

fid = fopen(TNAME,"r");

j = 0;
while(fscanf(fid,"%lf,%lf,%lf", &tailTemp[j][0], &tailTemp[j][1],
&tailTemp[j][2]) != EOF)
       ++j;
fclose(fid);
numStokesletsTail = j;

tail = (double**)malloc(numStokesletsTail*sizeof(double*));
tail[0] = (double*)malloc(numStokesletsTail*3*sizeof(double));
for(i=1; i<numStokesletsTail; i++)
             tail[i] = tail[i-1] + (long)3;
for(i=0; i<numStokesletsTail; i++){
tail[i][0] = tailTemp[i][0];     tail[i][1] = tailTemp[i][1];
tail[i][2] = tailTemp[i][2];     free(tailTemp[i]);        }

j = 0;
fid = fopen(HNAME,"r");
while(fscanf(fid,"%lf,%lf,%lf", &headTemp[j][0], &headTemp[j][1],
&headTemp[j][2]) != EOF)
++j;
```

```
fclose(fid);
numStokesletsHead = j;

head = (double**)malloc(numStokesletsHead*sizeof(double*));
head[0] = (double*)malloc(numStokesletsHead*3*sizeof(double));
for(i=1; i<numStokesletsHead; i++)
       head[i] = head[i-1] + (long)3;

for(i=0; i<numStokesletsHead; i++){
       head[i][0] = headTemp[i][0];     head[i][1] = headTemp[i][1];
       head[i][2] = headTemp[i][2];     free(headTemp[i]);  }

Ntotal = numStokesletsHead + numStokesletsTail;
printf("numStokesletsHead   =   %d\n",numStokesletsHead);
printf("numStokesletsTail   =   %d\n",numStokesletsTail);
printf("numStokesletstotal  =   %d\n",Ntotal);

//     printf("GHH -----------------------------\n");
for(m=1; m<=numStokesletsHead; m++){
for(n=1; n<=numStokesletsHead; n++){
if(m==n){
Shh = 2.00/(8*PI*vis*stokesletradiushead);
for(i=1; i<=3; i++){
for(j=1; j<=3; j++){
if(i==j){
GHH[(3*m-4+i)+3*numStokesletsHead*(3*n-4+j)] = Shh;}else{
GHH[(3*m-4+i)+3*numStokesletsHead*(3*n-4+j)] = 0;}}}}else{
xmn = head[m-1][0] - head[n-1][0];  ymn = head[m-1][1] - head[n-1][1];  zmn =
head[m-1][2] - head[n-1][2];
rmn = sqrt(xmn*xmn + ymn*ymn + zmn*zmn);
for(i=1; i<=3; i++){
for(j=1; j<=3; j++){
if(i==1&&j==1) Shh =
(pow(rmn,2)+2*pow(stokesletradiushead,2)+xmn*xmn)/pow(pow(rmn,2)+pow(stokeslet
radiushead,2),1.5);
if(i==2&&j==2) Shh =
(pow(rmn,2)+2*pow(stokesletradiushead,2)+ymn*ymn)/pow(pow(rmn,2)+pow(stokeslet
radiushead,2),1.5);
if(i==3&&j==3) Shh =
(pow(rmn,2)+2*pow(stokesletradiushead,2)+zmn*zmn)/pow(pow(rmn,2)+pow(stokeslet
radiushead,2),1.5);
if(i==1&&j==2) Shh = (xmn*ymn)/pow(pow(rmn,2)+pow(stokesletradiushead,2),1.5);
if(i==1&&j==3) Shh = (xmn*zmn)/pow(pow(rmn,2)+pow(stokesletradiushead,2),1.5);
if(i==2&&j==1) Shh = (ymn*xmn)/pow(pow(rmn,2)+pow(stokesletradiushead,2),1.5);
if(i==2&&j==3) Shh = (ymn*zmn)/pow(pow(rmn,2)+pow(stokesletradiushead,2),1.5);
if(i==3&&j==1) Shh = (zmn*xmn)/pow(pow(rmn,2)+pow(stokesletradiushead,2),1.5);
if(i==3&&j==2) Shh = (zmn*ymn)/pow(pow(rmn,2)+pow(stokesletradiushead,2),1.5);
Shh /= 8*PI*vis;
GHH[(3*m-4+i)+3*numStokesletsHead*(3*n-4+j)] = Shh;}}}}}

Ntime = ceil(Time/dt);
Ntime = 1;
for(it=0;it<Ntime;it++){
start = second();
for(m=1; m<=numStokesletsTail; m++){
```

```
for(n=1; n<=numStokesletsHead; n++){
xmn = tail[m-1][0] - head[n-1][0];  ymn = tail[m-1][1] - head[n-1][1];  zmn =
tail[m-1][2] - head[n-1][2];
rmn = sqrt(xmn*xmn + ymn*ymn + zmn*zmn);
for(i=1; i<=3; i++){
for(j=1; j<=3; j++){
if(i==1&&j==1) Shh =
(pow(rmn,2)+2*pow(stokesletradiushead,2)+xmn*xmn)/pow(pow(rmn,2)+pow(stokeslet
radiushead,2),1.5);
if(i==2&&j==2) Shh =
(pow(rmn,2)+2*pow(stokesletradiushead,2)+ymn*ymn)/pow(pow(rmn,2)+pow(stokeslet
radiushead,2),1.5);
if(i==3&&j==3) Shh =
(pow(rmn,2)+2*pow(stokesletradiushead,2)+zmn*zmn)/pow(pow(rmn,2)+pow(stokeslet
radiushead,2),1.5);
if(i==1&&j==2) Shh = (xmn*ymn)/pow(pow(rmn,2)+pow(stokesletradiushead,2),1.5);
if(i==1&&j==3) Shh = (xmn*zmn)/pow(pow(rmn,2)+pow(stokesletradiushead,2),1.5);
if(i==2&&j==1) Shh = (ymn*xmn)/pow(pow(rmn,2)+pow(stokesletradiushead,2),1.5);
if(i==2&&j==3) Shh = (ymn*zmn)/pow(pow(rmn,2)+pow(stokesletradiushead,2),1.5);
if(i==3&&j==1) Shh = (zmn*xmn)/pow(pow(rmn,2)+pow(stokesletradiushead,2),1.5);
if(i==3&&j==2) Shh = (zmn*ymn)/pow(pow(rmn,2)+pow(stokesletradiushead,2),1.5);
Shh = Shh/(8*PI*vis);
GTH[(3*m-4+i)+3*numStokesletsTail*(3*n-4+j)] = Shh;}}}}

      //           printf("GHT -----------------------------\n");
for(m=1; m<=numStokesletsHead; m++){
for(n=1; n<=numStokesletsTail; n++){
xmn = head[m-1][0] - tail[n-1][0];  ymn = head[m-1][1] - tail[n-1][1];  zmn =
head[m-1][2] - tail[n-1][2];
rmn = sqrt(xmn*xmn + ymn*ymn + zmn*zmn);
for(i=1; i<=3; i++){
for(j=1; j<=3; j++){
if(i==1&&j==1) Shh =
(pow(rmn,2)+2*pow(stokesletradiustail,2)+xmn*xmn)/pow(pow(rmn,2)+pow(stokeslet
radiustail,2),1.5);
if(i==2&&j==2) Shh =
(pow(rmn,2)+2*pow(stokesletradiustail,2)+ymn*ymn)/pow(pow(rmn,2)+pow(stokeslet
radiustail,2),1.5);
if(i==3&&j==3) Shh =
(pow(rmn,2)+2*pow(stokesletradiustail,2)+zmn*zmn)/pow(pow(rmn,2)+pow(stokeslet
radiustail,2),1.5);
if(i==1&&j==2) Shh = (xmn*ymn)/pow(pow(rmn,2)+pow(stokesletradiustail,2),1.5);
if(i==1&&j==3) Shh = (xmn*zmn)/pow(pow(rmn,2)+pow(stokesletradiustail,2),1.5);
if(i==2&&j==1) Shh = (ymn*xmn)/pow(pow(rmn,2)+pow(stokesletradiustail,2),1.5);
if(i==2&&j==3) Shh = (ymn*zmn)/pow(pow(rmn,2)+pow(stokesletradiustail,2),1.5);
if(i==3&&j==1) Shh = (zmn*xmn)/pow(pow(rmn,2)+pow(stokesletradiustail,2),1.5);
if(i==3&&j==2) Shh = (zmn*ymn)/pow(pow(rmn,2)+pow(stokesletradiustail,2),1.5);
Shh = Shh/(8*PI*vis);
GHT[(3*m-4+i)+3*numStokesletsHead*(3*n-4+j)] = Shh;}}}}

//           printf("GTT -----------------------------\n");
for(m=1; m<=numStokesletsTail; m++){
for(n=1; n<=numStokesletsTail; n++){
if(m==n){
Shh = 2.00/(8*PI*vis*stokesletradiustail);
```

```
for(i=1; i<=3; i++){
for(j=1; j<=3; j++){
if(i==j){
GTT[(3*m-4+i)+3*numStokesletsTail*(3*n-4+j)] = Shh;
}else{
GTT[(3*m-4+i)+3*numStokesletsTail*(3*n-4+j)] = 0;
}}}}else{
xmn = tail[m-1][0] - tail[n-1][0];  ymn = tail[m-1][1] - tail[n-1][1];  zmn =
tail[m-1][2] - tail[n-1][2];
rmn = sqrt(xmn*xmn + ymn*ymn + zmn*zmn);

for(i=1; i<=3; i++){
for(j=1; j<=3; j++){
if(i==1&&j==1) Shh =
(pow(rmn,2)+2*pow(stokesletradiustail,2)+xmn*xmn)/pow(pow(rmn,2)+pow(stokeslet
radiustail,2),1.5);
if(i==2&&j==2) Shh =
(pow(rmn,2)+2*pow(stokesletradiustail,2)+ymn*ymn)/pow(pow(rmn,2)+pow(stokeslet
radiustail,2),1.5);
if(i==3&&j==3) Shh =
(pow(rmn,2)+2*pow(stokesletradiustail,2)+zmn*zmn)/pow(pow(rmn,2)+pow(stokeslet
radiustail,2),1.5);
if(i==1&&j==2) Shh = (xmn*ymn)/pow(pow(rmn,2)+pow(stokesletradiustail,2),1.5);
if(i==1&&j==3) Shh = (xmn*zmn)/pow(pow(rmn,2)
+pow(stokesletradiustail,2),1.5);
if(i==2&&j==1) Shh = (ymn*xmn)/pow(pow(rmn,2)+pow(stokesletradiustail,2),1.5);
if(i==2&&j==3) Shh = (ymn*zmn)/pow(pow(rmn,2)+pow(stokesletradiustail,2),1.5);
if(i==3&&j==1) Shh = (zmn*xmn)/pow(pow(rmn,2)+pow(stokesletradiustail,2),1.5);
if(i==3&&j==2) Shh = (zmn*ymn)/pow(pow(rmn,2)+pow(stokesletradiustail,2),1.5);
Shh = Shh/(8*PI*vis);
GTT[(3*m-4+i)+3*numStokesletsTail*(3*n-4+j)] = Shh;}}}}}

      //           printf("G  ----------------------------\n");
for(i=1;i<=3*Ntotal;i++){
      for(j=1;j<=3*Ntotal;j++){
      if((i<=3*numStokesletsHead)&&(j<=3*numStokesletsHead)){G[i-
      1+(3*Ntotal)*(j-1)] = GHH[i-1+(3*numStokesletsHead)*(j-1)];}
      if((i> 3*numStokesletsHead)&&(j<=3*numStokesletsHead)){G[i-
      1+(3*Ntotal)*(j-1)] = GTH[i-3*numStokesletsHead-
      1+(3*numStokesletsTail)*(j-1)];}
      if((i<=3*numStokesletsHead)&&(j> 3*numStokesletsHead)){G[i-
      1+(3*Ntotal)*(j-1)] = GHT[i-1+(3*numStokesletsHead)*(j-
      3*numStokesletsHead-1)];}
      if((i> 3*numStokesletsHead)&&(j> 3*numStokesletsHead)){G[i-
      1+(3*Ntotal)*(j-1)] = GTT[i-3*numStokesletsHead-
      1+(3*numStokesletsTail)*(j-3*numStokesletsHead-1)];}
}}

      //           printf("Ld ----------------------------\n");
for(i=1; i<=Ntotal; i++){
if(i<=numStokesletsHead){
irx[0][0] = 0;  irx[0][1] =  head[i-1][2]-zcm;  irx[0][2] = -head[i-1][1]+ycm;
irx[1][1] = 0;  irx[1][0] = -head[i-1][2]+zcm;  irx[1][2] =  head[i-1][0]-xcm;
irx[2][2] = 0;  irx[2][0] =  head[i-1][1]-ycm;  irx[2][1] = -head[i-1][0]+xcm;
for(j=1; j<=3; j++){
```

```
for(k=1; k<=3; k++){
	IRX[(3*i-4+j)+3*Ntotal*(k-1)]   = eye[j-1][k-1];
	IRX[(3*i-4+j)+3*Ntotal*(k+2)]   = irx[j-1][k-1];
	IRXT[(k-1)+6*(3*i-4+j)]   = eye[j-1][k-1];
	IRXT[(k+2)+6*(3*i-4+j)]   = irx[j-1][k-1];
	IRXLd[(3*i-4+j)+3*Ntotal*(k-1)]   = eye[j-1][k-1];
	IRXLd[(3*i-4+j)+3*Ntotal*(k+2)]   = irx[j-1][k-1];}}
	angle = atan2(head[i-1][2],head[i-1][1]);
	Ld1 = 0;
	Ld2 = WH*sqrt(pow(head[i-1][1],2)+pow(head[i-1][2],2))*(-sin(angle));
	Ld3 = WH*sqrt(pow(head[i-1][1],2)+pow(head[i-1][2],2))*(+cos(angle));
}else{
	irx[0][0] = 0;  irx[0][1] =  tail[i-numStokesletsHead-1][2]-zcm;
	irx[0][2] = -tail[i-numStokesletsHead-1][1]+ycm;
	irx[1][1] = 0;  irx[1][0] = -tail[i-numStokesletsHead-1][2]+zcm;
	irx[1][2] =  tail[i-numStokesletsHead-1][0]-xcm;
	irx[2][2] = 0;  irx[2][0] =  tail[i-numStokesletsHead-1][1]-ycm;
	irx[2][1] = -tail[i-numStokesletsHead-1][0]+xcm;
for(j=1; j<=3; j++){
	for(k=1; k<=3; k++){
		IRX[(3*i-4+j)+3*Ntotal*(k-1)]   = eye[j-1][k-1];
		IRX[(3*i-4+j)+3*Ntotal*(k+2)]   = irx[j-1][k-1];
		IRXT[(k-1)+6*(3*i-4+j)]   = eye[j-1][k-1];
		IRXT[(k+2)+6*(3*i-4+j)]   = irx[j-1][k-1];
		IRXLd[(3*i-4+j)+3*Ntotal*(k-1)]   = eye[j-1][k-1];
		IRXLd[(3*i-4+j)+3*Ntotal*(k+2)]   = irx[j-1][k-1];
		}}

angle = atan2(tail[i-numStokesletsHead-1][2],tail[i-numStokesletsHead-1][1]);
Ld1 = 0;
Ld2 = WT*sqrt(pow(tail[i-numStokesletsHead-1][1],2)+pow(tail[i-
numStokesletsHead-1][2],2))*(-sin(angle));
Ld3 = WT*sqrt(pow(tail[i-numStokesletsHead-1][1],2)+pow(tail[i-
numStokesletsHead-1][2],2))*(+cos(angle));
		}
Ld[3*i-3] = Ld1;    Ld[3*i-2] = Ld2;    Ld[3*i-1] = Ld3;
IRXLd[18*Ntotal+3*i-3] = Ld1;    IRXLd[18*Ntotal+3*i-2] = Ld2;
IRXLd[18*Ntotal+3*i-1] = Ld3;}
                    //          copy to device
checkCudaErrors(cudaMalloc ((void**)&d_G      , sizeof(double)    *
3*Ntotal*3*Ntotal));
checkCudaErrors(cudaMalloc ((void**)&d_Ld     , sizeof(double)    * 3*Ntotal));
checkCudaErrors(cudaMalloc ((void**)&d_IRXT   , sizeof(double)    *
3*Ntotal*6));
checkCudaErrors(cudaMalloc ((void**)&d_IRXLd  , sizeof(double)    *
3*Ntotal*7));
checkCudaErrors(cudaMalloc ((void**)&d_invGLd , sizeof(double)  *
3*Ntotal*1));
checkCudaErrors(cudaMalloc ((void**)&d_MB     , sizeof(double)  * 6*7));
checkCudaErrors(cudaMalloc ((void**)&d_M        , sizeof(double)  * 6*6));
checkCudaErrors(cudaMalloc ((void**)&d_B        , sizeof(double)  * 6*1));
checkCudaErrors(cudaMalloc ((void**)&d_Vcm1   , sizeof(double)  * 7*1));

checkCudaErrors(cudaMemcpy(d_G,G,sizeof(double)*3*Ntotal*3*Ntotal,
cudaMemcpyHostToDevice));
```

```
checkCudaErrors(cudaMemcpy(d_Ld, Ld,sizeof(double)*3*Ntotal,
cudaMemcpyHostToDevice));
checkCudaErrors(cudaMemcpy(d_IRXT, IRXT , sizeof(double) * 3*Ntotal * 6
, cudaMemcpyHostToDevice));
checkCudaErrors(cudaMemcpy(d_IRXLd,IRXLd, sizeof(double) * 3*Ntotal * 7
, cudaMemcpyHostToDevice));
checkCudaErrors(cusolverDnCreate(&handle));
checkCudaErrors(cublasCreate(&cublasHandle));
checkCudaErrors(cudaStreamCreate(&stream));
checkCudaErrors(cusolverDnSetStream(handle, stream));
checkCudaErrors(cublasSetStream(cublasHandle, stream));

linearSolverLU(handle, 3*Ntotal, d_G, 3*Ntotal, d_IRXLd, 7);
checkCudaErrors(cublasDgemm_v2(cublasHandle, CUBLAS_OP_N, CUBLAS_OP_N,
6,7,3*Ntotal,&one,d_IRXT,6, d_IRXLd, 3*Ntotal, &zero, d_MB, 6));
checkCudaErrors(cudaMemcpy(MB,d_MB,sizeof(double)*6*7,
cudaMemcpyDeviceToHost));
for(i=0;i<6*7;i++){ if(i<6*6){M[i] = MB[i];} if(i>=6*6){ B[i-36] = -
MB[i];}if(i>=6*6){BB[i-36] = -MB[i];}}
checkCudaErrors(cudaMemcpy(d_M,M,sizeof(double)*6*6,cudaMemcpyHostToDevice));
checkCudaErrors(cudaMemcpy(d_B,B,sizeof(double)*6*1,cudaMemcpyHostToDevice));

linearSolverLU(handle,6, d_M, 6, d_B, 1);
checkCudaErrors(cudaMemcpy(B,d_B,sizeof(double)*6*1,cudaMemcpyDeviceToHost));
for(i=0;i<6;i++){Vcm[i]=B[i];}
for(i=0;i<6;i++){Vcm1[i]=Vcm[i];}      Vcm1[6] = 1.0;
checkCudaErrors(cudaMemcpy(d_Vcm1,Vcm1,sizeof(double)*7*1,cudaMemcpyHostToDevi
ce));
checkCudaErrors(cublasDgemm_v2(cublasHandle, CUBLAS_OP_N, CUBLAS_OP_N,
3*Ntotal, 1, 7, &one, d_IRXLd, 3*Ntotal, d_Vcm1, 7, &zero, d_invGLd,
3*Ntotal));
checkCudaErrors(cudaMemcpy(invGLd, d_invGLd, sizeof(double)*3*Ntotal*1,
cudaMemcpyDeviceToHost));

Fxh = 0;    Fyh = 0;    Fzh = 0;    Txh = 0;    Tyh = 0;    Tzh = 0;
for(i=0;i<numStokesletsHead;i++){
       Fxh +=  invGLd[3*i];     Fyh += invGLd[3*i+1];     Fzh += invGLd[3*i+2];
       Txh += head[i][1]*invGLd[3*i+2]-head[i][2]*invGLd[3*i+1];
       Tyh += head[i][2]*invGLd[3*i]  -head[i][0]*invGLd[3*i+2];
       Tzh += head[i][0]*invGLd[3*i+1]-head[i][1]*invGLd[3*i];    }

for(i=0;i<numStokesletsTail;i++){
       tail1 = tail[i][0];
       tail2 = cos(WT*dt)*tail[i][1] - sin(WT*dt)*tail[i][2];
       tail3 = sin(WT*dt)*tail[i][1] + cos(WT*dt)*tail[i][2];
       tail[i][0] = tail1; tail[i][1] = tail2; tail[i][2] = tail3;}

fid =
fopen(OUTP,"a");fprintf(fid,"%f,%f,%f,%f,%f,%f,%f,%f,%f,%f,%f,%f,%f,%f\n",it*dt,V
cm[0], Vcm[1], Vcm[2], Vcm[3], Vcm[4], Vcm[5], Fxh, Fyh, Fzh, Txh, Tyh,
Tzh);fclose(fid);
stop = second();    time_solve = stop - start;
printf("Case:\t %d iteration:\t%i of %4.0f\t Time Left:\t%3.3f
minutes.\n",ii+1,it+1,ceil(Time/dt),(Ntime-it)*time_solve/60); }}
cudaDeviceReset();  return 0;}
```